Vibrations and Phase Stabilities of Crystalline Coronene

(Alternate Format Thesis)

Bannister, Nicola

Award date:
2021

Awarding institution:
University of Bath

Vibrations and Phase Stabilities of Crystalline Coronene

submitted by

Nicola Bannister

for the degree of Doctor of Philosophy

of the

University of Bath

Department of Physics

December 2020

COPYRIGHT

Declaration of any previous submission of the work

The material presented here for examination for the award of a higher degree by research has not been incorporated into a submission for another degree.

Candidate's signature .....

Declaration of authorship

I am the author of this thesis, and the work described therein was carried out by myself personally, with the exception of x-ray diffraction measurements presented in Chapters 3, 4 and 5 which were performed under instruction by Dr. G. Kociok-Köhn in the Material and Chemical Characterisation Facility (MC^2) at University of Bath. Dr. G. Kociok-Köhn also provided details of the methodology. Dr. S. Crampin and Dr. E. Da Como contributed to the formulation of ideas, supervised the theoretical and experimental programmes and contributed to the interpretation of data and writing of the manuscript presented in Chapter 5. Dr. E. Da Como also assisted with purification and crystal growth of γ-coronene presented in Chapter 3. Dr. J. Skelton provided advice on the DFT-D3 calculations presented in Chapters 4, 5 and 6. Dr. T. Batten assisted with Raman measurements presented in Chapter 5.

Candidate's signature .....

Acknowledgements

Firstly I would like to thank my supervisors Dr. Simon Crampin and Dr. Enrico Da Como for their invaluable advice, continuous support, and patience during my PhD. I would also like to thank Dr. Jonathan Skelton, University of Manchester, for his assistance with the Density Functional Theory calculations at every stage of the research project. My gratitude extends to Dr. Tim Batten, Renishaw, for his assistance with the low-frequency Raman measurements and to Dr. Gabrielle Kociock Köhn, Material and Chemical Characterisation Facility (MC^2), University of Bath, for performing the x-ray diffraction measurements as part of this research project. Next I would like to offer my sincere thanks to Prof. Daniel Wolverson, University of Bath, for allowing me to borrow his equipment for the polarised Raman measurements. I am also grateful to Wendy Lambson for her technical support during chemical laboratory work. I would like to offer my special thanks to Dr. Charles Sayers for all his help and for being such a fantastic colleague throughout our time as PhD students.

My gratitude extends to the Engineering and Physical Sciences Research Council (EPSRC) Centre for Doctoral Training in Condensed Matter Physics (CDT-CMP) and their staff for providing this opportunity, funding this project and supporting me throughout. To my fellow cohort members, thank you for your friendship and encouragement over the years. My appreciation also goes to the Balena High Performance Computing (HPC) Service at the University of Bath and the Material and Chemical Characterisation Facility (MC^2) at the University of Bath.

I would like to offer my thanks for the support I have received from the University of Bath student services and external services. I have valued this greatly. My appreciation also goes to all the friends I have made along this journey, for all the laughter we have shared and support you have shown. Last but not least, I would like to express my deep and sincere gratitude to my parents Julie and David, my brother Matt and my partner Peter for their unwavering love, support and encouragement over the past few years.

Abstract

Polymorphism, the ability of a material to exist in multiple structures, is a general phenomenon that is important in a wide range of fields from single crystal organic electronics to pharmaceuticals, food and explosives. This extensive impact makes predicting the existence and stability of polymorphs valuable, yet due to the large configurational space and small energy differences it remains a challenge. Here the two normal pressure polymorphs of coronene, a model molecular system for nanographenes and disk like organic semiconductors, are investigated by Raman spectroscopy and dispersion corrected Density Functional Theory (DFT-D). γ-coronene is the naturally occurring form, whilst the low temperature β-phase, only recently discovered in 2015, requires the application of a magnetic field during crystal growth to form crystals in standard conditions. This work investigates the crystal growth of β-coronene, the vibrations of both polymorphs and their thermodynamic phase stabilities.

High-purity crystals of γ-coronene were successfully grown using a physical vapour transport method. Crystal growth of β-coronene was attempted, but no crystals of β-coronene were formed. Instead the β-phase was accessed by cooling γ-coronene crystals below the phase transition temperature of $\sim$150 K. Structures of both polymorphs relaxed using DFT-D3 reproduce experimental lattice parameters to within 1.6% (2.1%) for γ- (β-) coronene. Raman active intramolecular and lattice vibrations have been followed across the γ- to β-phase transition, with DFT-D3 calculations used to interpret the Raman spectra and, on the basis of polarisation dependence of peak positions and intensities, mode assignment performed. The vibrational density of states and dispersion curves are calculated and Gibbs free energies in the harmonic and quasi-harmonic approximations determined. At all temperatures and in both approximations γ-coronene is predicted to be the most stable polymorph with no phase transition indicated. The error in the calculated Gibbs free energies is estimated to be 10-20 meV.

Recommendations for future work are made. Further investigation is required into the crystal growth of β-coronene to produce a reliable and reproducible method. Vibrational frequency calculations including anharmonic effects would be beneficial in solving the few remaining mysteries in the intramolecular Raman spectra. Calculating phase stabilities with higher level theories is recommended, specifically relaxing structures and calculating lattice energies using the hybrid many-body interaction method.

Contents

Chapter 1

Introduction

Technology underpins much of today's society. We are constantly interacting with computers: in 2012 it was estimated that each person was surrounded by an average of 30-40 processors daily [1]. Since then the amount of technology we use has continued to increase, with the covid-19 pandemic and subsequent lockdowns massively accelerating this growth, in particular our internet usage with internet services reporting an increase of 40-100% compared to pre-lockdown levels [2]. The majority of this technology is based on silicon electronics, however there are limits as to what silicon can do. Organic electronics has the capability to overcome some of these limitations and as such is an area of highly active research [1] and an industry in its own right [3]. Low-cost, light-weight, flexible, disposable and wearable electronics, light-emitting diodes, smart tags, sensors and solar cells are some of the fields of active development [4, 5]. Yet our understanding of the fundamental properties of organic electronics is still limited. Greater understanding will aid in the design of better semiconductors, lead to improvements in device performance and possibly result in novel device concepts and prototypes [4].

In the last decade electronic devices based on single crystals of organic semiconductors have seen rapid development [6] allowing intrinsic fundamental electronic transport properties to be accessed. This increased interest in organic single crystals is due to their high structural order, high chemical purity and the availability of efficient methods of fabrication [5]. A critical requirement in this case is that of good phase homogeneity and as such the understanding and control of polymorphism, the ability of a chemical compound to exist in multiple structures, is necessary [7].

This project investigates the vibrations and phase stability of the two normal pressure polymorphs of the molecular crystal coronene using dispersion-corrected Density

Functional Theory (DFT-D) and Raman spectroscopy. Crystal growth of the recently synthesised β polymorph [8] is also pursued.

1.1 Polymorphism and why it is important

Polymorphism is the ability of a chemical compound to exist in two or more different crystalline structures, that is identical liquid/vapour states are formed from two or more crystal structures [9, 10]. The same concept applied to elements is known as allotropy. Polymorphism was first observed in 1798 when Klaproth discovered that the minerals calcite and aragonite have the same chemical composition, $CaCO_3$ [9]. Since then, polymorphism has been found in a wide range of compounds and is a general phenomenon [9, 10]. Polymorphism is of importance in a wide range of fields from organic semiconductors to food, explosives and pharmaceuticals [8, 10–12].

Polymorphs tend to have similar chemical properties due to their identical chemical composition, however their mechanical, optical and electronic properties (which are structure-dependent) may differ widely [9, 10]. The study of polymorphism is therefore exciting with new phenomena (and polymorphs) available to be discovered and explored. Polymorphism can however cause a variety of problems, for example in the pharmaceutical industry polymorphs of medications can exhibit radically different solubilities which can affect their bioavailability and hence effectiveness [11]. Furthermore, other problems such as drug recalls, suspension of drug production and the dispution of patents have all occurred for reasons connected to polymorphism [12].

Polymorphism is characterised by the reversibility of the phase transition: where it is reversible the system is enantiotropic, and where it is irreversible the system is said to be monotropic [9]. In an enantiotropic polymorph pair there is a cross-over in free energy below the melting point at the transition temperature. This means one polymorph is thermodynamically stable below the transition temperature and the second polymorph is thermodynamically stable above the transition temperature. Nevertheless it is possible for the system to remain in the less favourable polymorph for an extended period of time due to the dynamics of the transition. In a monotropic polymorph pair one polymorph always has a lower free energy than the other and is therefore always the most thermodynamically stable. The second polymorph, the metastable form, can exist for extended periods of time, if not indefinitely, providing the experimental conditions are not changed, again due to the dynamics of the phase transition [13]. Some chemical compounds exhibit both enantiotropic and monotropic polymorphism, for example in the twenty plus phases of ice several polymorphs are metastable and exhibit monotropic

phase transitions whilst others show enantiotropic behaviour, with changes in pressure and/or temperature producing reversible phase transitions [14, 15].

Prediction of the existence and stability of polymorphs is extremely challenging due to the typically large complex configurational space [12] and small energy differences between polymorphs [16]. One study [17] illustrates this issue: of 508 polymorphic organic molecules investigated more than half were reported to have less than 2 kJ/mol separation in lattice energy with only 5% exceeding 7.2 kJ/mol. A second study finds similar results: 59% of polymorphs differ in energy by less than 2 kJ/mol and nearly 90% differ in energy by 4 kJ/mol [18]. These values are of the order k_BT (=2.5 kJ/mol) at room temperature (298 K) and within the so called 'chemical accuracy' of 4 kJ/mol required to make realistic experimental predictions [19]. In fact, the accurate prediction of crystal structures including polymorphic species is of such importance that since 1999 the Cambridge Crystallographic Data Centre (CCDC) have coordinated a series of blind tests to motivate and assess the accuracy of different approaches to the accurate crystal structure prediction of small organic molecules [20].

1.2 Molecular crystals

A molecular crystal is one in which the crystal lattice is formed of molecules held together by dispersion forces (otherwise known as van der Waals (vdW) forces or instantaneous-dipole-induced-dipole forces). An every day example is that of ice where the intramolecular bonding (between atoms) in the water molecule is covalent and intermolecular bonding (between molecules) is from hydrogen bonding. Note that ice forms in many different structures and is thus polymorphic [14].

Dispersion bonds differ from covalent ones in several ways: they are much weaker than covalent bonds with typical bond lengths of 3-5 Å compared to 1-2 Å, follow a R^{-6} dependence, and are not directional [21]. This gives rise to an interesting set of properties in molecular crystals, including low melting points and large thermal expansion coefficients [21, 22].

Polyaromatic hydrocarbons (PAHs) are one of the most fundamental structural families in organic molecular crystals. The molecules are planar, or near planar, and so adopt one of four well-defined packing types (figure 1-1(a-d)): herringbone (HB), sandwich-herringbone (SHB), γ-herringbone and β-herringbone. In HB, SHB and γ structures, stability results from C$\cdots$H intermolecular interactions, whereas in β stability is due to C$\cdots$C interactions [23]. Despite the generality of polymorphism, in

PAHs it is rare. Perylene and pyrene are two known cases, both occuring in the HB and SHB structures [24].

1.3 Coronene

Coronene is a member of the PAH family formed of six joined benzene rings as shown in figure 1-2 (a),(b). It is a particularly interesting PAH due to its high molecular symmetry (D_{6h}), planar disk-like shape and 24 electron π-system [8]. Coronene has been studied in relation to graphene [25] with molecule pair interactions giving further insight into graphene stacking [26] and it has been reported that coronene can be used as a building block for graphene nanoribbons [27]. Coronene has a wider impact too, for example it is a candidate for active layer compounds in photovoltaic applications [28], has been identified as one of the most likely molecules, when ionized, to explain astronomical unidentified infra-red bands [29] and has been identified as a hydrocarbon superconductor in the form K_3-coronene [30].

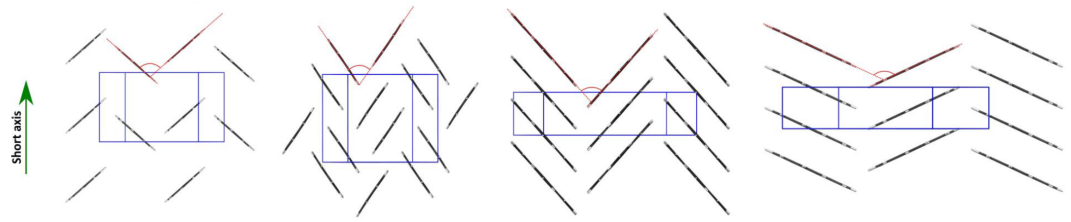

(a) (b) (c) (d)

Figure 1-1: The four packing configurations for polyaromatic hydrocarbon molecular crystals: (a) herringbone, (b) sandwich herringbone, (c) γ-herringbone and (d) β-herringbone structures [8].

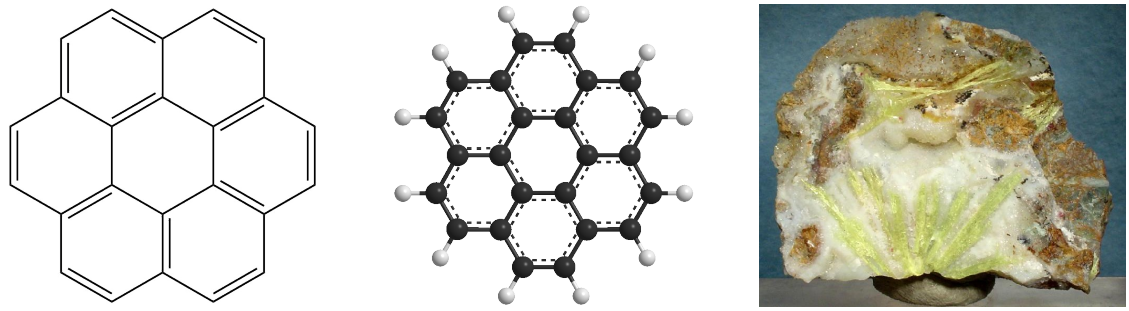

(a) (b) (c)

Figure 1-2: The molecular structure of coronene in the (a) skeletal and (b) ball and stick models. Carbon is shown in black and hydrogen in white. (c) A specimen of Carpathite (yellow crystals), the naturally occurring mineral form of coronene [31].

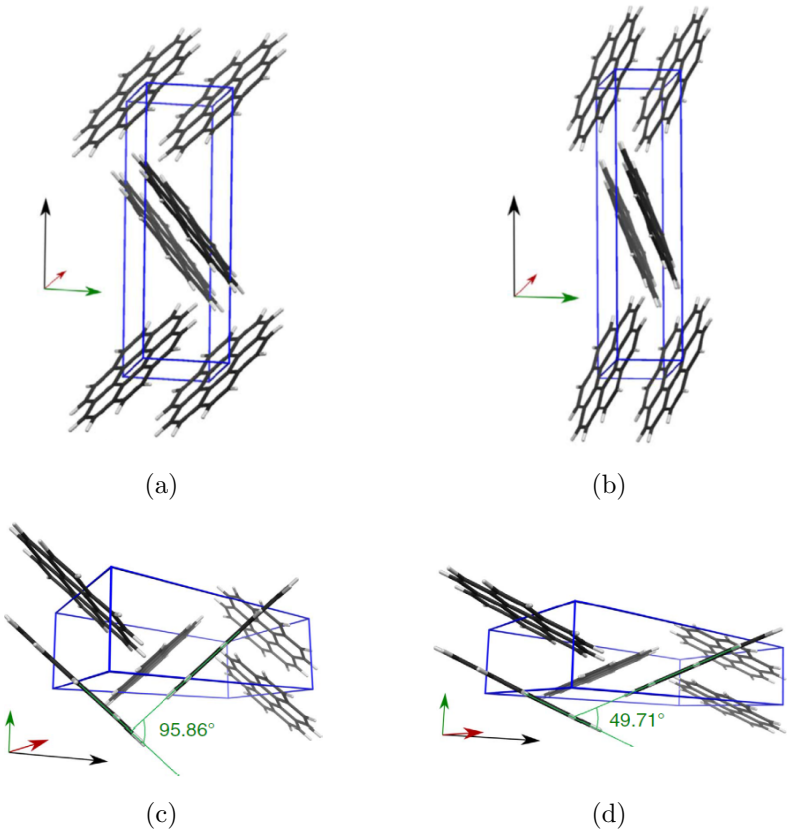

Figure 1-3: Unit cells (blue boxes) for γ-coronene (a),(c) and β-coronene (b),(d). (c) and (d) clearly show the difference in nearest neighbour angle between the two polymorphs. Red, green and black arrows indicate the directions of the a, b and c axes respectively [8].

Coronene is found naturally in the mineral Carpathite, a specimen of which is shown in figure 1-2 (c). Here it crystallises in a γ-herringbone structure, illustrated in figure 1-3 (a),(c). The lattice parameters of the monoclinic crystal structure are $a = 10.02$ Å, $b = 4.67$ Å, $c = 15.60$ Å and $\beta = 106.7°$ obtained from single crystal x-ray diffraction (XRD) performed at 150 K [8]. The inter-planar distance (d_π) is 3.43 Å, which is noted to be "consistent with parallel π-stacking" [8].

From as early as 1972, anomalous results for crystalline coronene in the low temperature regime have been observed in Raman and fluorescence spectra [32], luminescence spectra [33, 34], ^{13}C NMR spectrocopy [35], in exciton bandwidths [36] and heat-capacities [37]. A phase transition in the region 140 K to 180 K was proposed based on these data [32–34, 36].

In 2015 a new polymorph of coronene with a β-herringbone structure, illustrated in figures 1-3 (b),(d), was synthesised and stabilised at room temperature and pressure by growth in a 1 T magnetic field. The lattice parameters of the monoclinic crystal structure

have been identified as $a = 10.39$ Å, $b = 3.84$ Å, $c = 17.23$ Å and $\beta = 96.24°$ with an inter-planar distance of 3.48 Å using single crystal XRD at 150 K [8]. Furthermore this β polymorph was established as the low temperature phase, accessible by cooling γ-coronene below ∼150 K. This discovery has enabled further examination of the aforementioned spectroscopic anomalies, which are explained by the new β polymorph [38].

One puzzle that still remains however is the lattice energy ranking of the two polymorphs found using DFT-D [8]. These calculations showed that the β structure has a lower lattice energy than the γ structure indicating that β-coronene is energetically preferred by 3.8 kJ/mol [8], yet γ-coronene forms at room temperature. Nevertheless temperature and vibrations play key roles in thermodynamics and hence phase stability, forming a likely source of this inconsistency. Solving this puzzle is a primary goal of this project.

1.4 Overview

First the relevant theory is introduced in Chapter 2. The thermodynamics behind this stability puzzle are introduced, including a detailed description of the vibrational contributions. Next the different types of vibrations in molecular crystals and how they can be measured experimentally are explained. Finally the Density Functional Theory (DFT) framework is detailed and discussed, including dispersion corrections and their importance and how to calculate vibrational frequencies, thermodynamic properties using the quasi-harmonic approximation and Raman intensities.

Next in Chapter 3 the method of crystal growth for γ-coronene is detailed, followed by attempts at synthesising β-coronene at room temperature and pressure in a 1 T magnetic field. Following this, in Chapter 4 the γ- and β-coronene structures predicted with DFT-D are examined with respect to experimental structures. The intramolecular vibrations of the two coronene polymorphs are also studied at the zone centre using Raman spectroscopy and the results interpreted with DFT-D calculations of the isolated molecule and two crystalline structures. In Chapter 5 the lattice vibrations are then studied similarly.

Last to be investigated in Chapter 6 is the polymorph stability puzzle. DFT-D calculations are extended to study vibrations across the first Brillouin zone. This allows the phase stabilities to be calculated in the harmonic and quasi-harmonic approximations. The predicted thermal expansion in the quasi-harmonic approximation is compared

to experiment. Shortfalls in these computational methods and potential solutions are discussed.

Finally Chapter 7 summarises the key results and findings and suggests future avenues to explore.

Chapter 2

Theory

This chapter introduces relevant theoretical aspects. First the thermodynamics of phase stabilities is introduced with an emphasis on the role vibrations play. Next the types of vibrations in molecular crystals are detailed alongside descriptions of how they can be measured experimentally. Finally the Density Functional Theory (DFT) framework is introduced. Key points in the derivation of DFT are given, followed by a discussion of the different types of dispersion corrections available. How vibrational frequencies both at the zone centre and across the first Brillouin zone are calculated is outlined, and the techniques used in literature are analysed and discussed. The methods for calculating thermodynamic variables by using the quasi-harmonic approximation are explained and discussed. Lastly the method for calculating Raman tensors and intensities is presented.

2.1 Phase stability

For polymorphic compounds, the most stable polymorph at a constant temperature, T, and pressure, p, is the one which has the lowest Gibbs free energy

$$G = U + pV - TS, \tag{2.1}$$

where U is the internal energy, V is volume and S is entropy [39]. A related quantity is the Helmholtz free energy

$$F = U - TS, \tag{2.2}$$

which is the free energy that must be minimised for systems at constant temperature and volume.

Statistical mechanics links these macroscopic variables to microscopic states, which are described by the partition function

$$Z = \sum_i \exp\left(-\frac{\epsilon_i}{k_B T}\right), \tag{2.3}$$

where ϵ_i is the energy of state i and k_B is simply the Boltzmann constant. The Helmholtz free energy is

$$F = -k_B T \ln Z. \tag{2.4}$$

Other macroscopic variables, such as specific heat capacity, can then be derived.

In the independent degrees of freedom approximation, the total energy E, of the system can be written as a linear sum of subenergies: it is assumed that each type of energy state is independent of the others [40]. For example for a molecule with translational, rotational, vibrational and electronic energy states one can write

$$E = E_{tra} + E_{rot} + E_{vib} + E_{el}. \tag{2.5}$$

In reality this is not always true: for a diatomic molecule the vibrational frequency (and hence vibrational energy levels) will be modified if the molecule is rotating due to the introduction of a centrifugal potential [41]. In crystalline materials this problem does not occur, with only the electronic and vibrational energy contributions present [42].

From equation (2.3), the total partition function for our system can be written as a product of the partition functions for the vibrational, Z_{vib}, and electronic, Z_{el}, components

$$Z = Z_{vib} Z_{el}. \tag{2.6}$$

Hence the total Helmholtz free energy can be written as a linear combination of vibrational and electronic components. The electronic component, F_{el}, is simply the lattice energy, U_{latt}. This gives

$$G = U_{latt} + F_{vib} + pV. \tag{2.7}$$

Thus both crystal structure and vibrations contribute to phase stability.

The thermodynamic contribution made by vibrations is typically studied in the harmonic approximation. Atoms are assumed to not move far from their equilibrium positions such that the anharmonic potential energy between atom pairs can be approximated by a harmonic function [43]. According to the equipartition theorem the average energy of a vibration is $k_B T$, which at 300 K is 26 meV. For a hydrogen molecule

this additional energy is very small in comparison to the depth of the potential energy well (with an experimentally derived value of 4.74 eV [44]) leading to small changes in bond length of a few percent as a result of the vibration. This suggests that the harmonic approximation is indeed reasonable. The calculation of vibrational frequencies within the harmonic approximation, and the benefits and drawbacks of this approach are further discussed in section 2.3.2.

In the harmonic approximation vibrations act as quantum harmonic oscillators. Quantum theory gives energy levels, ϵ_n, of a harmonic oscillator with frequency, ω_i, as

$$\epsilon_{n,i} = \left(n + \frac{1}{2}\right)\hbar\omega_i, \tag{2.8}$$

where n is an integer and $\hbar$ is the reduced Planck's constant. It follows that the partition function for a single oscillator, $Z_{vib,i}$, [39, 45] is

$$Z_{vib,i} = \sum_{n=0}^{\infty} \exp\left[-\frac{\left(n+\frac{1}{2}\right)\hbar\omega_i}{k_B T}\right] = \frac{\exp\left(-\frac{\hbar\omega_i}{2k_B T}\right)}{1-\exp\left(-\frac{\hbar\omega_i}{k_B T}\right)}, \tag{2.9}$$

and the contribution to the free energy from the vibrational mode with frequency ω_i is

$$F_{vib,i} = \frac{\hbar\omega_i}{2} + k_B T \ln\left[1-\exp\left(-\frac{\hbar\omega_i}{k_B T}\right)\right]. \tag{2.10}$$

Extending this over the full set of vibrational frequencies of the system gives the vibrational free energy

$$F_{vib} = \overbrace{\sum_i \frac{\hbar\omega_i}{2}}^{\text{zero-point energy}} + \overbrace{k_B T \sum_i \ln\left[1-\exp\left(-\frac{\hbar\omega_i}{k_B T}\right)\right]}^{\text{thermal/entropy related contributions}}. \tag{2.11}$$

As $T \to 0$, the second sum tends to 0, leaving only the first contributing, known as the zero-point energy. At a finite temperature, thermally active vibrations decrease F_{vib}, stabilising the crystal structure.

The Gibbs free energy is then the minimum of equation (2.7) with respect to volume [46]

$$G(T,p) = \min_V \left[U_{latt}(V) + F_{vib}(T,V) + pV\right]. \tag{2.12}$$

This is often calculated within the quasi-harmonic approximation (QHA), where the harmonic approximation is applied at each volume. The QHA is a reasonable approxi-

mation across a wide temperature range, where the temperature stays below and away from the melting temperature of the solid [47].

In the case of polymorphs, the difference in volumes is typically small such that the pV term in equation (2.1) can be neglected when considering relative stabilities [9]. The Helmholtz free energy is then a useful approximation in comparing relative stabilities.

This thermodynamic picture, while helpful, does not fully describe the phase stability of polymorphs. The main problem is that the transformation from one polymorph to another is not instantaneous: there is a rate involved in the transition. This rate depends on an energy barrier, the activation energy E_A, opposing the transition, itself a function of the experimental conditions. In the case of enantiotropic polymorph pairs the transformation speed has a prefactor of $\exp\left(\frac{-E_A}{k_B T}\right)$. Providing the activation energy is high so the rate of transformation is slow, a polymorph can exist in a metastable state outside of it's thermodynamically stable region. If the rate of transformation is negligible then it is possible for the metastable state to exist indefinitely, providing environmental conditions are not changed [9]. An example is the existence of diamond which is thermodynamically less stable than its allotrope graphite.

The relative stabilities of polymorphs has been widely investigated in the literature, although many studies neglect the effect of vibrations which may account for some incorrect energy rankings in comparison with experiment. One exception to this is Ref. [17], and its follow up [48], where the effects of vibrations were included by calculating the Helmholtz free energy at 0 K and 300 K [17] or melting points [48] for 418 organic molecular crystal polymorph families. The polymorphs investigated comprised of up to 55 atoms per unit cell containing elements H, C, N, O, F, S and Cl. It was observed that at temperatures up to 300 K 9% [17] of polymorph pairs swapped stability due to vibrational contributions and extending the study up to the melting points increased this to 21% [48].

Many individual examples of polymorph phase stabilities may be found in the literature. One particularly interesting example is the antidepressant medication aripiprazole. The chemical structure is shown in figure 2-1. It exists in eight solid forms held together by dispersion forces. The stabilities of two of these forms were investigated by Delaney *et al.* by DFT-D2 calculations [49]. Form VIII is stable at low temperature with a lattice energy lower than form II by 1.33 kJ/mol. Form VIII was experimentally observed to convert into form II at a temperature of 225 ± 1 K. Calculations of the Helmholtz free energy plus a constant pV term predicted the transition temperature at 211 K. Given the general level of agreement found in studies, the close agreement between the transition temperature measured and calculated is probably fortuitous.

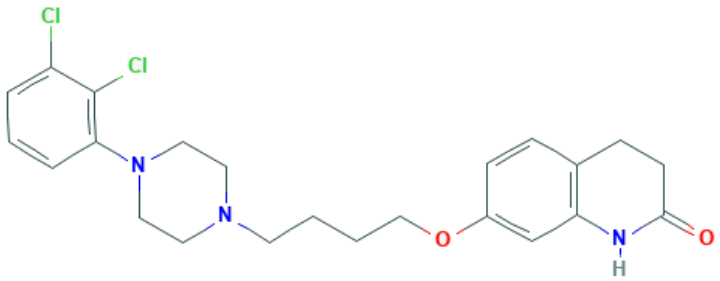

Figure 2-1: Chemical structure of the antidepressant medication Aripiprazole [50].

From thermodynamics and these studies, it is clear that investigating the vibrational frequencies and hence thermodynamic stabilities, may allow the conundrum of the stabilities of γ- and β-coronene to be solved.

2.2 Vibrations in molecular crystals and their measurement

The two types of bonding in molecular crystals give rise to two distinct types of vibrations: intramolecular and intermolecular vibrations. Intramolecular vibrations involve the movement of atoms within individual molecules, predominantly associated with the stretching of covalent bonds. Typically there are small or no changes in frequencies of these modes between the isolated molecule and the crystal [22], hence the relative stabilities of polymorphs are not usually affected by intramolecular vibrations. For an isolated molecule there are $3N - 6$ modes where N is the number of atoms in the molecule. There are 36 atoms in a coronene molecule giving rise to 102 modes.

Intermolecular vibrations, otherwise known as lattice vibrations or phonons, involve the movement of whole molecules about their equilibrium positions: the individual molecules can to a good approximation be considered rigid. These modes depend on the dispersion forces and so can differ significantly between polymorphs, providing a 'fingerprint' of the individual crystal structure [7]. Thus phonons affect the relative thermodynamic stabilities. In total there are $6M$ phonon modes in a molecular crystal containing M molecules per unit cell. In both γ- and β-coronene there are 2 molecules per unit cell giving 12 phonon modes each. Of these phonon modes, 3 are acoustic modes with a frequency of 0 at wavevector $\mathbf{k} = 0$. The acoustic modes correspond to translations of the entire unit cell. The remaining 9 are known as optical phonon modes with a frequency greater than 0 at all wavevectors. Broadly there are two types

of phonons: ones involving translational movements of the molecule(s) and a second group involving rotational movements, also known as librations. Phonons are, with a few exceptions, lower in frequency than intramolecular modes, typically in the range 10 to 150 cm^{-1} [7]; and due to the relatively large masses of molecules and weak dispersion forces also lower in frequency than phonons in covalently bonded crystals. This allows phonons in molecular crystals to be thermally excited at lower temperatures [22].

Experimentally four methods can be used to probe vibrations: inelastic neutron scattering and Raman, infra-red (IR) and terahertz spectroscopy. Inelastic neutron scattering can examine the dispersion of vibrations throughout the Brillouin zone. Since neutrons interact weakly with matter, to get sufficient scattering intensity large crystals are required. For example a crystal with diameter 21 mm and length 30 mm of deuterated naphthalene, a PAH formed of two joined benzene rings, was used for inelastic neutron scattering [22]. Deuterium was used as it has a much higher scattering intensity than hydrogen. Typical crystals of both polymorphs of coronene are much smaller than this: the crystals Potticary *et al.* grew were typically 7.5 mm in length for γ-coronene and 25 mm in length for β-coronene with typical thicknesses ≤ 1 mm and have a thin needle like shape [8]. Thus inelastic neutron scattering for coronene is unlikely to be feasible due to the relatively small crystal sizes.

Raman, IR and terahertz spectroscopy all probe the vibrational frequencies at the centre of the Brillouin zone (Γ point, wave vector $\mathbf{q} = 0$) only. Terahertz, low-wavenumber Raman and far-IR spectroscopy can be used to probe vibrations below 200 cm^{-1} where phonon frequencies are expected. Assignment of modes in this region is exceptionally difficult without theoretical predictions [11].

In Raman spectroscopy, a laser illuminates a sample which scatters the photons both elastically (Rayleigh scattering) and inelastically. Inelastic scattering occurs when an excitation in the system, usually a vibration, combines with the incoming photon (anti-Stokes scattering) to excite the system to a virtual energy level. The system then decays emitting a photon of higher energy than that of the laser. Alternatively a photon from the laser excites the system to a virtual energy level and a lower energy photon is emitted leaving the system in an excited state (Stokes scattering). A full mathematical description is given in section 2.3.4. Typically in Raman spectroscopy, the Stokes scattered light is collected and presented as a shift in wavenumber with respect to the incidence laser radiation.

In IR spectroscopy the sample is illuminated by a broad band source which emits a spectrum of frequencies simultaneously. This is typically performed in one of three ranges where near-IR is 14,000-4000 cm^{-1}, mid-IR is 4000-400 cm^{-1} and far-IR is 400-

10 cm^{-1}. Photons with energies equivalent to an excitation of the system, such as a vibration, are absorbed, exciting the sample. The remaining photons are measured.

Terahertz spectroscopy covers the range 0.3 to 20 THz, equivalent to 3.33 to 667 cm^{-1}. Terahertz time-domain spectroscopy (THz-TDS) is the most commonly used terahertz technique [51] and has been used in a wide range of fields including chemistry, materials science, engineering and medicine [52]. In addition to studying vibrations, polymorphism, various spin excitations, free-carrier absorption in semiconductors, the superconducting gap and conductivities of various materials have also been studied [53, 54]. In THz-TDS a femtosecond near-IR optical pulse is emitted from a laser and split along two lines. The first travels to an emitter which produces a pulse of terahertz radiation. This illuminates the sample and photons with energies equivalent to an excitation of the sample, such as a vibration, are absorbed leaving the system in an excited state. The remaining photons in the terahertz pulse travel on to the detector. The second near-IR pulse travels directly to the detector and acts as an optical gate ensuring that the detector is only active for a short period of time determined by the pulse width of the near-IR pulse. Varying the path length of this second near-IR pulse allows the electric field of the terahertz radiation to be measured as a function of time. A Fourier transform then gives the phase and amplitude of the terahertz radiation in the frequency domain [52].

Not all vibrations are able to be observed with Raman, IR or terahertz spectroscopy. Vibrations that are IR active are also terahertz active and correspond to motion causing a change in the dipole moment, whilst vibrations that are Raman active are those causing a change in polarisability [51, 55]. Group theory allows the IR/terahertz and Raman activity of vibrations to be determined [56].

For coronene, the irreducible representation of an isolated molecule using standard Mulliken notation [57] is

$$\begin{aligned}\Gamma_{3N} =& 6A_{1g} + 6A_{2g} + 2B_{1g} + 4B_{2g} + 6E_{1g} + 12E_{2g} + \\ & 2A_{1u} + 4A_{2u} + 6B_{1u} + 6B_{2u} + 12E_{1u} + 6E_{2u},\end{aligned} \tag{2.13}$$

of which $3A_{2u}+11E_{1u}$ are IR/terahertz active and $6A_{1g}+6E_{1g}+12E_{2g}$ are Raman active. The irreducible representation of the Γ-point vibrations for both γ- and β-coronene is

$$\Gamma_{3N} = 54A_g + 54A_u + 54B_g + 54B_u, \tag{2.14}$$

where $53A_u + 52B_u$ are IR/terahertz active and $54A_g + 54B_g$ are Raman active. These symmetry labels are used during the discussion of intramolecular vibrations in Chapter 4 and lattice vibrations in Chapter 5.

2.3 Density Functional Theory

Density Functional Theory (DFT) is a theory of correlated many-body systems routinely used for first principle electronic structure calculations. DFT arises from a need to solve the many-body Schrödinger equation, a problem that is impossible to solve for more than three bodies analytically. Instead a series of approximations and theorems are applied giving an approximate solution in what we call DFT.

A full mathematical description of DFT can be found in many sources, for example Refs. [58, 59]. Here the main steps, including any assumptions and approximations, are detailed to give a basic understanding of how DFT works and where its limitations lie.

The time independent Schrödinger equation is

$$\hat{H}\Psi = E_{\text{tot}}\Psi, \tag{2.15}$$

where E_{tot} is the total energy of the stationary state of the system with wavefunction Ψ and $\hat{H}$ is the Hamiltonian. Ψ depends on the positions of all electrons, $\mathbf{r}$, and nuclei, $\mathbf{R}$, in the system. For a system with N electrons and M nuclei the wavefunction is $\Psi = \Psi(\mathbf{r}_1, \cdots, \mathbf{r}_N, \mathbf{R}_1, \cdots, \mathbf{R}_M)$. Using Hartree atomic units, specifically energies in Hartree, lengths in bohr and masses in units of m_e, it can be shown [59] that the many-body Hamiltonian is

$$\begin{aligned}\hat{H} = & \underbrace{\sum_i \left(-\frac{\nabla_i^2}{2}\right)}_{\text{electron kinetic energy}} + \underbrace{\frac{1}{2}\sum_{i\neq j}\frac{1}{|\mathbf{r}_i - \mathbf{r}_j|}}_{\text{electron Coulomb interaction}} \\ & + \underbrace{\sum_I \left(-\frac{\nabla_I^2}{2M_I}\right)}_{\text{nuclei kinetic energy}} + \underbrace{\frac{1}{2}\sum_{I\neq J}\frac{Z_I Z_J}{|\mathbf{R}_I - \mathbf{R}_J|}}_{\text{nuclei Coulomb interaction}} - \underbrace{\sum_{iI}\frac{Z_I}{|\mathbf{r}_i - \mathbf{R}_I|}}_{\text{electron-nuclei interactions}},\end{aligned} \tag{2.16}$$

where M_I is the mass and Z_I is the atomic number of nuclei I. Note that sums over indices i and j are to N and sums over indices I and J are to M.

This is of course a very general problem applying to solids, liquids and gases, and as such is an immensely complex problem to solve. In order to simplify we restrict our study to solids and molecular structures. This allows the Born-Oppenheimer approximation

to be applied where the nuclei are considered "fixed", since their masses are much greater than that of electrons, allowing their motion to be neglected whilst solving for the electronic degrees of freedom. The problem then becomes a system of electrons moving in a fixed external potential due to the nuclei, with the Coulomb interaction of the nuclei a constant, E_{II}. The simplified many-electron Hamiltonian is then

$$\begin{aligned}\hat{H}\left(\mathbf{r}_1, \cdots, \mathbf{r}_N\right) &= \sum_i \left(-\frac{\nabla_i^2}{2}\right) + \frac{1}{2}\sum_{i\neq j}\frac{1}{|\mathbf{r}_i - \mathbf{r}_j|} + \sum_i V_{\text{ext}}(\mathbf{r}_i) + E_{II} \\ &= \hat{T} + \hat{U} + \hat{V} + E_{II},\end{aligned} \tag{2.17}$$

where

$$V_{\text{ext}}(\mathbf{r}_i) = -\sum_I \frac{Z_I}{|\mathbf{r}_i - \mathbf{R}_I|}, \tag{2.18}$$

$$E_{II} = \frac{1}{2}\sum_{I\neq J}\frac{Z_I Z_J}{|\mathbf{R}_I - \mathbf{R}_J|}, \tag{2.19}$$

and $\hat{T}$, $\hat{U}$ and $\hat{V}$ are the operators for kinetic energy, potential energy due to electrons and potential energy due to nuclei. The solution to this remains a formidable task for a system of any signficant size. Two theorems first proved by Hohenberg and Kohn in 1964 [60] simplify this problem.

The first theorem is "for any system of interacting particles in an external potential $V_{\text{ext}}(\mathbf{r})$, the potential $V_{\text{ext}}(\mathbf{r})$ is determined uniquely, except for a constant, by the ground state particle density $n_0(\mathbf{r})$" [58]. Therefore all the properties of the system are completely determined when $n_0(\mathbf{r})$ is known. Mathematically, a one-to-one mapping between $V_{\text{ext}}(\mathbf{r})$ and $n_0(\mathbf{r})$ exists

$$V_{\text{ext}}(\mathbf{r}) \longleftrightarrow n_0(\mathbf{r}). \tag{2.20}$$

The second theorem is that there exists a universal functional for the energy, $E[n]$, which is valid for any $V_{\text{ext}}(\mathbf{r})$; and for any particular $V_{\text{ext}}(\mathbf{r})$, $n_0(\mathbf{r})$ gives the global minimum of $E[n]$, the ground state energy. Thus $E[n]$ alone is sufficient to derive the ground state energy and density [58]. Mathematically

$$E[n] = \overbrace{\langle\psi[n]|\hat{T} + \hat{U}|\psi[n]\rangle}^{F[n]} + \int \mathrm{d}\mathbf{r}\; n(\mathbf{r})V_{\text{ext}}(\mathbf{r}) + E_{II}, \tag{2.21}$$

$$E_{\text{ground}} = E[n_0(\mathbf{r})]. \tag{2.22}$$

These theorems however give no indication of how to find the functional $F[n]$ other than through the fully interacting many-body system. The Kohn-Sham approach reformulates the problem into one which has independent particles [61], resulting in a slightly simpler unknown functional that can be approximated.

Two assumptions are made in the Kohn-Sham ansatz: the exact ground state density can be represented by the ground state density of an auxiliary system of non-interacting particles and an auxiliary Hamiltonian, consisting of the usual kinetic operator and an effective local potential. The total energy of the system is

$$E_{\mathrm{KS}}[n] = T_S[n] + \int \mathrm{d}\mathbf{r}\; n(\mathbf{r}) V_{\mathrm{ext}}(\mathbf{r}) + E_{\mathrm{Hartree}}[n] + E_{II} + E_{xc}[n], \tag{2.23}$$

where $T_S[n]$ is the independent-particle kinetic energy, $E_{xc}[n]$ is the exchange-correlation energy and $E_{\mathrm{Hartree}}[n]$ is the classical Coulomb self-interaction of $n(\mathbf{r})$ (the Hartree energy)

$$E_{\mathrm{Hartree}}[n] = \frac{1}{2} \int \mathrm{d}^3 r \mathrm{d}^3 r' \frac{n(\mathbf{r}) n(\mathbf{r}')}{|\mathbf{r} - \mathbf{r}'|}. \tag{2.24}$$

The exchange-correlation energy contains all many-body effects and, if known, would allow the calculation of the ground state properties of the many-body electron system.

There are many different approximations for $E_{xc}[n]$, that can be broadly split into three groups: the local density approximation (LDA), gradient expansion approximations (GGAs), and hybrid functionals [58]. LDA functionals depend solely on the electron density and are exact for an infinite uniform electron gas. Unfortunately this means chemical bonds and molecular properties are not accurately described [62]. In the late 1980s attempts were made to improve on this and GGA functionals were born [63]. GGA functionals depend on both the electron density and its gradient and can be either non-empirical where the functional form satisfies exact constraints from quantum mechanics, or semi-empirical where free parameters are fit to accurate reference values [62]. There are many GGA functionals such as PBE [64], revPBE [65] and BLYP [66, 67]. PBE, used in this work, is empirical in nature whilst revPBE and BLYP are semi-empirical. In the early 1990s hybrid functionals were introduced, where a fraction of the GGA exchange is replaced with Hartree-Fock exchange. This fraction is determined by fitting parameters to data sets such as atomisation energies, and the resulting functionals have higher accuracy for systems close to those used in the fitting, but greater inaccuracies in others [62, 63]. Examples of hybrid functionals include B3LYP [67, 68], PBE0 [69] and B3PW91 [68, 70].

The density and energy of the ground state of a many-body electron problem is found by self-consistently solving the Kohn-Sham equations

$$H^{\sigma}_{\mathrm{KS}}\psi^{\sigma}_{i}(\mathbf{r}) = \varepsilon^{\sigma}_{i}\psi^{\sigma}_{i}, \tag{2.25}$$

where ε_i are the eigenvalues, σ indicates spin state and H_{KS} is the effective Hamiltonian

$$H^{\sigma}_{\mathrm{KS}}(\mathbf{r}) = -\frac{1}{2}\nabla^2 + V^{\sigma}_{\mathrm{KS}}(\mathbf{r}), \tag{2.26}$$

with

$$V^{\sigma}_{\mathrm{KS}}(\mathbf{r}) = V_{\mathrm{ext}}(\mathbf{r}) + \frac{\delta E_{\mathrm{Hartree}}}{\delta n(\mathbf{r},\sigma)} + \frac{\delta E_{xc}}{\delta n(\mathbf{r},\sigma)} \tag{2.27}$$

$$= V_{\mathrm{ext}}(\mathbf{r}) + V_{\mathrm{Hartree}}(\mathbf{r}) + V^{\sigma}_{xc}(\mathbf{r}) \ . \tag{2.28}$$

There are several numerical methods for solving the Kohn-Sham equations. Plane waves and atomic orbitals are two that are typically used in DFT programs. The plane wave method represents the Kohn-Sham wavefunctions as a linear combination of plane waves

$$\psi_{i,\mathbf{k}}(\mathbf{r}) = \sum_{\mathbf{G}} c_i(\mathbf{k}+\mathbf{G}) \exp\left[\mathrm{i}\left(\mathbf{k}+\mathbf{G}\right)\cdot\mathbf{r}\right], \tag{2.29}$$

where the sum is over the reciprocal lattice vectors with $\mathbf{G} = m_1\mathbf{b}_1 + m_2\mathbf{b}_2 + m_3\mathbf{b}_3$ where m_1, m_2 and m_3 are integers and the $\mathbf{b}_i$ vectors are primitive reciprocal space lattice vectors. In the plane wave method, an energy cutoff, $E_{\mathrm{cut}} = |\mathbf{G}_{\mathrm{max}}|^2/2$, is typically used to specify the number of plane waves to be used, with more used for greater accuracy [59].

In order to reduce computational cost allowing larger systems to be studied, pseudopotentials are typically used. Here the "frozen core" approximation is used, separating states with core and valence with only the valence states involved in bonding. This is performed by first calculating the Kohn-Sham wavefunction including the core electrons - the "all-electron" wavefunction - selecting a cutoff radius r_c, and replacing the wavefunction in the pseudization region $0 < r < r_c$ with a smooth function that has the same electron density as the all-electron wavefunction, as illustrated in figure 2-2 (a). This resulting wavefunction is known as a pseudo-wavefunction. The nuclear potential must also be adjusted to include the effect of the core states, in what is known as the pseudopotential, illustrated in figure 2-2 (b). It is selected such that beyond r_c it matches the all-electron Kohn-Sham potential and inside the pseudization region

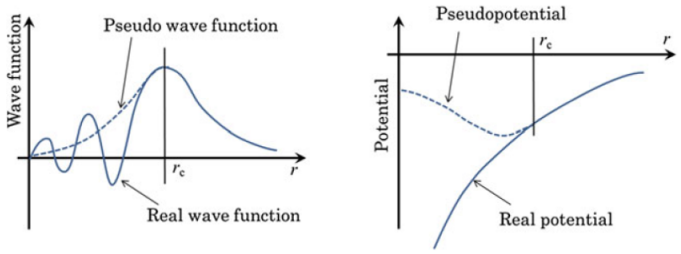

(a) (b)

Figure 2-2: Depiction of (a) pseudo-wavefunction and (b) pseudopotentials with their real or "all electron" counterparts. The pseudization range is between 0 and the cutoff radius r_c. Reproduced from [71].

the solution of the Kohn-Sham equations is exactly the pseudo-wavefunction. Further details are given in Ref. [59].

In the atomic orbital method a linear combination of atomic orbitals (LCAO) are used to represent the Kohn-Sham wavefunction

$$\psi_i(\mathbf{r}) = \sum_{i,nlm} c_{i,nlm}\phi_{nlm}(\mathbf{r} - \mathbf{R}_i), \tag{2.30}$$

where n, l and m are the principle, angular and azimuthal quantum numbers and i indexes the atoms in the unit cell. The set of plane waves/atomic orbitals used is known as the basis set. The Vienna *ab initio* simulation package (VASP) computer program [72] used in this work uses plane waves and pseudopotentials.

In order to relax the nuclei to their equilibrium positions the forces on the nuclei must be calculated. Since the wavefunctions of nuclei are much more localised than that of electrons, the nuclei are considered as classical particles with Hamiltonian

$$\hat{H}^{\text{classical}}_{\text{nuclei}} = \sum_I \frac{\mathbf{P}_I^2}{2M_i} + \underbrace{\frac{1}{2}\sum_{i\neq j}\frac{Z_I Z_J}{|\mathbf{R}_I - \mathbf{R}_J|} + E(\{\mathbf{R}\})}_{=U(\{\mathbf{R}\})}, \tag{2.31}$$

where $\mathbf{P}$ is the classical momentum operator and $E(\{\mathbf{R}\})$ is the total electronic energy for the given nuclei coordinates, calculated using the Kohn-Sham equations. The function $U(\{\mathbf{R}\})$ is known as the potential energy surface (although it is really a hyper surface). The equilibrium structure (or structures in the case of allotropes and polymorphs) is one which minimises U, i.e. where the forces

$$\mathbf{F}_I = -\frac{\partial U}{\partial \mathbf{R}_I}, \tag{2.32}$$

are equal to zero. The Hellmann-Feynman theorem simplifies the calculation of these forces [59].

DFT is a well established theory and known to be effective in studying molecules, nanostructures, solids, surfaces and interfaces [59, 73]. As a result a huge range of applications exist from astrophysics [74] to energy storage [75], nuclear [76], pharmaceuticals [77, 78], protein folding [79], solar cells [80] and superconductors [81], to name a only few. One of the key successes of DFT is its ability to predict and reproduce quantitative results: DFT has successfully predicted structures, such as silane (SiH_4) [82], which were later confirmed by experiment [83], and a wide variety of material properties have been calculated in the DFT framework that are consistent with experimental observations from superconducting critical temperatures and associated behaviours of the heat capacity [59] to vibrational frequencies and intensities [84, 85] and phase diagrams [59]. Additionally computational experiments can be performed, for example studying conditions under which thick films of polar materials can be formed. This was long thought to be impossible until DFT calculations predicted perfect film growth of MgO in the presence of hydrogen, a prediction that was later realised experimentally [86].

Clearly DFT is a powerful tool for first principles electronic structure calculations, and the advent of high-performance computing has made it even more so as larger and larger systems are able to be studied within reasonable time scales. However, DFT is not without its problems. These include that strictly speaking only ground state properties can be calculated, band gaps are often incorrect, dispersion forces are not well described, optical absorption spectra are typically red shifted and transition metal oxides are sometimes incorrectly predicted as metallic. Yet it remains a reasonable starting point for more complex calculations [59].

In this work the main issue is the incorrect description of dispersion forces. Higher order methods such as the random phase approximation (RPA), quantum Monte Carlo (QMC) calculations or many-body perturbation theory (MBPT) are successful in describing these dispersion interactions quite accurately [87]. Unfortunately they come with a high computational cost that makes them unsuitable for large systems. Thus a range of dispersion-corrected DFT (DFT-D) methods have been developed.

2.3.1 Dispersion corrections

The problem with standard density functionals is that they do not give the correct $-1/R^6$ asymptotic dependence that is necessary at distances where dispersion bonds

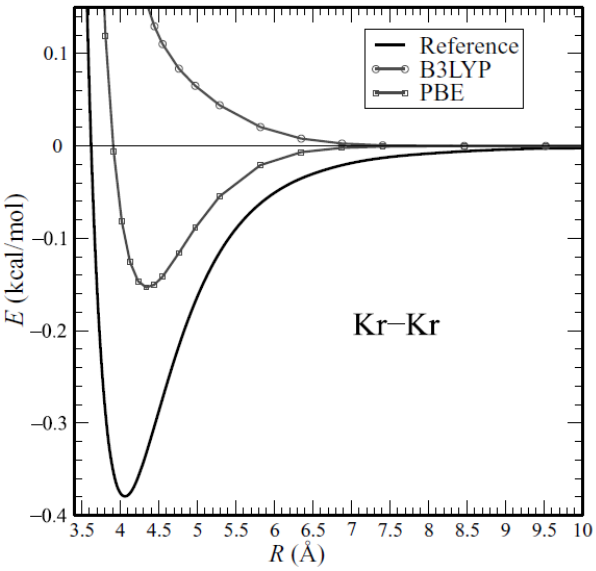

Figure 2-3: Potential energy curve for Kr_2 with PBE and B3LYP functionals in comparison with the "gold standard" CCSD(T) reference data [88].

form [88]. Figure 2-3 illustrates this where despite PBE finding a bound state for Kr-Kr, it is too large a bond length and with too small a binding energy, and additionally B3LYP does not find a bound state at all [88, 89]. Whilst some density functionals may give bound states, not all do and when they do, they do not give the correct bond lengths and binding energies. A good description of this behaviour is important not only in the determination of structures and lattice energies [11, 89] but also when considering vibrational frequencies both at and away from the Γ-point [90].

The reason standard density functionals do not properly describe dispersion forces is because instantaneous density fluctuations are not included and they are 'short-sighted': they depend on the density in local and semi-local ways [89, 91]. This means they do perform well at short distances but not more distantly. The addition of a term that provides the correct $-1/R^6$ asymptotics leads to a problematic mid-range region. It is therefore necessary to merge the two regimes seamlessly, which typically introduces some empirical nature to the dispersion corrections.

A range of methods exist to account for dispersion corrections within the DFT framework. Klimeš and Michaelides [89] suggested categorising these by the level of approximations made, creating a heirarchy or 'ladder' of dispersion methods illustrated in figure 2-4. It is expected that as one moves up the ladder accuracy will increase (as well as computational cost, usually). Whilst this is generally true it may not be for specific cases as it is still possible for each method to fail [89].

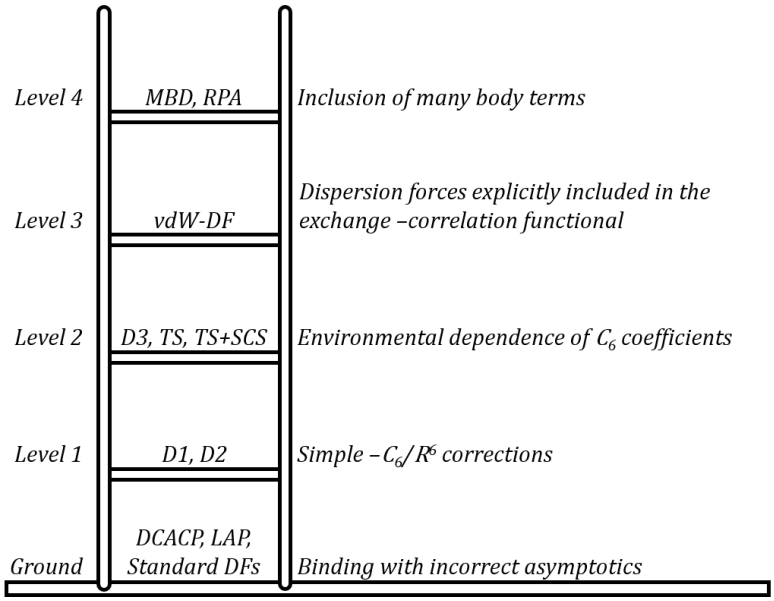

Figure 2-4: Heirarchy or 'ladder' of dispersion corrections available within the DFT framework. Based on Ref. [89].

Level 0 methods do not account for the correct R^{-6} dependence, level 1 methods include a simple pairwise C_6/R^6 correction and level 2 introduces environmental dependence into the C_6 coefficients used. Level 3 is where long-range nonlocal interactions are specifically incorporated in the exchange-correlation functional and many body effects are included in level 4. Examples of each are given in figure 2-4, and are discussed in the following text.

The level 1 method DFT-D2 was the most popular method (based upon number of citations in the Web of Science Core Collection up to the end of 2019) until 2016 where it was surpassed in popularity by the improved DFT-D3 method (level 2). DFT-D2 has previously been used to investigate the structures and lattice energies of crystalline coronene [8]. Vibrational frequencies calculated as part of this project using DFT-D2 did not closely agree with experiments, so DFT-D3 was instead explored.

Level 1: DFT-D2

The DFT-D2 method was introduced in 2006 [92] by Grimme as an improvement on his original D1 method published in 2004 [93]. Here the total energy is given by

$$E_{DFT-D2} = E_{KS-DFT} + E_{disp}, \tag{2.33}$$

where E_{KS-DFT} is the energy given by a standard density functional and E_{disp} is a pairwise dispersion term

$$E_{disp} = -\sum_{n=6,8,\ldots}\sum_{AB} s_n \frac{C_n^{AB}}{R_{AB}^n} f_{dmp}\left(R_{AB}\right), \tag{2.34}$$

where s_n are the global scaling factors, C_n^{AB} are the dispersion coefficients for atom pair AB, R_{AB} is the interatomic distance and $f_{dmp}\left(R_{AB}\right)$ is a damping function used to avoid singularities at small R. For D2, the first sum is truncated at $n = 6$ since higher order terms ($n > 6$) are "short-ranged and strongly interfere with the damping function" [92].

The s_6 scale factors that scale the C_6 terms are different for each standard density functional due to the variation in behaviour of the intermolecular potential, particularly at intermediate distances [93]. They were determined by a least-squares optimization of the interaction energy deviations for 40 noncovalently bonded complexes (ranging from hydrogen bonded, nonaromatic, benzene and larger aromatic complexes to rare gas dimers and complexes with 3$^{\text{rd}}$ row elements) [92]. However the optimal values of these s_6 coefficients are dependent on the molecular species being studied [77, 94–97]. Furthermore, the volume and lattice parameters of systems do not always exhibit consistent behaviour with respect to the s_6 parameter: a study on creatine [98] shows that the volume changes linearly whilst the lattice parameters do not. In fact one can use the s_6 parameter to expand and contract crystal lattices to mimic thermal expansion/contraction [98].

The C_6 coefficients are

$$C_6^{AB} = \sqrt{C_6^A C_6^B}, \tag{2.35}$$

$$C_6^A = 0.05 N I_p^A \alpha^A, \tag{2.36}$$

where I_p is the calculated atomic ionization potential (DFT/PBE0 level), α is the calculated static dipole polarizability (DFT/PBE0 level) and $N = 2, 10, 18, 36, 54$ for rows 1-5 of the periodic table respectively. The 0.05 proportionality constant keeps the C_6 values consistent to within 5-10% of those in the D1 method. The values and combinations of C_6 values used in DFT-D2 are calculated consistently across the periodic table, an improvement from D1. A major problem with this approach however is that these C_6 values are fixed for each element but the electronic character of an atom in a molecule can be very different to the free atom and also vary between molecular environments.

The damping function f_{dmp} can take several forms. Here

$$f_{dmp}\left(R_{AB}\right) = \frac{1}{1+\exp\left(-d\frac{R_{AB}}{R_r}-1\right)}, \tag{2.37}$$

where $d = 20$ (reduced from the DFT-D1 method) and $R_r = r_A + r_B$, the sum of atomic vdW radii. The vdW radii were "derived from the radius of the $0.01a_0^{-3}$ electron density contour from ROHF/TZV computations of the atoms in the ground state" [92]. Other radii have been proposed, for example Federov *et al.* [99] proposed using larger vdW radii based on experiments [100]. This form of the damping function was chosen as it "decays at small R fast enough to zero such that the dispersion corrections between atoms well below typical van der Waals distances are negligible" [93] so that 'normal' bonds remain unaffected. However, the specific form of the damping function is a "thorny issue" [89] as it has to be adjusted (using the s_6 coefficients) for each density functional and it can have a significant impact on binding energies.

Clearly the D2 method is an improvement on level 0 methods that do not account for dispersion forces correctly at all, but it has a lot of empirical character. This means that for each system fitting of empirical parameters may be required to obtain reasonable agreement with experiment. Level 2 methods attempt to solve some of the issues present in the D2 method.

Level 2: DFT-D3, -TS and -XDM

The exchange-dipole moment (XDM) dispersion correction was first introduced in 2005 [101] and later in 2007 placed on firmer theoretical foundations [102–104]. The TS (Tkatchenko Scheffler) method was introduced next in 2009 [105], followed closely by the D3 method in 2010 [106]. Both TS and D3 attempt to include a description of the environmental dependence of the C_6 coefficients, however they take very different approaches. Meanwhile XDM is based on an entirely different idea.

The D3 method is similar to D2, with the dispersion energy also governed by equation (2.34), up to and including $n = 8$. Environmental dependence is introduced through the C_6 and C_8 coefficients by the use of a fractional coordination number, CN. Roughly, CN for a given atom is the number of bonding directions, for example for carbon $CN = 2$ in ethyne, $CN = 3$ in ethene and $CN = 4$ in ethane. The structures of

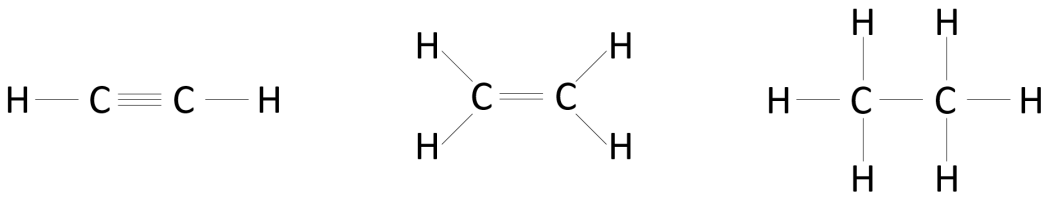

(a) (b) (c)

Figure 2-5: Chemical structures of (a) ethyne, (b) ethene and (c) ethane.

these molecules are shown in figure 2-5. More specifically

$$CN^A = \sum_{B \neq A}^{N_{at}} \frac{1}{1 + \exp\left(-k_1 \left[k_2 \frac{R_{A,cov} + R_{B,cov}}{r_{AB}} - 1\right]\right)}, \tag{2.38}$$

where R_{cov} is a scaled covalent radius and r_{AB} is the internuclear distance with $k_1 = 16$ and $k_2 = 4/3$ to give reasonable values for C-C bonding [106].

C_6 coefficients are then calculated for pairs of atoms with known coordination numbers. In a given molecule, coordination numbers are calculated for each atom, then C_6^{AB} values are found by interpolating between precomputed reference values, schematically shown in figure 2-6. Full mathematical details are in Ref. [106]. The C_6 reference values are calculated from first principles using the Casimir-Polder formula

$$C_{6,ref}^{AB} = \frac{3}{\pi} \int_0^{\inf} \alpha^A(i\omega)\, \alpha^B(i\omega)\, d\omega, \tag{2.39}$$

where $\alpha(i\omega)$ is the averaged dipole polarizability at imaginary frequency $i\omega$.

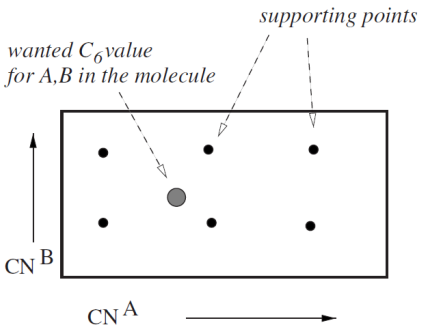

Figure 2-6: Schematic diagram showing how the interpolation of coordination numbers, CN, is performed [106].

The C_8 coefficients are calculated from the C_6 coefficients by

$$C_8^{AB} = 3C_6^{AB}\sqrt{Q^A Q^B}, \tag{2.40}$$

$$Q^A = s_{42}\sqrt{Z^A}\frac{< r^4 >^A}{< r^2 >^A}, \tag{2.41}$$

where $< r^4 >$ and $< r^2 >$ are "simple multipole-type expectation values derived from atomic densities which are average geometrically to get the pair coefficients" [106], Z is the atomic number and s_{42} is a redundant parameter since the C_8 coefficients are scaled in the damping function.

In order for the $n = 8$ term to be included, the damping function is different to D2. This allows the $n = 8$ term to be numerically stable, and also gives a more clear cut separation between short and long ranged dispersion effects. The D3 damping function is

$$f_{dmp,n}(r_{AB}) = \frac{1}{1 + 6\left(\frac{r_{AB}}{s_{r,n}R_0^{AB}}\right)^{-\alpha_n}}, \tag{2.42}$$

where $s_{r,n}$ are order dependent scaling factors for the cutoff radii R_0, α_n controls the steepness of the damping functions with $\alpha_6 = 14$ and $\alpha_8 = 16$. The four scaling factors are $s_6 = s_{r,8} = 1$ with s_8 and $s_{r,6}$ dependent on the density functional, introducing two empirical terms into the method. Cutoff radii R_0^{AB} are specifically computed for all AB pairs and occurs where the first-order DFT interaction energy between the pair of atoms equals a cutoff energy set such that R_0^{CC} is the same as in DFT-D2 ($R_0^{CC} = 2.91$ Å).

A second damping option is available known as Becke-Johnson damping or DFT-D3(BJ), with

$$E_{disp}^{D3(BJ)} = -\frac{1}{2}\sum_{A\neq B}\left[s_6\frac{C_6^{AB}}{R_{AB}^6 + \left[f\left(R_{AB}^0\right)\right]^6} + s_8\frac{C_8^{AB}}{R_{AB}^8 + \left[f\left(R_{AB}^0\right)\right]^8}\right], \tag{2.43}$$

$$f\left(R_{AB}^0\right) = a_1 R_{AB}^0 + a_2, \tag{2.44}$$

where s_6=1, s_8 is dependent on the density functional, a_1 and a_2 are free fit parameters, and $R_{AB}^0 = \sqrt{\frac{C_8^{AB}}{C_6^{AB}}}$. In Becke-Johnson damping the potential tends towards a fixed value, whereas for the 'zero-damping' in equation (2.42) it tends towards zero, illustrated in figure 2-7. Whilst Becke-Johnson damping "basically requires special adjustment of the standard correlation density functional used" [88], 'zero-damping' introduces a small repulsive force at short distances, which may produce longer interatomic distances in special cases. Whilst each damping function comes with drawbacks it is worth noting

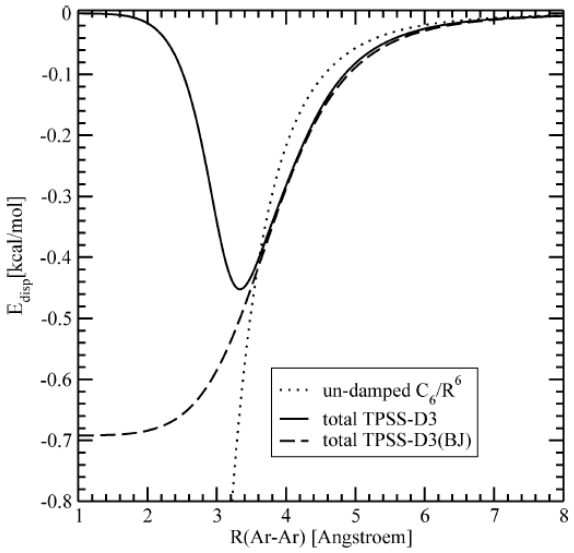

Figure 2-7: Dispersion correction energy for a pair of argon atoms separated by distance R, showing the undamped, 'zero-damping' (DFT-D3) and Becke-Johnson damping (DFT-D3(BJ)) methods [107].

that Becke-Johnson damping involves three empirical parameters whilst 'zero-damping' only involves two.

DFT-D3 and DFT-D3(BJ) are asymptotically correct with all functionals [106], and can easily be applied to any standard density functional without a significant loss of accuracy [88]. It provides a consistent description for all chemically relevant elements from H to Pu [106].

The TS method is also similar to D2, including only the $n = 6$ term in the dispersion energy in equation (2.34). Environmental dependence is included in a rather different way to D3: C_6 and van der Waals radii are scaled by using an effective volume, V^{eff}, with reference to the free atom in vacuum, V^{free}

$$C_6^{AA,eff} = \left(\frac{V_A^{eff}}{V_A^{free}}\right)^2 C_6^{AA,free}, \tag{2.45}$$

$$R_{eff}^0 = \left(\frac{V^{eff}}{V^{free}}\right)^{\frac{1}{3}} R_{free}^0. \tag{2.46}$$

These scaled C_6^{AA} values are then used to calculate C_6^{AB} by

$$C_6^{AB} = \frac{2C_6^{AA}C_6^{BB}}{\frac{\alpha_B^0}{\alpha_A^0}C_6^{AA} + \frac{\alpha_A^0}{\alpha_B^0}C_6^{BB}}, \tag{2.47}$$

where α_A^0 is the polarizability of the atom in free space and values for this and C_6^{AA} are obtained from the Chu & Dalgarno database [108].

The damping function for the TS method is different to D2 and both D3 methods - full details are in Ref. [105]. One scaling factor, s_R, is introduced in the damping function which is density functional dependent and said to be obtained by fitting to the S22 database, although exact values were not given [105]. The S22 database contains binding energies of 22 different model complexes containing only carbon, nitrogen, oxygen and hydrogen and cover a range of dispersion interactions [109]. Equilibrium structures were obtained using either CCSD(T) or the highly accurate MP2 method and binding energies calculated using CCSD(T) calculations [109], the "gold standard" in computational chemistry [11].

The XDM method is similar to the DFT-D2, -D3 and -TS methods in that an additional dispersion correction term is included in the total electronic energy, as in equation (2.33), but the form of this and idea behind it is very different. Here the dispersion energy of two neutral fragments is described as the electrostatic interaction of the instantaneous dipoles formed by electrons and their associated exchange holes. This produces dispersion coefficients that are aware of their chemical environment. Full mathematical details are given in Refs. [101, 103, 110].

Level 3: vdW functionals

The first vdW functional (vdW-DF1) was introduced in 2004 [111]. A variety of modifications since have produced several variations, known collectively as the vdW functionals.

vdW functionals include the nonlocal vdW interaction explicitly in the exchange-correlation energy

$$E_{xc} = E_x^{GGA} + E_c^{LDA} + E_c^{nl}, \tag{2.48}$$

where the correlation energy has been split into two pieces [112]. The nonlocal component [111, 112] is

$$E_c^{nl} = \frac{1}{2} \int d^3r d^3r' n(\mathbf{r}) \phi(\mathbf{r}, \mathbf{r}') n(\mathbf{r}'), \tag{2.49}$$

where $n(\mathbf{r})$ is the electron density at position $\mathbf{r}$ and $\phi(\mathbf{r}, \mathbf{r}')$ is the vdW kernel: a function of $n(\mathbf{r})$ and its gradient and dependent on $\mathbf{r} - \mathbf{r}'$. E_c^{nl} has been designed to be exact in the vdW asymptote and to vanish for a uniform electron gas to give a seamless theory [112].

In vdW-DF1 the nonlocal energy component is combined with revPBE [111] whilst PW86 (a GGA exchange energy functional) is used in vdW-DF2 [91]. Further vdW functionals such as optPBE-vdW and optB88-vdW involve optimisation of the exchange energy functionals, PBE and B88 respectively, with reference to the S22 database [113]. Broadly the differences between vdW functionals are in the kernel and the standard density functional the nonlocal component is combined with.

Level 4: MBD

The Many Body Dispersion (MBD) method was introduced in 2012 in the form MBD@SCS where '@SCS' indicates that the polarizabilities used within the method were calculated using the self-consistent screening method [114]. The MBD@rsSCS (range-separated SCS) was introduced in 2014 as a refined version of MBD@SCS [115]. The MBD method includes many-body terms and is based on the application of the random phase approximation (RPA) to the adiabatic-connection fluctuation-dissipation theorem (ACFDT).

Performance

A dispersion correction that performs well across a variety of cases is more likely to perform well in the coronene system studied here. Since the S22 test set was used for fitting scaling factors in several methods it is not a good indicator of performance. Instead we look to the C21 and slightly refined X23 test sets.

The C21 and X23 test sets consist of experimentally derived 0 K lattice energies and crystal structures of 21 or 23 molecular crystals respectively that span a range of dispersion interactions [110, 116]. The X23 test set contains the 21 crystals in the C21 test set with two additional systems [116]. In both sets experimental sublimation enthalpies are reduced to lattice energies with thermal and zero-point vibrational effects carefully accounted for through PBE-XDM or PBE-TS calculations for C21 and X23 respectively [110, 116]. The X23 set improves on the C21 set by including phonon dispersion and anharmonicity [116]. This use of DFT-D calculations is noteworthy as not only does it increase the error in the final 0 K lattice energies, it may also impart a bias towards these dispersion correction methods when considering the performance of various DFT-D methods.

The mean absolute error (MAD) of lattice energies for the C21/X23 test sets are shown in figure 2-8 (a). PBE-D3 performs best with PBE-XDM and PBD-MBD close behind. The MAD for PBE-XDM is based on the C21 test set that, as previously

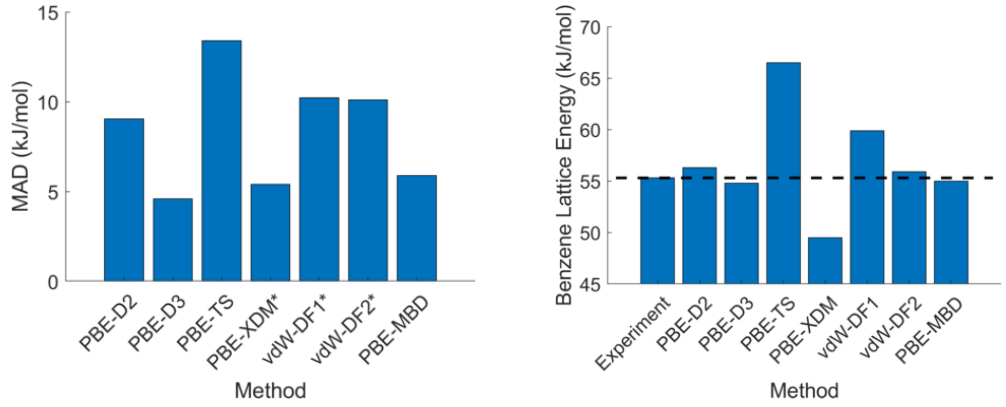

Figure 2-8: (a) Mean absolute deviation of the lattice energies for the C21 (indicated with *) or slightly adjusted X23 test sets [11, 110, 116]. (b) Lattice energies of crystalline benzene [11]. The dashed horizontal line indicates the experimental value which is, to within error, comparable with the "gold standard" coupled-cluster 2+3+4 body method (not shown here).

mentioned, used this method in reducing sublimation enthalpies to lattice energies, potentially introducing a bias towards this method in these results. In combination with a second functional, PBE0, the MBD method performs better than D3 [11] indicating that these two methods have a similar overall performance. PBE-TS performs the worst (MAD=13.4 kJ/mol [116]) on the X23 dataset, and is even worse on the C21 dataset (MAD=16.97 kJ/mol [110]) suggesting that its use in the creation of the X23 dataset may indeed have introduced some bias. Nevertheless this poor performance is surprising given it predicts reasonable cell lengths and angles (MAD of 0.05 Å and 0.14° respectively) [110]. PBE-D2, vdW-DF1 and vdW-DF2 perform similarly.

Another common performance benchmark is the lattice energy of the benzene crystal, figure 2-8 (b). The data presented here was gathered from a variety of sources with different computational details, and as such any comparisons are imperfect. However again PBE-D3 and PBE-MBD perform well. vdW-DF2 also performs well in this system, although it is known to perform less well elsewhere [11]. PBE-D2 also gives a reasonable result. PBE-TS again performs worst (66.5 kJ/mol), and PBE0-TS is only marginally better (62.0 kJ/mol). PBE-XDM and vdW-DF1 perform badly underestimating and overestimating the lattice energy by 5.8 kJ/mol respectively.

From these performance benchmarks it is easy to see why D3 has become the most popular method. Whilst MBD has a good performance, is relatively young and so is not yet as popular. One drawback of these performance tests is that vibrational frequencies, and hence the shape of the potential energy surface around the minimum,

are not examined. It may be that some methods provide a better description of the vibrations and potential energy surface than others.

2.3.2 Vibrational frequencies

There are two methods of calculating vibrations within the DFT framework: the finite differences method and density functional perturbation theory (DFPT).

Typically vibrational frequencies are calculated within the harmonic approximation. Again the Born-Oppenheimer approximation is enacted since it known to perform well in the case of lattice vibrations in nearly all materials [58]. This gives nuclei displacements that vary in time as

$$\mathbf{u}_I(t) = \mathbf{R}_I(t) - \mathbf{R}_I^0 = \mathbf{u}_I \exp(i\omega t), \tag{2.50}$$

where ω is the frequency, t is time and the displacements correspond to the real part of the exponential term. Starting from Newton's equations of motion it can be shown [58, 59] that the equation of motion for the nuclei is

$$-\omega^2 M_I u_{I\alpha} = -\sum_{J,\beta} K_{I\alpha,J\beta} u_{J\beta}, \tag{2.51}$$

where α and β are cartesian directions and $K_{I\alpha,J\beta}$ are the Born-von Karman force contants

$$K_{I\alpha,J\beta} = \frac{\partial^2 U}{\partial R_{I\alpha} \partial R_{J\beta}}. \tag{2.52}$$

The vibrational frequencies and modes are found by constructing the dynamical mass-weighted matrix, $\mathbb{D}$, with components

$$\mathbb{D}_{I\alpha,J\beta} = \frac{K_{I\alpha,J\beta}}{(M_I M_J)^{\frac{1}{2}}}. \tag{2.53}$$

Equation (2.51) then takes the form

$$\mathbb{D}u = \omega^2 u, \tag{2.54}$$

where u is a vector of $u_{I\alpha}$ values. This can be diagonalised, with the eigenvalues yielding the vibrational frequencies and the eigenvectors the associated atomic displacements.

In the finite differences method used in this work, the force constants are obtained as

$$K_{I\alpha,J\beta} \simeq -\frac{\Delta F_{I\alpha}}{\Delta R_{J\beta}}. \tag{2.55}$$

Simply, the nuclei are each displaced from equilibrium in turn by a small amount $\pm\Delta R_{J\beta}$ and the forces in the system determined for each new set of nuclear coordinates. The difference in forces between the two geometries, $\Delta F_{I\alpha}$, is determined and the force constants calculated using equation (2.55). After all geometries are probed, $\mathbb{D}$ is constructed, diagonalised and the eigenvectors and eigenvalues are calculated. For systems of reasonable size this atom by atom approach is computationally very expensive and so where possible the symmetry of the system is used to reduce effort.

Vibrational frequency calculations using DFT have been used successfully in a wide variety of crystals, both inorganic [117] and organic [97, 118], including cases where the crystal has been put under pressure [78, 119]. In molecular crystals, dispersion correction methods spanning the entire ladder (figure 2-4) have been used with success, although which method is more comparable to experiment depends on the specific system. One study [120] assessed the reliability of a range of dispersion correction methods, namely MBD@rsSCS, optPBE-vdW functional, PBE-D3(BJ), -TS, -D2 and PBE with no vdW correction, by comparing calculated low wavenumber Raman spectra with experimental results for five molecular crystals containing carbon, hydrogen, sulphur and oxygen. The five molecular crystals included polymorphs of two molecules. The MBD@rsSCS and PBE-D3(BJ) methods performed equally well predicting Raman spectra in close agreement with experiments where the experimental geometry was used. The Raman spectra for MBS@rsSCS was also calculated using the relaxed unit cell and again the predicted Raman spectra were in good agreement with experiments [120].

As alluded to in the previous paragraph, for molecular crystals two common techniques are used: fixing the unit cell to experimental lattice parameters, for example in Refs. [12, 121–123], and using DFT-D methods to relax the geometry and calculate vibrational frequencies, for example in Refs. [49, 78, 90, 94–98, 118, 124, 125]. As to which method is the better is of some debate, and some studies have used multiple methods to determine which works best in their specific case, for instance in Ref. [77]. Fixing the unit cell is rationalised by the fact that phonon modes are very sensitive to the unit cell volume: where DFT predicts a unit cell volume lower than experiment, phonon frequencies are over predicted [126]. Nonetheless a recent study shows that this 'fix' does not always bring calculated frequencies into good agreement with experiment for all vdW correction methods [120]. The view taken here is that fixing the unit cell is not ideal as it produces strain in the crystal, which previous work has shown may produce erroneous frequencies due to poorly represented dispersion forces [95].

Anharmonic and temperature effects can also be important. In 'soft' molecular crystals, thermal expansion can be relatively large causing changes in the vibrational

potential energy surface and hence vibrational frequencies [127]. Furthermore potential energy curves are anharmonic, as seen in figure 2-3, and this anharmonic nature is not described by the harmonic approximation giving rise to some differences between calculated and experimental results. Calculating anharmonic contributions is a formidable computational task: 2 million CPU hours were used to calculate the anharmonic contributions for paracetamol (80 or 160 atoms/unit cell for forms I or II respectively) [12] and hence is not typically performed.

Some of these additional effects on frequencies have been accounted for in intramolecular modes by applying a scale factor to calculated frequencies [78, 128–130]. However whilst scaling may improve the agreement for some frequencies it does not for others due to the varying amount of anharmonicity present in the modes [118]. The application of scale factors to intermolecular modes is noted to be "at best difficult, if not impossible" [120] due to the lack of consistent global shifting of frequencies across a variety of molecular crystals. Due to these difficulties no scaling has been used in this work.

Vibrational Density of States and Dispersion

In section 2.1 it was shown that vibrations play a role in the phase stabilities of polymorphs. To calculate the Helmholtz vibrational contribution to the phase stabilities in equation (2.11), a sum over all vibrational modes must be taken

$$F_{vib} = \sum_i \frac{\hbar\omega_i}{2} + k_B T \sum_i \ln\left[1 - \exp\left(-\frac{\hbar\omega_i}{k_B T}\right)\right]. \tag{2.56}$$

Given that vibrational modes have a dispersive nature across the unit cell, the summations must cover frequencies over all wave vectors, $\mathbf{q}$, in the Brillouin zone. This can be written as

$$F_{vib}(T) = \sum_{\mathbf{q},j} \frac{\hbar\omega_{\mathbf{q},j}}{2} + k_B T \sum_{\mathbf{q},j} \ln\left[1 - \exp\left(-\frac{\hbar\omega_{\mathbf{q},j}}{k_B T}\right)\right], \tag{2.57}$$

where j is the mode index. In practise, the set of wavevectors $\mathbf{q}$ within the Brillouin zone is replaced by a representative sample. Therefore to determine the vibrational contribution to the free energy, the dispersion of vibrations across the Brillouin zone must be calculated. In the present work this was done by constructing a supercell and then using Γ-point sampling. The use of supercells allows vibrational frequencies at specific points in the first Brillouin zone, often at key symmetry points and along their directions, to be determined from band folding. Vibrational frequencies at other wavevectors are found by interpolating between these exact values.

A related quantity is the phonon density of states, $g(\omega)$. In Phonopy [47], used in this work, the vibrational density of states is calculated as

$$g(\omega) = \frac{1}{N} \sum_{\mathbf{q},j} \delta(\omega - \omega_{\mathbf{q},j}), \tag{2.58}$$

where N is the number of unit cells in the supercell [47]. $g(\omega)$ is constructed such that the integral over frequency becomes $3n_a$ where n_a is the number of atoms per unit cell. Therefore once the vibrational frequencies at wavevectors across the Brillouin zone have been calculated it is simple to determine the vibrational density of states. The vibrational density of states can be determined experimentally by neutron or inelastic x-ray scattering [131, 132].

Brown-Altvater *et al.* performed an in depth study [90] on the phonon dispersion of the molecular crystal naphthalene. Naphthalene is also a poly-aromatic hydrocarbon (PAH) consisting of two joined benzene rings, space group P21/a with 2 molecules per unit cell arranged in a herringbone structure. Thus it is related to coronene and the results therefore particularly noteworthy. Neutron scattering data is available for deuterated naphthalene at 6 K [133] and compared to the results of DFT calculations in Ref. [90]. A supercell of size $2 \times 4 \times 2$ was used for the phonon dispersion calculations coupled with the vdW-DF-cx functional, a modified version of the vdW-DF2 functional [134]. The lattice parameters were reported as $a = 8.08$ (8.06) Å, $b = 5.93$ (5.91) Å, $c = 8.63$ (8.75) Å and $\beta = 124.7$ (124.4)° for the experimental (and vdW-DF-cx calculation). The DFT calculations showed remarkable consistency with the experimental results, figure 2-9, with all minor discrepancies accounted for by considering the significance of the longer c-axis. The success of these calculations suggest a similar sized supercell will be appropriate for studying the vibrations of coronene.

2.3.3 Thermodynamics in the quasi-harmonic approximation

In order to calculate the Gibbs free energy in equation (2.12)

$$G(T,p) = \min_{V} \left[U_{latt}(V) + F_{vib}(T,V) + pV \right], \tag{2.59}$$

the volume of the unit cell must first be perturbed. There are two types of volume expansion: isotropic and anisotropic. Isotropic expansion assumes the lattice vectors scale proportionally and lattice angles remain fixed for all volumes. In anisotropic expansion the six lattice parameters are allowed to change with no constraints. Clearly anisotropic expansion is more realistic as most crystals are anisotropic to some degree.

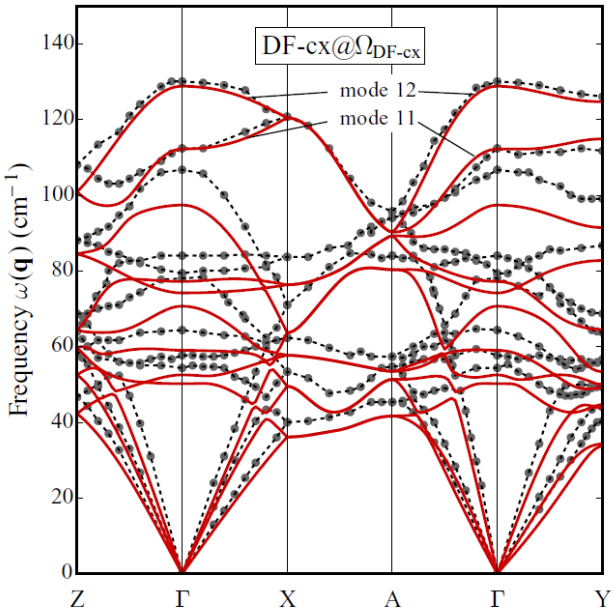

Figure 2-9: Calculated phonon dispersion (solid lines) compared with neutron-scattering experiments of d8-naphthalene at 6 K (grey circles, dashes to guide the eye). Reproduced from [90].

Anisotropy is particularly important in crystals containing larger molecules and layered materials [135]. However a full anisotropic approach is significantly more computationally complex since it involves minimising the Gibbs free energy over six degrees of freedom (the three lattice vectors and three angles) rather than simply the volume. Instead a simplified quasi-anisotropic approach is often used where the unit cell is isotropically expanded and contracted then relaxed with the volume fixed. Applying pressure to change the unit cell volume is a second option used in the literature [136]. The quasi-anisotropic method, whilst widely used, does not perform well in all scenarios: for example the lattice parameters for resorcinol using the quasi-anisotropic expansion approach agree with those from the full anisotropic method, but for piracetam the quasi-anisotropic method misses the anisotropic nature and instead resembles the isotropic method [135].

Next the harmonic approximation is applied to each expanded and contracted structure to calculate the vibrational contribution to the Helmholtz free energy. This can be performed through full calculations as previously detailed, however calculating frequencies across the first Brillouin zone for many volumes is rather computationally expensive. Instead some studies employ Grüneisen parameters, where a linear dependence of vibrational frequencies on volume is assumed. This reduces the number

of volumes vibrational frequencies must be calculated to three: one expanded, one contracted and the equilibrium volume structure. The accuracy of this approach is uncertain: a study of resorcinol and piracetam finds small (up to 2 meV) deviations in the quasi-harmonic Gibbs free energy at 300 K using Grüneisen parameters [135], whilst the thermal expansion of diamond has a large difference of 10% at 1600 K [137]. Furthermore Erba *et al.* found that this linear fitting gives "a poor description of the volume dependence, of phonon frequencies" [138] and that cubic fitting was more appropriate. Due to the questionable level of accuracy that can be obtained, in this work the decision was taken to perform full calculations.

Finally the Helmholtz free energy as a function of volume is calculated and fitted for each temperature by an equation of state and the minimum volume and free energy determined, illustrated in figure 2-10. The minima give the quasi-harmonic Helmholtz free energy as a function of temperature, which with the addition of the $pV(T)$ term allows the quasi-harmonic Gibbs free energy to be calculated. From this further thermodynamic properties may also be computed such as the thermal expansion coefficient

$$\alpha_V = \frac{1}{V}\frac{\mathrm{d}V}{\mathrm{d}T}. \tag{2.60}$$

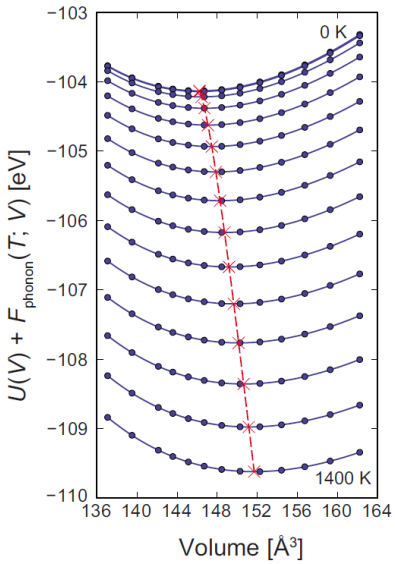

Figure 2-10: Helmholtz free energy, $U_{\mathrm{latt}}(V) + F_{\mathrm{vib}}(T, V)$, as a function of unit cell volume of Ti_3SiC_2. Circles denote calculated Helmholtz free energy at every 100 K between 0 and 1400 K. Solid curves show fitted Vinet equation of state. Minimums are denoted by crosses and the dashed line is a guide to the eye. Reproduced from Ref. [46].

Various equations of state exist, with the Murnaghan equation of state being a popular choice [127, 139–142]. Other options include Vinet [46, 47], Rose-Vinet [135] and Birch-Murnaghan [137]. In the Murnaghan equation of state, used in this work, the free energy is

$$F(V) = F_0 + \frac{B_0 V}{B_0'}\left[\frac{(V_0/V)^{B_0'}}{B_0' - 1} + 1\right] - \frac{B_0 V_0}{B_0' - 1}, \tag{2.61}$$

where F_0 is the free energy equilibrium, V_0 is the equilibrium volume, B_0 is the bulk modulus and B_0' is the dimensionless first derivative of B_0 with respect to pressure. These four parameters are fitted for each temperature curve. The Murnaghan equation was not developed nor optimised for molecular crystals and therefore low quality fits can occur producing errors in the Helmholtz energy. This can introduce some uncertainty into subsequent thermodynamic properties [142]. Nevertheless since it is the minima that are of interest, the impact of these errors is likely small.

2.3.4 Raman intensities

Raman intensities, or rather Raman tensors which can then be used to determine Raman intensities, can be found from the results of DFT calculations. Here the theoretical background of Raman scattering is introduced outlining the material properties that are required to calculate Raman intensities.

The interaction of light and matter is represented by

$$\mathbf{P} = \epsilon_0 \chi \mathbf{E}, \tag{2.62}$$

where $\mathbf{P}$ is the polarisation, $\mathbf{E}$ is the electric field, χ is the dielectric susceptibility of the material and ϵ_0 is the permittivity of free space. The components of $\mathbf{P}$ are,

$$P_j = \epsilon_0 \chi_{jk} E_k, \tag{2.63}$$

where j and k are spatial coordinates and χ_{jk} is a second rank tensor. Taking incident light of frequency ω_I and wavevector $\mathbf{k}_I$ with electric field

$$\mathbf{E}(\mathbf{r}, t) = \mathbf{E}(\mathbf{k}_I, \omega_I) \cos(\mathbf{k}_I \cdot \mathbf{r} - \omega_I t), \tag{2.64}$$

and displacements of atoms due to a phonon of frequency ω_{ph} and wave vector $\mathbf{q}$

$$\mathbf{u}(\mathbf{r}, t) = \mathbf{u}(\mathbf{q}, \omega_{ph}) \cos(\mathbf{q} \cdot \mathbf{r} - \omega_{ph} t), \tag{2.65}$$

it can be shown [143] that the time dependence of the polarisation components for first-order Raman scattering is

$$P_j(\mathbf{r},t,\mathbf{u}) = \frac{1}{2}\varepsilon_0 \left(\frac{\partial \chi_{jk}\left(\mathbf{k}_I,\omega_I\right)}{\partial u_l}\right)_{u=0} u_l\left(\mathbf{q},\omega_{ph}\right) E_k\left(\mathbf{k}_I,\omega_i\right) \times \Big(\underbrace{\cos\left[\left(\mathbf{k}_I+\mathbf{q}\right)\cdot\mathbf{r}-\left(\omega_I+\omega_{ph}\right)t\right]}_{\text{anti-Stokes}} + \underbrace{\cos\left[\left(\mathbf{k}_I-\mathbf{q}\right)\cdot\mathbf{r}-\left(\omega_I-\omega_{ph}\right)t\right]}_{\text{Stokes}}\Big), \tag{2.66}$$

where l is also a spatial coordinate. This gives rise to two terms, Stokes and anti-Stokes, where there has been a transfer of momentum between the incident photons and the phonon mode. The Raman tensor is

$$R_{jk,l} = \left(\frac{\partial \chi_{jk}\left(\mathbf{k}_I,\omega_I\right)}{\partial u_l}\right)_{u=0} u_l\left(\mathbf{q},\omega_{ph}\right), \tag{2.67}$$

in terms of which the Raman intensity for the l^{th} mode is

$$I \propto |e_j^S \cdot R_{jk,l} \cdot e_k^I|^2, \tag{2.68}$$

where e_j^S is the unit vector describing the polarisation direction of the scattered light and e_k^I is the unit vector describing the polarisation direction of the incident light. Therefore to calculate the Raman tensor one must know the dielectric susceptibility of the material. Methods of calculating the dielectric function are described in Refs. [58, 144].

Off-the-shelf DFT programmes such as VASP used in the present work usually output the Raman tensor, or Raman intensities for given directions, and sometimes the 'Raman activity', an orientational average of the Raman intensities that is experimentally equivalent to measurements taken from polycrystalline samples.

2.4 Summary

In this chapter the thermodynamic picture of phase stabilities in polymorphism has been introduced and the contribution from vibrations detailed. The kinetic aspect of phase stabilities has been briefly discussed and studies on phase stabilities in the literature examined.

Next the two types of vibrations that occur in molecular crystals, specifically intramolecular and lattice vibrations, have been presented. The key details of four

methods to measure these vibrations, namely inelastic neutron scattering, Raman, IR and terahertz spectroscopy, have been briefly described. Selection rules that determine which vibrations can be measured with Raman, IR and terahertz spectroscopy have been summarised and symmetry labels for the coronene molecule, γ- and β-coronene presented with the associated Raman and IR/terahertz activities. These symmetry labels are used throughout in the discussion of calculated vibrational modes. Raman spectroscopy is used to investigate the intramolecular vibrations of γ- and β-coronene in Chapter 4 and the lattice vibrations in Chapter 5.

The mathematics underpinning density functional theory (DFT) has been briefly outlined with key assumptions and approximations highlighted and the successes and drawbacks of DFT discussed. For this work, the main issue in standard DFT is identified as the inadequate description of dispersion interactions. Thus dispersion corrections that attempt to rectify this have been extensively detailed and their performance discussed. Next the mathematics for calculating vibrational frequencies within the DFT framework has been introduced and examples in the literature discussed. The importance of the vibrational density of states and dispersion curves, and the method used to calculate these in this work, has also been described. The method for calculating thermodynamic properties within the quasi-harmonic approximation has been introduced and the associated benefits and drawbacks of the approximation examined. Finally the theoretical background to Raman scattering and the method for calculating Raman intensities has been detailed. Dispersion corrected density functional theory (DFT-D) is used in Chapters 4 and 5 to relax the structures of γ- and β-coronene, calculate their vibrational frequencies, and produce Raman spectra which are then used to interpret experimental results. In Chapter 6, the DFT-D computations are extended to calculate the vibrational density of states, dispersion curves and thermodynamic quantities to study the phase stabilities of γ- and β-coronene.

Chapter 3

Crystal growth

At standard room temperature and pressure, coronene naturally exists in the γ-phase which is therefore relatively simple to grow. Several methods for this have been presented in the literature, including crystallisation from a supersaturated solution of coronene in toluene [8] and by physical vapour transport (PVT) in a nitrogen stream [145]. The PVT method produces high-purity crystals, particularly when the commercially available starting material is further purified. PVT has been used to produce crystals of coronene that have been used in studies of the luminescence spectra [145], exciton scattering [34, 36] and exciton-phonon coupling [33]. In contrast synthesis of β-coronene is relatively new, having only been discovered in 2015 [8]. The crystallisation method involved filtering a hot (93°C) supersaturated solution of coronene in toluene and cooling inside a 1 T magnetic field. This produced orange crystals in the β-phase. To date no other research has been published which reproduces this remarkable crystal growth. Here our purification and PVT method for growing high purity γ-coronene crystals subsequently used in Raman spectroscopy presented in Chapters 4 and 5 is detailed, and the method of growing β-coronene crystals is investigated.

3.1 Purification

Powdered γ-coronene of 97% purity was sourced from Sigma-Aldrich or TCI-UK and twice purified by sublimation under vacuum (10^{-3} mbar), figure 3-1. Powdered γ-coronene was set inside an ampoule. A cold finger was placed into the ampoule and a seal formed using vacuum grease. 18°C water was circulated through the cold finger using a water chiller. The ampoule was placed under vacuum and heated to 190°C in a beaker of silicon oil on a hot plate. The set-up was wrapped in foil to avoid possible

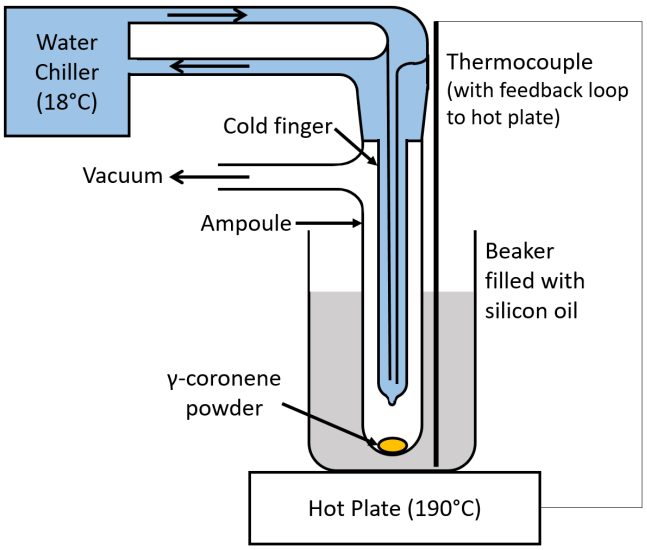

Figure 3-1: Set-up for purification of γ-coronene by sublimation in vacuum. The water chiller was set to 18°C, approximately room temperature, to avoid water condensing on the pipes and dripping into the hot silicon oil. The set-up was wrapped in foil to avoid possible degradation of the coronene by light.

degradation of the coronene by light. The set-up was left overnight, for up to 24 hours, until all coronene had sublimated and condensed on the cold finger. Impurities of dark colour remained at the bottom of the ampoule. The cold finger was removed and the purified coronene scraped off. The set-up was dismantled, cleaned and the process repeated. All purified coronene was stored in sealed and foil wrapped vials in a nitrogen glove box.

In Raman measurements a high fluorescent background was recorded from unpurified γ-coronene on silicon, even when using a laser wavelength of 785 nm corresponding to an energy well below the gap, as illustrated in figure 3-2. This background was significantly reduced after one purification step, indicating impurities are a source of significant levels of background fluorescence. A second sublimation step was tested and found to be essential in reducing the background to near zero. The peaks in these Raman spectra are investigated and discussed in Chapter 4.

3.2 Growth of γ-coronene

Crystals of γ-coronene were grown using a physical vapour transport method in a three zone furnace, similar to that of pure perylene reported in Ref. [146]. Quartz boats

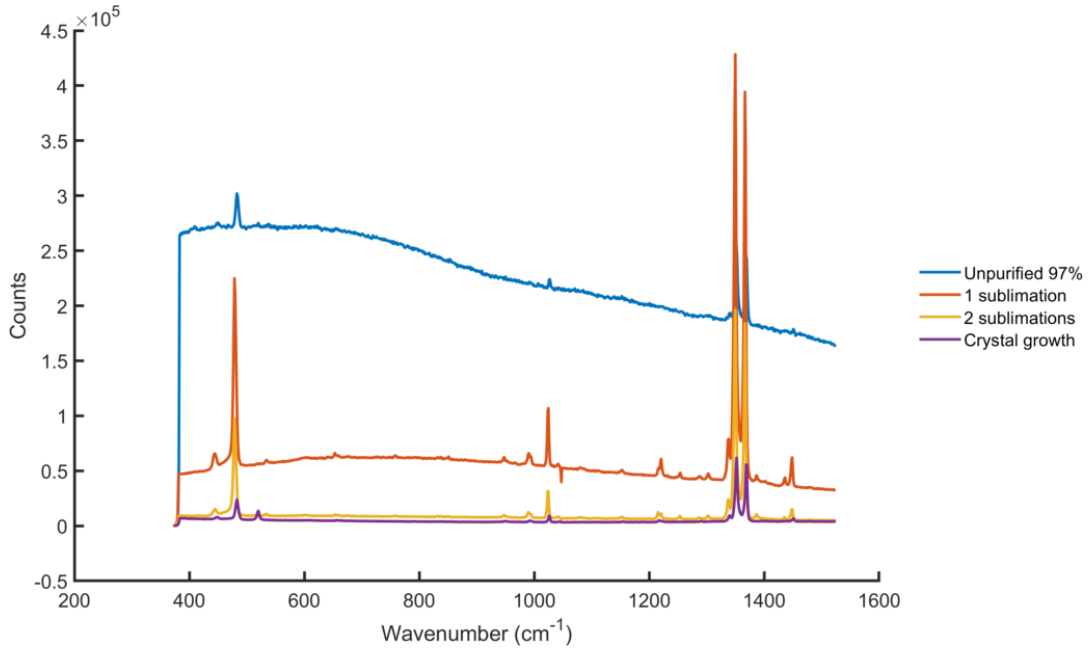

Figure 3-2: Raman spectra of 97% purity coronene compared to samples after one and two sublimations and a single γ-coronene crystal grown from twice sublimated coronene. A 785 nm laser was used at 50% power with 30 cumulative accumulations at 1 s each. The background decreases with each subsequent sublimation step, to approximately zero for the single crystal obtained from growth detailed in section 3.2.

10 cm in length were placed inside a clean quartz tube. The twice purified γ-coronene was placed on a platform in a quartz boat at one end of the long tube. This was placed inside the furnace set to 175°C (cold zone), 225°C (central zone) and 275°C (hot zone). The boat filled with coronene was located in the hot zone. Gaseous argon was set to flow from the hot to cold zones at a rate of approximately 40 cm^3/min to assist transfer of sublimed coronene down the tube. After 2 days the furnace was allowed to cool. Upon removal, the boat with source material was empty and ∼20 cm further down the tubing small crystals of coronene coated the inside of the quartz boats, figure 3-3 (a)(b). The boats were individually removed and γ-coronene crystals carefully removed from the inside. The crystals came out in bundles, figure 3-3 (c), and were carefully separated for use in further experiments.

The structure of a crystal was examined by single-crystal x-ray diffraction which confirmed the crystal as γ-coronene, with lattice parameters $a = 10.08$ Å, $b = 4.69$ Å, $c = 15.64$ Å and $\beta = 106.06°$ giving a volume $V = 710$ $Å^3$ and an intracell molecular angle of $\phi = 85.34°$ at 290 K. Single-crystal XRD was performed by Dr. G. Kociok-Köhn at the Material and Chemical Characterisation Facility (MC^2) at the University of Bath [147]. Further results are presented in Chapter 4.

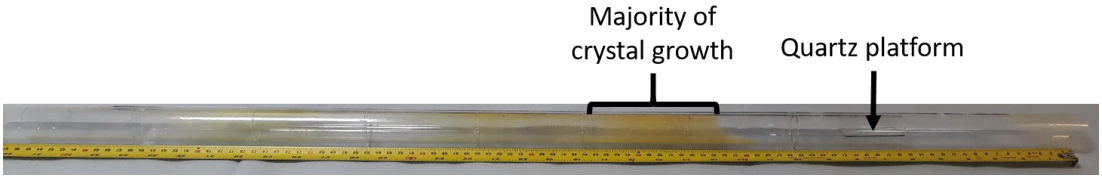

(a)

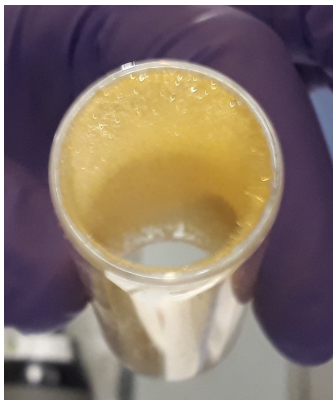

(b)

(c)

Figure 3-3: Crystal growth of γ-coronene in a three zone furnace. (a) The long tube with quartz boats and positions of the quartz platform and region of crystal growth indicated, (b) a quartz boat with crystals coating the inside face and (c) (top) example bundles of crystals and (bottom) a single crystal separated from the bundle on millimetre paper.

3.3 Attempted growth of β-coronene

Potticary *et al.* [8] successfully crystallised β-coronene at standard room temperature and pressure by cooling a filtered supersaturated coronene in toluene solution from 93°C to room temperature inside a 1 T magnetic field. It is the application of this magnetic field that is believed to be the key component in forming the β-phase in place of the γ-phase. Indeed even a reduced magnetic field of 0.8 T was insufficient to form β-coronene, suggesting that 1 T is close to the threshold for crystallisation of the β-phase [8]. It is therefore critical for the magnetic field in the region of crystal growth to have a strength of at least 1 T, and to be homogeneous.

3.3.1 Magnet characterisation

A 1 T permanent Neodymium Iron Boron (NdFeB) magnet was sourced from Magnet Sales and Service Ltd. The magnet had a C shaped configuration with two sets of NdFeB magnets magnetically coupled to a steel yoke. The magnets were 10 cm × 5 cm with a gap of 6 mm between poles. The magnetic field strength was measured between the poles using a Hall probe and is presented in figure 3-4. The inner 2 × 6 cm region (white box) was identified for crystal growth as the most homogeneous region with the magnetic field varying between 1.09 T and 1.12 T. The magnetic field is above 1 T in the inner 3 × 8 cm (grey dashed box) giving some safety margin for error in positioning during crystal growth.

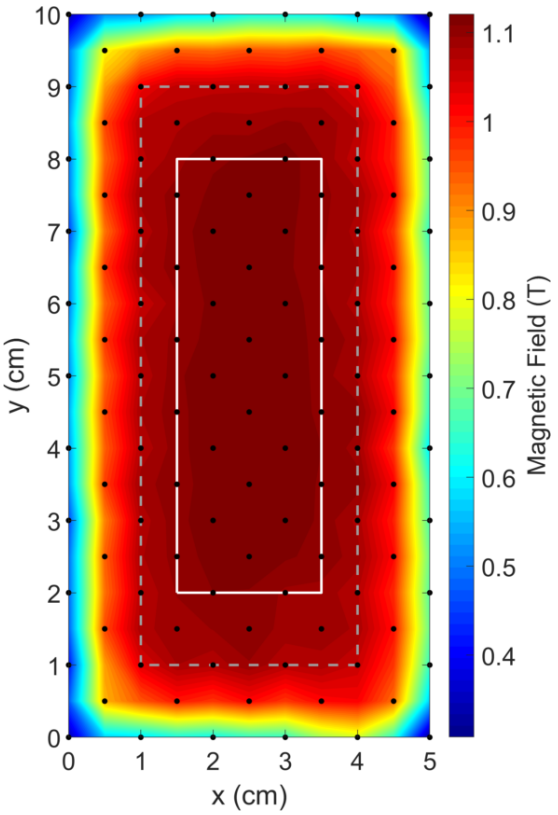

Figure 3-4: Magnetic field strength between the poles of the 1 T magnet measured using a Hall probe. Black dots indicate where measurements were taken and the colourmap was produced by interpolating between these points. The magnetic field is above 1 T in the inner 3 × 8 cm (grey dashed box). The inner 2 × 6 cm region (white box) is the most homogeneous region and selected for crystal growth. A maximum error of 0.1 T was recorded at the edges of the magnet due to large variations of field strength from small changes in position of the hall probe due to the rapid drop of magnetic field with distance. Inside the grey box, the maximum error was 0.02 T.

3.3.2 Method

It was attempted to replicate the crystal growth of β-coronene reported by Potticary *et al.* in Ref. [8]. The basic steps are outlined here. Any deviations are detailed with the respective results.

Purified γ-coronene was dissolved in toluene at a concentration of at least 2.5 mg/ml in order to create a supersaturated solution. The sealed vial was heated to 93°C in a beaker of silicon oil on a hot plate.

A schematic diagram of the experimental apparatus used for crystal growth is shown in figure 3-5 (a). The 1 T magnet was place on top of aluminium stilts inside an oven with a short clamp stand. The oven was calibrated by inserting a thermocouple through a hole in the top. Marks were made on the heating dial corresponding to the settings required for a set of temperatures. A small hole was made in a cork bung and a 5 mm NMR tube threaded through. The bung was placed atop the magnet with the NMR tube located in the inner 2×6 cm crystal growth region of the magnetic field. A 2 ml glass syringe was suspended in a clamp above the NMR tube. The syringe plunger and a glass pipette were placed in a clean beaker inside the oven. Finally a dimmable light bulb was placed under the NMR tube and a USB endoscope camera positioned facing the tube such that the crystal growth could be monitored with the oven door closed.

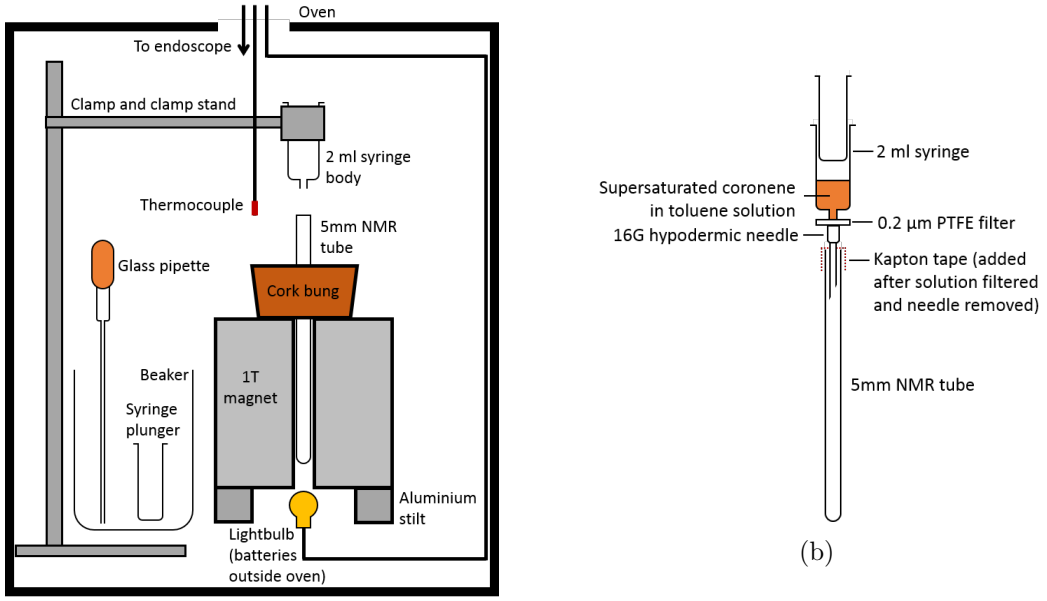

Figure 3-5: Set-up for attempted β-coronene crystal growth: (a) contents of the oven prior to heating and (b) filtration method inside the oven.

The oven was heated to 93°C and the contents allowed to come to thermal equilibrium overnight. The supersaturated solution, and beaker containing silicon oil, were placed inside the oven and the door closed. When the thermocouple indicated that the oven air temperature had recovered to ≥90°C, a 16 G hypodermic needle and 0.2 μm Fisherbrand non-sterile PTFE syringe filter were connected to the syringe body with the needle end inside the NMR tube. The supersaturated solution was pipetted into the syringe, the plunger inserted and the solution filtered into the NMR tube, figure 3-5 (b). Placing the filter and hypodermic needle into the oven prior to use resulted in degradation such that the solution would not pass through the filter. The silicon oil and supersaturated solution were removed from the oven and the door closed. When the oven air temperature had again recovered to ≥90°C, the syringe, filter and needle were removed and Kapton tape used to seal the NMR tube, and the oven again closed. Standard NMR tube lids were unsuitable for sealing the NMR tube as they deformed at 93°C. Throughout this process the time spent with the oven door open was kept to a minimum.

The filtered solution was left for an hour to equilibrate, then the oven was cooled to 50°C over a 1 hour period. The NMR tube was observed through the USB endoscope. If crystals had formed at this stage it would indicate that removal of any small crystals by filtration was not successful. Lastly the oven was turned off and allowed to cool to room temperature overnight.

3.3.3 Results

Many attempts were made at growing β-coronene. Figure 3-6 shows the crystals formed from one such attempt. Here a 1.3 ml solution of 2.7 mg/ml coronene in toluene was prepared and heated to 93°C inside the oven. The solution was left for 10 days prior to use. The NMR tube was sealed with DuraSeal. The oven was allowed to cool by 10°C every 24 hours prior to being turned off at 50°C. Three days later the oven was opened and yellow-brown crystals were revealed, figure 3-6. The remaining solution was poured out and the NMR tube left inside the oven to fully dry. After evaporation some white residue was left inside the tube indicating contamination. It was later determined that this was from the DuraSeal, hence a switch to Kapton tape in later experiments. Nevertheless the crystals were removed and examined by single crystal XRD. They were found to be in the γ-phase. None of these initial attempts resulted in β-coronene, although the crystal colours ranged from yellow to brown. High purity crystals of γ-coronene are yellow, as shown from the crystal growth in figure 3-3, suggesting the brown colour may arise from impurities.

'Ageing'

It was suggested by Dr. J. Potticary [148] who grew the original β-coronene crystals [8] that leaving the supersaturated solution at 93°C to 'age' the solution may aid in growth of β-coronene crystals. In the initial discovery of β-coronene it transpired that the solution had been left for a number of weeks.

25.9 mg of purified coronene was dissolved into 10.0 ml of toluene producing a solution of concentration 2.6 ± 0.1 mg/ml. This solution was heated to 93°C as detailed. A series of crystal growths were performed at 15 days, 22 days, 29 days and 36 days, figure 3-7. Crystals were collected from the NMR tubes and ranged from yellow to yellow-brown, appearing more brown as the solution aged. The unit cell of a sample crystal from each growth was determined by single-crystal XRD. All crystals were found to be the γ-phase.

Doping with dicoronylene

Dicoronylene, a PAH with chemical formula $C_{48}H_{20}$ consisting of two molecules of coronene fused together, naturally crystallises in the β-herringbone structure, figure 3-8, with lattice parameters $a = 10.376$ Å, $b = 3.832$ Å, $c = 31.914$ Å and $\beta = 90.24°$ [149]. The intracell molecular angle is $\phi = 50.32°$. Crystals of dicoronylene appear red to the naked eye. Due to its β structure, a hypothesis was made that dicoronylene could be used to seed the β form of coronene.

This experiment was attempted twice. A second NMR tube was placed inside the oven, outside of the magnet, to act as a control. For the first growth, 13.0 mg of coronene and 2.5 mg of dicoronylene were dissolved in 5.2 ml of toluene and heated to 93°C on a hot plate. Filtration commenced on day four. Excess solute was left in the solid state at the bottom of the solution, indicating the solution had reached saturation. The solute was red suggesting it was mainly dicoronylene that had not dissolved. For the second growth attempt, in order to aid in dissolution of dicoronylene an additional 4.5 ml of toluene was added to the leftover solution, approximately double the volume that remained. This was completed in two stages: +2.0 ml on day five and +2.5 ml on day seven. The crystal growth was performed four days after the final toluene addition, on day eleven.

Figure 3-9 shows example crystals from both growth attempts. Crystals from the second growth appeared redder in colour compared to the first attempt, indicating that perhaps more dicoronylene was present. Single crystal XRD was performed on crystal

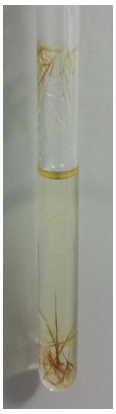

Figure 3-6: Crystals inside a 5 mm NMR tube from an early attempt at β-coronene crystal growth inside the oven. Single crystal XRD determined the structure to be the γ-phase.

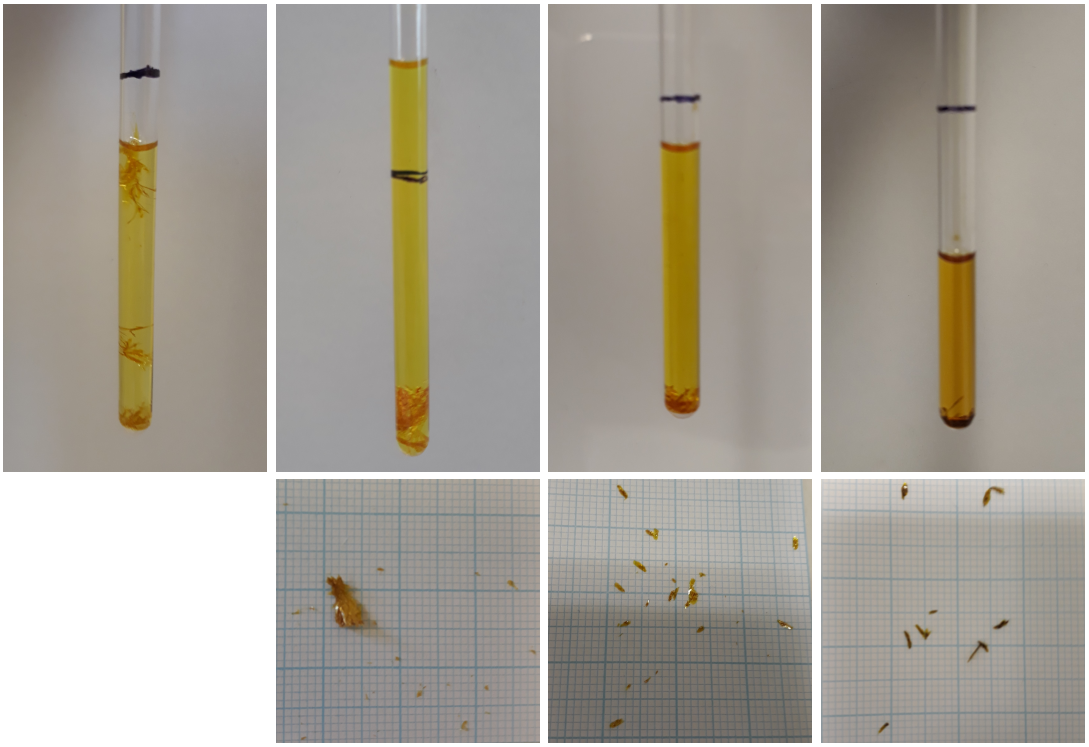

(a) (b) (c) (d)

Figure 3-7: Series of crystals grown after 'ageing' the supersaturated coronene solution for (a) 15 days, (a) 22 days, (a) 29 days and (a) 36 days. Top - NMR tube upon removal from the oven, bottom - crystals extracted on 1 mm square paper. All samples were determined to be γ-coronene.

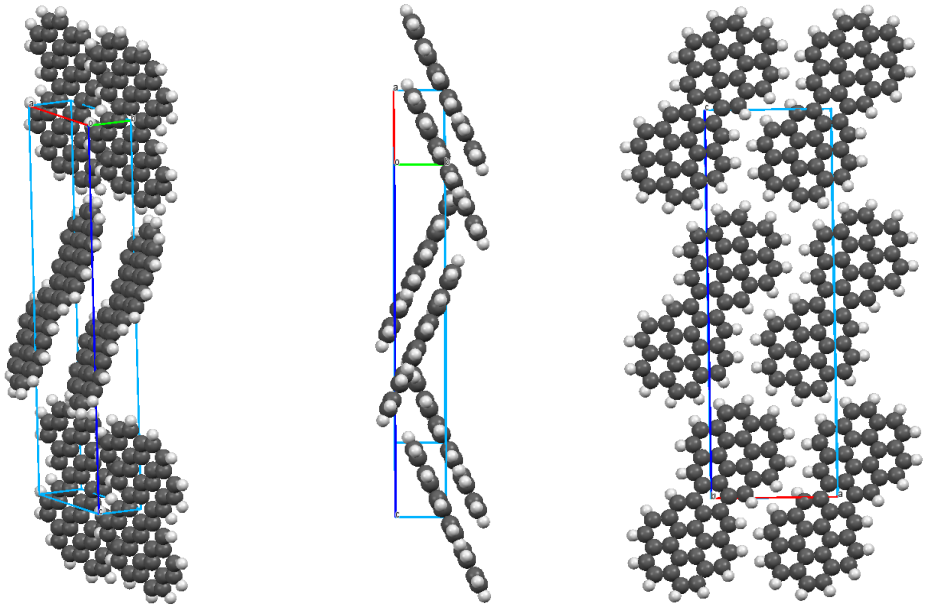

(a) (b) (c)

Figure 3-8: Unit cells (blue) of dicoronylene [149]. (b) clearly shows the β-herringbone packing with an intracell molecular angle, ϕ=50.32°. Red, green and dark blue lines indicate the directions of the a, b and c axes respectively.

samples from each attempt and all were established to be in the γ-phase. Thus we conclude that doping with dicoronylene does not seed β-coronene crystals.

Summary and outlook

Despite many attempts, crystals of β-coronene at room temperature were not formed. Neither 'ageing' the solution nor doping with dicoronylene made any difference to the resulting crystal structure.

It is possible that β-coronene is a "*disappearing polymorph*". A disappearing polymorph is one which has been prepared at least once and has been established by some experimental measurement. Subsequent attempts to prepare said polymorph using the same procedure then fail leading to a different, and typically more stable, form or a mixture of the two [150]. Here γ-coronene is more stable at room temperature and pressure and therefore grows preferentially to β-coronene, once β-coronene 'disappears' (if it appears at all). Nevertheless β-coronene may still be accessed by cooling crystals of γ-coronene below the phase transition temperature to where β-coronene is more thermodynamically stable.

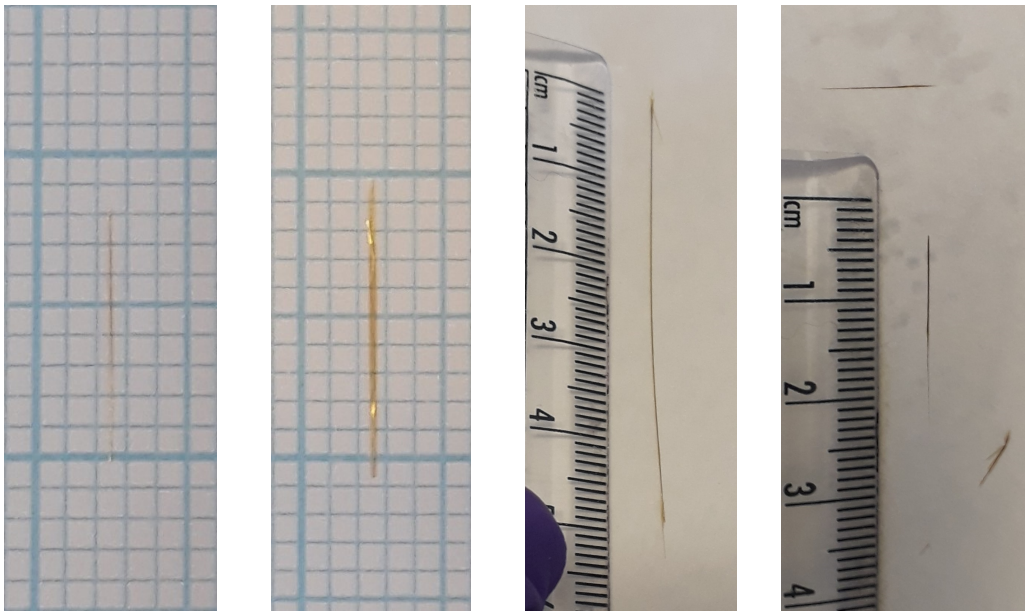

(a) (b) (c) (d)

Figure 3-9: Example crystals from dicoronylene doped coronene growth. Attempt 1 (a) inside the magnet and (b) outside the magnet on 1 mm squared paper. Attempt 2 (c) inside the magnet and (d) outside the magnet. Crystals from attempt 2 appear redder than attempt 1 and the crystals obtained from inside the magnet are significantly larger. All crystals were determined to be of the γ polymorph of coronene by single crystal XRD.

The intriguing phenomena of disappearing polymorphs is known in the pharmaceutical industry where there have been multiple cases that have led to patents disputes and withdrawal of medications from the market. It is suggested that a key mechanism in disappearing polymorphs is seeding of the new stable form. These seeds can be so small they are invisible to the naked eye and exist in the atmospheric dust in a laboratory [150]. This may be why we were unable to grow β-coronene crystals in our laboratory: the more stable γ-form has been used previously and it is likely there are microscopic seeds in the laboratory that were unknowingly contaminating our supersaturated solution of coronene in toluene. Another possible source of seeding could be from incomplete dissolution of γ-coronene and subsequent microscopic particles that pass through the filter into the crystal growth solution. I believe the former cause of seeding is more likely since Potticary *et al.* also filtered their solution using a 0.22 µm PTFE filter and successfully formed β-coronene crystals [8]. There are two possible methods of overcoming this problem that have been successfully used in other cases [150]. Firstly using a new laboratory at a new location and new staff who have not come into contact with γ-coronene previously. This would reduce the number of γ-coronene

seeds present and may allow β-coronene to be formed. However since γ-coronene is used in the preparation of the supersaturated solution it is likely that any new location would eventually become sufficiently seeded with γ-coronene that β-coronene again 'disappears'. A second solution is to thoroughly clean the laboratory. This method has been successful in the case of benzocaine:picric acid. Here "discarding all samples, washing the equipment and laboratory benches and waiting 8-12 days" [151] allowed the disappearing polymorph to be recovered, albeit temporarily. Repeating the cleaning process allowed the disappearing polymorph to be recovered again, indicating that in this case thorough cleaning is an adequate and repeatable solution.

Previous studies have shown that templating using a seed crystal requires good lattice matching [152]. In this work dicoronylene was chosen as a dopant purely based on the β-herringbone packing and similarity to coronene molecules. It does not have good lattice matching with β-coronene which explains why the addition of this dopant did not result in the growth of β-coronene. A possible avenue of future work is to search for crystal structures of other compounds that have good lattice matching and therefore could successfully act as a template for the growth of β-coronene.

There are a few possible further avenues to investigate with regards to the experimental method. Firstly the oven used in this work did not have accurate temperature control. As discussed the temperature was calibrated, although the accuracy of this is questionable since ambient conditions will have some impact. Furthermore the hole in the top of the oven will have created an uneven temperature profile. The hole in the top also allows some light into the set-up which could have an effect on the nucleation in the supersaturated solution. A newer model of oven with accurate temperature control and a fully enclosed case would be helpful in ensuring accurate temperature control and would allow the internal light level to be controlled.

Secondly the length of time the filtered supersaturated solution is left inside the magnetic field at 93°C prior to cooling could be investigated. Here the filtered supersaturated solution was left for approximately an hour prior to cooling, yet Potticary *et al.* [8] stated they left the filtered solution inside the magnetic field for 4 hours prior to cooling. This length of time was not expected to be a key variable since crystallisation does not occur until the temperature falls below 50°C. Nevertheless it is a deviation from the published method and therefore worth further investigation.

3.4 Summary

Crystals of γ-coronene were successfully grown using a physical vapour transport method in a three zone furnace. Prior to crystal growth, commercially sourced 97% pure coronene was twice purified by sublimation under vacuum. The second purification step was vital in removing impurities to suppress background noise in Raman measurements. These crystals were used in subsequent Raman spectroscopy experiments to probe vibrational properties and are presented in Chapters 4 and 5.

Unfortunately despite many attempts, crystals of β-coronene were not synthesised. The method published by Potticary *et al.* [8] was followed closely and other avenues, specifically 'ageing' the supersaturated coronene in toluene solution and doping with dicoronylene, were attempted. Due to the failure in replicating the crystallisation of β-coronene at standard room temperature and pressure, the β-phase was instead accessed by cooling aforementioned high-purity γ-coronene crystals below the phase transition to β-coronene at $\sim$150 K. The vibrational properties of β-coronene were studied at these low temperatures by Raman spectroscopy and are presented in Chapters 4 and 5.

Chapter 4

Intramolecular vibrations

To date calculations of the intramolecular vibrational frequencies of crystalline coronene have not been presented in literature, and instead spectra taken on crystalline samples interpreted using isolated molecule calculations giving an incomplete and in some cases ambiguous mode assignment. Here the vibrations of the isolated coronene molecule and intramolecular vibrations of γ- and β-coronene are calculated using DFT-D3 and used to interpret in-house Raman spectra and those previously presented in the literature.

4.1 Literature review

Extensive work in the 1970 and 80s presented both experimental Raman and IR spectra of coronene [153, 154]. These were interpreted and assigned by several force-field methods, for example the five parameter approximation [154, 155], the Califano-Neto method [155] and others. These methods involved significant parameterisation, often initially based on values derived from the analysis of benzene and naphthalene but later adjusted to fit experimental observations. Furthermore, in-plane and out-of-plane vibrations were considered separately with different parameterisations. The variety of methods and parameters used meant significantly different frequencies were calculated for particular modes, for example one ranging in value from 653 cm^{-1} to 847 cm^{-1}, a difference of nearly 200 cm^{-1} [155]. This wide range of frequency predictions meant there was significant difficulty in completing a clear mode assignment. Later in the 1990s the Restricted Hartree Fock (RHF) method was applied using several basis sets [156]. This method was said to give "a satisfactory spectrum for both frequencies and intensities" [156] of IR modes, although discrepancies >60 cm^{-1} still occurred even though a scale factor was applied to the frequencies, and some intensities were over predicted. Further

experiments were also performed in the 1990s, aimed at understanding the IR spectra recorded from isolated molecules in outer space [157].

An attempt at mode assignment has been made by Fleicher and Pulay [158] for both IR and Raman, but is ambiguous. Three Raman peaks at 1013 cm^{-1}, 1046 cm^{-1} and 1199 cm^{-1} found by Babkov *et al.* [153] were not included in their assignment, nor commented on. Further ambiguity arises in the tabulated data where two peaks are assigned to one mode, for example peaks at 1232 cm^{-1} and 1292 cm^{-1} are assigned to an E_{2g} mode together, yet their frequencies differ by nearly 60 cm^{-1} and no reasoning is given for this. Todorov *et al.* [159] revised this mode assignment in 2010, considering an out-of-plane distortion of the coronene molecule that reduces the symmetry from D_{6h} to C_{2h} [159]. This enabled some of the previously unassigned "phantom bands", the infra-red multiplet at approximately 545 cm^{-1} and Raman bands at 571 cm^{-1} and 828 cm^{-1}, to be accounted for. However an infra-red doublet at 847 cm^{-1} remains "a bit obscure" [159] and the Raman band at 571 cm^{-1} is assigned to a mode nearly 80 cm^{-1} higher, leaving some features unaccounted for. Whilst this work correctly identifies that coronene in the solid state exhibits a reduction in symmetry in the out-of-plane direction compared to the isolated molecule, it does not consider any in-plane deformations also present in the crystalline phases, and the β-phase, not known at the time of the research is obviously not considered.

The experimental spectra underpinning these works were obtained at inconsistent, and not always stated, temperatures and often on crystalline samples, yet the calculations are based on isolated molecules. Whilst this is a reasonable approximation for the intramolecular modes, it is evident that the crystalline environment does need to be included due to the aforementioned in-plane distortions arising from the crystal field. In this chapter a full and detailed analysis of the intramolecular modes of both phases of crystalline coronene is presented using state of the art DFT-D calculations, allowing a full mode assignment to be made.

4.2 Methods

4.2.1 Experimental details

All crystals used in this work were grown in-house as detailed in Chapter 3.

Single crystal x-ray diffraction

Crystals were characterised using x-ray diffraction in the Materials and Chemical Characterisation Facility (MC^2), University of Bath [147]. Data collection was carried out at four different temperatures, starting at 290 K, decreasing to 200 K at 300 K/hour and stabilising for 2 minutes, then further decreasing to 150 K and 80 K with a stabilising time of 10 minutes. Diffraction datasets were collected on a Rigaku SuperNova, Dual, Cu at zero, EosS2 single crystal diffractometer using monochromated Cu-Kα radiation with $\lambda = 1.54184$ Å. A symmetry-related (multi-scan) absorption correction was applied with CrysAlisPro 1.171.38.43. Structures were solved with SHELXT and refined by full-matrix least-squares fits on F^2 [160], with additional analysis performed using SHELXle [161]. It was found that the crystals deteriorated at 80 K, preventing further characterisation [162].

Raman

Raman measurements were performed at the University of Bath Material and Chemical Characterisation Facility (MC^2) [147] using a Renishaw InVia Raman spectrometer operated in backscatter geometry with a 785 nm excitation laser with nominal intensity 140 mW, and a long working distance 50× objective lens. A 785 nm laser was required in order to minimise fluorescence of coronene which is known to absorb wavelengths up to ∼600 cm^{-1} and ∼800 cm^{-1} for γ- and β-coronene respectively [8]. The spectral resolution was approximately 1 cm^{-1}. A custom setup was used to control the temperature, as shown in figure 4-1. A cryostat was mounted on a manual x-y stage atop an electronic z stage mounted on a stand and inserted into the microscope. The temperature was controlled electronically with an accuracy of 0.1 K. A crystal of γ-coronene was mounted directly onto the copper substrate of the cryostat using GE varnish to ensure good thermal contact. Placing a γ-coronene crystal onto a silicon substrate on the copper substrate was attempted but did not have sufficient thermal conductivity. If this is to be repeated in future I recommend mounting crystals on silicon then onto the copper using GE varnish in both steps to ensure good thermal conductivity. Silicon is a preferable substrate as it produces a single peak in the Raman spectra at 521 cm^{-1}, whilst copper gives a large background signal, particularly when the sample is thin.

Measurements were taken in two wavenumber ranges: 25 to 1240 cm^{-1} (low) and 1220 to 2160 cm^{-1} (high). These measurements were taken sequentially since the extended range feature of the spectrometer was too slow at scanning the entire range within the time it to cool by 1 K. During analysis the two data sets were combined.

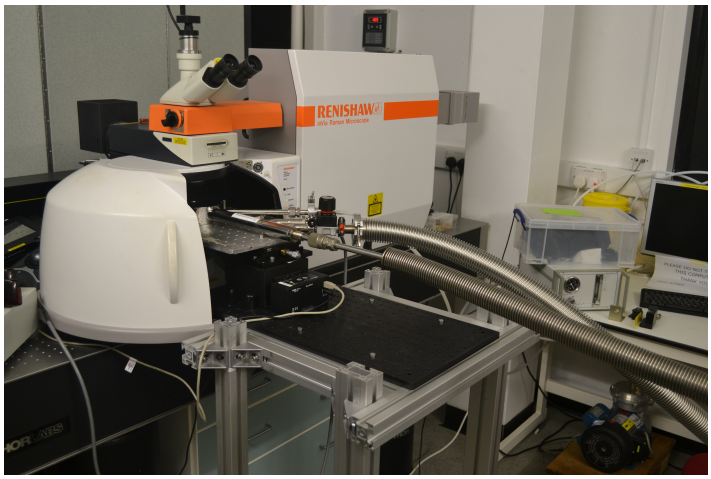

Figure 4-1: Photograph showing the custom setup for temperature dependent Raman measurements.

Three experiments were undertaken: a continuous temperature sweep from room temperature down to 80 K, and two polarisation sweeps at room temperature and 110 K. During the temperature sweep, the temperature continuously decreased at a slow rate of between 2.5 and 1 K/min. This allowed both the low and high range measurements to be performed within a 1 K temperature interval. A 5% laser power for 5 s with one acquisition was used. During this process the γ-coronene crystal, figure 4-2 (a), was observed to shatter at 137 K. It was difficult to find the resulting crystal fragments as the fragmentation is violent and produces very small crystals. Cooling continued throughout and the fragment shown in figure 4-2 (b) was found and measurements resumed at 125 K. Cooling continued to 80 K. Below 110 K the focal point drifted off the crystal and despite moving back onto the crystal, the background noise was too erratic for the data to be useful. Drift during measurements was a result of the vibrations from the membrane pump attached to the transfer tube.

For both polarisation experiments a rotatable $\lambda/2$ waveplate was placed in the incident laser beam path. The waveplate was rotated electronically from 0 to 90° with an accuracy better than 1°. A linear polariser of known orientation was placed in the output laser beam between sample and detector. A 5% laser power for 5 s with 5 cumulative acquisitions was used. For the low temperature measurements, the temperature was set to 110 K and a suitable crystal fragment, figure 4-3 (b), was found. For the room temperature measurements a new γ-coronene crystal was placed on a silicon substrate, figure 4-3 (a), and the cryostat was not used.

To analyse the polarised Raman measurements, it is necessary to know the polarisation of the input laser light and selected output polarisation with respect to the sample.

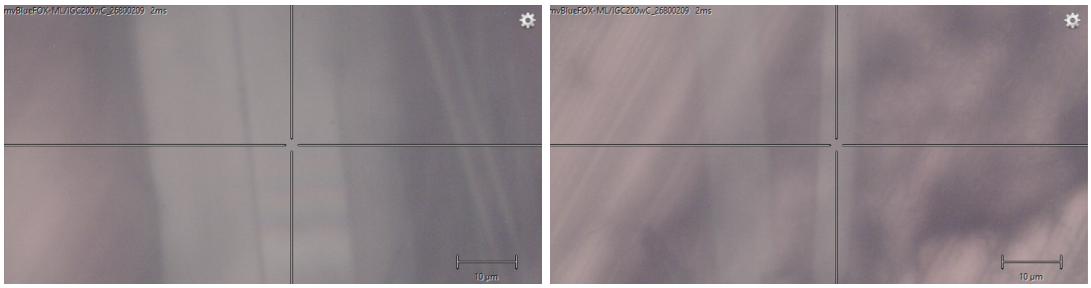

(a) (b)

Figure 4-2: Images of the (a) γ-coronene crystal at 300 K and (b) the β-coronene crystal fragment at 125 K on copper (taken with a $\times$50 objective lens) that were used in the temperature sweep experiment.

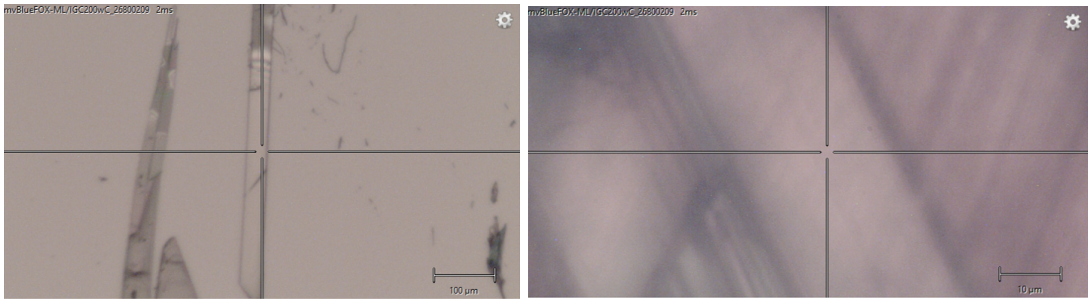

(a) (b)

Figure 4-3: Images of the (a) γ-coronene crystal on silicon at room temperature (taken with a $\times$5 objective lens) and (b) the β-coronene crystal fragment on copper at 110 K (taken with a $\times$50 objective lens) that were used in the polarisation experiments.

Figure 4-4 (a) shows the path of the laser beam inside the spectrometer and how the input polarisations are affected by the path of the beam. Figure 4-4 (b) shows how these map onto the x-y plane in which the crystal lies.

Spectral analysis

Firstly the broad background was removed using polynomial fitting in MATLAB, excluding ranges in which there were clear peaks. The low and high range spectra were fitted individually. The peaks were then fitted using Voigt profiles. Raman peaks are intrinsically Lorentzian, however there is some additional Gaussian broadening arising from the instrumentation and thus a convolution of the two, a Voigt profile, is most accurate [163]. Indeed, fitting either a Lorentzian or Gaussian line-profile proved unsatisfactory. One drawback of using Voigt profiles is that peak positions and heights must be reasonably well estimated in order for the fitting to be performed. The

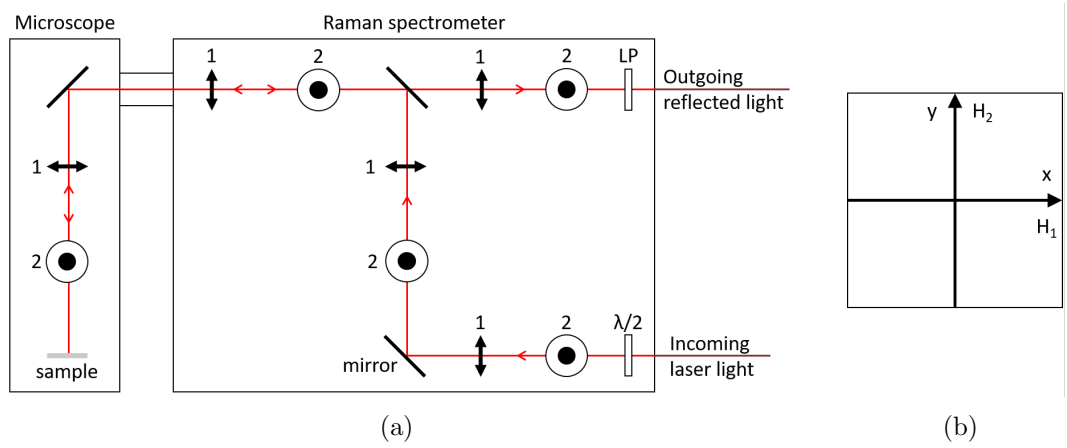

Figure 4-4: Representation of how input polarisation directions map onto the sample surface. A $\lambda/2$ waveplate was placed immediately after the input of the inherently polarised laser light, as shown, allowing the polarisation to be rotated. A vertical (1) polarisation is rotated through the spectrometer by mirrors and maps onto the x-axis of the sample plane. A horizontal (2) polarisation does not rotate and maps onto the y-axis of the sample plane. A linear polariser (LP) was placed in the path of the outgoing light allowing components containing H_1 or H_2 to be measured.

Lorentzian and Gaussian widths are less important and starting with widths that are too narrow is recommended [163]. An off-the-shelf fitting procedure from the MATLAB file exchange [164–166] was modified to enable simultaneous fitting of spectra as detailed below. The default tolerances were used.

Polarisation data was fitted first with all polarisation spectra per polymorph fitted simultaneously. Peak positions, Gaussian and Lorentzian widths were kept constant with only peak heights allowed to vary with polarisation. The background-removed low and high range data were joined by removing any overlapping points from the high range data. Peak positions were estimated manually and to obtain a reasonable initial estimate of peak heights, Gaussian peaks were fitted. The inputs into the Voigt profile fitting were the estimated peak positions, Gaussian peak heights, a Lorentzian width of 0.1 cm^{-1} and a Gaussian width of 1 cm^{-1}. Errors were estimated by fitting with input peak positions increased and decreased by 2 cm^{-1}. Peak positions were found to have an error of ± 0.2 cm^{-1} and peak heights an error of ± 5 counts, equivalent to 0.1% of the maximum height in the fitted region. Figure 4-5 shows a fitted spectra for γ-coronene with a vertical output analyser and an input polarisation of 0°.

The temperature sweep data was fitted second. Here all spectra for each polymorph, that is prior to shattering in the γ-phase and after shattering in the β-phase, were fit simultaneously. Peak positions were allowed to vary with Gaussian and Lorentzian widths kept constant. The relative peak heights within each spectra were kept constant

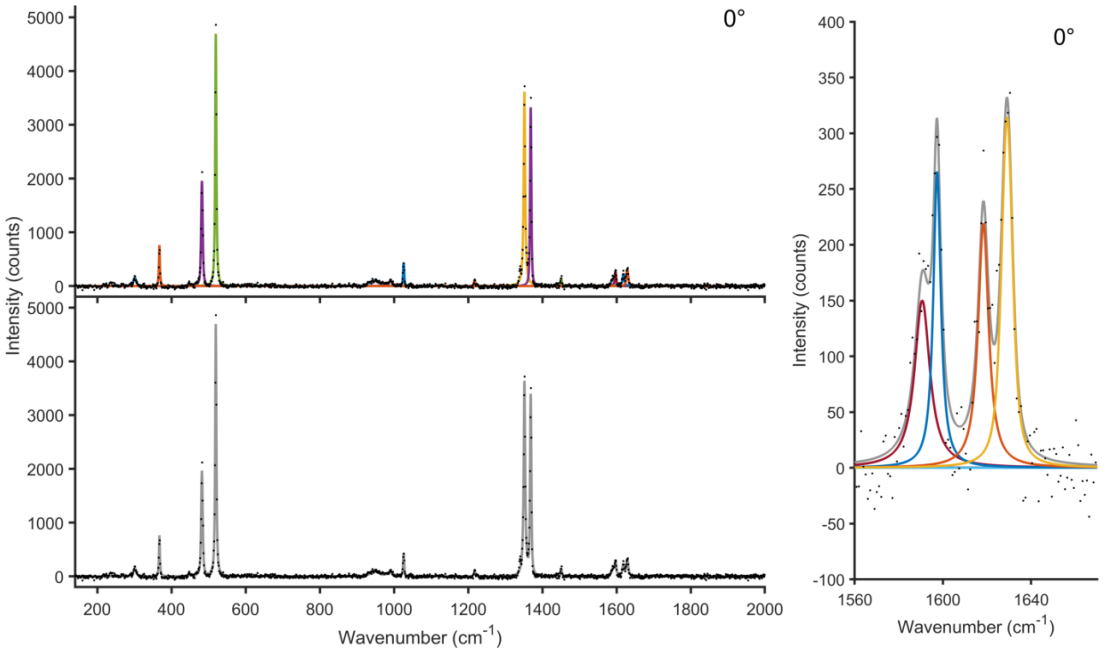

(a) (b)

Figure 4-5: Raman spectra of γ-coronene at 0° (dots) with a vertical output analyser and (a) top - fitted individual Voigt profiles, bottom - total profile and (b) fitted individual profiles (colour) and total profile (grey) in the range 1560 cm^{-1} to 1660 cm^{-1}. Fitting with Voigt profiles reproduces the peaks and envelope well.

by using a scaling factor to account for variations in the number of counts. Peak positions obtained from polarisation fits were used as inputs with Lorentzian and Gaussian widths of 0.1 cm^{-1} and 1 cm^{-1} used as before. Input peak heights were again estimated by Gaussian fits. An error on peak position of ± 1 cm^{-1}, estimated using the same method as above.

4.2.2 Computations

Energy calculations and structural optimisations were performed using the Vienna *ab initio* simulation package (VASP) code [72]. The PBE functional [64] was employed with PAW pseudopotentials [167, 168] and a kinetic energy cut off of 850 eV for the plane-wave basis. The Grimme-D3 scheme [88, 106] was used to account for van der Waals forces. For both structures, a Γ centred $2 \times 3 \times 1$ Monkhorst-Pack k-point mesh was used to sample the Brillouin zone. Increasing k-point sampling to $3 \times 4 \times 2$, as used in previous work [8], gave a difference in the lattice energies of 3 meV and a <0.3% change in unit cell parameters. Total-energy calculations were considered converged when the energy change between two successive electronic steps was less

than 10^{-8} eV. Structures were allowed to fully relax until all forces acting on the atoms were $<10^{-4}$ eV/Å. Phonopy [47, 169] was used to calculate vibrational frequencies and eigenvectors within the harmonic approximation. VASP was used as the force calculator with a finite displacement step of 0.015 Å. Raman activity tensors were calculated using a central-differences scheme [170–172] with required dielectric constants calculated using VASP. The symmetry labels of vibrational modes were output by Phonopy from inbuilt group tables. [162]

The input crystalline structures were derived from experiments. For the β-phase a structure was also relaxed starting from previously reported DFT results [8] which produced an identical final structure. For the isolated molecule calculations the input structure was determined by using a D_{6h} symmetry, a C-C bond length of 1.4 Å, and a C-H bond length of 1.0 Å, and C-C-C and C-C-H bond angles of 120° such that the atoms were arranged hexagonally.

In the isolated molecule calculations one molecule was placed in the centre of a hexagonal unit cell in the x-y plane with cell parameters $a = b = 25$ Å and $c = 10$ Å. It was verified that there was no significant dispersion of the electronic states, validating the cell parameters used. The atomic positions were first allowed to relax. Subsequent frequency and Raman activity tensor calculations were performed following the same method as the crystalline structures.

The kinetic energy cut off and k-point sampling of the Monkhorst-Pack grid for the crystalline phases were determined by single point energy convergence testing using the input γ-coronene structure. The kinetic energy was varied between 400 eV and 1000 eV with a Γ centred $1 \times 1 \times 1$ Monkhorst-Pack k-point mesh, figure 4-6 (a). 850 eV was chosen as the kinetic energy cut-off to be used in this work with a difference in single point energy of 0.004% to 1000 eV, the maximum tested, and a 22% increase in speed per single point calculation. The k-point sampling was initially investigated by determining the single point energy with a variety of mesh sizes with a kinetic energy cutoff of 400 eV, figure 4-6 (b). The maximum mesh tested was a Γ centred $3 \times 7 \times 3$ Monkhorst-Pack k-point mesh, shown by the green star in figure 4-6 (b). A variety of k-point meshes gave single-point energies close to this maximum mesh, shown by the black box. The smallest k-point mesh in this range is a $2 \times 3 \times 1$ mesh, highlighted by the light blue circle, and was used here. It is worth noting that the aforementioned $3 \times 4 \times 2$ mesh gives results within this converged region, however this slows each single point calculation by 40 s. One final test was carried out by performing a full structural optimisation of both polymorphs using a $3 \times 4 \times 2$ Monkhorst-Pack k-point mesh and a kinetic energy cutoff of 850 eV, as detailed above.

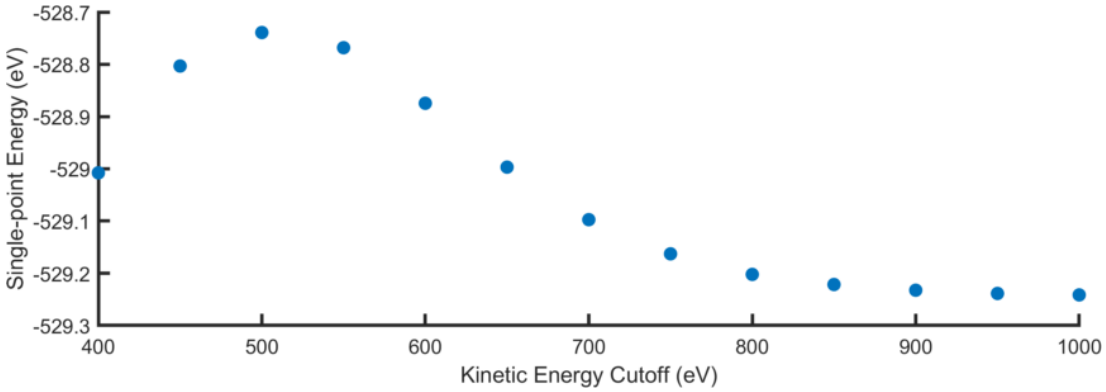

(a)

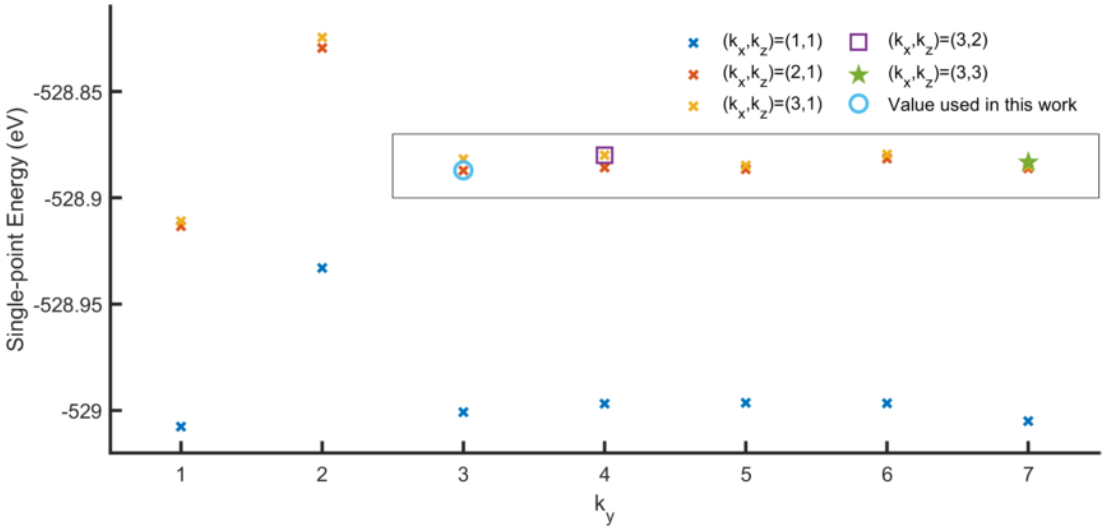

(b)

Figure 4-6: Convergence testing of (a) the kinetic energy cutoff and (b) k-point sampling using single-point energy calculations performed on the input γ-coronene structure. (a) A kinetic energy cutoff of 850 eV was chosen with a difference in single point energy of 0.004% compared to 1000 eV. (b) The largest k-point mesh sampled, $3 \times 7 \times 3$, is depicted by the green star. Meshes that perform with similar accuracy are within the black box. A mesh of $2 \times 3 \times 1$ used in this work is highlighted by the light blue circle and the mesh, $3 \times 4 \times 2$, used in previous studies on coronene [8] is represented by the purple square.

Polarised Raman Intensity Calculations

In order to interpret the polarisation dependency of Raman active modes found experimentally, the input polarisation of the laser, and output polarisation measured must be known in the same co-ordinate system as the Raman tensor. From Chapter 2.3.4, the Raman intensity for the l^{th} mode is

$$I \propto |e_j^S \cdot R_{jk,l} \cdot e_k^I|^2, \tag{4.1}$$

where $R_{jk,l}$ is the Raman tensor, e_j^S is the unit vector describing the direction of the scattered light and e_k^I is the unit vector describing the direction of the incident light.

Raman tensors are calculated in the orthogonal (x_c, y_c, z_c) basis of the crystal. For both coronene polymorph calculations, the primitive vector $\vec{a}$ lays along x_c and the primitive vector $\vec{b}$ along y_c. The vector $\vec{c}$ is at an angle β to the a-axis and perpendicular to $\vec{b}$, figure 4-7 (a). Mathematically

$$\vec{a} = |\vec{a}| \cdot \hat{x}_c, \tag{4.2}$$

$$\vec{b} = |\vec{b}| \cdot \hat{y}_c, \tag{4.3}$$

$$\vec{c} = |\vec{c}| \left(\cos\beta \cdot \hat{x}_c + \sin\beta \cdot \hat{z}_c\right). \tag{4.4}$$

From face indexing, the laser light was identified as being incident on the (1 0 -1) face. Let $\hat{u}$ be the unit vector in the $\vec{b}$ direction and $\hat{w}$ be the unit vector perpendicular to this on the (1 0 -1) face as described in figure 4-7 (b),(c)

$$\hat{u} = \vec{b}/|\vec{b}| = \hat{y}_c, \tag{4.5}$$

$$\hat{w} = \widehat{(\vec{a} + \vec{c})}. \tag{4.6}$$

Substituting equations (4.2) and (4.4) into equation (4.6)

$$\hat{w} = \frac{(|\vec{a}| + |\vec{c}|\cos\beta) \cdot \hat{x}_c + |\vec{c}|\sin\beta \cdot \hat{z}_c}{\sqrt{|\vec{a}|^2 + |\vec{c}|^2 + 2|\vec{a}||\vec{c}|\cos\beta}}. \tag{4.7}$$

Figure 4-8 shows how the unit cell relates to the formation of coronene crystals. The long edge of the crystal is formed by stacking unit cells in the $\vec{b} \equiv \hat{y}_c$ direction. This is the shortest lattice vector and therefore the fastest direction for the crystal to grow.

Let (x_e, y_e, z_e) refer to the experimental reference frame. First consider the simple case where the long edge of the crystal, $\vec{b} \equiv \hat{y}_c$, is parallel to $\hat{y}_e$, figure 4-9 (a). Here

$$\hat{x}_e = \hat{w}, \tag{4.8}$$

$$\hat{y}_e = \hat{u}. \tag{4.9}$$

Rotating the crystal by an angle θ in a counter-clockwise direction about the z_e axis, figure 4-9 (b), gives

$$\hat{x}_e(\theta) = \cos\theta \cdot \hat{w} - \sin\theta \cdot \hat{u}, \tag{4.10}$$

$$\hat{y}_e(\theta) = \sin\theta \cdot \hat{w} + \cos\theta \cdot \hat{u}. \tag{4.11}$$

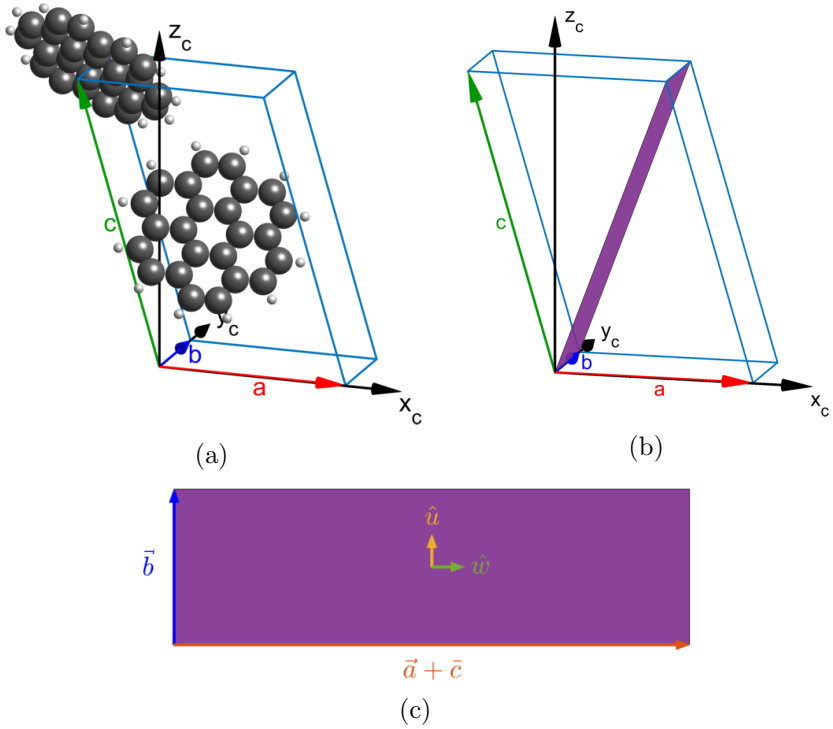

Figure 4-7: (a),(b) Unit cell (light blue) of γ-coronene calculated using DFT-D3 with the a-axis (red), b-axis (blue) and c-axis (green) shown in relation to the orthogonal x_c-, y_c- and z_c-axes in which the Raman tensor is calculated. (b) The (1 0 -1) face (purple) upon which the laser is incident. (c) View of the (1 0 -1) face defining the directions of $\hat{u}$ and $\hat{w}$.

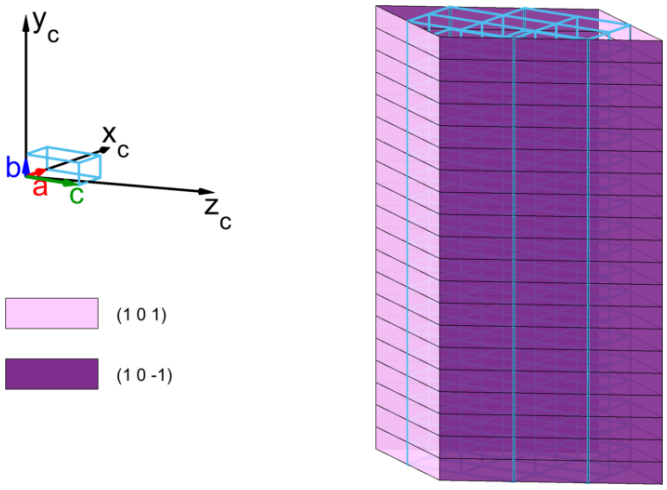

Figure 4-8: Right - Structure of a typical γ-coronene crystal with individual unit cells (light blue) indicated. The vertical length of the crystal is in the $\vec{b} \equiv \hat{y}_c$ direction. The (1 0 -1) (purple) and (1 0 1) (pink) faces found experimentally by face indexing are shown. Left - Individual unit cell (light blue) with the a-axis (red), b-axis (blue) and c-axis (green) and the orthogonal x_c-, y_c- and z_c-axes in the same orientation as those that form the crystal on the right.

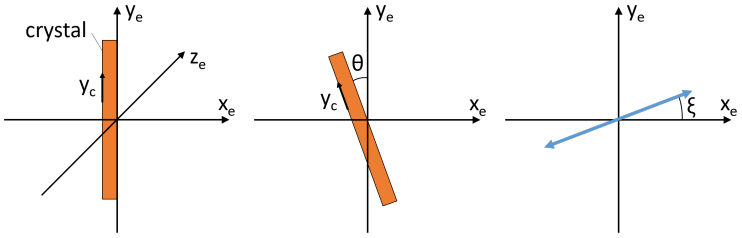

(a) (b) (c)

Figure 4-9: (a) A crystal with long edge, the b-axis along the $\hat{y}_c$ direction, lying along the experimental y_e-axis. (b) A crystal with long edge, b-axis, $\hat{y}_c$ direction, rotated counter-clockwise by an angle θ around the z_e axis. (c) Indication of a polarisation direction, blue arrow, rotated counter-clockwise by angle ξ from the experimental x_e-axis around z_e.

Finally the unit vector describing the polarisation of either incident or scattered light, as in equation (4.1), at an angle ξ measured in a counter-clockwise direction from $\hat{x}_e$ around the z_e axis, figure 4-9 (c), is

$$\hat{e}(\xi, \theta) = \hat{x}_e(\theta) \cos \xi + \hat{y}_e(\theta) \sin \xi. \tag{4.12}$$

4.3 Results and analysis

A series of single crystal x-ray diffraction measurements were taken on a γ-coronene crystal. The unit cell parameters, volume and intracell molecular angle as a function of temperature are compared with the predicted '0 K' structure from DFT-D3 in figure 4-10. The single crystal XRD lattice parameters show a linear dependency on temperature, and when extrapolated to '0 K' are $a = 9.98$ Å, $b = 4.65$ Å, $c = 15.50$ Å and $\beta = 106.82°$ giving a volume $V = 688$ Å^3 and an intracell molecular angle of $\phi = 86.83°$.

DFT-D3 calculations successfully predict a γ-coronene structure with lattice parameters $a = 9.98$ Å, $b = 4.76$ Å, $c = 15.42$ Å and $\beta = 106.38°$ giving $V = 703$ Å^3. The intracell molecular angle is $\phi = 85.96°$. The main differences between the calculated and experimental structures are a larger b-axis and a smaller c-axis. The calculated structure gives lattice parameters within 1.6% of the 290 K experimental structure, and within 2.5% of the extrapolated γ-phase '0 K' structure. The intracell molecular angle is within 0.7% and 1.0% of the 290 K and '0 K' experimental structures respectively. This good agreement between calculated and experimental structures gives confidence in using DFT-D3 to interpret other experimental results.

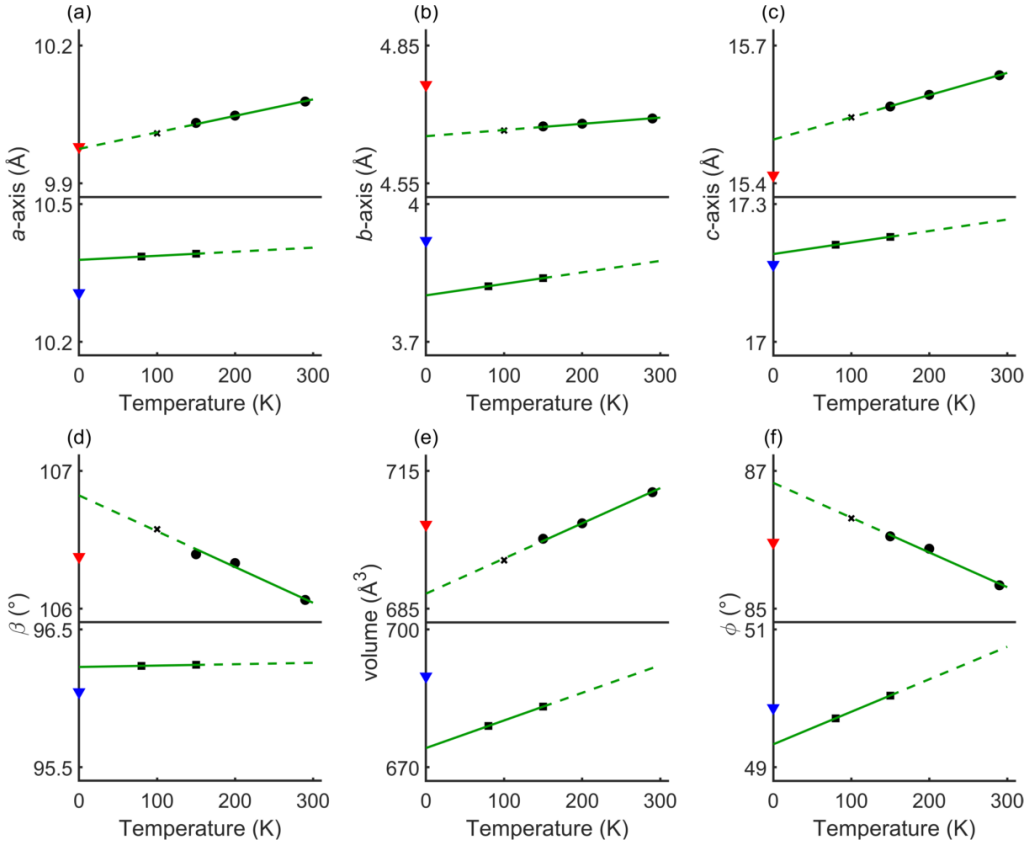

Figure 4-10: Temperature dependence of (a)-(c) lattice parameters, (d) cell angle β, (e) cell volume and (f) intracell molecular angle ϕ. Top panels show γ-coronene and bottom panels β-coronene. Red and blue triangles are from our DFT-D3 calculations for γ- and β-coronene respectively. Black circles show our measurements from single crystal x-ray diffraction, black $\times$ show data from Ref. [173] and black squares are from Ref. [8]. Green lines show the fitted linear trendlines. Reproduced from [162].

A β-coronene structure is also successfully predicted by DFT-D3. The calculated lattice parameters are $a = 10.31$ Å, $b = 3.92$ Å, $c = 17.17$ Å and $\beta = 96.05°$ giving $V = 690$ Å^3, with an intracell molecular angle of $\phi = 49.86°$. Since γ-coronene crystals fragment into microscopic sized pieces during the phase transition to β-coronene at ~150 K it was not possible to measure the lattice parameters of β-coronene by single crystal XRD here. The calculated structural parameters are compared to previously reported β-coronene lattice parameters from Ref. [8], figure 4-10. Here the main differences between calculated and experimental structures are a decrease in the a-axis and an increase in the b-axis. The calculated structure gives lattice parameters within 2.1% of the 150 K experimental structure and within 3.1% of the extrapolated '0 K' structure. The intracell molecular angle is within 0.4% and 1.1% of the 150 K and '0 K'

structures respectively. Again this good agreement between calculated and experimental structures indicates that DFT-D3 is suitable for further calculations.

On cooling the γ-coronene crystal in this Raman setup, the crystal shattered at 137 K. In order to confirm a phase transition occurred the low wavenumber range was studied. Figure 4-11 shows the raw data taken during the temperature sweep in the range 20 to 120 cm^{-1}. At low wavenumbers phonon modes are probed which are dependent on the crystalline environment and thus provide a signature of the polymorph present [7]. Two peaks are observed in the spectra both above and below 137 K. However both peak positions are observed to significantly shift downwards in frequency below 137 K after the crystal has shattered and the second peak is broader. This clear change in spectra is consistent with the occurance of a phase transition accompanying the shattering of the crystal at 137 K. Since this data is very close to the cut off of the Raman spectrometer, it is not useful to make any further conclusions here and this region is investigated in more detail in Chapter 5 where a different low-wavenumber Raman setup was used.

During the temperature sweep a small but non negligible background was observed in the γ-coronene regime prior to the crystal shattering, figure 4-12. After shattering the background significantly increased in the β-coronene regime. There are several

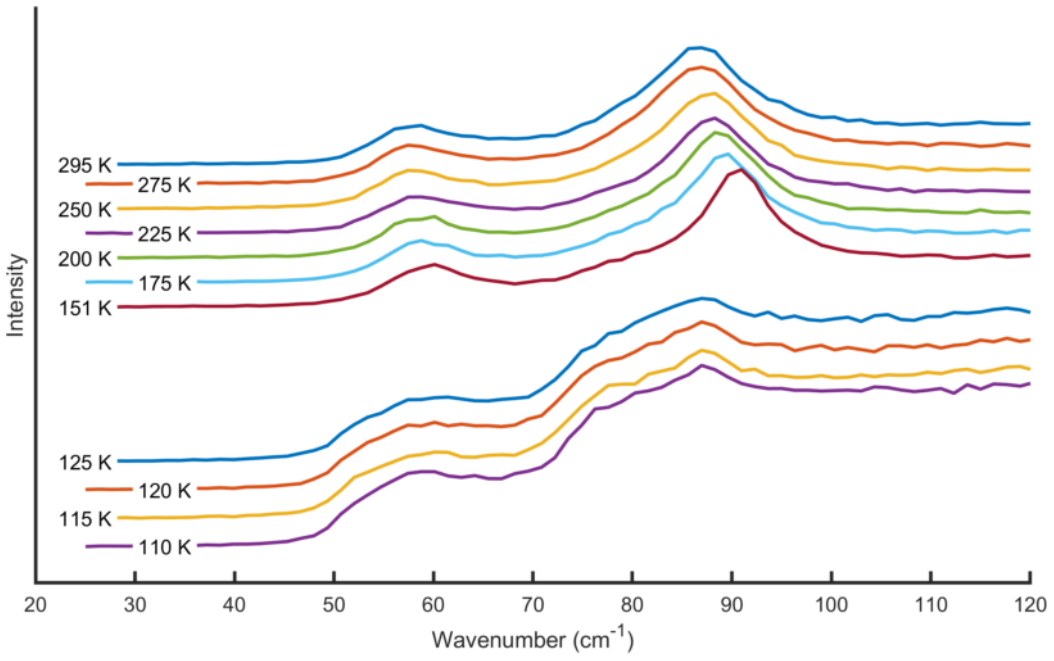

Figure 4-11: Raw low wavenumber Raman spectra taken on cooling a γ-coronene crystal. The crystal fragmented at 137 K. Changes in the low wavenumber region indicate a phase transition has occurred. Individual spectra are offset for clarity.

reasons for this: firstly β-coronene is expected to absorb to wavelengths higher than γ-coronene [8], and secondly the crystal fragments that were produced upon shattering are very thin and more transparent than the larger γ-coronene crystal, allowing laser light to penetrate through to the copper substrate surface. As seen in figure 4-12 a broad feature at $\sim$300 cm^{-1} appears in the 125 K spectrum. DFT calculations do not predict such a peak and the intramolecular vibrations that are probed in this region are expected to be similar in both polymorphs so it is unlikely this peak arises from the β-coronene fragment itself. Furthermore there is a large signal from copper oxide (CuO) at this wavelength (bottom panel figure 4-12), and thus we assign this peak to the presence of the copper substrate.

Figure 4-13 shows spectra taken on cooling from 295 K to 110 K with the background removed. The γ- and β-coronene spectra are nearly identical, excluding the phonon range and the anomalous broad peak at $\sim$300 cm^{-1}, as previously discussed. The 175 K spectrum shows some low level variations in the 1600 to 2000 cm^{-1} region, however

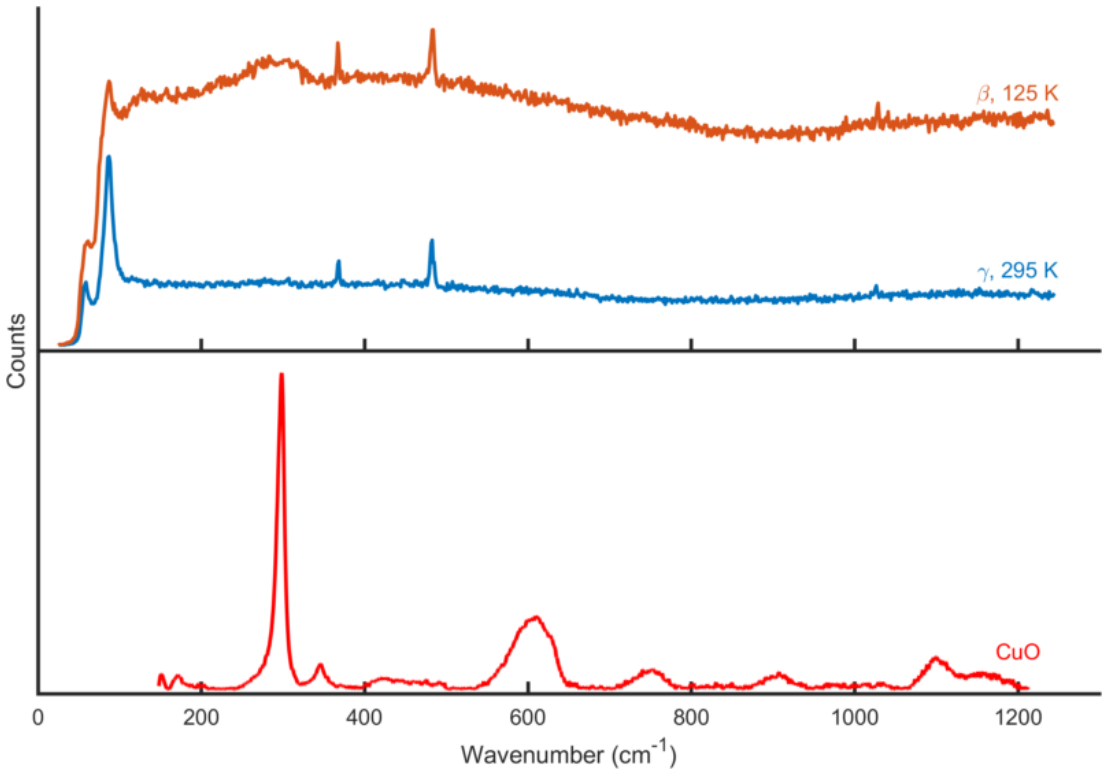

Figure 4-12: Top - raw data from the temperature sweep obtained at 295 K (blue) on a γ-coronene crystal and at 125 K (orange) on a crystal fragment of β-coronene. Bottom - Raman spectra of unorientated copper oxide (CuO) taken with a 785 nm laser from the RRUFF database - Tenorite R060978 [174]. In the β-coronene spectrum a broad feature is seen at $\sim$ 300 cm^{-1} consistent with the most intense peak at 298 cm^{-1} from CuO.

these are simply a remnant from background fitting as this does not appear in any other spectra. In total 11 peaks can be identified and fitted for both polymorphs, with positions at 295 K at 368 cm^{-1}, 482 cm^{-1}, 1026 cm^{-1}, 1217 cm^{-1}, 1352 cm^{-1}, 1369 cm^{-1}, 1452 cm^{-1}, 1591 cm^{-1}, 1597 cm^{-1}, 1618 cm^{-1} and 1629 cm^{-1}. In general peak positions are observed to decrease with temperature.

Orientationally averaged Raman intensities were calculated for both polymorphs and the isolated molecule and are compared to the experimental results in figure 4-14. A Gaussian broadening of 3 cm^{-1} has been applied to the computational results to capture the impact of experimental resolution, which particularly affects modes that are very close together. Calculated Raman spectra using both the isolated molecule and crystalline structures reproduce experimental results well. The frequencies and intensities produced by isolated molecule and crystalline calculations are similar and a full comparison of the intramolecular modes is detailed in Appendix A. The frequencies in the crystalline structures are increased with respect to the isolated molecule, reproducing

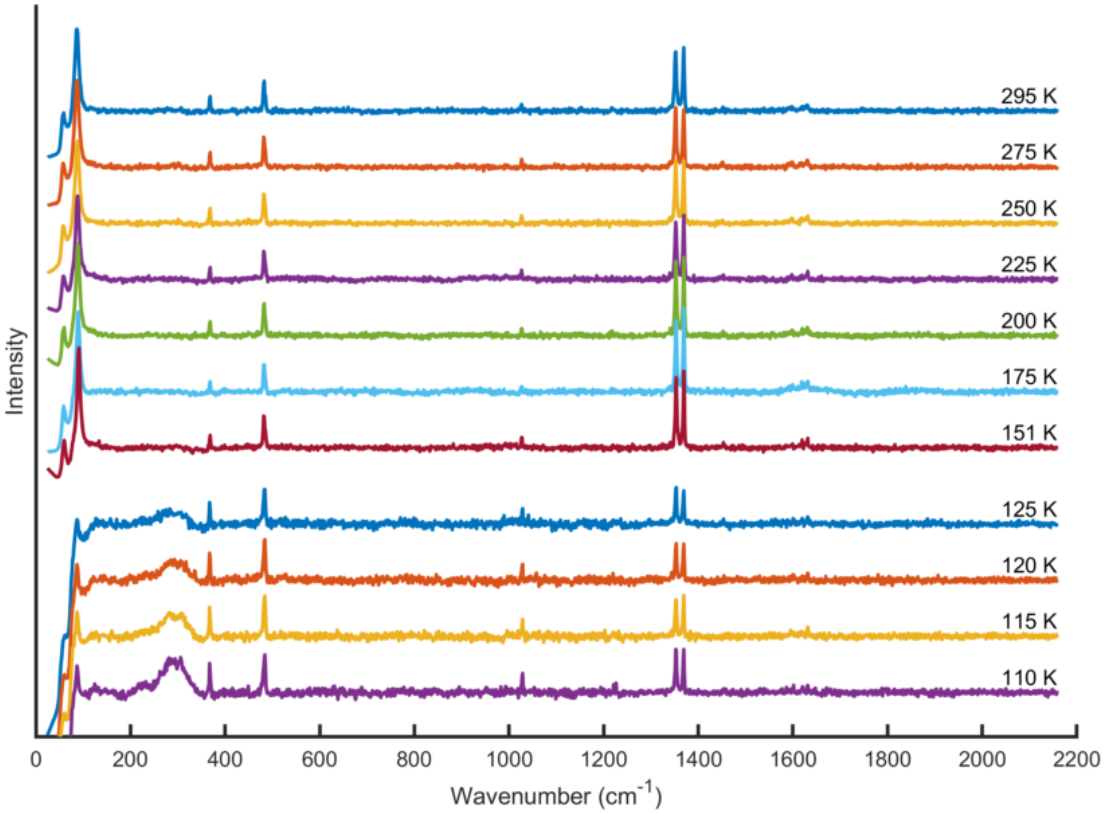

Figure 4-13: Raman spectra collected during cooling of a γ-coronene crystal from 295 K to 110 K. The crystal fragmented at 137 K converting into the β-phase and little change is observed in the spectra above 400 cm^{-1}. Background envelopes have been removed. Individual spectra are offset for clarity.

the experimental spectra marginally better. The two most prominent peaks, at 1352 cm^{-1} and 1369 cm^{-1}, are known to be Fermi resonance peaks between a combination band comprising of 368 cm^{-1} and 994 cm^{-1} modes and a band which the literature states is at 1334 cm^{-1} [158]. Since Fermi resonance arises from anharmonicity it is not captured within these calculations and hence our calculations shows just a single peak at ∼1368 cm^{-1}, whereas experimentally there are two. Computations also suggest two peaks at ∼1590 cm^{-1} and 1610 cm^{-1}, whereas in experiment four peaks have been fitted in this region.

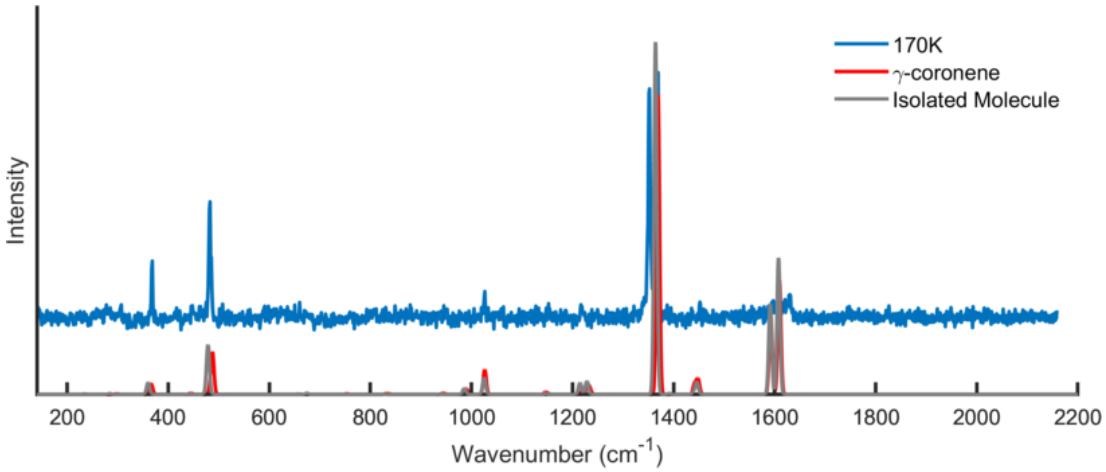

(a)

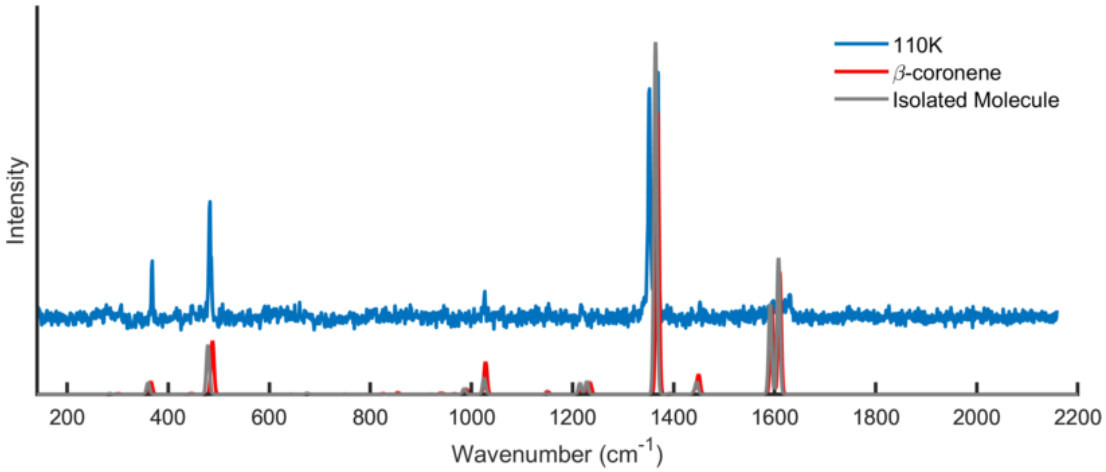

(b)

Figure 4-14: Individual Raman spectra (blue) taken at (a) 170 K and (b) 110 K during cooling. The calculated orientationally averaged Raman spectra (red) for (a) γ-coronene and (b) β-coronene are shown alongside the isolated molecule (grey). A Gaussian broadening of 3 cm^{-1} was applied to all calculated spectra to account for experimental broadening.

In the case of spectra recorded during the room temperature polarisation sweeps the background and noise level were significantly reduced since there were no vibrations from operating the cryostat, and a silicon substrate was used. This results in more peaks being visible. Figure 4-15 shows the spectra obtained with a vertical output analyser. Equivalent figures with the output analyser in the horizontal position are shown in Appendix B. Sixteen peaks have been fitted including one at 521 cm^{-1} arising from the silicon substrate. Peak positions are given in table 4.1. In the range 1550 to 1650 cm^{-1}, figure 4-15 (b), four peaks were fitted on the account of an asymmetrical line shape at 1590 cm^{-1} and two distinct peaks occurring in most of the spectra above this. For this output analyser direction, all peaks start at a maximum at 0° then decrease in intensity to a minimum at 90°. Here some peaks decrease to within the noise level, whilst others remain visible. All peaks then increase in intensity again up to 180°. Figure 4-17 shows

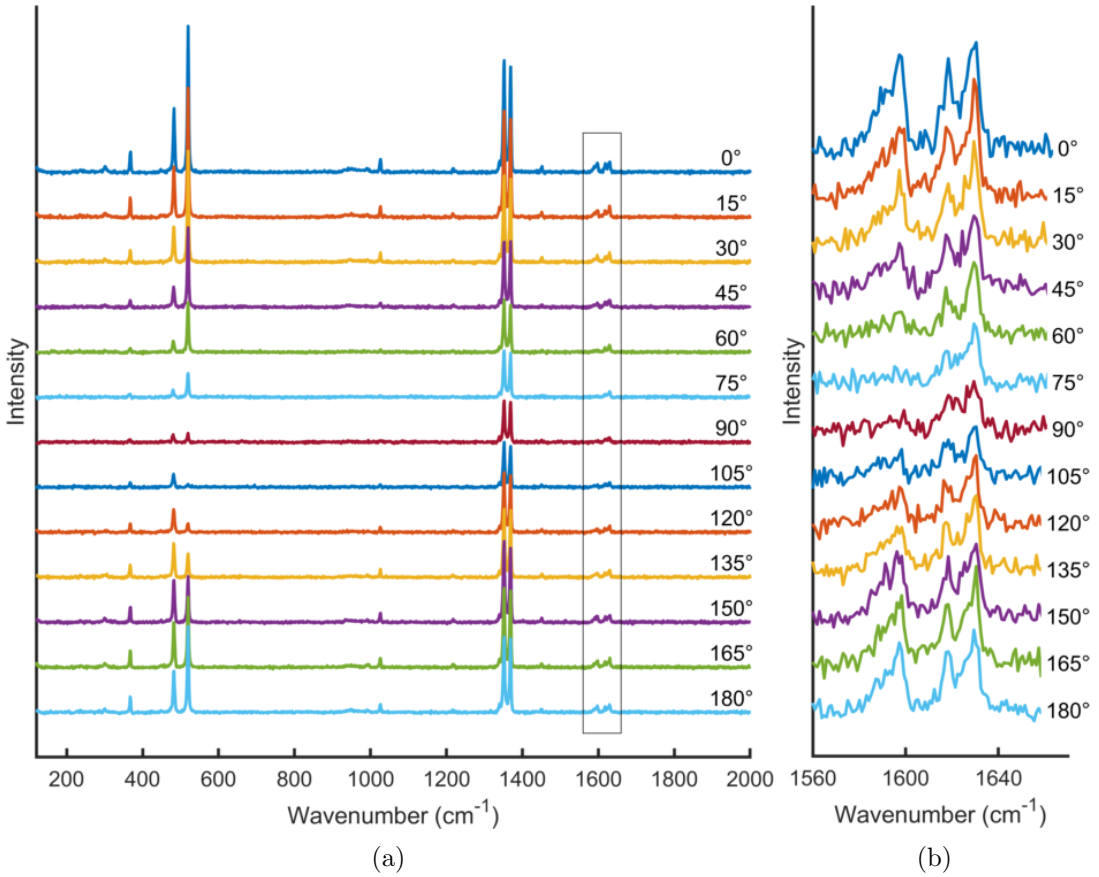

Figure 4-15: Polarisation angle dependence of Raman spectra of a γ-coronene crystal at room temperature with a vertical output analyser. Individual spectra are offset for clarity. Background envelopes have been removed. The region highlighted by the box in (a) is shown in greater detail in (b).

the intensity as a function of polarisation angle, displaying this behaviour in more detail with polar plots from both analyser orientations shown.

In order to interpret the experimental polar plots with the DFT-D3 computations it is necessary to reproduce the experimental geometry in the theoretical calculations. Thus the orientation of the crystal with respect to the laser and polarisation directions must be known. Face indexing was performed on the γ-coronene crystal used here and the faces are shown in figure 4-16. This confirms that the long axis is the b-axis, as expected. By comparison to figure 4-3 (a) the (1 0 1) face is the incident face. Theoretical polar plots were produced from computational Raman activity tensors using this information. Several modes, 301 cm^{-1}, 448 cm^{-1} and 990 cm^{-1}, showed different polarisation dependence compared to experiment, specifically the figure of eights were rotated by 90° with respect to experimental measurements. Several crystals had been placed on the silicon substrate in order to select a good crystal, one with a smooth face, to use in this experiment. When the crystal was removed for face indexing there was some uncertainty that the correct crystal was taken. Additionally in Chapter 5 the γ-coronene crystal used had a similar shape, yet the (1 0 -1) face was found to be the incident face. Given this information the computational analysis was re-run with an incident face of (1 0 -1) and all discrepancies in polarisation dependence were resolved. Additionally relative intensities were better reproduced. We conclude that the crystal

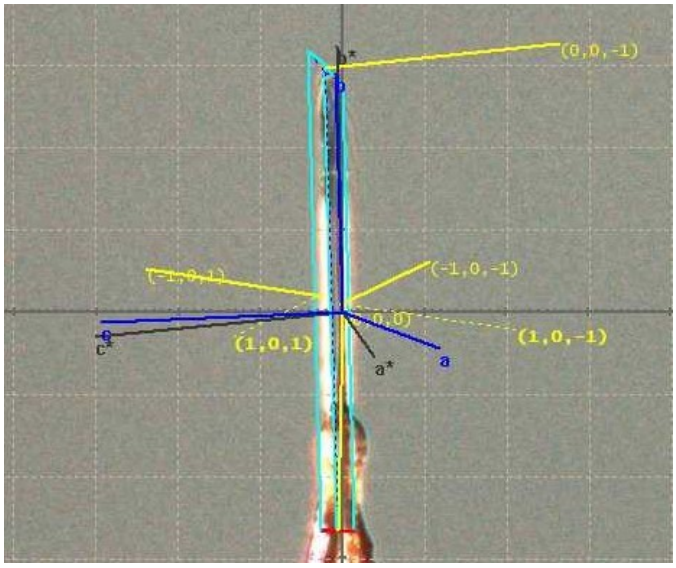

Figure 4-16: Face indexing of a γ-coronene crystal using x-ray diffraction. Due to uncertainty in the removal of the correct crystal from the silicon substrate, it is believed this is not the correct indexing used in the γ-coronene polarisation measurements. Further details are given in the text.

used in this room temperature polarisation Raman experiment had an incident face of (1 0 -1). One result worth noting from this is that it is possible to determine the incident face from the polarisation dependence of Raman spectra where high-quality computational results are also available. A benefit of this is the crystal is not damaged during Raman measurements and can be used for subsequent experiments.

The intensity as a function of input polarisation angle taken with both the vertical and horizontal analysers is compared to computational results in figure 4-17. Due to computational results having several modes very close together in frequency, the computational plots are a sum of intensities of these groups of modes given in table 4.1. The groups were determined by first comparing the experimental frequency to the Raman active isolated molecule modes. From the comparison of isolated molecule and crystalline modes, the γ-coronene mode groups to be combined were determined. For the two Fermi resonance peaks at 1351 and 1369 cm^{-1}, all modes which contribute are included, that is the modes equivalent to the 367 cm^{-1} and 990 cm^{-1} are included alongside the 1364 cm^{-1} modes. Combining modes creates a gap at the minimum intensity of the figure of eight which is more pronounced in some results. In general the computations reproduce the experimental results well, with some discrepancies in intensity possibly arising from the analysis of experimental spectra, and some figure of

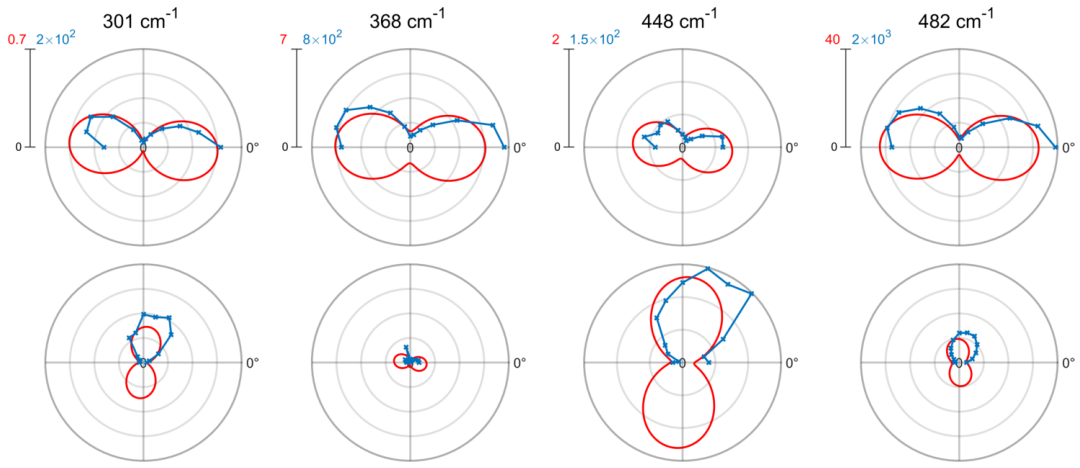

Figure 4-17: Raman intensity as a function of polarisation angle for γ-coronene. Plots are shown in vertical pairs with the output analyser vertical (top) and horizontal (bottom) in each pair. The experimental frequency is given above each pair. Experimental peak intensities (blue) are found by plotting the Voigt profile per peak and taking the maximum number of counts. Calculated intensities (red) are determined as detailed in section 4.2.2. The scale for experimental and calculated intensities within each pair is kept constant. Continues on next page.

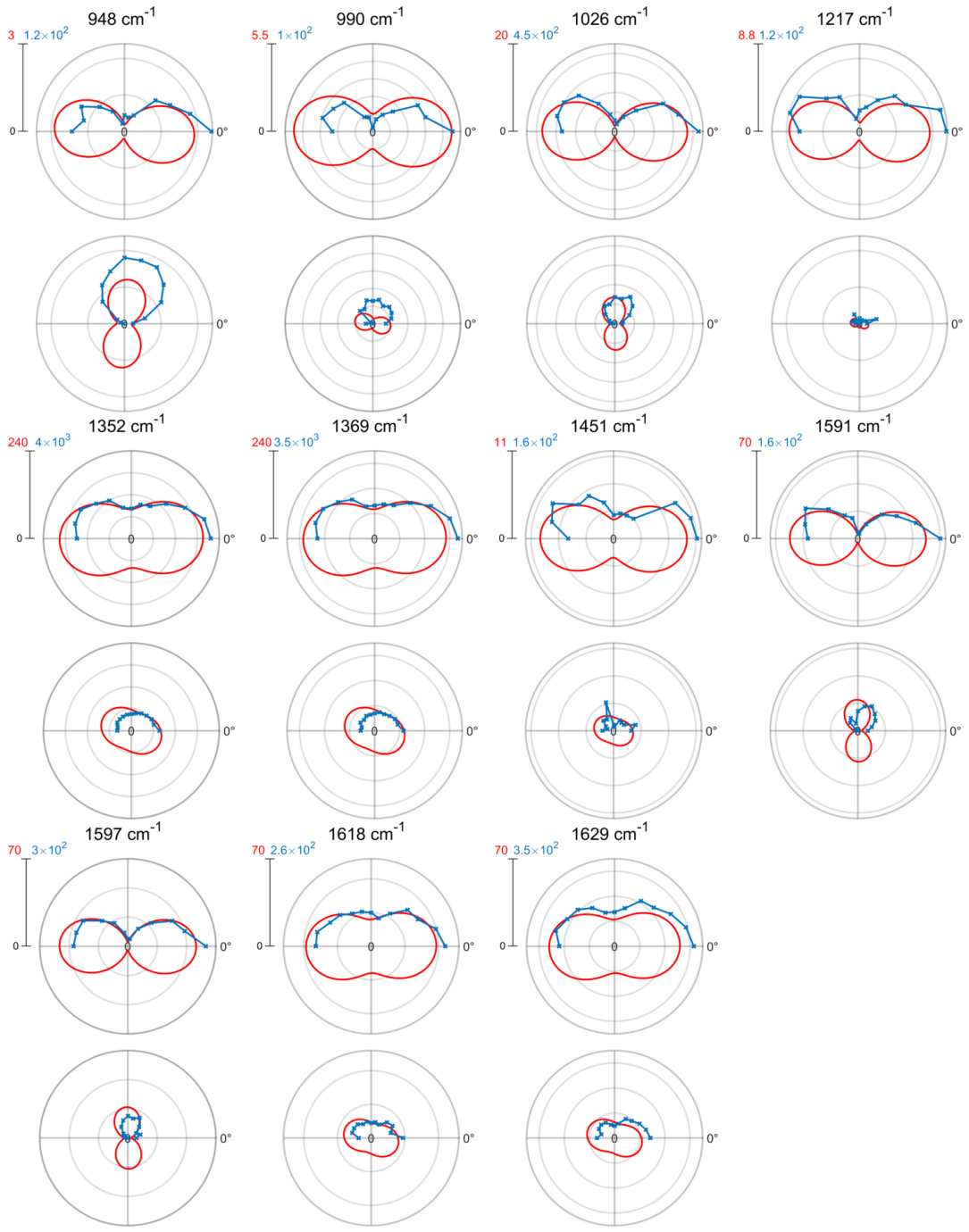

Figure 4-17: Cont. Raman intensity as a function of polarisation angle for γ-coronene. Plots are shown in vertical pairs with the output analyser vertical (top) and horizontal (bottom) in each pair. The experimental frequency is given above each pair. Experimental peak intensities (blue) are found by plotting the Voigt profile per peak and taking the maximum number of counts. Calculated intensities (red) are determined as detailed in section 4.2.2. The scale for experimental and calculated intensities within each pair is kept constant.

Table 4.1: Assignment of intramolecular modes for γ-coronene. Each measured frequency is matched to the isolated molecule calculations and to the γ-coronene structure calculations. The symmetry of the modes for the calculations is given. The intramolecular modes of the isolated molecule and γ-coronene calculations were matched by comparing the eigenvectors of each molecule individually. Full details of this are given in Appendix A.

Experimental frequency (cm^{-1})	Isolated molecule calculation (cm^{-1})	γ-coronene calculation (cm^{-1})	
301	283.59 (E_{1g})	293.39 (A_g)	298.66 (B_g)
		299.29 (A_g)	300.07 (B_g)
368	360.22 (E_{2g})	362.19 (B_g)	365.14 (A_g)
		365.60 (B_g)	366.47 (A_g)
448	441.13 (E_{1g})	442.42 (B_g)	443.85 (A_g)
		445.10 (B_g)	445.67 (A_g)
482	478.58 (A_{1g})	484.83 (B_g)	487.55 (A_g)
	482.80 (E_{2g})	481.32 (B_g)	482.02 (A_g)
		483.86 (A_g)	485.74 (B_g)
948	938.20 (E_{1g})	943.58 (A_g)	944.27 (A_g)
		945.53 (B_g)	949.91 (B_g)
990	985.89 (E_{2g})	988.03 (A_g)	989.35 (B_g)
		989.64 (B_g)	990.38 (A_g)
1026	1025.17 (A_{1g})	1026.26 (A_g)	1028.36 (B_g)
1217	1214.87 (A_{1g})	1215.84 (A_g)	1216.99 (B_g)
1352	1364.30 (A_{1g})	1369.27 (A_g)	1369.39 (B_g)
1369			
1451	1439.59 (E_{2g})	1441.11 (B_g)	1441.59 (A_g)
		1442.84 (A_g)	1443.49 (B_g)
	1446.08 (E_{2g})	1447.07 (A_g)	1447.31 (B_g)
		1449.17 (A_g)	1449.18 (B_g)
1591	1591.25 (A_{1g})	1591.81 (B_g)	1592.17 (A_g)
1597			
1618	1607.72 (E_{2g})	1608.69 (B_g)	1608.88 (A_g)
1629		1609.95 (A_g)	1610.50 (B_g)

eights rotated slightly which may arise from the (1 0 -1) crystal face being slightly off perpendicular to the incident laser beam.

Figure 4-18 shows the polarisation sweep with a vertical output analyser taken at 110 K on a β-coronene crystal fragment with the background removed. Equivalent figures with the output analyser in the horizontal position are shown in Appendix B. In the range 1300 to 1700 cm^{-1} some remnants of the additional background noise remains increasing the uncertainty on peak heights to ≈100 counts. Due to this increased background only the regions with clear peaks were used in further analysis, namely 300 to 550 cm^{-1} and 1300 to 1420 cm^{-1}. Four peaks were fit to this data at 367 cm^{-1},

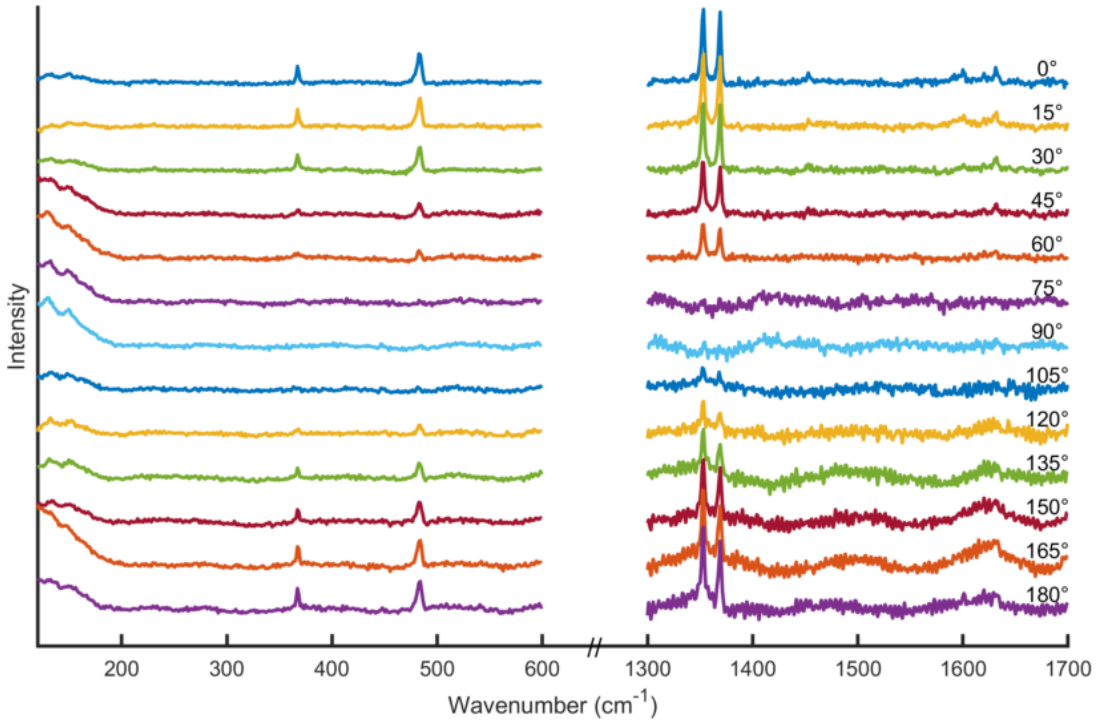

Figure 4-18: Polarisation angle dependence of Raman spectra of a β-coronene crystal fragment at 110 K with a vertical output analyser. Individual spectra are offset for clarity. Background envelopes have been removed. Due to excessive background noise the range 600 cm^{-1} to 1300 cm^{-1} is excluded.

483 cm^{-1}, 1353 cm^{-1} and 1369 cm^{-1}, consistent with those found in γ-coronene to within experimental error. All have a maximum intensity at 0° and decrease in intensity to a minimum at 90°, where they are not visible above the noise level, before increasing in intensity up to 180°.

Peak height as a function of polarisation for the four fitted peaks is compared to computational results in figure 4-19. Since the fragment was microscopic and had to be kept below the phase transition temperature to be preserved, it was not possible to experimentally determine the faces directly. Thus the crystal faces were assumed to be the same as γ-coronene with the rotation of the crystal in the experimental frame, $\theta = 27°$, as described in in figure 4-9 (b). Similar to γ-coronene, the peaks at 1353 cm^{-1} and 1369 cm^{-1} are Fermi resonances and all involved modes were combined in the computational analysis. Despite the face indexing assumption, the experimental and computational polar plots show excellent agreement and allow an assignment of modes to be made, given in table 4.2.

The experimental peaks found in this work are compared to those given in literature and interpreted with the isolated molecule and γ-coronene calculations in table 4.3.

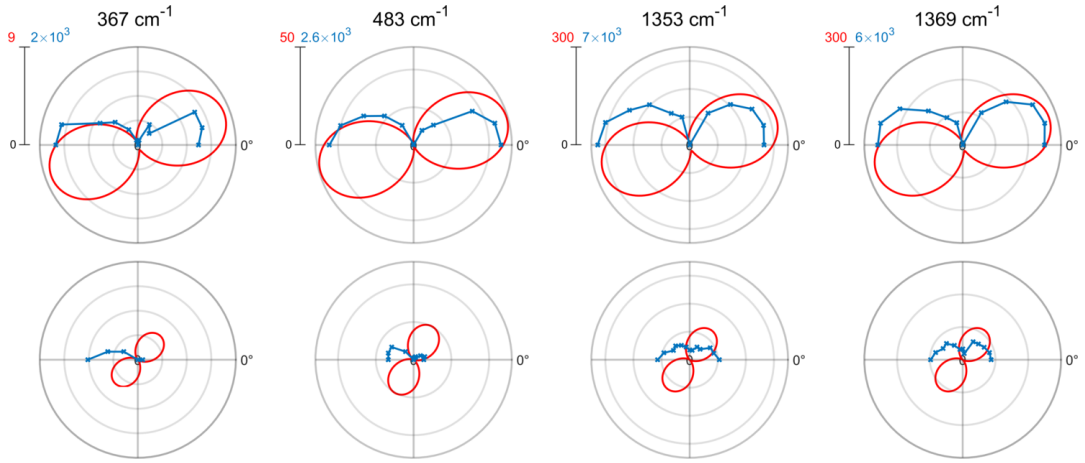

Figure 4-19: Raman intensity as a function of polarisation angle for β-coronene. Plots are shown in vertical pairs with the output analyser vertical (top) and horizontal (bottom) in each pair. The experimental frequency is given above each pair. Experimental peak intensities (blue) are found by plotting the Voigt profile per peak and taking the maximum number of counts. Calculated intensities (red) are determined as detailed in section 4.2.2. The scale for experimental and calculated intensities within each pair is kept constant.

Table 4.2: Assignment of intramolecular modes for β-coronene. Each measured frequency is matched to the isolated molecule calculations and β-coronene calculations. The modes predicted at $\sim$990 cm^{-1} are included since they are observed in the Fermi resonance peaks through contributing to the combination band. The symmetry of the modes for the calculations is given. The intramolecular modes of the isolated molecule and β-coronene calculations were matched by comparing the eigenvectors of each molecule individually. Full details of this are given in Appendix A.

Experimental frequency (cm^{-1})	Isolated molecule calculation (cm^{-1})	β-coronene calculation (cm^{-1})	
367	360.22 (E_{2g})	361.22 (B_g)	365.05 (A_g)
		365.76 (A_g)	365.84 (B_g)
483	478.58 (A_{1g})	484.37 (B_g)	487.51 (A_g)
	482.80 (E_{2g})	482.10 (B_g)	482.20 (A_g)
		484.34 (A_g)	487.27 (B_g)
(included in Fermi resonance)	985.89 (E_{2g})	988.14 (A_g)	989.95 (B_g)
		991.07 (A_g)	992.56 (B_g)
1353 1369	1364.3 (A_{1g})	1368.39 (A_g)	1368.53 (B_g)

Only one peak from literature could not be assigned: 571 cm^{-1} from Ref. [32] taken at low temperature. There are no modes predicted in our isolated molecule nor in either crystalline structures at or near this value. Todorov *et al.* have suggested this peak is due to a mode at 648 cm^{-1} [159]. Indeed our crystalline calculations are consistent with theirs predicting Raman active modes in the 620 to 680 cm^{-1} range. However, given that all other peaks are within a few wavenumbers of our calculated modes, it seems unlikely that this 571 cm^{-1} peak corresponds to modes at least 50 cm^{-1} higher. Furthermore we do not observe any clear peaks close to 571 cm^{-1} in any of our spectra and it is not measured in other literature, including the extensive spectra from Babkov *et al.* [153, 175]. Thus we suggest this peak is anomalous and unlikely to be from coronene.

The peaks around ∼830-840 cm^{-1} are interesting. At room temperature Ohno *et al.* found one weak peak at 830 cm^{-1} whilst at low temperature they found two: one weak at 828 cm^{-1} and one strong at 840 cm^{-1} [32]. In our isolated molecule calculations there is only one Raman active mode in this region at 828 cm^{-1}, however there are other symmetry forbidden modes in this region. In γ-coronene calculations, we find the Raman active mode splits into four ranging from 830 cm^{-1} to 837 cm^{-1}, and a Raman active pair at 854 cm^{-1} that corresponds to an isolated molecule mode at 856 cm^{-1} which is not Raman active. The total orientationally averaged intensity of the first four is 65.0 $Å^4amu^{-1}$ and the pair is 8.1 $Å^4amu^{-1}$. In β-coronene, we find the isolated molecule Raman active mode splits again into four modes ranging from 829 cm^{-1} to 844 cm^{-1} and this isolated molecule Raman inactive mode splits into a Raman active pair at 854 cm^{-1}, as shown in Appendix A, table A.2. The total spatially averaged intensity of the first four is 59.5 $Å^4amu^{-1}$ and the pair is 91.0 $Å^4amu^{-1}$. This change in intensity of the two mode groups explains the second peak Ohno *et al.* found at 840 cm^{-1} in their low temperature spectrum. Todorov *et al.* found reducing the symmetry of the isolated coronene molecule from D_{6h}, as used in our isolated molecule calculations, to C_{2h}, allowed the mode at 857 cm^{-1} to become Raman active and had previously assigned these modes similarly. It is unclear whether the Raman measurements in Ref. [153] were taken at room temperature or low temperature and therefore which polymorph is being measured. Since the peak at 846 cm^{-1} is closest to the low temperature 840 cm^{-1} peak found by Ohno *et al.*, we assign this to the pair at 854 cm^{-1} in β-coronene.

The peaks Babkov *et al.* found at 1232 cm^{-1}, 1250 cm^{-1} and 1292 cm^{-1} are puzzling [153]. In the isolated molecule calculations there are three modes in the range 1215 cm^{-1} to 1229 cm^{-1}, which in γ-coronene split into a total of eight modes spread out well in the range 1216 cm^{-1} to 1235 cm^{-1}, and which in β-coronene they also split into eight modes ranging from 1218 cm^{-1} to 1236 cm^{-1}. None of the modes are calculated to lie close to

Table 4.3: Comparison of Raman peaks from literature with the peaks found from our room temperature polarisation measurements performed on a γ-coronene crystal, and interpreted with respect to all Raman active modes predicted by DFT-D3 calculations on γ-coronene. The only peak unassigned from literature is that at 571 cm^{-1} from Ref. [32] at low temperature. All frequencies are in cm^{-1} . Calculated intensities are in $Å^4amu^{-1}$ and f indicates the mode is forbidden.

Experimental frequencies and symmetries from literature				Our RT Raman peaks	Isolated molecule calculations		γ-coronene calculations				
RT [32]	77 K [32]	[153, 175]	[154]		υ	I	υ_1	υ_2	υ_3	υ_4	I_{total}
					156.15 (B_{1g})	f	176.04	176.10			8.8
					216.77 (B_{2g})	f	234.38	235.75			20.1
				301	283.59 (E_{1g})	3.3	293.39	298.66	299.29	300.07	33.7
369	369	365 (e_{2g})	366	368	360.22 (E_{2g})	32.0	362.19	365.14	365.60	366.47	436.4
435	435			448	441.13 (E_{1g})	2.1	442.42	443.85	445.10	445.67	61.9
482	487	485 (a_{1g})	480	482	478.58 (A_{1g})	128.9	484.83	487.55			1573.5
					482.80 (E_{2g})	0.3	481.32	482.02	483.86	485.74	132.3
					622.44 (A_{2g})	f	623.45	624.13			1.0
					641.47 (B_{2g})	f	642.54	645.16			7.0
					656.36 (E_{1g})	0.0	655.02	661.23	661.35	663.33	26.2
					674.58 (E_{2g})	4.7	675.72	676.31	679.29	679.50	14.5
					746.43 (B_{1g})	f	750.48	753.42			34.5
830	828				828.74 (E_{1g})	0.6	829.86	835.34	837.30	837.48	65.0
	840	846 (e_{2g})			855.77 (B_{2g})	f	853.76	853.90			8.1
		905 (e_{2g})			917.26 (A_{2g})	f	918.95	920.24			4.4
		930 (e_{1g})		948	938.20 (E_{1g})	1.5	943.58	944.27	945.53	949.91	71.3
					952.71 (B_{2g})	f	959.45	966.13			12.0

Continued on next page

Table 4.3: Comparison of Raman peaks from literature with the peaks found from our room temperature polarisation measurements performed on a γ-coronene crystal, and interpreted with respect to all Raman active modes predicted by DFT-D3 calculations on γ-coronene. The only peak unassigned from literature is that at 571 cm^{-1} from Ref. [32] at low temperature. All frequencies are in cm^{-1} . Calculated intensities are in $Å^4amu^{-1}$ and f indicates the mode is forbidden.

Experimental frequencies and symmetries from literature				Our RT Raman peaks	Isolated molecule calculations		γ-coronene calculations				
RT [32]	77 K [32]	[153, 175]	[154]		υ	I	υ_1	υ_2	υ_3	υ_4	I_{total}
		993 (e_{2g})		990	985.89 (E_{2g})	16.9	988.30	989.35	989.64	990.38	246.7
		1084 (a_{1g})		1026	1025.17 (A_{1g})	44.9	1026.26	1028.36			942.9
					1147.35 (E_{2g})	3.6	1145.62	1146.88	1150.38	1152.87	137.6
		1232 (e_{2g})		1217	1214.87 (A_{1g})	31.2	1215.84	1216.99			147.8
		1250 (a_{1g})			1221.83 (A_{2g})	f	1223.75	1226.44			30.0
		1292 (e_{2g})		†	1228.53 (E_{2g})	35.6	1229.60	1229.94	1233.78	1235.35	474.4
1354	1354	1350 (a_{1g})	1340	1352	1364.30 (A_{1g})	912.1	1369.27	1369.39			11185.7
1371	1369	1370 (a_{1g})	1357	1369							
					1391.39 (E_{2g})	3.7	1393.82	1393.97	1396.63	1396.66	11.1
		1434 (e_{2g})		1451	1439.59 (E_{2g})	5.7	1441.11	1441.59	1442.84	1443.49	408.4
					1446.08 (E_{2g})	33.6	1447.07	1447.31	1449.17	1449.18	606.6
					1533.93 (A_{2g})	f	1535.41	1535.67			9.7
1584	1584	1584 (a_{1g})		1591	1591.25 (A_{1g})	235.2	1591.81	1592.17			3072.1
		1603 (a_{1g})		1597							0.0
1631	1625	1631 (e_{2g})		1618	1607.72 (E_{2g})	353.8	1608.69	1608.88	1609.95	1610.50	4384.9
	1633			1629							

† a shoulder exists on the 1217 cm^{-1} peak in some polarisation spectra, however it was not resolvable above the noise

1250 cm^{-1} or 1292 cm^{-1}. Without further information it is not possible to assign these modes accurately and therefore they have been assigned as a group to the calculated modes in the range 1215 cm^{-1} to 1236 cm^{-1}.

The final interesting points arise when considering the four peaks we found in the range 1591 cm^{-1} to 1629 cm^{-1} (figure 4-15, table 4.1). Four peaks have not been observed in this region previously. Ohno *et al.* found two peaks at 1584 cm^{-1} and 1631 cm^{-1} at room temperature, yet three peaks at 1584 cm^{-1}, 1625 cm^{-1} and 1633 cm^{-1} at 77 K [32]. Babkov *et al.* found three peaks at 1584 cm^{-1}, 1603 cm^{-1} and 1631 cm^{-1} [153, 175]. Yet in our isolated molecule calculations there are only two modes at 1591 cm^{-1} and 1608 cm^{-1}. In the γ-coronene calculations there are two groups: a pair at 1592 cm^{-1} and a group of four ranging from 1609 cm^{-1} to 1611 cm^{-1}. In β-coronene there are also two groups: a pair at 1593-1594 cm^{-1} and a group of four ranging from 1608 cm^{-1} to 1611 cm^{-1}. It was suggested by Babkov *et al.* [153] that a second Fermi resonance occurs in this range between a fundamental mode at ∼1590 cm^{-1} and a combination band comprising of $595 + 995$ cm^{-1}. However this was questioned by Fleischer and Pulay [158] whose calculations did not predict a mode at 595 cm^{-1}, which is consistent with our calculations. Fleischer and Pulay do suggest a Fermi resonance may be possible with a combination band comprising of modes at 659 and 934 cm^{-1}. Our isolated molecule calculations predict modes close to these at 656 cm^{-1} and 938 cm^{-1} both with E_{1g} symmetry. These could combine to form a combination band with symmetry $A_{1g}+A_{2g}+E_{2g}$, which would allow Fermi resonance with both the 1591 cm^{-1} A_{1g} and 1608 cm^{-1} E_{2g} modes. Following this through with the crystalline frequencies and symmetries for both polymorphs, various combination bands are possible which are able to resonate with the equivalent higher frequency modes. It may be that a combination of Fermi resonances produces four peaks in this range, however since this is anharmonic behaviour it is not captured within our calculations. In order to fully investigate this range methods beyond the harmonic approximation are required.

4.4 Summary

The intramolecular vibrations of both γ- and β-coronene have been investigated by Raman and interpreted using DFT-D3 calculations. Raman peaks of coronene from literature have also been examined and interpreted using DFT-D3 calculations.

DFT-D3 calculations successfully yield optimised γ- and β-coronene experimental structures. For γ- (β-) coronene, lattice parameters are reproduced within 1.6% (2.1%)

and the intracell angle within 0.7% (0.4%) compared to x-ray structures collected at 290 K (150 K) on single crystals.

Upon cooling a γ-coronene crystal, a change in peak positions in the low-wavenumber range (< 120 cm^{-1}) occurred after the crystal shattered at 137 K confirming a phase transition had happened. Further investigations into the low wavenumber range are detailed in Chapter 5. Both above and below the phase transition a further eleven peaks were identified. Raman spectra calculated for an isolated coronene molecule and for the γ- and β-structures reproduced the experimental spectra well. The crystalline calculations were found to predict the experimental frequencies marginally better. The main discrepancy between calculations and experiment is the single peak calculations predict at 1364 cm^{-1} where experimentally a well known Fermi resonance produces two at 1352 cm^{-1} and 1369 cm^{-1}. Our calculations do not reproduce this behaviour as it is caused by anharmonic effects.

Polarised Raman spectra were fitted using Voigt profiles. For the room temperature data, sixteen peaks were fitted including a peak at 521 cm^{-1} arising from the silicon substrate. Due to a large amount of background noise only four peaks were fitted to the low temperature polarised Raman spectra. The experimental crystal orientation and incident and measured polarisation directions were replicated in calculations of Raman intensity as a function of input polarisation angle. Our calculations successfully reproduce the figure of eight behaviour and relative intensities of the experimental intensity polar plots for both polymorphs, allowing a mode assignment to be made.

Our calculations do not predict any modes that could correspond to the peak Ohno *et al.* reported at 571 cm^{-1} [32], so we suggest that it is anomalous and unlikely to be from coronene. Our crystalline calculations explain the absence of a peak at 840 cm^{-1} at room temperature and its appearance in the low temperature spectra of Ohno *et al.* [32]. The peaks Babkov *et al.* found at 1232 cm^{-1}, 1250 cm^{-1} and 1292 cm^{-1} remain puzzling and further experimental investigation of these peaks is required for a more accurate mode assignment. The final mysteries are the additional peaks in the range 1590 cm^{-1} to 1630 cm^{-1}. Fleischer and Pulay [158] suggest a Fermi resonance as a possible cause of the additional peaks and our calculations do not exclude this possibility. It is clear that to fully interpret the Raman spectra of coronene, calculations which include anharmonic behaviour and are capable of simulating Fermi resonances are required.

Chapter 5

Lattice vibrations

Lattice vibrations, or phonons, can provide a fingerprint of molecular crystal structure since their frequencies depend upon the detailed interaction between the molecules within the system, which vary with separation and orientation [7]. Furthermore the thermodynamic stability of molecular crystals relies on both intramolecular and phonon vibrations, making it important to have a good description of both. A correct theoretical description of the phonon modes in molecular crystals is one of the most rigorous tests for any dispersion-corrected DFT model [176] as they probe the details of the potential energy surface. Thus success in the prediction of phonon modes would add confidence in our ability to use DFT-D3 for thermodynamic calculations.

This chapter investigates the phonon modes of both polymorphs of coronene by following the low-frequency Raman spectra across the phase transition, and studies the polarisation dependence of peak positions and intensities for both γ- and β-coronene. These experimental results are interpreted with DFT-D3 calculations, and the spectra rationalised by understanding the associated atomic motions.

5.1 Introduction

The phonons of crystalline coronene measured with Raman were first presented in 1972 by Ohno *et al.* [32]. Studying a powder sample they found three peaks at 40 cm^{-1}, 57 cm^{-1} and 87 cm^{-1} at room temperature, and four peaks at 43 cm^{-1}, 52 cm^{-1}, 77 cm^{-1} and 90 cm^{-1} at 77 K. This suggested a phase transition takes place within this temperature range, which we now know is from γ-coronene to β-coronene [8], and occurs at approximately 150 K.

Only very recently have these modes been studied again. In 2018 Salzillo *et al.* reported high-quality low-frequency Raman spectra of single crystals as a function of temperature and modelled them with DFT-D3(BJ) and DFT-MBD [177]. Both of these DFT-D methods reproduced γ- and β-coronene structures, and vibrational frequencies and Raman intensities calculated with DFT-D3(BJ) are in agreement with experiments. However although both structures were successfully relaxed, the unit cell volumes were fixed to experimental values for vibrational frequency and Raman intensity calculations which, as previously discussed in Chapter 2.3.2, introduces some strain on the resulting structure that is not ideal. This approach is also unsatisfactory in terms of using DFT calculations with low-frequency Raman for polymorph determination independent of XRD measurements, as suggested in Ref. [177], since x-ray structure determination is used to find the experimental unit cell volumes. Furthermore in their analysis "Lorentzian bands with fwhm's [were] chosen to conform to the experimental features" [177], an aspect of fitting that one would prefer to avoid. Salzillo *et al.* report polarised Raman and full analysis of modes as supplementary information. A full polarised Raman spectra is not presented, instead "H-H" and "V-H" configurations are shown corresponding to incoming and scattered light in parallel or cross-polarisation, although the specifics of these configurations are not given and the measurements are not interpreted with the computations. One noteworthy finding is the mechanical inhibition of the phase transition on cooling to as low as 79 K by placing a glass slide atop the γ-coronene crystal.

In this work we go beyond Salzillo *et al.* by measuring the polarised Raman spectra with an incident polarisation between 0° and 180° for two perpendicular output polarisations. These spectra are interpreted with DFT-D3 calculations allowing a definitive mode assignment to be made. The details of the associated atomic motion is studied in depth and used to explain the individual spectra and their remarkable differences between the polymorphs.

The methods employed here are similar to those used in the work presented in Chapter 4. The same computations were used since the vibrational frequencies and Raman intensities were calculated simultaneously. The method for crystal growth was identical to that detailed in Chapter 3, with new crystals grown for this work. The single-crystal XRD analysis was performed as before. There were some slight differences in the Raman measurements: firstly they were performed at Renishaw where Volume Bragg grating notch filters (Eclipse) were available allowing the low-frequency range of the Raman spectra to be accessed, and secondly the Linkam THMS600 stage was used for temperature control. The same rotatable $\lambda/2$ waveplate from the University of

Bath was used, and the experiments undertaken in a similar manner to Chapter 4. The methods used for the spectral analysis and the polarised Raman intensity calculations were as previously described.

5.2 Publication entitled: "Lattice vibrations of γ- and β-coronene from Raman microscopy and theory"

This declaration concerns the article entitled: Lattice vibrations of γ- and β-coronene from Raman microscopy and theory				
Publication status (tick one)				
Draft manuscript	**Submitted**	**In review**	**Accepted**	**Published**
				✓
Publication details	Bannister, N., Skelton, J., Kociok-Köhn, G., Batten, T., Da Como, E. and Crampin, S., 2019. Lattice vibrations of γ-and β-coronene from Raman microscopy and theory. *Physical Review Materials*, 3(12), p.125601 doi: 10.1103/PhysRevMaterials.3.125601			
Copyright status				
I hold the copyright for this material			Copyright is retained by the publisher, but I have been given permission to replicate the material here	
			✓	
Candidates contribution to the paper (provide details, and also indicate as a percentage)	The candidate ... • Formulation of ideas: Contributed to round table team discussions, 35% • Design of methodology: Developed crystal growth protocols, fitting of experimental spectra and visualisation of modes for analysis, 75% • Experimental work: Performed crystal growth, all Raman measurements and DFT-D3 calculations, 90% • Presentation of data in journal format: Wrote initial and subsequent drafts of manuscript, including choice of data, and style of presentation, 85%			
Statement from candidate	This paper reports on original research I conducted during the period of my Higher Degree by Research candidature.			
Signed			**Date**	

PHYSICAL REVIEW MATERIALS **3**, 125601 (2019)

Lattice vibrations of γ- and β-coronene from Raman microscopy and theory

Nicola Bannister,[1] Jonathan Skelton,[2] Gabriele Kociok-Köhn,[3] Tim Batten,[4] Enrico Da Como,[1] and Simon Crampin[1]

[1]*Department of Physics, University of Bath, Claverton Down, Bath BA2 7AY, United Kingdom*

[2]*School of Chemistry, University of Manchester, Manchester M13 9PL, United Kingdom*

[3]*Department of Chemistry and Material and Chemical Characterisation Facility (MC^2), University of Bath, Claverton Down, Bath BA2 7AY, United Kingdom*

[4]*Renishaw plc, Wotton-under-Edge, Gloucestershire GL12 7DW, United Kingdom*

(Received 1 May 2019; revised manuscript received 6 August 2019; published 6 December 2019)

We combine polarization-resolved low-frequency Raman microscopy and dispersion-corrected density-functional calculations (DFT-D3) to study polymorph-dependent lattice vibrations in coronene, a model molecular system for nanographenes and disklike organic semiconductors that exhibits two crystalline structures with distinct electronic and optical properties. Changes in low-energy Raman-active lattice phonons are followed across the γ- to β-phase transition at 150 K. Raman frequencies calculated using DFT-D3 agree to within 4 cm^{-1}, and on the basis of polarization dependence of peak positions and intensities we achieve a clear mode assignment. Studies of the associated atomic motions show how the pure librational and rotational modes of γ-coronene change into mixed roto-librations in the β-phase, explaining the remarkable differences in Raman spectra of the two phases.

DOI: 10.1103/PhysRevMaterials.3.125601

I. INTRODUCTION

The lattice dynamics of molecular solids have a significant impact on their electronic and optical properties [1]. In technological applications, phonons influence charge transport in molecular semiconductors, ultimately limiting maximum carrier mobilities in organic electronic devices [2–5], and the performance of materials for thermoelectric applications [6]. More fundamentally, the vibrational spectrum contributes to the relative thermodynamic stability of crystalline structures [7], and it must be considered when attempting to explain polymorphism, the existence of different crystal structures for the same molecular compound [8]. Here we report a combined experiment and theory study of lattice vibrations in the two different polymorphs of the molecular crystal coronene.

Molecular crystals are held together by dispersive forces (van der Waals), which dominate intermolecular interactions, but they are far weaker than the strong intramolecular covalent bonds. As a consequence, the description of their structural, phononic, and electronic properties by *ab initio* density functional theory (DFT) methods remains challenging. Even the most recently developed exchange-correlation functionals do not describe dispersion, which is the fundamental interaction for the cohesive energy in these van der Waals solids [9]. Phenomenologically, the distinction between inter- and intramolecular interactions is usually reflected in the vibrational modes, allowing a classification into intermolecular phonons and intramolecular vibrational modes [10]. Although the distinction is not always well defined, as modes with mixed character can occur, phonons are typically observed at frequencies $<$200 cm^{-1}, while the spectrum at high frequencies is dominated by intramolecular modes. On account of their origin being the intermolecular van der Waals interactions, it is the low-frequency modes that are most sensitive to variations in crystal structure, and able to be used as probes to test the validity of dispersion-corrected DFT methods [11]. Experimentally, they can be readily observed with low-frequency Raman spectroscopy, a technique that has also proven to be effective for studies of polymorphism in several condensed polyaromatic systems [8] as well as being used to estimate electron-phonon coupling in organic semiconductors [4,12], highlighting the importance of Raman for understanding charge transport in this fascinating class of materials [13]. Beyond molecular crystals, another class of van der Waals solids, the transition-metal chalcogenides, also exhibit a clear distinction between modes involving covalent and noncovalent bonds, and Raman spectroscopy of interlayer phonons has proven useful in studying polytypism and film thickness in few-layer systems [14–16].

The *ab initio* DFT-based description of molecular crystals using dispersion corrections has attracted substantial interest in recent years. This has been motivated by the design of theoretical tools aimed at predicting thermodynamic stability of polymorphic crystal structures, especially in connection with pharmaceuticals. Because of the intermolecular nature of low-frequency phonons, a correct theoretical description of such excitations is recognized as one of the most rigorous tests for any dispersion-corrected DFT model [11]. Additionally, the already mentioned role of phonons in determining the relative thermodynamic stability of different crystal structures points toward their correct description as the first step in any attempt to explain the complex scientific problem of polymorphism.

Among organic aromatic semiconductors such as pentacene, tetracene, perylene, and others that exhibit

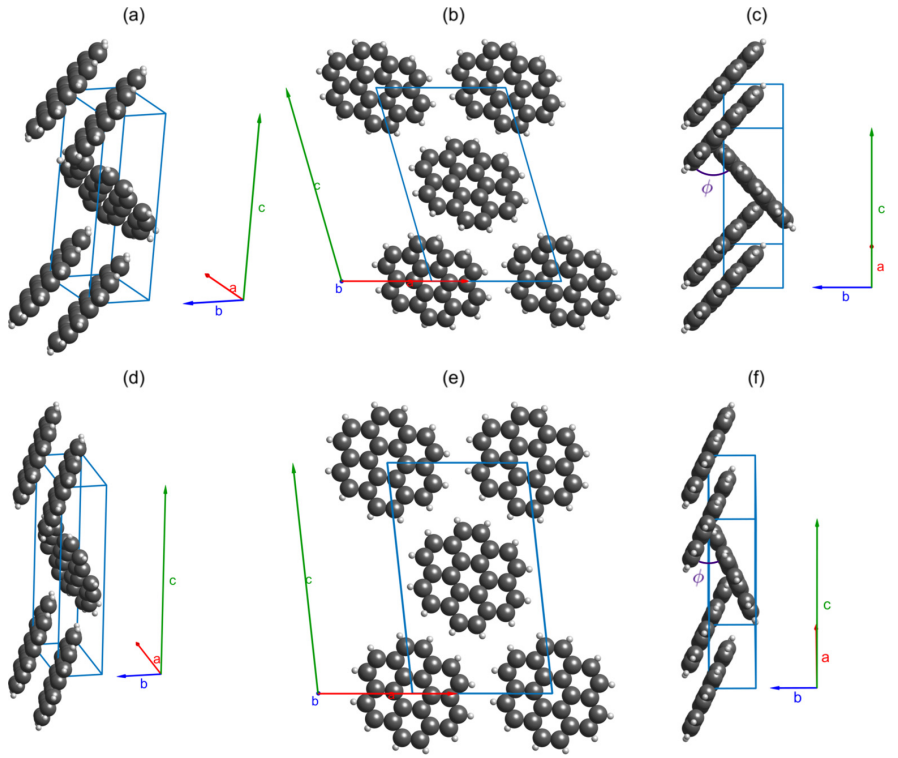

FIG. 1. Crystal structures of (a)–(c) γ- and (d)–(f) β-coronene obtained at 290 and 150 K, respectively. The γ-coronene structure was measured in this work using single-crystal x-ray diffraction while the β-coronene structure is taken from Ref. [26]. Clearly visible are the changes in the lengths of cell vectors $\vec{b}$ and $\vec{c}$, the decrease in the angle, β, between cell vectors $\vec{a}$ and $\vec{c}$, and the large change in the intracell molecular angle, ϕ, between the molecular planes of the two translationally inequivalent $C_{24}H_{12}$ molecules within the unit cell.

polymorphism, coronene has garnered much interest [17–21]. Several optical spectroscopy experiments have indicated structural phase transitions upon cooling single crystals [22–26] and also under pressure [23,27], and the existence of two stable crystalline structures has been reported [26]. Very recently, Salzillo *et al.* have reported high-quality low-wave-number Raman spectra of single crystals as a function of temperature, and modeled them using dispersion-corrected density-functional theory [28]. Upon cooling below $T \simeq 150$ K, the common phase, γ, transforms into a second phase, the β phase. Both phases contain two molecules per unit cell, but with a major difference in the angle between the molecular planes [Figs. 1(c) and 1(f)]. In this work, we use low-frequency Raman spectroscopy and the dispersion-corrected density-functional theory model DFT-D3 to study the Raman spectrum across the phase transition, assigning the spectra and establishing the key differences between the polymorphs. We consider this as the first step toward the identification of an adequate *ab initio* model for the description of phonons and future discussions on their roles in the phase transition. We identify the Raman-active phonons of γ-coronene as rotations and librations of the molecules with axes almost perpendicular and parallel to the plane of π bonds, respectively. In β-coronene, the axes of rotation and libration are instead at intermediate angles with respect to the molecular plane and result in modes that appear to be combinations of librations and rotations. We also explain the correlation between the geometrical characteristics of the modes and the Raman activity.

II. METHODS

A. Computations

Energy calculations and structural optimizations were performed using the Vienna *ab initio* simulation package (VASP) code [29]. The Perdew-Burke-Ernzerhof (PBE) functional [30] was employed with projector augmented wave (PAW) pseudopotentials [31,32] and a kinetic energy cutoff of 850 eV for the plane-wave basis. The Grimme-D3 scheme [33,34] was used to account for van der Waals forces. For both structures, a Γ-centered $2 \times 3 \times 1$ Monkhorst-Pack k-point mesh was used to sample the Brillouin zone. Increasing k-point sampling to $3 \times 4 \times 2$, as used in previous work [26], gave a difference in the lattice energies of 3 meV and a $<0.3\%$ change in unit-cell parameters. Total-energy calculations were considered converged when the energy change between two successive electronic steps was less than 10^{-8} eV. Structures were allowed to fully relax until all forces acting on the atoms were $<10^{-4}$ eV/Å. Phonopy [35,36] was used to calculate vibrational frequencies and eigenvectors within the harmonic approximation. VASP was used as the force calculator with a finite displacement step of 0.015 Å. Raman

activity tensors were calculated using a central-differences scheme [37–39] with required dielectric constants calculated using VASP. The symmetry labels of vibrational modes were output by Phonopy from in-built group tables.

B. Crystal growth

Crystals of γ-coronene were grown using a physical transport method in a three-zone furnace [40]. Powdered γ-coronene crystals of 97% purity were sourced from Sigma-Aldrich and twice purified by sublimation under vacuum. The purified γ-coronene was placed on a platform in a quartz boat at one end of a quartz tube inside the furnace. The furnace was heated to 175, 225, and 275 °C at the end, middle and sample end, respectively. Gaseous argon was set to flow from hot to cold at a rate of approximately 40 cm^{-3}/min. After 2 days the furnace was allowed to cool, and crystals were removed. The two purification steps were found to be critical in reducing the fluorescence background in Raman experiments enabling better resolution of the peaks—the origin of the residual fluorescence is unknown but could be linked to a defect-enhanced two-photon absorption process as recently observed in rubrene [41]. Crystals of β-coronene were obtained by cooling the purified γ-coronene crystals below 150 K.

C. Single-crystal x-ray diffraction

Data collection was carried out at four different temperatures, starting at 290 K, decreasing to 200 K at 300 K/h and stabilizing for 2 min, then further decreasing to 150 and 80 K with a stabilizing time of 10 min. Diffraction datasets were collected on a Rigaku SuperNova, Dual, Cu at zero, EosS2 single-crystal diffractometer using monochromated Cu $K\alpha$ radiation with $\lambda = 1.541\,84$ Å. A symmetry-related (multiscan) absorption correction was applied with CrysAlisPro 1.171.38.43. Structures were solved with SHELXT and refined by full-matrix least-squares fits on F^2 [42], with additional analysis performed using SHELXle [43]. We found that the crystals deteriorated at 80 K, preventing further characterization.

D. Raman

Raman measurements were performed using a Renishaw InVia Raman spectrometer operated in backscatter geometry, equipped with a 633 nm excitation laser, 2400 lines/mm grating, and a long working distance 50× objective lens (NA = 0.5). The spectral resolution of this configuration was better than 1 cm^{-1}. Volume Bragg grating notch filters (Eclipse) with a nominal cutoff of ± 10 cm^{-1} were used to measure the low-frequency Raman modes. The laser power incident on the sample was 4.0 ± 0.1 mW. To control the temperature during measurements, the sample was placed in a Linkam THMS600 stage and Raman measurements were collected through a quartz window, reducing the laser power to 3.7 ± 0.1 mW. The stage has an operational temperature range of 77 to 327 K and an accuracy of the order 0.1 K. For polarization measurements, a rotatable $\lambda/2$ waveplate, with an accuracy of $<1°$ on rotated angle between 0° and 90°, was placed in the path of the laser before the sample, and a linear polarizer was placed after the sample and in front of the detector. Peaks were fit using Voigt profiles [44–46] to account for the intrinsic Lorentzian line shapes and Gaussian broadening imposed by the instrumentation [47].

III. RESULTS AND DISCUSSION

We first compare the crystal structures of the two phases predicted from our DFT-D3 calculations to experimental measurements. We then present a comprehensive characterisation of the low-frequency Raman spectra across the phase transition. Initial mode assignments are made based on peak positions and confirmed by measuring the polarization dependence of the Raman activity. Finally, the differences in spectra of the two polymorphs is rationalised by analyzing the atomic motion associated with the vibrations.

A. Crystal structures

A series of single-crystal x-ray diffraction measurements were taken on a γ-coronene crystal; see Fig. 2. The lattice parameters show a linear temperature dependence, which produces extrapolated 0 K values of $a = 9.98$ Å, $b = 4.65$ Å, $c = 15.50$ Å, and $\beta = 106.82°$ giving a volume $V = 688$ $Å^3$ and an intracell molecular angle, as indicated in Fig. 1(c), of $\phi = 86.83°$.

Starting from the experimental γ-coronene structure, relaxation with DFT-D3 yields lattice parameters $a = 9.98$ Å, $b = 4.76$ Å, $c = 15.42$ Å, and $\beta = 106.38°$ giving $V = 703$ $Å^3$. The intracell molecular angle is $\phi = 85.96°$. As seen in Figs. 2(b) and 2(c), the main differences between the calculated and measured structures are a larger b-axis and a slightly smaller c-axis. These are within 1.6% of the lattice parameters measured at 290 K and within 2.5% of the extrapolated 0 K values, while ϕ is within 0.7% of the 290 K value and 1.0% of the 0 K extrapolation, indicating that our relaxed γ-coronene crystal structure is comparable to experiment. The level of agreement gives confidence in using DFT-D3 to interpret our experimental results.

The β phase was also optimized using DFT-D3. Relaxations starting from experimental lattice parameters and previously reported DFT results [26] both produced identical final structures. The calculated lattice parameters are $a = 10.31$ Å, $b = 3.92$ Å, $c = 17.17$ Å, and $\beta = 96.05°$ giving $V = 690$ $Å^3$, with an intracell molecular angle of $\phi = 49.86°$. Figure 2 shows a comparison between our DFT-D3 lattice parameters and the measured parameters in Ref. [26]. The largest differences with experimental measurements are a decrease in the predicted a-axis and an increase in the b-axis [Figs. 2(a) and 2(b)]. Our lattice parameters are within 2.1% of those measured at 150 K and within 3.1% of the extrapolated 0 K values. The intracell molecular angle is within 0.4% at 150 K and 1.1% of the 0 K extrapolation. This again indicates that DFT-D3 is appropriate for further calculations.

B. Raman

Figure 3(a) shows Raman spectra recorded from a single γ-coronene crystal while reducing the temperature at a rate of 15 K/min. Between 300 and 175 K, two peaks labeled A and B are visible, as observed in previous Raman measurements

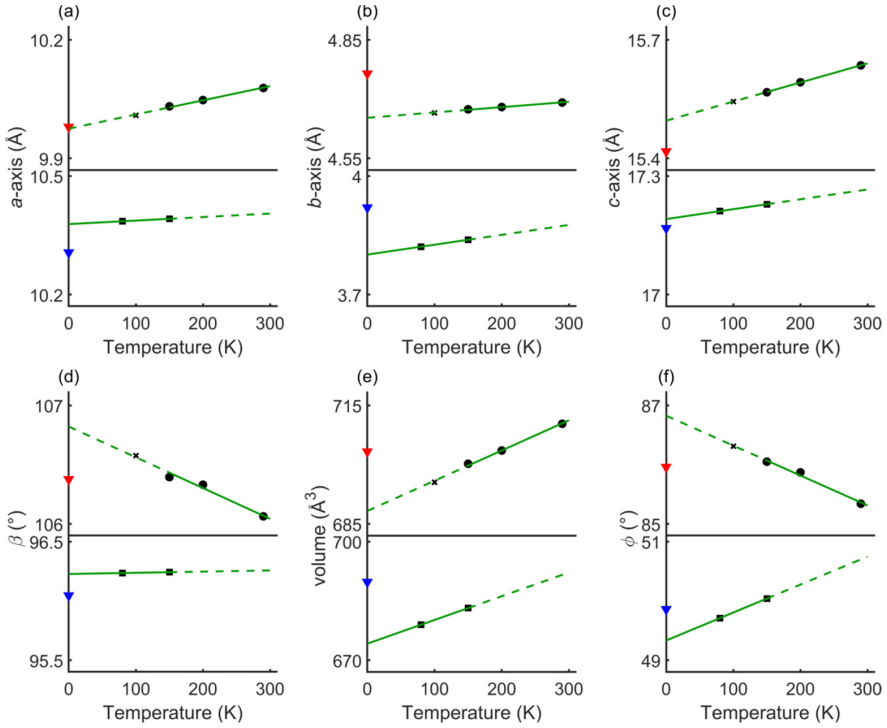

FIG. 2. Temperature dependence of (a)–(c) lattice parameters, (d) cell angle β, (e) cell volume, and (f) intracell molecular angle ϕ. Top panels show γ-coronene and bottom panels β-coronene. Red and blue triangles are from our DFT-D3 calculations for γ- and β-coronene, respectively. Black circles show our measurements from single-crystal x-ray diffraction, black $\times$ show data from Ref. [48], and black squares are from Ref. [26]. Green lines show the fitted linear trend lines.

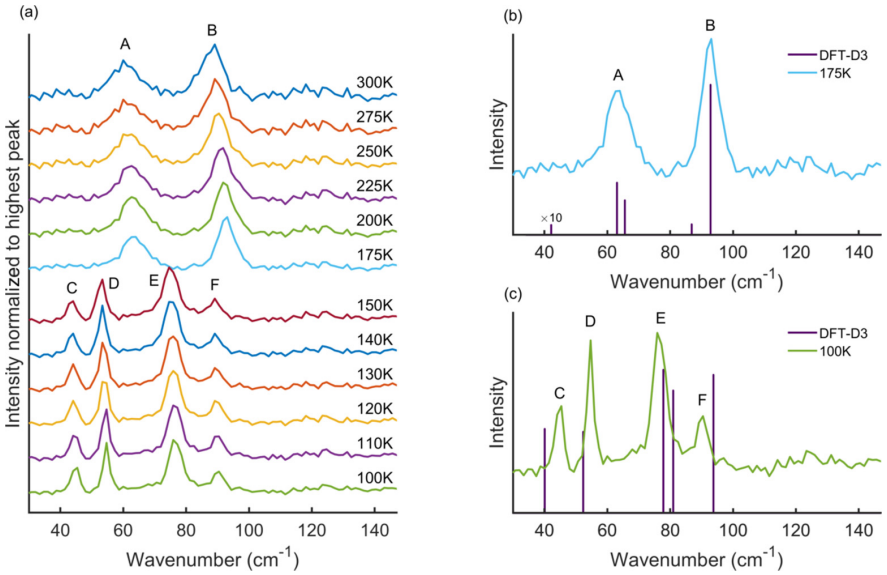

FIG. 3. (a) Raman spectra collected from a single γ-coronene crystal during a temperature sweep from 300 to 100 K. The crystal was observed to shatter at 163 K, corresponding to the striking change in spectral shape. For each spectrum, background envelopes have been removed and intensities normalized to the highest peak. Individual spectra are offset for clarity. Parts (b) and (c) compare Raman spectra in the two temperature regimes to orientationally averaged (powder) Raman intensities calculated using DFT-D3 for γ- and β-coronene, respectively.

TABLE I. Raman frequencies and intensities fitted from experimental spectra and from DFT-D3 calculations on γ-coronene. Modes 3 and 4 overlap in experiment due to their similar frequencies and line broadening effects producing peak A.

	175 K experiment		DFT-D3	
Mode ID	Frequency (cm^{-1})	Intensity (k counts)	Frequency (cm^{-1})	Intensity ($Å^4$ amu^{-1})
1	not observed		34.13	0.2
2	not observed		42.15	2.4
3	(A) 63.5	21.4	63.09	125.0
4			65.60	82.9
5	not observed		86.85	25.3
6	(B) 92.8	47.6	92.85	359.7

TABLE II. Raman frequencies and intensities fitted from experimental spectra and from DFT-D3 calculations on β-coronene. Peak E was fitted with two-component Voigt profiles giving E_1 and E_2.

	100 K experiment		DFT-D3	
Mode ID	Frequency (cm^{-1})	Intensity (kcounts)	Frequency (cm^{-1})	Intensity ($Å^4$ amu^{-1})
1	not observed		17.73	0.7
2	(C) 44.8	10.2	40.10	60.4
3	(D) 54.6	24.0	52.34	58.3
4	(E_1) 76.6	20.7	77.84	102.9
5	(E_2) 77.5	4.6	80.97	88.0
6	(F) 90.3	8.1	93.77	99.3

[22,28]. At 163 K the crystal was observed to shatter. Subsequent spectra recorded from a crystal fragment between 150 and 100 K show four peaks labeled C–F. It has recently been confirmed from x-ray experiments that a phase transition occurs at ∼150 K and the low-temperature phase was determined to be the β phase of coronene [26,49]. A second crystal fragment measured while increasing temperature gave consistent results [50]. In both phases, as the temperature decreases, the peaks shift to higher frequencies.

For γ-coronene, the calculations predict six Raman-active modes (Table I). These are compared with the experimental spectra in Fig. 3(b). The two lowest frequency modes at 34.13 cm^{-1} (mode 1) and 42.15 cm^{-1} (mode 2) are predicted to have very small intensities in comparison to the other four, which is consistent with these two modes being absent in the experimental spectra. Of the other modes, the first two are close in frequency [63.09 cm^{-1} (mode 3) and 65.60 cm^{-1} (mode 4)] and have similar intensities, such that line broadening causes the modes to overlap and produce peak A at 63.5 cm^{-1} in the experimental spectra. Mode 5 (86.85 cm^{-1}) is unlikely to be observed, as mode 6 (92.85 cm^{-1}) has >14 times higher intensity, making it hard to discern mode 5 above the background and/or the tail of mode 6. We note that the predicted intensities assume an orientational average of the Raman activity tensors, which means a quantitative comparison of the intensity profiles is not realistic given that the experiments were performed on a single crystal of unknown orientation, which will create a spatial dependence of the intensity. Despite this, however, the peak positions agree well, enabling a tentative mode assignment to be made.

For β-coronene, DFT-D3 again predicts six Raman-active modes (Table II), which are compared to the experimental spectra in Fig. 3(c). The lowest-frequency mode at 17.73 cm^{-1} (mode 1) is not observed in our experiments, due both to its low intensity and the frequency lying below our realistic analysis window of >30 cm^{-1} due to noise from other sources of scattering. Of the remaining five modes, Fig. 3(c) suggests that the two modes at 77.84 cm^{-1} (mode 4) and 80.97 cm^{-1} (mode 5) overlap in the experiments to produce peak E. The other three modes predicted at 40.10 cm^{-1} (mode 2), 52.34 cm^{-1} (mode 3), and 93.77 cm^{-1} (mode 5) can be individually resolved in the spectra. By fitting the experimental spectra with five Voigt profiles, peak E can be deconvoluted into two component peaks at 76.6 cm^{-1} (E_1) and 77.5 cm^{-1} (E_2). The other three peaks, C, D, and F, occur at 44.8, 54.6, and 90.3 cm^{-1}, respectively. Small discrepancies of up to 4 cm^{-1} in frequency between the experimental and predicted frequencies are observed, which we ascribe to a combination of small disparities in the predicted crystal structure, anharmonicity, and thermal effects.

To further confirm the assignment of modes, the full Raman tensors were calculated from DFT-D3 and used to simulate polarized Raman measurements, which are compared to experimental measurements in Figs. 4(a) and 4(b).

For γ-coronene, as the input polarization is rotated from 0° to 90°, the intensity of the A and B peaks decreases until they are unobservable above the noise level at 90°, and then increases again to a maximum at 180°. Neither of the peak positions changes with polarization, indicating that both have a single component, and thus both peaks were fitted to a single Voigt profile. All the polarized spectra were fitted simultaneously, with the peak positions and the Gaussian and Lorentzian widths constrained to be the same. The peak positions fitted here are lower in frequency than those listed in Table I as the polarization measurements were performed at room temperature [cf. Fig. 3(a)]. Intensity as a function of input polarization angle is shown in Fig. 4(c), and half figure-of-eight shapes were observed for both peaks.

To interpret these results using our calculations, it was necessary to determine the orientation of the crystal sample, so face indexing was carried out using x-ray diffraction [50]. The long crystal side, determined to be the *b*-axis, was aligned with the experimental vertical at 0°. With this knowledge, the Raman intensity as a function of input polarization was calculated using the Raman tensors [Fig. 4(c); for ease of analysis, modes 3 and 4 of γ-coronene were combined]. The combined intensity polar plot for modes 3 and 4 results in an oval shape, since both modes exhibit figure-of-eight behavior but with lobes at 90° to each other. Mode 6 also exhibits figure-of-eight behavior, with lobes at 0° and 180°. Mode 5 was excluded from the analysis as it is not resolved in the experimental measurements, and combining it with mode 6 when analyzing the calculation results was found to make an insignificant difference to the predicted polar plot. Our calculations correctly predict the polarization dependence of the intensities of all of the peaks, confirming our mode assignments. A second set of measurements was also performed

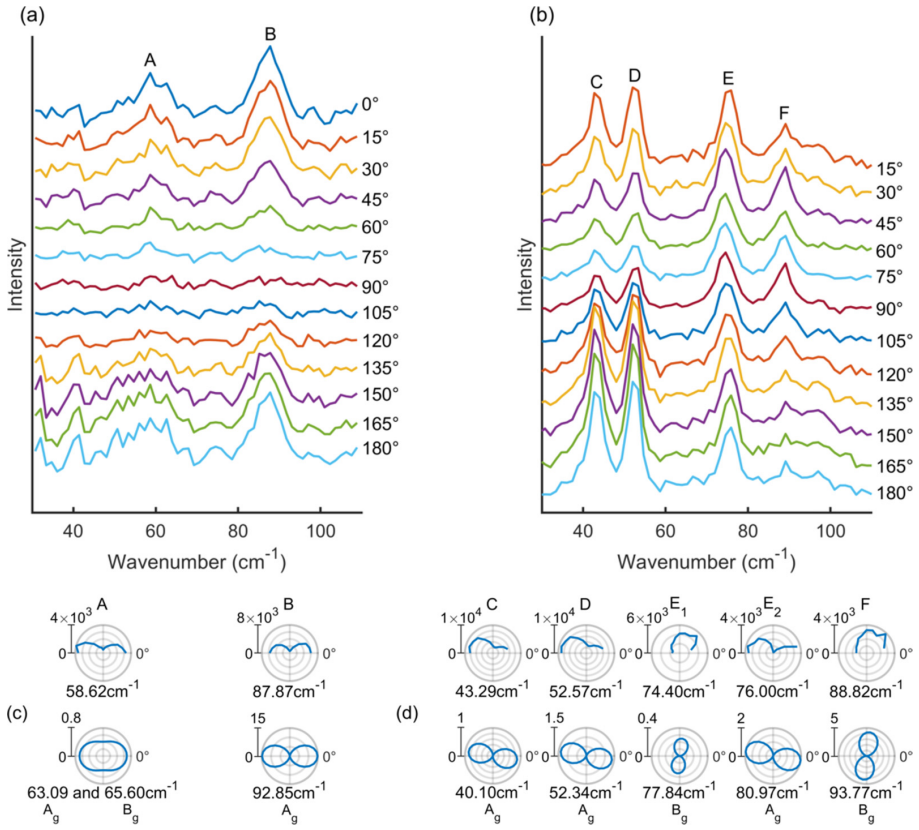

FIG. 4. Polarization angle dependence of Raman spectra for (a) γ- and (b) β-coronene, respectively. Individual spectra are offset for clarity. The peak intensity as a function of polarization angle for (c) γ- and (d) β-coronene. The top rows show profiles extracted by fitting the experimental spectra, while the bottom rows show the profiles predicted from our calculations. The 0° measurements for β-coronene have been excluded due to anomalies arising from local heating by the laser.

with the output polarizer rotated by 90° [50]—in these measurements, peak A was suppressed in intensity, meaning no useful data could be extracted, while the calculations again predicted the correct polarization dependence of the intensity of peak B, further confirming our mode assignments.

Low-temperature polarization measurements on the β-coronene phase were also carried out [Fig. 4(b)]. The positions of peaks C, D, and F exhibit no polarization dependence, while the position of peak E shifts slightly as the input polarization is varied, which confirms that peak E is indeed a combination of multiple modes, consistent with our earlier assignment [Fig. 3(c)]. The spectra were fitted to a set of five Voigt functions using the method detailed above. All five modes showed figure-of-eight dependencies on the polarization [Fig. 4(d)]. Peaks C, D, and E_2 show half figure of eights with lobes at ∼0° and ∼180°, while peaks E_1 and F show only one lobe at ∼90°. Note that the figures of eight are slightly rotated from 0° and 90°, which is due to the long side of the crystal fragment—assumed to be along the *b*-axis—being 8° away from the vertical (0°) in the experiments [50].

Since it was not possible to preserve the β-crystal fragment for face indexing, we generated polar plots from our calculations assuming the same face indexation as γ-coronene—both structures are very similar, and will therefore very likely have similar preferred crystal faces. The predicted intensity polar plots, accounting for the 8° offset, are shown in Fig. 4(d), and again demonstrate very good agreement with our experiments. We find that the calculations again predict the correct polarization dependences, providing a clear assignment of modes.

Results with the detector polarization rotated by 90° are presented in [50]. These again show four peaks, which we fitted to five Voigt profiles, and the polarization dependence of the intensities again shows good agreement with our simulations.

C. Atomic motion

The preceding results indicate that there are remarkable differences in Raman spectra of γ- and β-coronene despite their very similar structures. To understand this difference, we compared the atomic motion associated with the vibrations of the two polymorphs predicted by the calculations.

The vibrational motion associated with the Raman-active phonon modes of both polymorphs is shown in Fig. 5. All of the modes involve rocking-type rotations of the molecules around an axis indicated by purple lines, which makes an

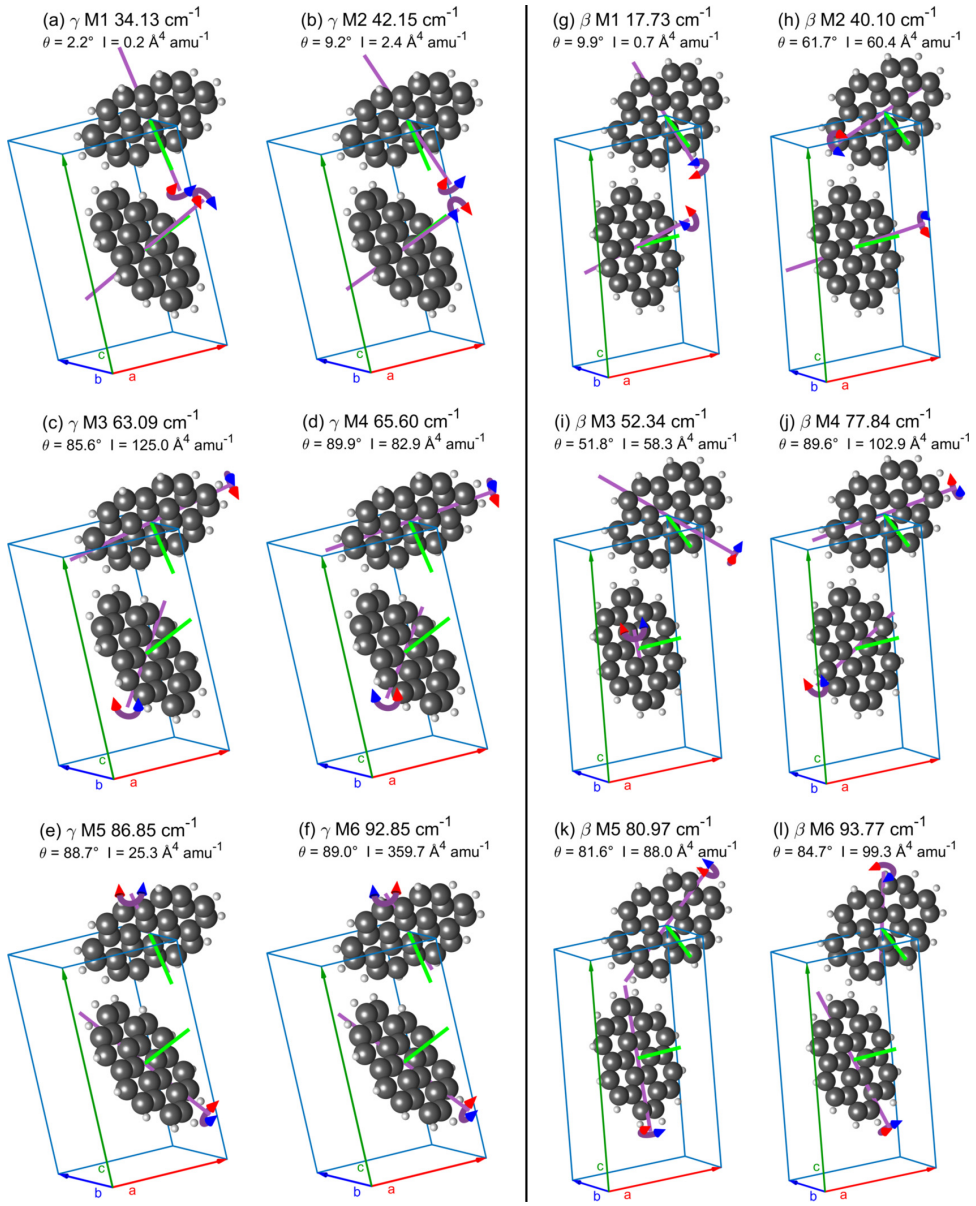

FIG. 5. Atomic motions associated with the Raman-active phonon modes in (a)–(f) γ- and (g)–(l) β-coronene. The frequency, the angle between the molecule normal and the axis of rotation, θ, and orientationally averaged Raman intensity, I, are given for each mode. Each illustration shows the motion of the two symmetrically inequivalent coronene molecules. The normal to the plane of each molecule is shown by a green line. The axis of rotation is shown with a purple line, and the direction of the rocking motion is shown by a purple arrow with a red and blue head. In any given plot, both molecules rotate in the same color direction at any instance.

angle θ to the normal of the molecular plane (the molecular normal axis) shown in green.

For γ-coronene, the six Raman-active modes can be grouped into sets of two. In the lowest-frequency pair, modes 1 and 2, the rotational axis is close to the molecular normal at $\theta = 2.2^\circ$ and 9.2°, respectively, indicating them to be rotational modes [Figs. 5(a) and 5(b)]. The difference between the molecular motions in the two modes is a reversal in the direction of one of the molecules. Since a molecule rotating exactly around its molecular normal will not produce any significant change in polarization, the small angle θ away from the normal in these modes will result in a small change in polarization, explaining the small intensities calculated for these modes and the fact that these peaks were not seen in our measured Raman spectra.

Modes 3–6 all have rotational axes that are almost perpendicular to the molecular normal and are therefore predominantly librations. Each rocking rotation of a molecule will

produce a significant change in polarization, accounting for the higher intensities for these modes compared to modes 1 and 2. Modes 3 and 4 both rock around similar axes but with one molecule rotating in the opposite direction relative to the other mode [Figs. 5(c) and 5(d)]. Mode 3 has a higher intensity than mode 4, which can be explained by considering the contribution each molecule makes to the total change in polarization and the effect the reversal of one rotation direction has: one can think of a "constructive" addition of the change in polarization from each molecule in mode 3 producing a larger change in polarization, and hence intensity, while in mode 4 a "destructive"-like addition occurs producing a smaller change in polarization and a lower intensity. Modes 5 and 6 exhibit similar behavior [Figs. 5(e) and 5(f)], albeit with a significantly larger difference in the intensities. We speculate this is due to the rotational axes of the molecules in modes 5 and 6 being more in line with each other than in modes 3 and 4, giving a stronger "constructive/destructive" effect and hence intensity difference.

Turning to β-coronene, we find that the vibrational motions are markedly different, although some similarities can be observed. The lowest-frequency mode 1 is similar to that in γ-coronene in that the rotational axis is close to the molecular normal such that the mode corresponds to a rotation-type vibration with a low intensity, and the directions of rotation of the molecules are similar. In contrast, modes 2 and 3 show fundamentally different motion from any of the modes in γ-coronene. An angle θ of 61.7° and 51.8°, respectively, produces a change in polarization large enough to be observed experimentally, and indicates a mix of rotational and librational motion.

Modes 4–6 have rotational axes close to perpendicular to the normal axes, i.e., they have librational character, but they do not couple together like in γ-coronene, with all the rotational axes in different directions. With respect to the molecule, mode 4 has similar orientation and rotation directions to the corresponding mode 4 in γ-coronene, whereas mode 5 has no obvious pair and mode 6 is similar to mode 5 in γ-coronene. All three of these modes give measurable intensities and none dominates over the others. Hence five modes (2–6) in the four peaks C–F, where peak E is deconvoluted into two peaks by fitting, are observed in our experimental spectra.

IV. CONCLUSION

The lattice vibrations of γ- and β-coronene have been investigated using low-frequency Raman measurements and the remarkable differences, given the similarity of the two polymorphs, rationalized with reference to the atomic motions predicted by DFT-D3 calculations. For γ- (β-) coronene, the calculations yield optimized structures with lattice parameters within 1.6% (2.1%) and an intracell angle within 0.7% (0.4%) of x-ray structures collected at 290 K (150 K) on single crystals. For both structures, the calculations predict six Raman-active phonon modes below 150 cm^{-1}, but taking into account differences in intensities and allowing for experimental resolution and a low wave number cutoff of 30 cm^{-1}, these are consistent with the two (four) peaks observed in Raman spectra taken from γ- (β-) coronene crystals, respectively, and which reflect contributions from three (five) modes with measured and calculated frequencies differing at most by 4 cm^{-1}.

The Raman spectra are consistent with the atomic motion predicted by the calculations. In γ-coronene, the modes are considered to be coupled into three pairs, with the lowest-frequency pair consistent with rotational motion giving rise to small intensities, and the remaining two pairs showing librational motion. In each pair, the axes of rotation were similar but with a reversal of direction of one molecule. In β-coronene, the lowest-frequency mode was found to be mostly rotational in character, and the three highest-frequency Raman-active phonon modes were mainly librational. The remaining two modes exhibit a mixture of rotational and librational behavior, with an angle between the rotational axis and molecular normal of ∼50°–60°. The excellent agreement between theory and experiment presented here justifies the study of lattice vibrations throughout the Brillouin zone using DFT-D3, a necessary step toward the understanding of phase stability and the phase transition. Both aspects will be reported on elsewhere.

ACKNOWLEDGMENTS

We are grateful to Wendy Lambson for technical support. J.S. is grateful to the University of Manchester for the award of a Presidential Fellowship. N.B. acknowledges funding and support from the Engineering and Physical Sciences Research Council (EPSRC) Centre for Doctoral Training in Condensed Matter Physics (CDT-CMP), Grant No. EP/L015544/1. This research made use of the Balena High Performance Computing (HPC) Service at the University of Bath. X-ray diffraction facilties were provided through the Chemical Characterisation and Analysis Facility (CCAF) at the University of Bath.

[1] M. Schwoerer and H. C. Wolf, *Organic Molecular Solids* (Wiley, Weinheim, Germany, 2007).

[2] T. F. Harrelson, V. Dantanarayana, X. Xie, C. Koshnick, D. Nai, R. Fair, S. A. Nuñez, A. K. Thomas, T. L. Murrey, M. A. Hickner, J. K. Grey, J. E. Anthony, E. F. Gomez, A. Troisi, R. Faller, and A. J. Moulé, Mater. Horizons **6**, 182 (2019).

[3] S. Fratini, S. Ciuchi, D. Mayou, G. T. de Laissardière, and A. Troisi, Nat. Mater. **16**, 998 (2017).

[4] A. Y. Sosorev, D. Maslennikov, I. Y. Chernyshov, D. Dominskiy, V. Bruevich, M. Vener, and D. Y. Paraschuk, Phys. Chem. Chem. Phys. **20**, 18912 (2018).

[5] M. Ando, M. Yoneya, T. B. Kehoe, H. Ishii, T. Minakata, M. Kawasaki, C. M. Duffy, R. Phillips, and H. Sirringhaus, Phys. Rev. Mater. **3**, 025601 (2019).

[6] L. Cigarini, A. Ruini, A. Catellani, and A. Calzolari, J. Phys. D **50**, 395502 (2017).

[7] R. G. Della Valle, E. Venuti, and A. Brillante, Chem. Phys. **202**, 231 (1996).

[8] A. Brillante, I. Bilotti, R. G. Della Valle, E. Venuti, and A. Girlando, CrystEngComm **10**, 937 (2008).

[9] L. Kronik and A. Tkatchenko, Acc. Chem. Res. **47**, 3208 (2014).

[10] S. Califano, V. Schettino, and N. Neto, *Lattice Dynamics of Molecular Crystals* (Springer, Berlin, Heidelberg, 1981).
[11] S. Hirata, K. Gilliard, X. He, J. Li, and O. Sode, Acc. Chem. Res. **47**, 2721 (2014).
[12] M. Anderson, C. Ramanan, C. Fontanesi, A. Frick, S. Surana, D. Cheyns, M. Furno, T. Keller, S. Allard, U. Scherf, D. Beljonne, G. D'Avino, E. von Hauff, and E. Da Como, Phys. Rev. Mater. **1**, 055604 (2017).
[13] A. Girlando, L. Grisanti, M. Masino, I. Bilotti, A. Brillante, R. G. Della Valle, and E. Venuti, Phys. Rev. B **82**, 035208 (2010).
[14] J.-U. Lee, K. Kim, S. Han, G. H. Ryu, Z. Lee, and H. Cheong, ACS nano **10**, 1948 (2016).
[15] G. Froehlicher, E. Lorchat, F. Fernique, C. Joshi, A. Molina-Sánchez, L. Wirtz, and S. Berciaud, Nano Lett. **15**, 6481 (2015).
[16] D. L. Duong, G. Ryu, A. Hoyer, C. Lin, M. Burghard, and K. Kern, ACS Nano **11**, 1034 (2017).
[17] Y. Zhao and D. G. Truhlar, J. Phys. Chem. C **112**, 4061 (2008).
[18] H. Ruuska and T. A. Pakkanen, J. Phys. Chem. B **105**, 9541 (2001).
[19] S. Blumstengel, S. Sadofev, and F. Henneberger, New J. Phys. **10**, 065010 (2008).
[20] S. R. Langhoff, J. Phys. Chem. **100**, 2819 (1996).
[21] Y. Kubozono, H. Mitamura, X. Lee, X. He, Y. Yamanari, Y. Takahashi, Y. Suzuki, Y. Kaji, R. Eguchi, K. Akaike, T. Kambe, H. Okamoto, A. Fujiwara, T. Kato, T. Kosugi, and H. Aogi, Phys. Chem. Chem. Phys. **13**, 16476 (2011).
[22] K. Ohno, T. Kajiwara, and H. Inokuchi, Bull. Chem. Soc. Jpn. **45**, 996 (1972).
[23] T. Yamamoto, S. Nakatani, T. Nakamura, K.-i. Mizuno, A. H. Matsui, Y. Akahama, and H. Kawamura, Chem. Phys. **184**, 247 (1994).
[24] S. Nakatani, T. Nakamura, K. Mizuno, and A. Matsui, J. Lumin. **58**, 343 (1994).
[25] A. M. Orendt, J. C. Facelli, S. Bai, A. Rai, M. Gossett, L. T. Scott, J. Boerio-Goates, R. J. Pugmire, and D. M. Grant, J. Phys. Chem. A **104**, 149 (2000).
[26] J. Potticary, L. R. Terry, C. Bell, A. N. Papanikolopoulos, P. C. Christianen, H. Engelkamp, A. M. Collins, C. Fontanesi, G. Kociok-Köhn, S. Crampin, E. Da Como, and S. R. Hall, Nat. Commun. **7**, 11555 (2016).
[27] X.-M. Zhao, J. Zhang, A. Berlie, Z.-X. Qin, Q.-W. Huang, S. Jiang, J.-B. Zhang, L.-Y. Tang, J. Liu, C. Zhang, G.-H. Zhong, H.-Q. Lin, and C. Xiao-Jia, J. Chem. Phys. **139**, 144308 (2013).
[28] T. Salzillo, A. Giunchi, M. Masino, N. Bedoya-Martínez, R. G. Della Valle, A. Brillante, A. Girlando, and E. Venuti, Cryst. Growth Des. **18**, 4869 (2018).
[29] G. Kresse and J. Hafner, Phys. Rev. B **47**, 558 (1993).
[30] J. P. Perdew, K. Burke, and M. Ernzerhof, Phys. Rev. Lett. **77**, 3865 (1996).
[31] P. E. Blöchl, Phys. Rev. B **50**, 17953 (1994).
[32] G. Kresse and D. Joubert, Phys. Rev. B **59**, 1758 (1999).
[33] S. Grimme, Wiley Interdiscip. Rev. Comput. Mol. Sci. **1**, 211 (2011).
[34] S. Grimme, J. Antony, S. Ehrlich, and H. Krieg, J. Chem. Phys. **132**, 154104 (2010).
[35] A. Togo, F. Oba, and I. Tanaka, Phys. Rev. B **78**, 134106 (2008).
[36] A. Togo and I. Tanaka, Scr. Mater. **108**, 1 (2015).
[37] A. Fonari and S. Stauffer, vasp_raman.py, https://github.com/raman-sc/VASP.
[38] J. M. Skelton, L. A. Burton, A. J. Jackson, F. Oba, S. C. Parker, and A. Walsh, Phys. Chem. Chem. Phys. **19**, 12452 (2017).
[39] J. Skelton, Phonopy-Spectroscopy, https://github.com/JMSkelton/Phonopy-Spectroscopy.
[40] J. Henderson, M. Masino, L. E. Hatcher, G. Kociok-Köhn, T. Salzillo, A. Brillante, P. R. Raithby, A. Girlando, and E. Da Como, Cryst. Growth Des. **18**, 2003 (2018).
[41] C. D. Cruz, H. H. Choi, V. Podzorov, E. L. Chronister, and C. J. Bardeen, J. Phys. Chem. C **122**, 17632 (2018).
[42] G. M. Sheldrick, Acta Crystallogr. C **71**, 3 (2015).
[43] C. B. Hübschle, G. M. Sheldrick, and B. Dittrich, J. Appl. Crystallogr. **44**, 1281 (2011).
[44] R. Wells, J. Quant. Spectrosc. Radiat. Transf. **62**, 29 (1999).
[45] S. M. Abrarov and B. M. Quine, Appl. Math. Comput. **218**, 1894 (2011).
[46] W. Gautschi, SIAM J. Numer. Anal. **7**, 187 (1970).
[47] R. J. Meier, Vib. Spectrosc. **39**, 266 (2005).
[48] O. Kataeva, M. Khrizanforov, Y. Budnikova, D. Islamov, T. Burganov, A. Vandyukov, K. Lyssenko, B. Mahns, M. Nohr, S. Hampel, and M. Knupfer, Cryst. Growth Des. **16**, 331 (2015).
[49] J. Potticary, R. Boston, L. Vella-Zarb, A. Few, C. Bell, and S. R. Hall, Sci. Rep. **6**, 38696 (2016).
[50] See Supplemental Material at http://link.aps.org/supplemental/10.1103/PhysRevMaterials.3.125601 for full list of calculated phonon modes, additional Raman measurements with temperature dependence and with polarizer in detection rotated by 90°, and crystal face indexing.

Supplementary Information for Lattice Vibrations of γ- and β-coronene from Raman and Theory

Nicola Bannister,[1] Jonathan Skelton,[2] Gabriele Kociok-Köhn,[3]
Tim Batten,[4] Enrico Da Como,[1] and Simon Crampin[1]

[1]*Department of Physics, University of Bath, Claverton Down, BA2 7AY Bath, UK*

[2]*School of Chemistry, University of Manchester, Manchester, M13 9PL, UK*

[3]*Department of Chemistry and Material and Chemical Characterisation Facility (MC^2), University of Bath, Claverton Down, BA2 7AY Bath, UK*

[4]*Renishaw plc, Wotton-under-Edge, Gloucestershire, GL12 7DW, UK*

(Dated: October 31, 2019)

I. PHONON MODES CALCULATED USING DFT-D3

TABLE I. Twelve lowest frequency modes calculated for γ- and β-coronene by DFT-D3, corresponding to the lattice vibrations. In the main text only modes which are Raman active are considered.

γ-coronene				**β-coronene**			
Mode ID	Frequency (cm^{-1})	Symmetry	Activity	Mode ID	Frequency (cm^{-1})	Symmetry	Activity
1	-0.37	-	-	1	-0.62	-	-
2	-0.30	-	-	2	-0.29	-	-
3	0.00	-	-	3	0.00	-	-
4	34.13	B_g	Raman	4	17.73	B_g	Raman
5	34.53	A_u	IR	5	39.28	A_u	IR
6	42.15	A_g	Raman	6	40.10	A_g	Raman
7	46.69	B_u	IR	7	41.37	B_u	IR
8	56.41	A_u	IR	8	52.34	A_g	Raman
9	63.09	A_g	Raman	9	58.05	A_u	IR
10	65.60	B_g	Raman	10	77.84	B_g	Raman
11	86.85	B_g	Raman	11	80.97	A_g	Raman
12	92.85	A_g	Raman	12	93.77	B_g	Raman

II. ADDITIONAL TEMPERATURE DEPENDENT RAMAN MEASUREMENTS AND ASSOCIATED CRYSTAL IMAGES

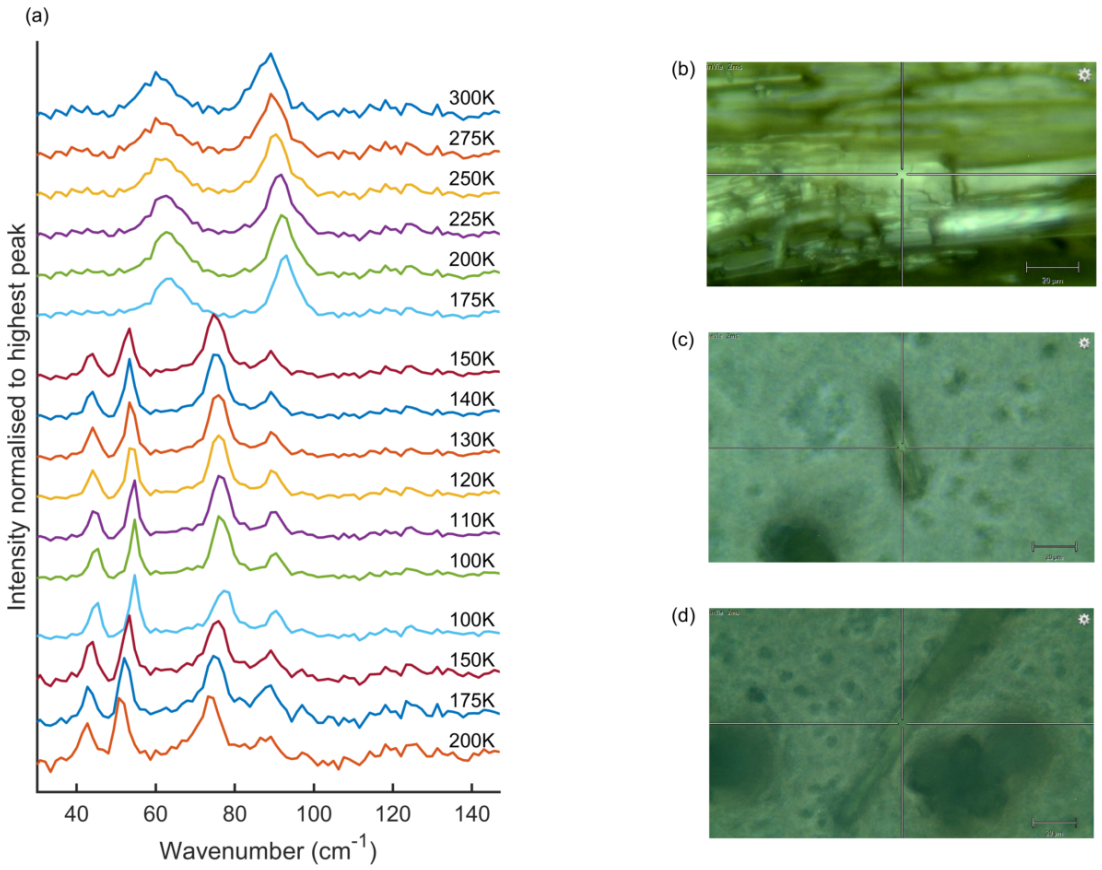

FIG. 1. (a) Raman spectra collected from a single γ-coronene crystal during a temperature sweep from 300 K to 100 K and returning to 200 K. The crystal was observed to shatter at 163 K, corresponding to the striking change in spectral shape. The new spectral shape continues to exist on heating to at least 200 K. Background envelopes have been removed and intensities normalised to the highest peak in each spectra. Images of the crystals are shown in (b) 300 K to 175 K (c) 150 K to 100 K and (d) 100 K to 200 K regimes.

III. FACE INDEXING

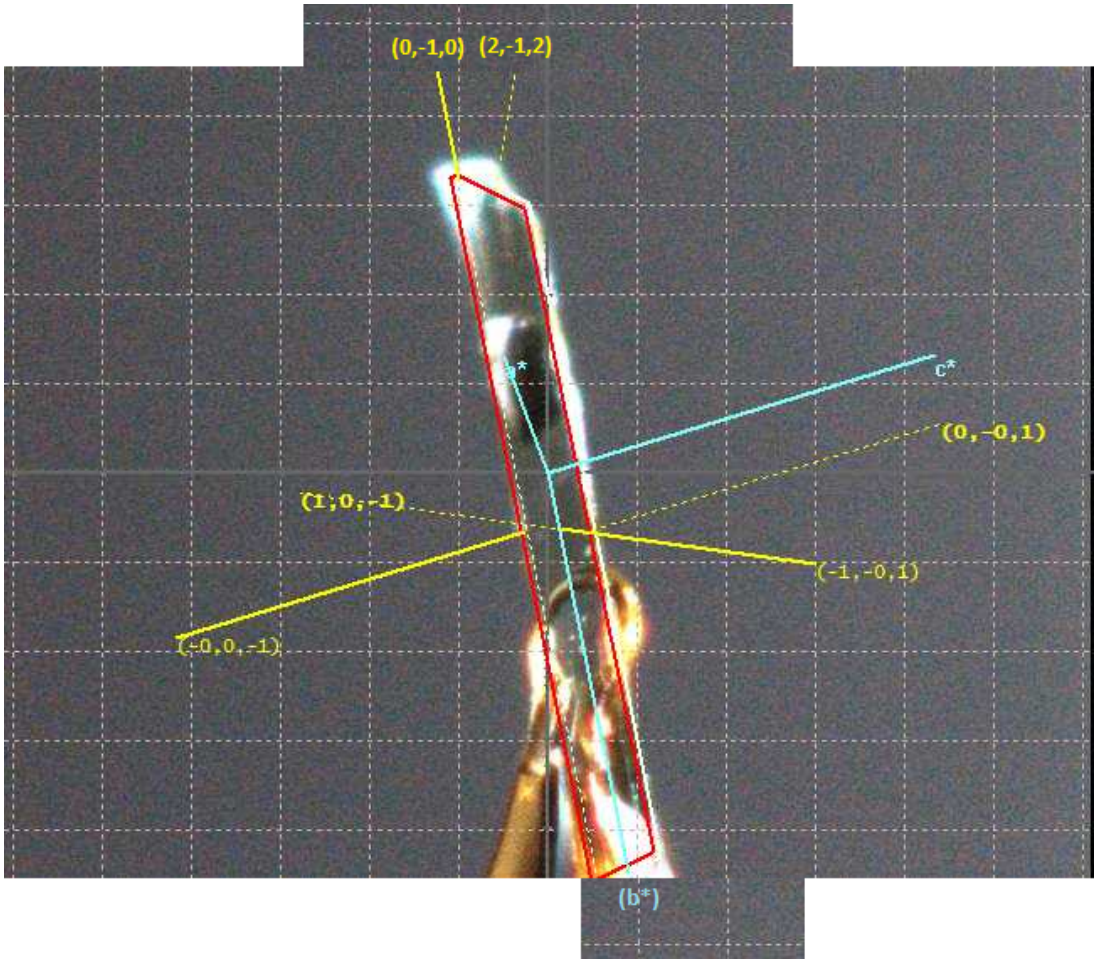

FIG. 2. Face indexing of the γ-coronene crystal used for room temperature polarised Raman experiments. The crystal was orientated as in this diagram with the [0 $\bar{1}$ 0] direction aligned to the experimental vertical at 0°.

IV. POLARISED RAMAN: SECOND OUTPUT POLARISATION

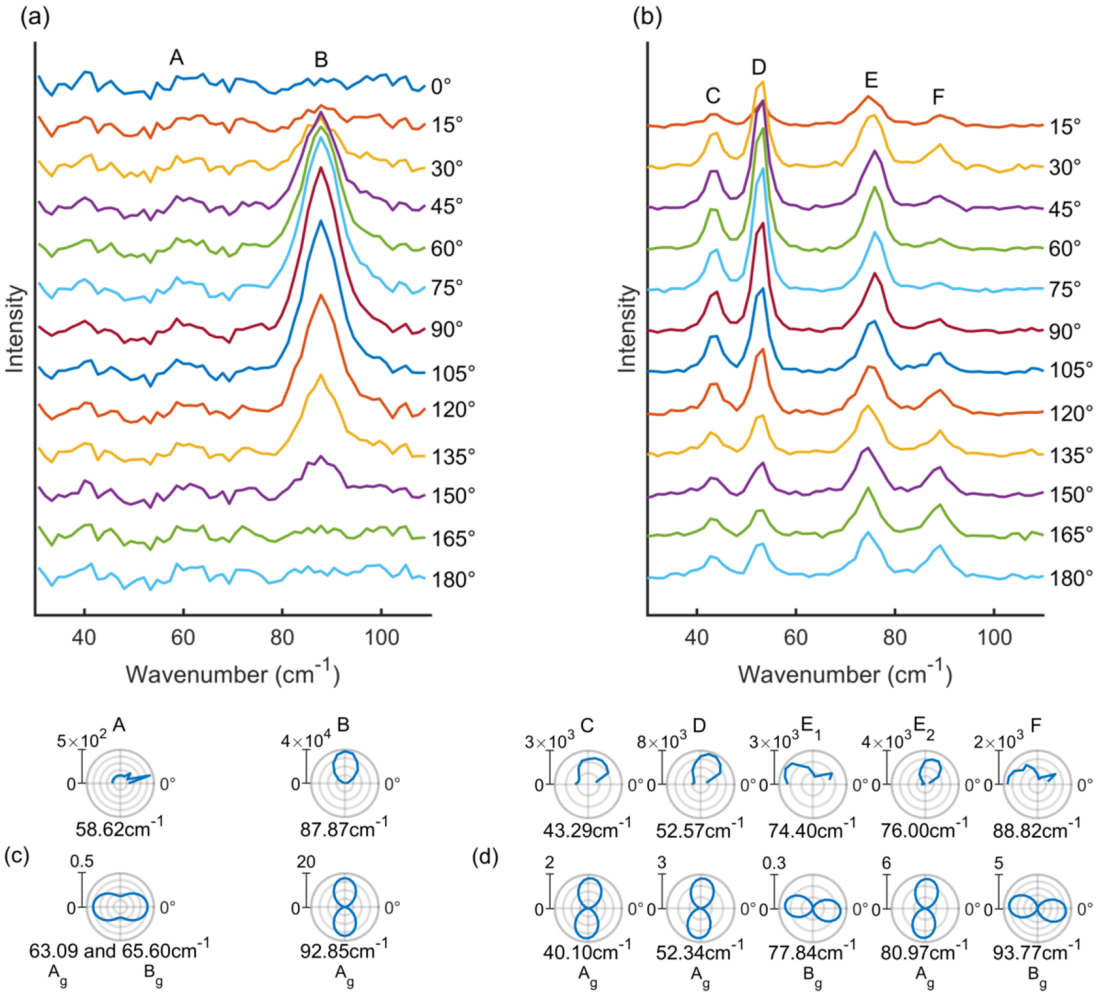

FIG. 3. Polarisation angle dependence of Raman spectra for (a) γ- and (b) β-coronene with the output polarisation rotated by 90° with respect to the set up used for figure 4 in the main text. Individual spectra are offset for clarity. The peak intensity as a function of polarisation angle for (c) γ- and (d) β-coronene. The top rows show profiles extracted by fitting the experimental spectra, while the bottom rows show the profiles predicted from our calculations. The 0° measurements for β-coronene have been excluded due to anomalies arising from local heating by the laser.

5.3 Summary

The work presented in section 5.2 completes the study of the vibrational modes of crystalline coronene. Two peaks have been observed in Raman spectra recorded from a single crystal of γ-coronene between 300 K and 175 K, which increase in frequency as the temperature decreases. At 175 K their positions are 63.5 cm^{-1} and 92.8 cm^{-1}. At 163 K the γ-coronene crystal shattered indicating a phase transition to β-coronene. Below this temperature four peaks have been observed. One peak with a clear asymmetric profile has been decomposed into two peaks during fitting. At 100 K the peaks lie at 44.8 cm^{-1}, 54.6 cm^{-1}, 76.6 cm^{-1}, 77.5 cm^{-1} and 90.3 cm^{-1}. These observed peak positions are consistent with those reported in Refs. [32, 177] to within 7 cm^{-1} (3 cm^{-1}) for γ-coronene at 175 K (300 K) and within 3 cm^{-1} for β-coronene at 100 K. On re-heating the four peaks of β-coronene have been observed to persist to at least 200 K, consistent with the hysteresis Salzillo *et al.* previously reported [177].

Twelve zone-centre phonon modes have been calculated for both γ- and β-coronene using DFT-D3, of which six are IR active and six Raman active. In γ-coronene the first experimental peak has contributions from two modes at 63.09 cm^{-1} and 65.60 cm^{-1} with the second peak assigned to one mode at 92.85 cm^{-1}. In β-coronene the corresponding five calculated Raman active modes are 40.10 cm^{-1}, 52.34 cm^{-1}, 77.84 cm^{-1}, 80.97 cm^{-1} and 93.77 cm^{-1}. The remaining three (one) Raman active modes for γ- (β-) coronene have low predicted intensities, which is consistent with them not being observed experimentally. Experimental polarised Raman spectra have been fitted with Voigt profiles and the resulting intensity polar plots show figure of eight behaviour, which is reproduced well by the DFT-D3 calculations, confirming the mode assignment.

The atomic motion of these Raman active phonon modes has also been studied. The Raman active modes involve rocking-rotation of the molecules whilst the IR active modes all involve translational motions of the molecules. In γ-coronene the first two Raman active modes are rotations (rocking-rotation around the normal to the molecular plane) and the remaining four are librations (rocking-rotation around an axis in the molecular plane). This is in stark contrast to the motions associated with the Raman-active phonon modes in β-coronene. There the first Raman active mode is a rotation, the final three are librations, but the remaining two exhibit mixed roto-librational behaviour with the rotational axis at 50-60° to the normal of molecular plane.

This work demonstrates that DFT-D is a powerful tool for interpreting Raman spectra, having the accuracy necessary to enable polymorph identification, and also enabling insights into the origin of the spectral differences between polymorphs. Our

DFT-D3 calculations predict phonon frequencies to within 4 cm^{-1} of experimentally observed values, and successfully describe the polarisation dependence of Raman spectra. This provides strong evidence that the theory describes the van der Waals forces well, and encourages the use of DFT-D3 for investigations into the phase stabilities of γ- and β-coronene.

Chapter 6

Phase stability

Here the phase stabilities of γ- and β-coronene are investigated, initially in the harmonic approximation by studying the Helmholtz free energy, F^{HA}, and later by applying the quasi-harmonic approximation and determining the Gibbs free energy, G^{QHA}. The predicted thermal expansion is compared to our previous DFT-D3 structures and experimental volumes presented in Chapter 4, giving an insight into how well the quasi-harmonic approximation performs for these two coronene polymorphs.

6.1 Literature review

The Helmholtz free energy in the harmonic approximation can give some useful insights into phase stabilities and the importance of vibrations to energetics. A large study of 418 polymorph pairs of organic molecules showed that at 300 K vibrational contributions led to a predicted phase transition in 9% of polymorph pairs [17]. The harmonic Helmholtz free energy has also been used to correctly predict the ordering of phase stabilities in specific systems such as the normal pressure polymorphs of piracetam, a drug for disorders of the nervous system. However, it is worth noting that the calculated phase transition temperatures were inaccurate [178]. The main problem in the harmonic approximation is the exclusion of thermal expansion which leads to temperature independent elastic constants and bulk moduli, constant-volume and constant-pressure specific heat capacities that are equivalent, and thermal conductivities and phonon lifetimes which are infinite. Neglecting thermal expansion is clearly a significant approximation.

Thermal expansion alters the lattice energy and arises as a result of the anharmonicity of vibrations. This is important in modelling thermochemistry, mechanical properties,

spectroscopy [141, 179] and even powder XRD [180]. Ideally the effects of temperature (and pressure) would be captured using molecular dynamics, for example by path integral simulations [179, 181]. Unfortunately these approaches are very computationally demanding and still have drawbacks [142]. A simpler option is to combine static electronic structure calculations, such as DFT, with a statistical-thermodynamic model. The quasi-harmonic approximation is one such model that is well established, having long been used in force field studies [140]. More recently it has been employed alongside DFT in metallic systems, semiconductors [127], metallic oxides [138] and lately in molecular crystals [127, 142, 180, 182–184].

In the quasi-harmonic approximation, vibrational frequencies and hence Helmholtz free energies are calculated in the harmonic approximation for a set of expanded and contracted unit cells. Next an equation of state is fitted to the Helmholtz free energy as a function of unit cell volume for a set of temperatures and the minima of each curve determined. This gives the temperature dependence of the Helmholtz free energy and unit cell volume, which allows the Gibbs free energy to be calculated. Further details are given in Chapter 2.3.3.

The quasi-harmonic approximation has been compared to higher level molecular dynamic models in a variety of studies and frequently only small differences observed [179]. For example in a study of three phases of ice, remarkable agreement was observed in predictions using the quasi-harmonic approximation and path integral molecular dynamics simulations, with the quasi-harmonic approximation correctly reproducing thermal expansion up to 100 K [181]. Experimental results have also been successfully reproduced with temperature trends and thermal expansion satisfactorily captured for 22 molecular crystals ranging from unit cells containing single atoms to small molecules [127]. Quantitative results such as the constant pressure specific heat capacities had excellent agreement with experiments in some cases, but in others differed by up to 50%. In other studies on molecular crystals [142, 180, 182, 183], trends in experimental results are again successfully reproduced, and in some cases quantitative agreement is reached. These studies demonstrate that the quasi-harmonic approximation in combination with DFT-D methods is capable of reproducing experimental observations qualitatively, but that at present quantitative predictions are fortuitous. Nevertheless applying the quasi-harmonic approximation may provide insights into the role thermal expansion plays in the phase stabilities of γ- and β-coronene.

Here the phase stabilities of γ- and β-coronene are calculated and studied using DFT-D3 in the harmonic approximation. Next the quasi-harmonic approximation is

applied and the phase stabilities again studied. Finally the thermal expansion in the quasi-harmonic approximation is examined.

6.2 Methods

To calculate the Helmholtz free energy within the harmonic approximation, first the vibrational frequency calculations were extended across the Brillouin zone. Phonopy [47, 169] was used to produce $2 \times 4 \times 1$ supercells of the γ- and β-coronene structures from Chapter 4. The supercell size was increased in each dimension until no imaginary frequencies were observed in the vibrational dispersion curves and density of states. The supercell of γ-coronene had a minimum length of 15.4 Å and β-coronene a minimum length of 15.6 Å, easily fulfilling the criteria of exceeding 10 Å in each direction that others have found necessary [127, 136]. Vibrational frequencies in the harmonic approximation of the supercells were calculated using Phonopy with a finite displacement of 0.015 Å and VASP [72] acting as the force calculator. For the $2 \times 3 \times 1$ k-point structure, in the supercell calculations the k-points were decreased to $1 \times 1 \times 1$ to give a similar k-point spacing as the single cell calculations. For the $3 \times 4 \times 2$ k-point structure, in the supercell calculations the k-points were decreased to $2 \times 1 \times 2$. The vibrational density of states, dispersion curves and Helmholtz free energies were calculated using Phonopy with a Γ-centred q-point mesh of $8 \times 16 \times 4$. The density of states was calculated on a set of discrete frequencies with a sampling of 0.01 THz (=0.33 cm^{-1}). The mesh size and frequency sampling were determined by convergence testing. This mesh size is also consistent with the criteria Hoja *et al.* found necessary for converging vibrational free energies, namely that the number of q-points, n, necessary in each direction is governed by $n \times a \geq 50$ Å where a is the unit cell length [136].

The number of k-points used in the structural relaxation was tested for convergence, table 6.1. Increasing the k-points for the structure relaxation from $2 \times 3 \times 1$ to $3 \times 4 \times 2$ gave a decrease (increase) in lattice energy of 3.10 meV/unit cell (1.63 meV/unit cell) and a decrease in zero-point energy of 0.02 meV/unit cell (0.78 meV/unit cell) for γ-(β-) coronene. This indicates that the majority of the uncertainty in the Helmholtz free energy is from the lattice energy contribution, and that the uncertainty in the Helmholtz free energy will have the same order of magnitude. Thus it is important to adequately converge the lattice energy. Increasing the structural k-points to $6 \times 8 \times 4$ gave an increase of 0.26 meV/unit cell and 0.03 meV/unit cell in lattice energy for γ- and β-coronene respectively. It was not possible to perform supercell calculations on the $6 \times 8 \times 4$ structure due to the large time requirement and limits on computational

Table 6.1: Convergence of the lattice energy, U_{latt}, zero-point energy and harmonic Helmholtz free energy, F^{HA}, at 0 K of γ- and β-coronene based on the number of k-points used in the structural relaxation. The values given in brackets indicate the change in value from the smaller k-point structure in the line above. Units are in meV per unit cell.

	k-points	U_{latt} (meV)	Zero-point energy (meV)	F^{HA}(0 K) (meV)
γ-coronene	$2 \times 3 \times 1$	-529146.25	14922.25	-514223.99
	$3 \times 4 \times 2$	-529143.14 (-3.10)	14922.27 (-0.02)	-514220.88 (-3.12)
	$6 \times 8 \times 4$	-529143.41 (+0.26)	-	-
β-coronene	$2 \times 3 \times 1$	-529155.82	14941.51	-514214.31
	$3 \times 4 \times 2$	-529157.45 (+1.63)	14942.28 (-0.78)	-514215.16 (+0.85)
	$6 \times 8 \times 4$	-529157.48 (+0.03)	-	-
γ-β	$2 \times 3 \times 1$	9.57	-19.25	-9.68
	$3 \times 4 \times 2$	14.30 (+4.73)	-20.02 (-0.76)	-5.71 (+3.97)
	$6 \times 8 \times 4$	14.07 (-0.23)	-	-

resource. Nevertheless we find that the $3 \times 4 \times 2$ k-point structure is converged to less than 1 meV/unit cell in lattice energy (and thus F^{HA}) whilst the $2 \times 3 \times 1$ k-point structure is converged an order of magnitude higher.

It is also important to consider the convergence of energy differences between polymorphs, table 6.1. This is not straightforward due to the differing size and shapes of the unit cells. Nevertheless there may be some cancellation of errors that reduces the overall error in relative energy differences. Here increasing the structural k-points from $2 \times 3 \times 1$ to $3 \times 4 \times 2$ decreases the lattice energy in γ-coronene and increases it in β-coronene, leading to a change in the difference in lattice energy of 4.73 meV/unit cell (33%), a larger change than for each polymorph individually. This highlights the need to converge energy differences alongside the energies of each polymorph individually. Further increasing the structural k-points to $6 \times 8 \times 4$ gives a change in the difference in lattice energies of -0.23 meV/unit cell (2%), suggesting that the $3 \times 4 \times 2$ k-point structure is now sufficiently converged with regards to lattice energy differences. Increasing the structural k-points from $2 \times 3 \times 1$ to $3 \times 4 \times 2$ gives a change in the difference of zero-point energies of -0.76 meV/unit cell (4%). Unfortunately since it was not possible to calculate the zero-point energy at the $6 \times 8 \times 4$ k-point level, there is some doubt as to whether the $3 \times 4 \times 2$ k-point structure has truly reached a converged value. Nevertheless, this is the highest level of accuracy available and was used in all following calculations. For ease of comparison, the $3 \times 4 \times 2$ k-point structure has energy

differences, $\Delta U_{\text{latt},\gamma-\beta}$ = 14.30 meV/unit cell = 0.69 kJ/mol of molecules, $\Delta\text{ZPE}_{\gamma-\beta}$ = -20.02 meV/unit cell = -0.97 kJ/mol of molecules, giving $\Delta F^{\text{HA}}_{\gamma-\beta}$ = -5.71 meV/unit cell = -0.28 kJ/mol of molecules. We note that differences in polymorphism, energy differences are typically less than 2 kJ/mol [17], and that these calculations are consistent with this.

To calculate the Gibbs free energy in the quasi-harmonic approximation, first the quasi-anisotropic approach to thermal expansion was used: volumes of the $3 \times 4 \times 2$ k-point structures of both polymorphs were isotropically scaled by -5.0%, -2.5%, 0.0%, +2.5% and +5.0%, and the structures relaxed with the unit cell volume fixed. Following the same procedure outlined above, $2 \times 4 \times 1$ supercells were constructed for each expanded and contracted volume, and F^{HA} calculated. Phonopy was used to fit the Murnaghan equation of state to F^{HA} as a function of volume at 1 K intervals. This allowed the temperature dependence of the unit cell volume to be determined along with the quasi-harmonic Helmholtz free energy. The quasi-harmonic Gibbs free energy was then calculated as in equation (2.12) by including the $pV(T)$ term. The Vinet and Birch-Murnaghan equations of state were also tested and made no appreciable differences in the Gibbs free energy or thermal expansion of either polymorph. The temperature interval was also tested and a decrease to 0.5 K made no appreciable difference to the results.

Figure 6-1 shows the Helmholtz free energy as a function of volume for temperatures between 0 K and 300 K in 10 K steps for γ-coronene. The Murnaghan equation of state fit to these curves is shown along with the minima. These fits give an indication where the quasi-harmonic approximation is likely to be valid, i.e. where the minimum is within the interpolated region. For γ-coronene we consider 247 K to be the maximum temperature for which the results are valid and for β this is 228 K, although the extrapolated values at higher temperatures may give reasonable results since the validity range is very system dependent [185].

6.3 Results and analysis

DFT-D3 calculations do not differentiate between intramolecular and phonon modes. It is therefore possible for modes to exist that contain contributions of both types as has been observed in other molecular crystals, such as anthracene, a PAH formed of three joined benzene rings [186]. It is likely that this mixing also occurs in γ- and β-coronene, and a full analysis of the atomic motion, such as that presented in Ref. [186], is required to quantify this. Here the labels “intramolecular” and “phonon” continue to be used,

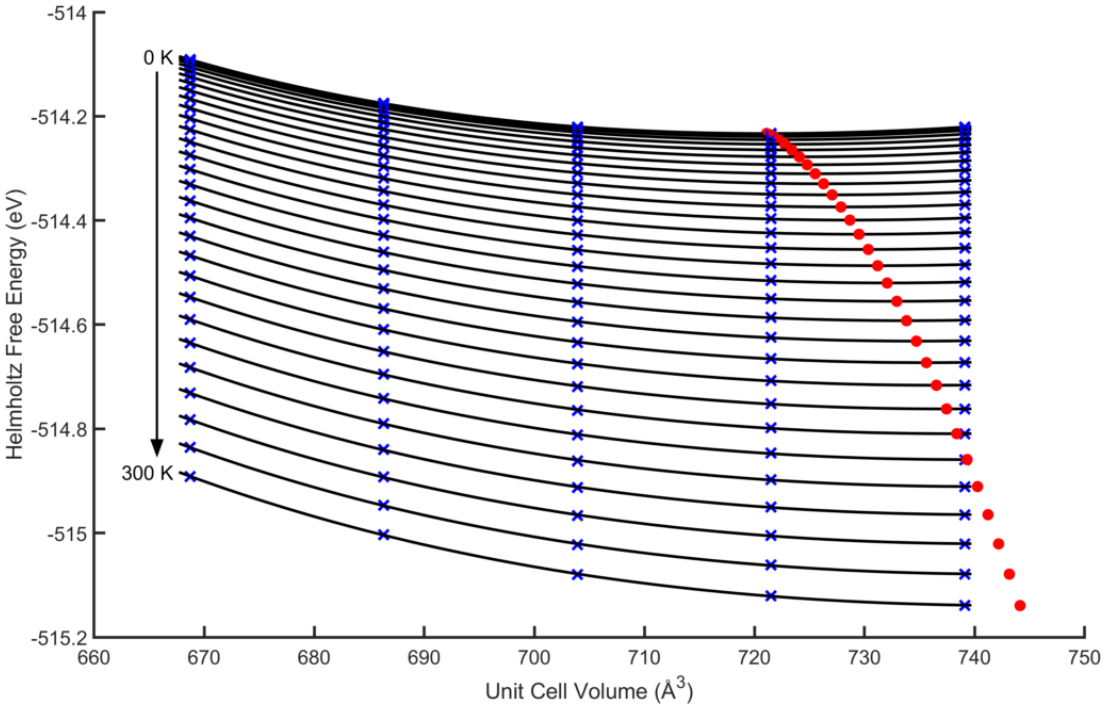

Figure 6-1: The calculated volume dependent harmonic Helmholtz free energies of γ-coronene unit cells at 10 K temperature steps between 0 K and 300 K (blue crosses), fitted with the Murnaghan equation of state (solid black line). The minimum volume for each temperature curve is shown (red circles). Above 250 K the minimum falls outside the volume range of the computed points.

referring to the predominant vibration type and maintaining consistency with the modes presented in Chapters 4 (intramolecular) and 5 (phonon).

The calculated vibrational dispersion curves and densities of states in the phonon range for γ- and β-coronene are shown in figure 6-2. The dispersion curve is plotted along a path through the high symmetry points in the Brillouin zone, illustrated in figure 6-3, consistent with the path along which the band structure is presented in Ref. [8]. In γ-coronene there is a separation between phonon and intramolecular modes at 101 cm^{-1}, whilst in β-coronene the phonon and intramolecular modes overlap in frequency across the Brillouin zone, suggesting there may be a greater degree of mixing of intramolecular and phonon mode character in β-coronene. There is no experimental data to compare these dispersion curves to, as neutron scattering experiments are not possible due to the small crystal sizes of both polymorphs. The γ-coronene crystals grown in this work were typically a few millimetrers in length, as seen in figure 3-3 (c), and $100 - 500$ µm in width (figures 4-2 (a) and 4-3 (a)), whilst β-coronene crystal fragments were ~ 100 µm in length and up to ~ 20 µm in width (figures 4-2 (b) and 4-3 (b)).

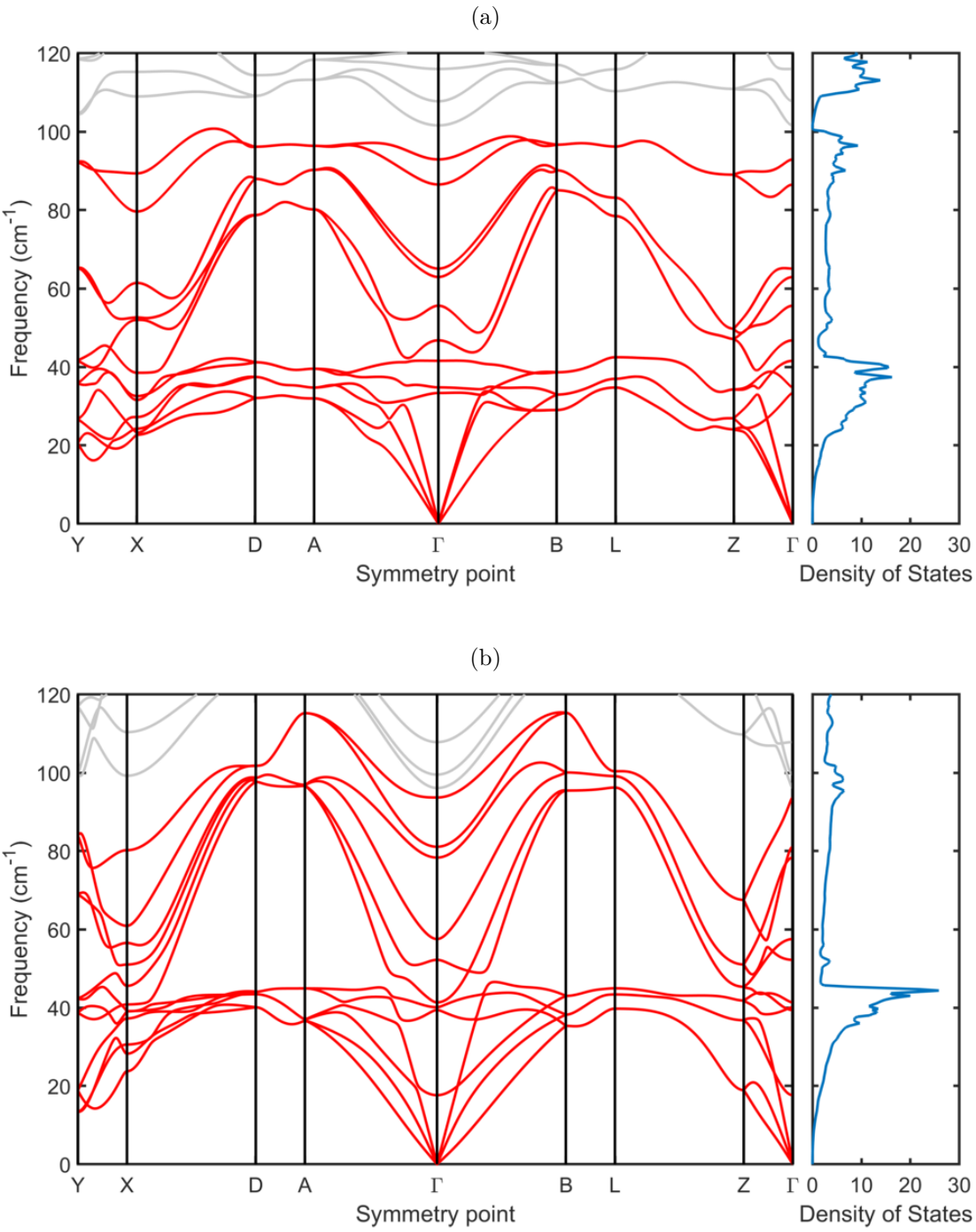

Figure 6-2: Vibrational dispersion curves and density of states (number of states/(unit cell × cm^{-1})) up to 120 cm^{-1} for (a) γ- and (b) β-coronene. Left panels - Dispersion curves of the phonon modes (red) from Chapter 5 and intramolecular modes (grey) from Chapter 4 through the high symmetry points. Right panels - Vibrational density of states.

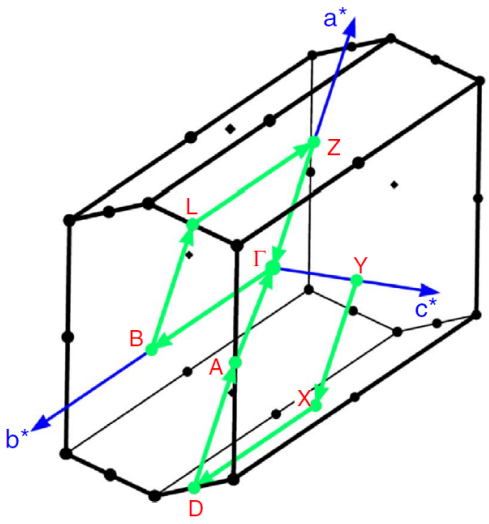

Figure 6-3: Depiction of the first Brillouin zone with reciprocal lattice vectors and a path through the high symmetry points shown. Reproduced from Ref. [8].

Figure 6-4 shows the vibrational dispersion curves for both polymorphs across the entire frequency range. The intramolecular modes exhibit significantly less dispersion than the phonon modes, with the amount of dispersion decreasing with increasing frequency. This little to no dispersion is typical of intramolecular modes [22]. Again the amount of dispersion in the β-coronene modes is greater than in γ-coronene.

The vibrational density of states are compared in figure 6-5. The density of states is zero in both polymorphs between 1700 and 3000 cm^{-1} (not shown), separating the intramolecular modes involving carbon (and hydrogen) motions and those involving only hydrogen motion. The intramolecular density of states displays groups of sharp peaks, the sharpness depending on the amount of dispersion of these modes, shown in figure 6-4. There are clear differences in the intramolecular density of states of the two polymorphs, with the density of states in β-coronene shifted to higher frequencies than γ-coronene and also typically broader and lower due to the increased dispersion. This is also true in the phonon density of states, where below 50 cm^{-1} the density of states rises at a lower frequency in γ-coronene than β-coronene and then drops sharply at around 42 cm^{-1} in γ-coronene, whilst the drop in β-coronene is sharper at 45 cm^{-1}.

To understand the importance of the phonon and intramolecular modes in relation to their phase stabilities, the zero-point energy defined in equation (2.11) was calculated in three frequency ranges, displayed in table 6.2. The lowest range from 0 to 167 cm^{-1} includes all the phonon modes and six intramolecular modes. The cut was made at 167 cm^{-1} as this was the first point at which the density of states for both γ- and

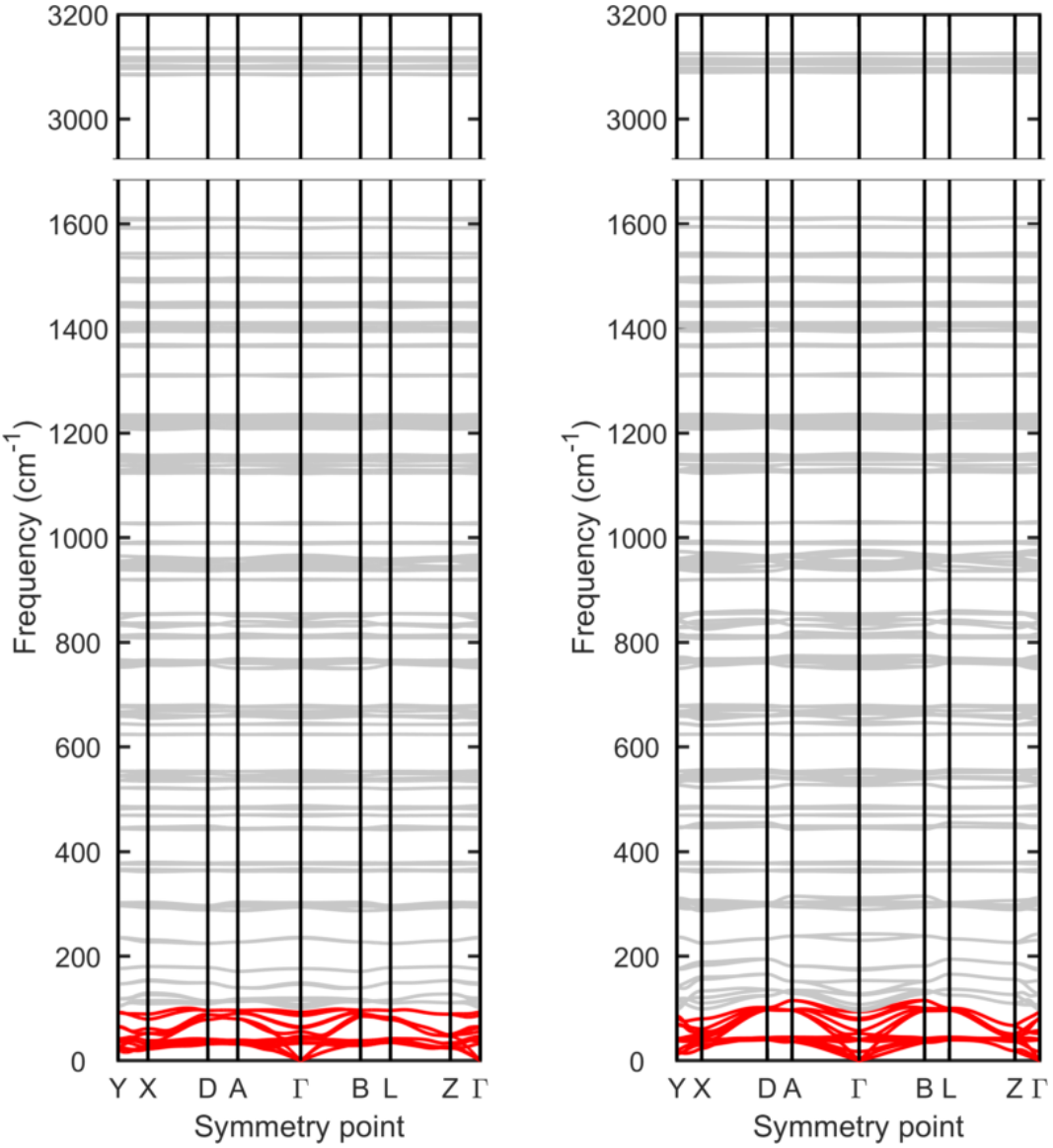

Figure 6-4: Vibrational dispersion curves of (a) γ- and (b) β-coronene displaying phonon modes (red) and intramolecular modes (grey). There are no modes between 1700 cm^{-1} and 3000 cm^{-1}.

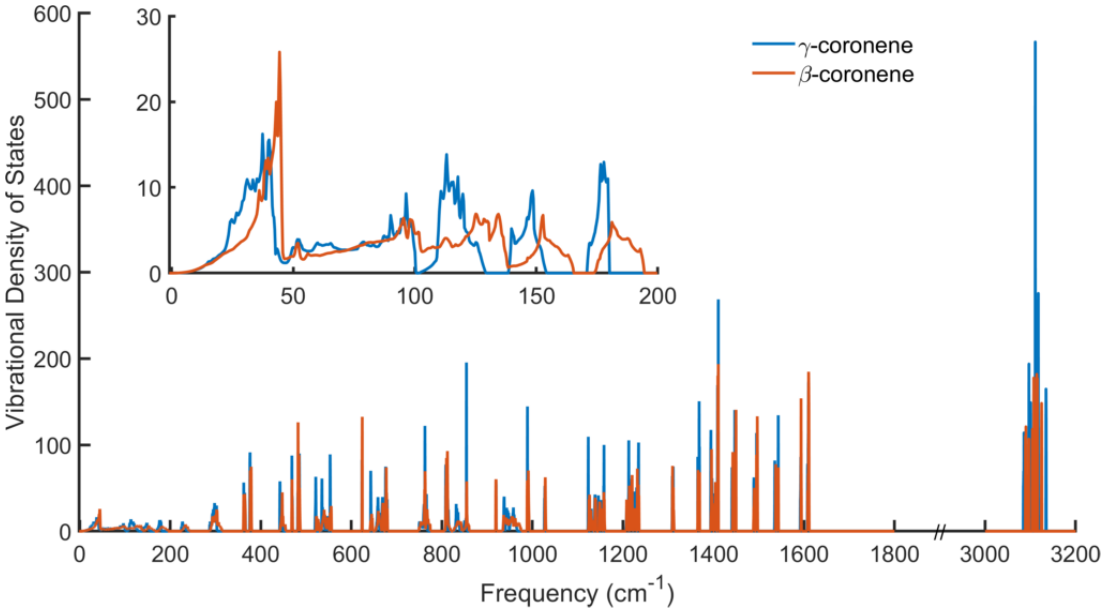

Figure 6-5: Vibrational density of states (number of states/(unit cell × cm^{-1})) of γ- and β-coronene. The inset shows the density of states in the phonon region in more detail.

Table 6.2: The zero-point energies of both polymorphs calculated in three ranges covering phonon modes and the first six intramolecular modes (0 to 167 cm^{-1}), remaining intramolecular modes involving motions of the carbon and hydrogen atoms (167 to 2000 cm^{-1}) and intramolecular modes involving motions of only the hydrogen atoms (2000+ cm^{-1}). The splits were all made at natural gaps where the density of states is zero for both polymorphs.

Frequency Range (cm^{-1})	Zero-point energy (meV/unit cell)		
	γ-coronene	β-coronene	$\Delta(\gamma - \beta)$
0 to 167	87.22	92.59	-5.37
167 to 2000	10211.62	10227.10	-15.48
2000 +	4623.86	4621.80	2.06

β-coronene is zero. The second range from 167 to 2000 cm^{-1} includes the remaining intramolecular modes that involve motions of both carbon and hydrogen, and the final range is 2000 cm^{-1} and above including the intramolecular modes with hydrogen motions only. The zero-point energy for the phonons stabilise γ by 5.37 meV/unit cell, the intramolecular carbon and hydrogen modes stabilise γ by 15.48 meV/unit cell and the intramolecular hydrogen only modes stabilise β by 2.06 meV/unit cell. This indicates that the intramolecular modes play as important, if not a more important, role as the phonons do in affecting the relative phase stabilities at 0 K. This is contrary to popular belief that it is the phonons which affect phase stabilities, not the intramolecular modes [16, 17].

The Helmholtz free energy calculated in the harmonic approximation is shown in figure 6-6 (a). The results give that F^{HA} of γ-coronene is lower than β-coronene, predicting that there is no phase transition and that γ-coronene is the most stable polymorph. This is contrary to experimental observations where crystals of γ-coronene shatter and transform into β-coronene at approximately 150 K. Including a temperature independent pV term to give the Gibbs free energy in the harmonic approximation, G^{HA}, makes no appreciable difference with $pV = 0.043$ (0.042) eV/unit cell for γ- (β-) coronene. The difference in F^{HA} between γ- and β-coronene at 0 K is 5.7 meV/unit cell and at 150 K the difference rises to 19.3 meV/unit cell, indicating our calculations have at least a 6 meV/unit cell error, and more likely around 20 meV/unit cell. Given the uncertainty in the lattice energy and zero-point energies from computational parameters are less than 1 meV/unit cell, it points to a possible failure of the assumptions made in the harmonic approximation. To assess this, thermal expansion and thus some anharmonic nature of the vibrations has been included by applying the quasi-harmonic approximation.

The Gibbs free energy calculated within the *quasi-harmonic* approximation, G^{QHA}, presented in figure 6-6 (b), also does not predict a phase transition, with γ-coronene predicted to be stable at all temperatures. Once again this is not in agreement with experimental observations. At 0 K the difference in G^{QHA} between the two polymorphs is 2.3 meV/unit cell and at 150 K this rises to 14.6 meV/unit cell, suggesting an error of at least 2.3 meV/unit cell but more likely around 10 to 20 meV/unit cell. Figure 6-7 shows the difference in energies between γ- and β-coronene in both harmonic and quasi-harmonic approximations. The Gibbs free energy calculated within the quasi-harmonic approximation is an improvement on the harmonic approximation in that it makes β-coronene closer to being more stable than γ-coronene at 0 K. The difference in G^{QHA} between polymorphs is consistently smaller in magnitude than the difference in G^{HA}, indicating that thermal expansion makes a fairly consistent impact on the free energy.

The total energetic effect of thermal expansion can be calculated as the difference between the Gibbs free energy calculated within the quasi-harmonic approximation (G^{QHA}) and the harmonic approximation (G^{HA}). This is displayed in table 6.3 at 0 K and 150 K. The thermal expansion contribution is -27.7 meV/unit cell for γ-coronene and -32.5 meV/unit cell for β-coronene at 150 K, indicating that thermal expansion has a larger effect on β-coronene than γ-coronene. These values are consistent with Nyman and Day [48] who found thermal expansion typically contributes 18 meV (=1.7 kJ/mol) and never more than 41 meV at the melting point of a large set of organic molecular

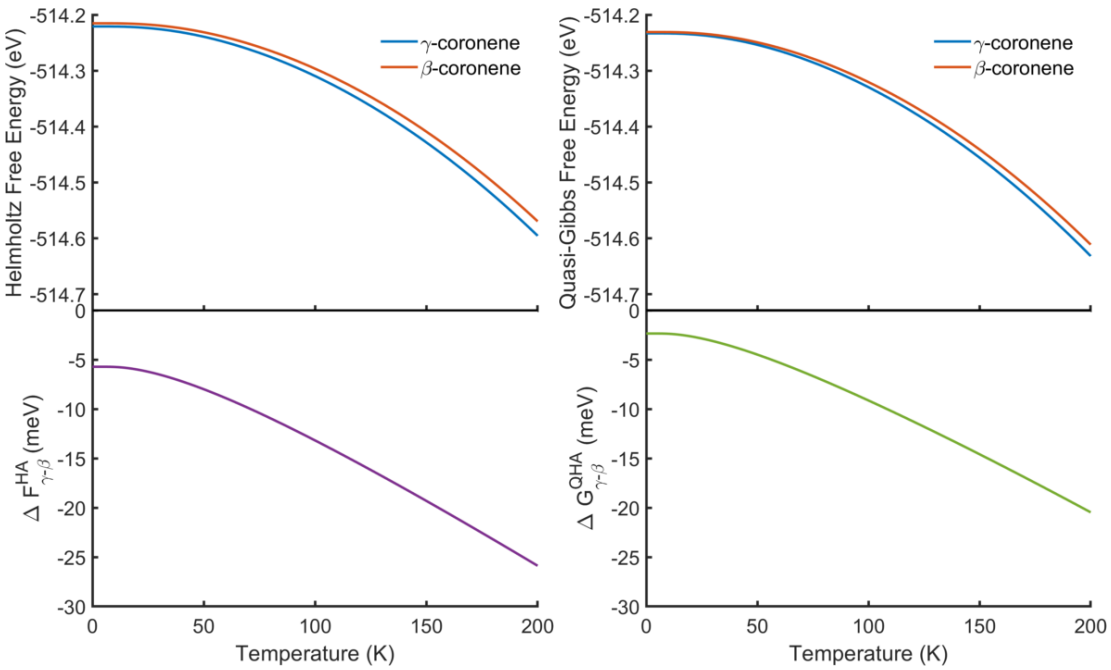

Figure 6-6: (Top) (a) Helmholtz free energy calculated within the harmonic approximation and (b) Gibbs free energy calculated within the quasi-harmonic approximation for γ- and β-coronene. (Bottom) The difference in (a) harmonic Helmholtz free energy and (b) quasi-harmonic Gibbs free energy between γ- and β-coronene. Units are per unit cell.

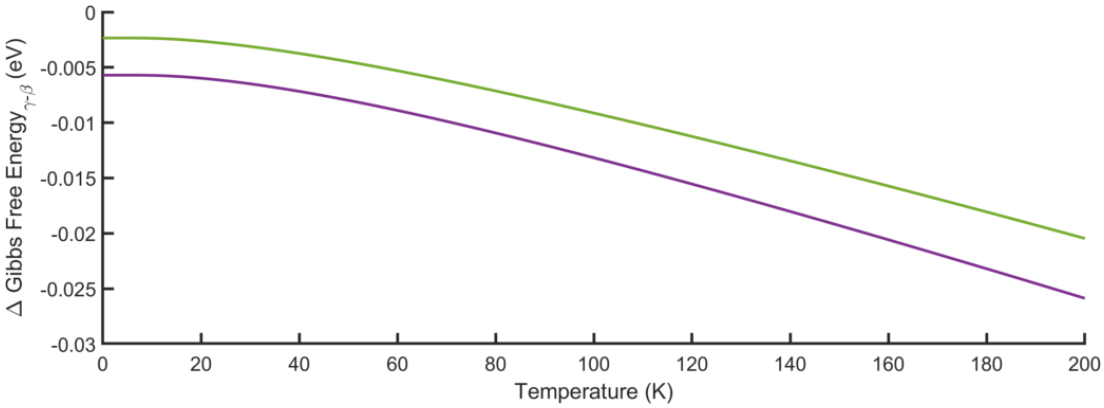

Figure 6-7: A comparison of the difference in G^{QHA} (green) and the difference in G^{HA} (purple) between γ- and β-coronene. Units are per unit cell.

Table 6.3: Energetic contribution of the thermal expansion: $G^{\mathrm{QHA}} - G^{\mathrm{HA}}$.

Polymorph	Thermal expansion contribution (meV/unit cell)	
	0 K	150 K
γ	-12.7	-27.7
β	-16.1	-32.5

crystals (the molecular crystals investigated comprised of up to 55 atoms per unit cell containing elements H, C, N, O, F, S and Cl). The difference in the thermal expansion contribution of γ- and β-coronene at 0 K is -3.4 meV/unit cell and at 150 K is -4.7 meV/unit cell, again consistent with the findings in Ref. [48].

Figure 6-8 shows how the volume as a function of temperature calculated within the quasi-harmonic approximation compares with our previous DFT-D3 structures and experimental results presented in Chapter 4. The quasi-harmonic approximation increases the calculated volumes at 0 K by 18.0 Å^3 (2.5%) and 18.6 Å^3 (2.7%) for γ- and β-coronene respectively. This expansion is a result of including the zero-point energy and is comparable to the 2% found for carbamazpine [180] and 2.6% for urea [182]. This expansion increases the over prediction of volumes from 2.5% to 4.8% for γ-coronene and from 3.1% to 5.1% for β-coronene compared to the extrapolated '0 K' expeirmental structure. At 300 K this is a 30 to 40 Å^3 (4.5 to 5.5%) over prediction in relation to experiments, with a greater over prediction for β-coronene.

The volumetric thermal expansion coefficient shows how well the quasi-harmonic approximation captures the rate of change of volume with temperature, illustrated in figure 6-9. For both polymorphs the thermal expansion coefficient shows a sharp rise at low temperatures and levels off as the temperature increases with the thermal expansion of γ-coronene greater than β-coronene at all temperatures. The experimental thermal expansion coefficient was calculated from the linear fits of volume as a function of temperature from figure 6-8 across 150 K to 300 K for γ-coronene giving an average $\alpha_V = (1.085 \pm 0.009) \times 10^{-4}$ K^{-1} and 80 K to 150 K for β-coronene giving $\alpha_V = (0.881 \pm 0.003) \times 10^{-4}$ K^{-1}. In order to make a fair comparison linear fits were also made to the quasi-harmonic volume curves of the across the same ranges giving $\alpha_V = (1.249 \pm 0.001) \times 10^{-4}$ K^{-1} for γ-coronene and $\alpha_V = (1.063 \pm 0.004) \times 10^{-4}$ K^{-1} for β-coronene, which are within the typical range of $0.8 - 2.4 \times 10^{-4}$ K^{-1} for organic molecular crystals found in Ref. [48]. Our calculated thermal expansion coefficients are over predicted by 0.16×10^{-4} K^{-1} (13%) and 0.18×10^{-4} K^{-1} (17%) for γ- and β-coronene respectively.

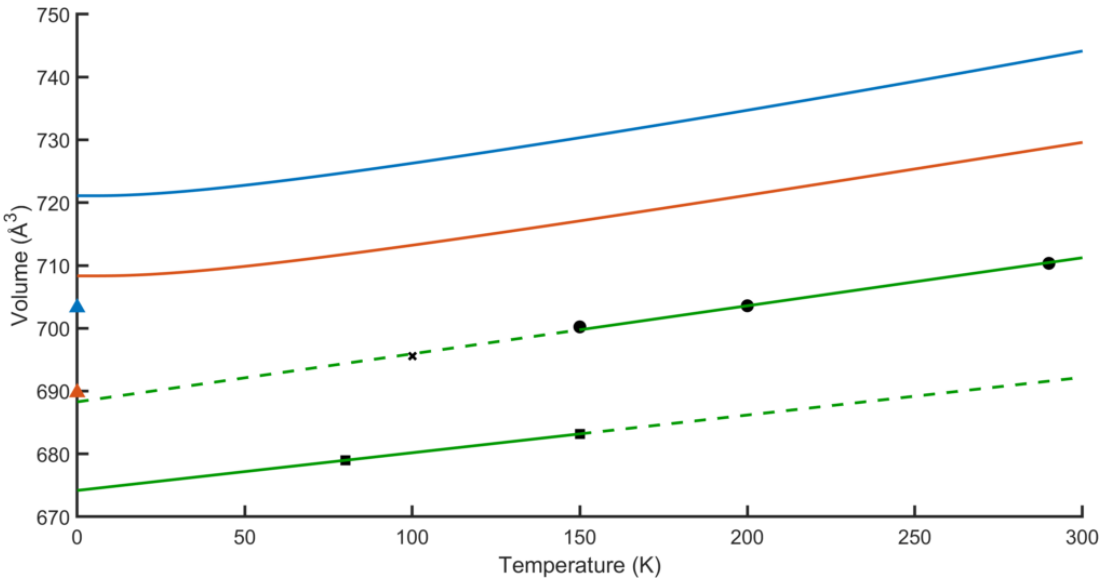

Figure 6-8: Temperature dependency of unit cell volumes calculated in the quasi-harmonic approximation for γ- (solid blue line) and β-coronene (solid orange line), compared to experimental results reproduced from figure 4-10. Black circles show our measurements, black $\times$ show data from Ref. [173] and black squares are from Ref. [8]. Green lines show the fitted linear trendlines. DFT-D3 unit cell volumes are indicated by blue/orange triangles for γ-/β-coronene respectively.

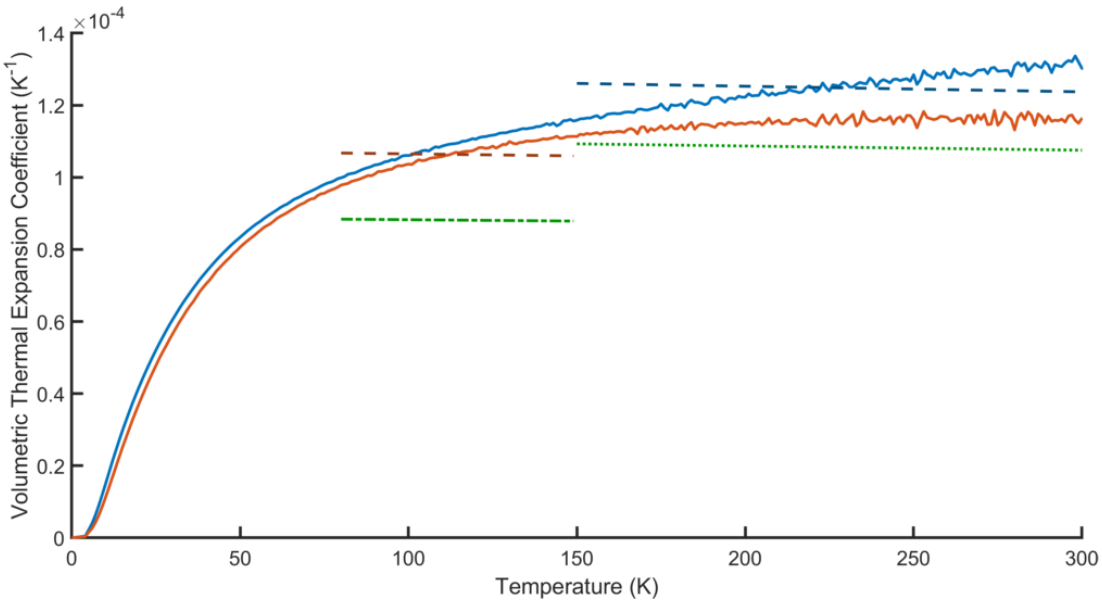

Figure 6-9: Temperature dependency of the volumetric thermal expansion coefficients of γ-(blue) and β-coronene (orange). Solid lines indicate the instantaneous coefficient and dashed lines indicate the coefficient calculated from a linear fit to volumes over the range shown. Experimental thermal expansion coefficients (green) calculated from linear fits to the volumes are indicated in dotted lines for γ-coronene and dot-dash lines for β-coronene.

The consistent over prediction in thermal expansion coefficient indicates a possible systematic error in the quasi-harmonic calculations, likely arising from the Helmholtz calculations for each volume and temperature prior to fitting with the equation of state. To test the sensitivity of these curves a 6^{th} volume at +7.5% was included for β-coronene and the analysis re-run. This made little difference to the Gibbs free energy, however the volume was found to increase more rapidly with temperature giving a thermal expansion coefficient that diverges instead of levelling off, such that the results were less consistent with experiment. This additional calculation at volume expansion +7.5% is therefore problematic, and given that it is the most expanded structure it is possible that the van der Waals forces are insufficiently described at the elongated distances present, leading to errors in the lattice energy. Indeed a sensitivity analysis by Červinka *et al.* suggested that the lattice energy contribution to the Helmholtz free energy as a function of volume had a larger impact on the thermal expansion than the vibrational contribution for methanol, and that a simple scaling was not sufficient to correctly the reproduce molar volume [142]. This suggests it may well be a problem with the D3 dispersion term incorrectly affecting the lattice energies of the expanded and contracted volumes since D3 and other pairwise dispersion corrections have been parameterised to reproduce equilibrium volumes and lattice energies.

Problems with the lattice energy calculation may also be impacting the relative phase stabilities. Table 6.4 shows the difference in lattice energies between γ- and β-coronene calculated using various dispersion corrections obtained from literature. The difference in lattice energy between γ- and β-coronene varies from 0.7 kJ/mol of molecules (this work) and 3.8 kJ/mol of molecules [8]. Clearly the dispersion correction method used has a significant impact on the difference in lattice energies, which will subsequently impact the calculation of relative phase stability. Therefore more advanced

Table 6.4: Difference in lattice energies between γ- and β-coronene calculated using various dispersion corrections.

Source	DFT software	Dispersion correction	$\Delta U_{latt}(\gamma - \beta)$ (meV per unit cell)	$\Delta U_{latt}(\gamma - \beta)$ (kJ/mol of molecules)
This work	VASP	D3	14.3	0.69
[8]	CASTEP	D2, default vdW radii	89	4.3
[8]	CASTEP	D2, vdW radii from [99]	79	3.8
[8]	VASP	TS	71	3.4
[177]	VASP	D3(BJ)	30	1.4
[177]	VASP	MBD	39	1.9

methods to calculate the lattice energies are required to reduce the uncertainty in the lattice energies and subsequent phase stability calculations.

More advanced methods to calculate lattice energies include the hybrid many-body interaction (HMBI) in which the total energy of the crystal is determined by combining a quantum mechanical treatment of individual molecules and their short-range dimer interactions with a force field treatment of longer-range and many-body effects [179, 184]. Indeed the lattice energy of benzene has been calculated to an accuracy below 10 meV using this method [187] and in combination with the quasi-harmonic approximation the phase diagram of methanol has been calculated to a quoted accuracy of 5 meV [184]. However even an accuracy of 5 meV gives rise to a phase transition temperature 80 K lower than experiments and a triple point 0.6 GPa above and 40 K below the experimental value [184]. Whilst these more advanced methods for the lattice energy are clearly valuable and provide greater accuracy, the errors on some predicted properties remain large. Furthermore they are computationally demanding, for example calculating the phase diagram of methanol required a few hundred thousand CPU hours [184].

Further possible issues in our method include the use of the quasi-anisotropic volume expansion. This gives structures that are at the minima of the lattice energy with respect to volume, which are not necessarily equivalent to structures at the minima of the Gibbs free energy. Abraham *et al.* proposed a full anisotropic volume expansion method which could be used to eliminate this issue [135]. Secondly the quasi-harmonic approximation does not include the intrinsic anharmonic nature of vibrations and fails to adequately describe highly anharmonic modes or systems at high temperatures [142]. More computationally demanding molecular dynamics methods would be required to improve on this approximation.

6.4 Summary

Vibrational frequencies of both polymorphs were calculated across the first Brillouin zone by performing finite difference calculations on supercell structures. In general the modes in β-coronene showed a greater amount of dispersion than γ-coronene. When considering frequencies across the first Brillouin zone, the phonon modes and intramolecular modes in γ-coronene were separated at 101 cm^{-1} whilst no separation occurred in β-coronene suggesting mixing of intramolecular and phonon mode character may be greater in β-coronene. The intramolecular modes show little dispersion leading to sharp peaks in the vibrational density of states. Clear differences were observed in the vibrational

density of states with a shift upwards in frequency in β-coronene and a broadening due to the increased dispersion.

The Helmholtz free energy within the harmonic approximation was calculated and did not predict a phase transition, with γ-coronene predicted to be the most stable polymorph. The Gibbs free energy calculated in the quasi-harmonic approximation also did not predict a phase transition with γ-coronene the most stable polymorph. Neither the harmonic approximation nor the quasi-harmonic approximation are in agreement with experimental observations with an error estimated to be 10-20 meV/unit cell to achieve a phase transition temperature of $\sim$150 K that is observed experimentally.

The energetic contribution to the thermal expansion is greater in β-coronene than γ-coronene. Applying the quasi-harmonic approximation expands the calculated unit cell volumes, raising the over prediction of volumes in comparison to '0 K' experimental volumes. The thermal expansion coefficient is also over predicted compared to experimentally derived values by 13% (17%) for γ- (β-) coronene. This consistent over prediction points to a systematic error in the quasi-harmonic calculations.

Possible sources of the errors in our calculations include an incorrect description of the expanded and contracted lattice energies due to the pairwise dispersion correction that is parametrised based on equilibrium structures, the use of a quasi-anisotropic volume expansion and the exclusion of intrinsic anharmonic effects in the harmonic approximation. More advanced methods are available to address each of these issues, each requiring additional computational resources. Future work could focus on targeting each of these issues in turn.

Chapter 7

Conclusions

In this work the vibrations and phase stabilities of the two polymorphs γ- and β-coronene have been studied using Raman spectroscopy and DFT-D3 calculations. The naturally occurring structure of crystalline coronene is the γ-phase. In 2015 β-coronene was discovered and stabilised at standard room temperature and pressure by applying a 1 T magnetic field during crystal growth. β-coronene was established as the low temperature phase of γ-coronene with a phase transition temperature of $\sim$150 K [8]. Initial DFT-D calculations showed that the lattice energy of β-coronene is lower than γ-coronene indicating that β-coronene is energetically preferred by 3.8 kJ/mol [8], yet γ-coronene forms preferentially at standard room temperature and pressure. As part of this work the crystal growth of β-coronene was investigated and unfortunately no crystals of β-coronene were synthesised. Instead the β-phase was accessed by cooling crystals γ-coronene below the phase transition temperature. The vibrations of both polymorphs have been investigated using Raman spectroscopy including polarisation dependence. DFT-D3 calculations successfully relaxed the structures of both polymorphs and reproduced experimental frequencies and Raman intensities allowing mode assignments to be made and the polarisation dependencies understood. Finally the thermodynamic phase stabilities have been investigated. Neither harmonic or quasi-harmonic calculations at the D3 level of dispersion correction predict a phase transition, with the error estimated at 10-20 meV/unit cell.

7.1 Summary

In Chapter 2 relevant theoretical aspects were introduced. First thermodynamic phase stabilities were introduced with an emphasis placed on the role of vibrations.

Next the types of vibrations in molecular crystals were introduced and how they can be measured experimentally has been discussed. Finally the DFT framework was introduced and dispersion corrections examined. Methods for calculating zone centre vibrational frequencies and across the Brillouin zone were detailed. The theory behind the calculation of thermodynamic variables was explained. Lastly the method for calculating Raman intensities was outlined.

Chapter 3 details the crystal growth of γ-coronene and investigates the method of growing β-coronene crystals originally reported in Ref. [8]. High purity γ-coronene crystals were successfully grown by a physical vapour transport method in a three zone furnace. Many attempts were made to grow crystals of β-coronene, yet none were successful. Beyond the published method [8], 'ageing' the supersaturated coronene in toluene solution and doping with dicoronylene were investigated.

The study of vibrations of crystalline coronene started with the intramolecular modes in Chapter 4. First DFT-D3 was used to reproduce experimental structures measured using single crystal x-ray diffraction. For γ- (β-) coronene lattice parameters are reproduced to within 1.6% (2.1%) and the intracell molecular angle within 0.7% (0.4%) compared to experimental structures collected at 290 K (150 K). Next the vibrations were probed using Raman spectroscopy. Upon cooling a γ-coronene crystal, the crystal shattered at 137 K coinciding with a change in low-frequency peak positions, suggesting a phase transition to β-coronene had occurred. Polarised Raman spectra were measured on a single crystal of γ-coronene at room temperature where sixteen peaks were resolved and on a crystal fragment in the β-phase at 110 K where, due to a large background signal, only four peaks were resolved. Upon fitting with Voigt profiles the resulting intensity polar plots were compared to those produced by DFT-D3 calculations with the experimental crystal orientation accounted for. The calculated intensity polar plots reproduced the polarisation dependency and relative intensities of the experimental intensity polar plots for both polymorphs, allowing a mode assignment to be made. The calculated Raman active vibrational frequencies were used to examine previous Raman measurements on coronene.

Chapter 5 investigates the lattice vibrations using DFT-D3 and Raman spectroscopy, completing the study of vibrations. Two peaks appeared in the low-frequency Raman spectra of a single crystal of γ-coronene at room temperature. Upon cooling the crystal shattered at 163 K below which four peaks were observed. Twelve zone-centre phonon modes were calculated for both γ- and β-coronene using DFT-D3, of which six are Raman active and six are IR active. Three (five) of these modes were observed in the Raman spectra of γ- (β-) coronene with the remaining modes too low in intensity

to be measured. A comparison of intensity polar plots from fits to polarised Raman spectra and equivalent plots produced using DFT-D3 allowed a firm mode assignment to be made, with frequencies differing by up to 4 cm^{-1}. The atomic motion of the phonon modes was also studied and used to explain the differences in Raman spectra. In γ-coronene the Raman active modes are either rotations or librations. In stark contrast β-coronene exhibits rotations, librations and two mixed roto-libration modes.

Finally Chapter 6 investigates the phase stabilities of γ- and β-coronene. The vibrational frequency calculations are extended over the Brillouin zone and vibrational dispersion curves and density of states presented. Clear differences were observed in the vibrational density of states with a shift upwards in frequency in β-coronene and a broadening due to a larger amount of dispersion. Neither the harmonic or quasi-harmonic Gibbs free energies predicted a phase transition, with γ-coronene the most stable polymorph at all temperatures. The error in these calculations is estimated to be around 20 meV/unit cell for the harmonic approximation and 10-20 meV/unit cell for the quasi-harmonic approximation (QHA) to achieve a phase transition temperature of $\sim$150 K. The thermal expansion was studied within the QHA. Applying this expands the unit cells of both polymorphs which produces a worse agreement with experimental structures. The thermal expansion coefficient is over predicted compared to experimentally derived values by 13% and 17% for γ- and β-coronene respectively, although both the calculated and experimental values are consistent with the typical ranges found for molecular crystals given in Ref. [48]. Various possible sources of error were discussed, including the description of the van der Waals bonding, the exclusion of anharmonic effects and the use of the quasi-anisotropic expansion method.

7.2 Recommendations for future work

Further investigation into the growth of β-coronene is required. First I recommend the "disappearing polymorph" phenomena be investigated. A new laboratory or a thorough clean of the current laboratory are my recommended first steps. In addition a temperature controlled glove box would be ideal to prevent cooling of the supersaturated solution during the filtration process. If unavailable a fully enclosed oven with accurate temperature control may also be suitable. A filter that can withstand temperatures of at least 93°C and therefore can be heated prior to use would also be beneficial. In addition to this equipment, I recommend that the length of time the filtered supersaturated solution is left in the magnetic field prior to cooling is investigated. Finally known crystal structures of other compounds could be screened for good lattice matching

with β-coronene, and should a suitable crystal structure be found it could be used as a template for crystal growth. If crystals of β-coronene that are stable at standard room temperature and pressure are successfully synthesised then further investigations into the properties of this new polymorph can be undertaken. These investigations could include studying the structure under pressure analogous to those presented for γ-coronene in Ref. [188].

As mentioned in Chapter 4, the peaks at 1232 cm^{-1}, 1250 cm^{-1} and 1292 cm^{-1} measured by Babkov *et al.* [153] are puzzling and have not been fully assigned through our calculations. The Raman measurements Babkov *et al.* presented were performed on a powder sample and I suggest these are repeated on a high-purity powder sample to confirm the existence and positions of the aforementioned peaks. If confirmed I suggest studying the Raman intensity predicted for modes spanning 1200 cm^{-1} to 1300 cm^{-1} using the DFT-D3 calculations presented here to determine crystal orientations that maximise the intensity of these modes. These orientations may then be measured experimentally using polarised Raman which may allow an accurate mode assignment to be made.

Furthermore the peaks in the range 1590 cm^{-1} to 1630 cm^{-1} remain puzzling. Two groups of modes are predicted by the crystalline DFT-D3 calculations, whilst previous experimental studies [32, 153, 154, 175] measured two or three peaks with various peak positions and four were resolved in this work. A Fermi resonance has been suggested to produce the additional peaks measured in this range [158]. Fermi resonances arise from anharmonic behaviour that are not captured in the DFT-D3 calculations presented here. In order to solve this puzzle, calculations that include anharmonic behaviour and that are capable of simulating Fermi resonances are required. A benchmark for such calculations could be reproducing the two peaks at 1352 cm^{-1} and 1369 cm^{-1} that are known Fermi resonances.

The results presented in Chapter 6 show that the Gibbs free energies calculated using the DFT-D3 method in the harmonic and quasi-harmonic approximations are not accurate enough to reproduce the experimentally observed phase transition. Therefore further investigations into the phase stabilities of γ- and β-coronene with higher levels of theory is recommended. A study of methanol by Červinka *et al.* suggested that the lattice energy contribution has a larger impact than the vibrational contribution on relative phase stabilities [142], and so I suggest using higher levels of theory to relax structures and calculate lattice energies as a first step. Applying the hybrid many-body interaction (HMBI) method to benzene predicted lattice energies to within 10 meV [187] and applying this method to study the phase diagram of methanol [184]

resulted in an accuracy of 5 meV, indicating the HMBI method may improve upon the accuracy of ∼10-20 meV/unit cell found in this work. In addition the aforementioned study of methanol [142] predicted smaller molar volumes using the HMBI method than DFT-D3(BJ), which if replicated for γ- and β-coronene may produce structures in closer agreement with experiments and better reproduce the thermal expansion. Hence I suggest in future work the HMBI method is applied to γ- and β-coronene to relax structures, calculate vibrational frequencies and finally Gibbs free energies. Other possible avenues to explore include applying the full anisotropic thermal expansion method of Abraham *et al.* [135] and including the intrinsic anharmonicity of vibrations by using molecular dynamics.

7.3 Final remarks

The reproducibility of synthesising crystals of β-coronene that are stable at standard room temperature and pressure remains a problem. Further work is needed to explore the crystal growth of β-coronene to develop a reliable and reproducible method.

Unfortunately DFT-D3 is not accurate enough to reproduce the phase transition between γ- and β-coronene in either the harmonic or quasi-harmonic approximations. Higher levels of theory are recommended as a focus for further study of this system. Nevertheless the DFT-D3 calculations presented here have successfully reproduced vibrational frequencies and Raman intensities of both polymorphs and explained some puzzles previously presented by the literature. This demonstrates the successes DFT-D3 can have in interpreting Raman spectra and further validate its place in electronic structure calculations.

Appendix A

Comparison of isolated molecule and intramolecular crystalline frequencies

Intramolecular vibrations of molecular crystals are typically the same, or very similar to, the vibrations of the isolated molecule. DFT-D3 calculations such as those presented in Chapter 4 produce not only vibrational frequencies but also vectors describing the associated atomic motion. Here the intramolecular vibrations of both γ- and β-coronene are compared to the isolated molecule by studying this atomic motion.

A.1 Method

An initial comparison was made mathematically. The eigenvectors of the dynamical mass weighted matrix $\mathbb{D}$ introduced in Chapter 2.3.2 are orthogonal

$$\mathbf{u}_i \cdot \mathbf{u}_j = \delta_{i,j}, \tag{A.1}$$

where $\mathbf{u}_i$ is an eigenvector of $\mathbb{D}$ describing the atomic motion of the vibrational mode i. This principle is used to compare eigenvectors of different structures: whilst the eigenvectors of different structures will not be orthogonal, vibrations with similar atomic motion will have dot products that are close to 1. To take the dot product the eigenvectors must be in the same coordinate space, that is the orientation of the molecules in x-y-z must be the same and the indexing of the atoms within the molecules must be consistent. The orientation of the isolated molecule is shown in figure A-1 and

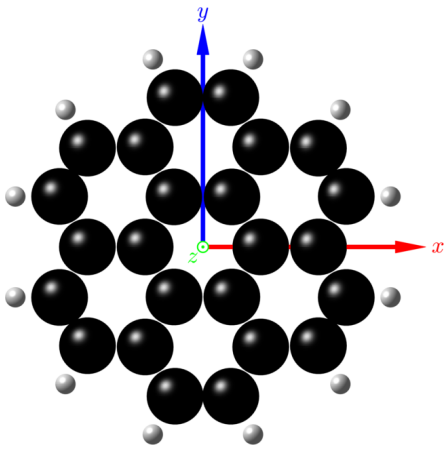

Figure A-1: Orientation of the isolated molecule in DFT-D3 calculations in global x (red arrow), y (blue arrow) and z (green arrow) axes. Carbon atoms are shown in black and hydrogen in white. Note that the x direction lies along a line of four carbon atoms.

each molecule in the unit cells of γ- and β-coronene was transformed to match this. A plane was fitted to each molecule and two directions $\hat{x}_{\text{plane}}$ and $\hat{y}_{\text{plane}}$ selected such that $\hat{x}_{\text{plane}}$ is the direction which is closest to the a-b plane of the unit cell, as illustrated in figure A-2. The molecular coordinates and eigenvectors were then transformed into the coordinate system of the associated planes.

For each mode of the isolated molecule, a vector was formed by duplicating the atomic motion to form a vector with the same length as that of the two molecules from the crystalline structures, taking care to ensure the ordering of atoms in the vectors was consistent. For each, the dot product was then taken with each of the crystalline modes, with the results ranked in order of dot product.

This dot product method worked well for identifying most crystalline modes with associated isolated molecule vibrations, with the dot product as high as 0.9997. However in some cases the assignment was unclear, with a smallest dot product of 0.527. In order to verify the simple assignments and determine those which were less clear, all modes were visualised and compared by eye. The dot product results were used as a guide and in most cases the dot product gave the correct assignment. In the remaining cases it was found that the intramolecular modes in the crystalline environments appeared to be mixtures of several from isolated molecule motions. In β-coronene this mixing was more common than in γ-coronene. This demonstrates that the crystalline environment affects the intramolecular vibrations beyond simply shifting frequencies, such that this impact should be included when making mode assignments and in further calculations that depend on vibrational properties, such as in calculations of thermodynamic variables.

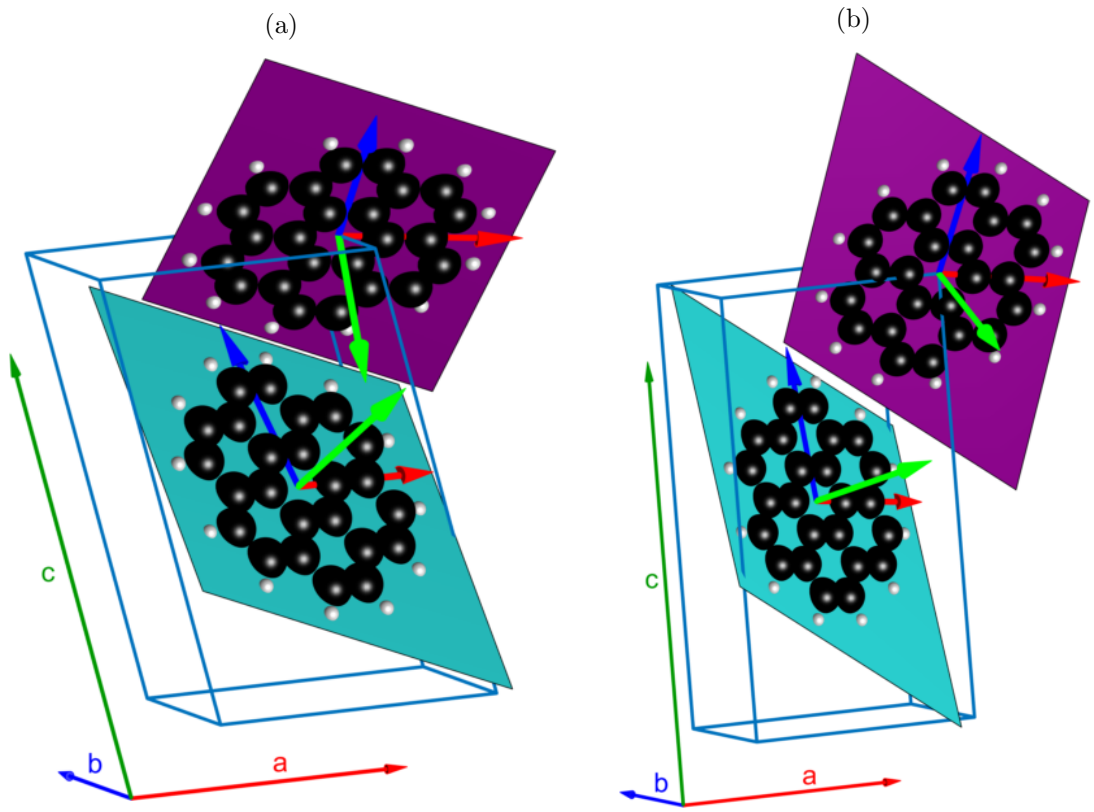

Figure A-2: Unit cells (light blue) of (a) γ- and (b) β-coronene with the lattice vectors $\vec{a}$ (red arrow), $\vec{b}$ (blue arrow) and $\vec{c}$ (green arrow) shown. The plane fit to each molecule is shown in purple/turquoise with the new coordinate system $\hat{x}_{\text{plane}}$ (red), $\hat{y}_{\text{plane}}$ (blue) and $\hat{z}_{\text{plane}}$ (green). $\hat{x}_{\text{plane}}$ was chosen to follow a line of four carbon atoms across the coronene molecule to give a consistent orientation with the isolated molecule calculation, and along the line which lies the closest to the a-b plane.

A.2 Isolated molecule and γ-coronene intramolecular vibrations

Table A.1: Comparison of calculated frequencies for an isolated coronene molecule with the associated intramolecular frequencies calculated for γ-coronene. Modes were compared using the dot product method and verified by visualising the vibrations of each molecule in the crystal and comparing to the isolated molecule vibrations.

Isolated Molecule Frequency (cm^{-1})	Irrep	Equivalent frequencies (cm^{-1}) and irreps in γ-coronene			
82.53	E_{2u}	101.71 (B_u)	107.88 (A_u)	115.90 (A_u)	120.03 (B_u)
119.12	A_{2u}	146.06 (A_u)	148.81 (B_u)		
156.15	B_{1g}	176.04 (B_g)	176.10 (A_g)		
216.77	B_{2g}	234.38 (A_g)	235.75 (B_g)		
283.59	E_{1g}	293.39 (A_g)	298.66 (B_g)	299.29 (A_g)	300.07 (B_g)
289.59	E_{2u}	299.09 (B_u)	300.00 (A_u)	300.83 (B_u)	302.33 (A_u)
360.22	E_{2g}	362.19 (B_g)	365.14 (A_g)	365.60 (B_g)	366.47 (A_g)
375.75	E_{1u}	376.32 (B_u)	376.48 (A_u)	377.26 (B_u)	378.58 (A_u)
441.13	E_{1g}	442.42 (B_g)	443.85 (A_g)	445.10 (B_g)	445.67 (A_g)
466.11	B_{2u}	468.11 (A_u)	470.34 (B_u)		
478.58	A_{1g}	484.83 (B_g)	487.55 (A_g)		
482.80	E_{2g}	481.32 (B_g)	482.02 (A_g)	483.86 (A_g)	485.74 (B_g)
517.53	A_{1u}	521.06 (B_u)	521.97 (A_u)		
536.01	E_{2u}	534.11 (A_u)	535.54 (A_u)	535.69 (B_u)	537.60 (B_u)
543.38	A_{2u}	541.83 (A_u)	547.62 (B_u)		
550.73	B_{1u}	553.09 (B_u)	554.20 (A_u)		
622.44	A_{2g}	623.45 (A_g)	624.13 (B_g)		
641.47	B_{2g}	642.54 (A_g)	645.16 (B_g)		
656.36	E_{1g}	655.02 (A_g)	661.23 (B_g)	661.35 (A_g)	663.33 (B_g)
667.40	B_{1u}	666.52 (B_u)	668.06 (A_u)		
674.58	E_{2g}	675.72 (A_g)	676.31 (B_g)	679.29 (A_g)	679.50 (B_g)
746.43	B_{1g}	750.48 (B_g)	753.42 (A_g)		
757.74	E_{2u}	756.82 (A_u)	757.89 (B_u)	762.01 (A_u)	762.98 (B_u)
761.34	E_{1u}	763.13 (A_u)	764.97 (B_u)	765.91 (A_u)	766.36 (B_u)
806.69	E_{1u}	808.10 (B_u)	808.75 (A_u)	810.11 (B_u)	810.20 (A_u)
808.54	E_{2u}	810.59 (B_u)	811.79 (A_u)	813.06 (B_u)	813.41 (A_u)

Continued on next page

Isolated Molecule Frequency (cm^{-1})	Irrep	Equivalent frequencies (cm^{-1}) and irreps in γ-coronene			
828.74	E_{1g}	829.86 (A_g)	835.34 (B_g)	837.30 (A_g)	837.48 (B_g)
846.74	A_{2u}	843.81 (A_u)	846.42 (B_u)		
855.77	B_{2g}	853.76 (A_g)	853.90 (B_g)		
917.26	A_{2g}	918.95 (A_g)	920.24 (B_g)		
930.84	A_{1u}	937.35 (B_u)	939.67 (A_u)		
938.20	E_{1g}	943.58 (A_g)	944.27 (A_g)	945.53 (B_g)	949.91 (B_g)
948.10	E_{2u}	945.53 (A_u)	952.54 (A_u)	954.06 (B_u)	959.76 (B_u)
952.71	B_{2g}	959.45 (A_g)	966.13 (B_g)		
985.89	E_{2g}	988.03 (A_g)	989.35 (B_g)	989.64 (B_g)	990.38 (A_g)
1025.17	A_{1g}	1026.26 (A_g)	1028.36 (B_g)		
1125.28	E_{1u}	1122.45 (A_u)	1123.52 (B_u)	1128.30 (A_u)	1131.30 (B_u)
1135.46	B_{2u}	1137.69 (A_u)	1139.14 (B_u)		
1147.35	E_{2g}	1145.62 (A_g)	1146.88 (B_g)	1150.38 (A_g)	1152.87 (B_g)
1153.57	B_{1u}	1158.12 (B_u)	1158.19 (A_u)		
1207.75	E_{1u}	1208.36 (B_u)	1210.00 (A_u)	1211.06 (A_u)	1211.92 (B_u)
1214.13	B_{2u}	1217.94 (A_u)	1219.43 (B_u)		
1214.87	A_{1g}	1215.84 (A_g)	1216.99 (B_g)		
1221.83	A_{2g}	1223.75 (B_g)	1226.44 (A_g)		
1228.53	E_{2g}	1229.60 (B_g)	1229.94 (A_g)	1233.78 (A_g)	1235.35 (B_g)
1306.62	E_{1u}	1308.15 (A_u)	1309.12 (B_u)	1309.40 (B_u)	1311.69 (A_u)
1361.43	B_{2u}	1365.55 (B_u)	1366.12 (A_u)		
1364.30	A_{1g}	1369.27 (A_g)	1369.39 (B_g)		
1391.39	E_{2g}	1393.82 (A_g)	1393.97 (B_g)	1396.63 (B_g)	1396.66 (A_g)
1399.56	B_{1u}	1401.50 (A_u)	1403.29 (B_u)		
1406.88	E_{1u}	1409.19 (B_u)	1409.33 (A_u)	1410.92 (B_u)	1410.95 (A_u)
1439.59	E_{2g}	1441.11 (B_g)	1441.59 (A_g)	1442.84 (A_g)	1443.49 (B_g)
1446.08	E_{2g}	1447.07 (A_g)	1447.31 (B_g)	1449.17 (A_g)	1449.18 (B_g)
1485.81	B_{2u}	1489.35 (A_u)	1490.12 (B_u)		
1492.28	E_{1u}	1493.14 (B_u)	1493.25 (A_u)	1495.35 (A_u)	1495.52 (B_u)
1533.93	A_{2g}	1535.41 (A_g)	1535.67 (B_g)		
1540.88	B_{1u}	1543.10 (B_u)	1543.35 (A_u)		
1591.25	A_{1g}	1591.81 (B_g)	1592.17 (A_g)		

Continued on next page

Isolated Molecule Frequency (cm^{-1})	Irrep	Equivalent frequencies (cm^{-1}) and irreps in γ-coronene			
1607.70	E_{1u}	1607.19 (B_u)	1608.03 (A_u)	1609.64 (A_u)	1609.96 (B_u)
1607.72	E_{2g}	1608.69 (B_g)	1608.88 (A_g)	1609.95 (A_g)	1610.50 (B_g)
3088.11	A_{2g}	These involve out of plane motions of only the hydrogen atoms and do not match those calculated in the crystalline structure			
3088.68	E_{1u}				
3089.54	E_{2g}				
3089.91	B_{1u}				
3105.86	B_{2u}				
3106.44	E_{2g}				
3107.48	E_{1u}				
3108.39	A_{1g}				

A.3 Isolated molecule and β-coronene intramolecular vibrations

Table A.2: Comparison of calculated frequencies for an isolated coronene molecule with the associated intramolecular frequencies calculated for β-coronene. Modes were compared using the dot product method and verified by visualising the vibrations of each molecule in the crystal and comparing to the isolated molecule vibrations.

Isolated Molecule Frequency (cm^{-1})	Irrep	Equivalent frequencies (cm^{-1}) and irreps in β-coronene			
82.53	E_{2u}	95.78 (A_u)	99.56 (B_u)	107.79 (A_u)	125.25 (B_u)
119.12	A_{2u}	128.78 (A_u)	153.34 (B_u)		
156.15	B_{1g}	172.97 (A_g)	175.60 (B_g)		
216.77	B_{2g}	230.12 (A_g)	242.12 (B_g)		
283.59	E_{1g}	288.77 (A_g)	297.55 (B_g)	299.95 (A_g)	303.30 (B_g)
289.59	E_{2u}	299.02 (A_u)	301.26 (B_u)	308.28 (A_u)	311.24 (B_u)
360.22	E_{2g}	361.22 (B_g)	365.05 (A_g)	365.76 (A_g)	365.84 (B_g)
375.75	E_{1u}	376.34 (B_u)	377.37 (A_u)	378.14 (B_u)	379.87 (A_u)
441.13	E_{1g}	444.03 (A_g)	445.44 (B_g)	446.25 (A_g)	448.27 (B_g)
466.11	B_{2u}	468.44 (A_u)	470.48 (B_u)		
478.58	A_{1g}	484.37 (B_g)	487.51 (A_g)		
482.80	E_{2g}	482.10 (B_g)	482.20 (A_g)	484.34 (A_g)	487.27 (B_g)
517.53	A_{1u}	526.40 (A_u)	526.52 (B_u)		
536.01	E_{2u}	532.12 (A_u)	533.25 (B_u)	534.26 (A_u)	
543.38	A_{2u}	539.75 (A_u)	541.31 (B_u)	549.04 (B_u)	
550.73	B_{1u}	552.31 (A_u)	556.34 (B_u)		
622.44	A_{2g}	623.69 (B_g)	624.07 (A_g)		
641.47	B_{2g}	642.41 (A_g)	647.35 (B_g)		
656.36	E_{1g}	653.79 (A_g)	663.22 (B_g)	664.58 (A_g)	667.64 (B_g)
667.40	B_{1u}	667.30 (B_u)	669.76 (A_u)		
674.58	E_{2g}	675.98 (B_g)	677.89 (A_g)	679.29 (A_g)	679.61 (B_g)
746.43	B_{1g}	749.11 (A_g)	753.35 (B_g)		
757.74	E_{2u}	755.21 (A_u)	758.30 (B_u)	761.87 (A_u)	763.10 (B_u)
761.34	E_{1u}	764.78 (A_u)	766.07 (B_u)	768.67 (A_u)	773.54 (B_u)
806.69	E_{1u}	811.35 (B_u)	811.36 (A_u)	812.02 (B_u)	813.35 (A_u)
808.54	E_{2u}	808.85 (A_u)	809.97 (B_u)	815.18 (A_u)	816.40 (B_u)

Continued on next page

Isolated Molecule Frequency (cm^{-1})	Irrep	Equivalent frequencies (cm^{-1}) and irreps in β-coronene			
828.74	E_{1g}	825.19 (A_g)	833.89 (B_g)	838.93 (A_g)	844.44 (B_g)
846.74	A_{2u}	838.32 (A_u)	848.04 (B_u)		
855.77	B_{2g}	854.30 (A_g)	854.41 (B_g)		
917.26	A_{2g}	918.70 (B_g)	919.11 (A_g)		
930.84	A_{1u}	938.02 (A_g)	941.02 (A_u)	941.38 (A_u)	
938.20	E_{1g}	942.34 (A_g)	943.51 (B_u)	949.62 (B_g)	
948.10	E_{2u}	950.30 (A_u)	954.21 (B_u)	954.96 (B_g)	
952.71	B_{2g}	966.34 (A_g)	968.69 (B_u)	975.24 (B_g)	
985.89	E_{2g}	988.14 (A_g)	989.95 (B_g)	991.07 (A_g)	992.56 (B_g)
1025.17	A_{1g}	1027.93 (A_g)	1029.97 (B_g)		
1125.28	E_{1u}	1124.91 (B_u)	1125.43 (A_u)	1129.63 (A_u)	1130.87 (B_u)
1135.46	B_{2u}	1139.99 (A_u)	1140.42 (B_u)		
1147.35	E_{2g}	1148.24 (A_g)	1148.31 (B_g)	1151.40 (A_g)	1152.75 (B_g)
1153.57	B_{1u}	1157.04 (A_u)	1160.24 (B_u)		
1207.75	E_{1u}	1207.79 (B_u)	1210.28 (A_u)	1215.09 (A_u)	1215.84 (B_u)
1214.13	B_{2u}	1220.10 (A_u)	1220.96 (B_u)		
1214.87	A_{1g}	1218.05 (A_g)	1219.72 (B_g)		
1221.83	A_{2g}	1222.72 (B_g)	1228.63 (A_g)		
1228.53	E_{2g}	1232.94 (A_g)	1233.06 (B_g)	1235.79 (A_g)	1235.87 (B_g)
1306.62	E_{1u}	1309.05 (A_u)	1309.52 (B_u)	1310.15 (B_u)	1313.08 (A_u)
1361.43	B_{2u}	1365.54 (B_u)	1365.98 (A_u)		
1364.30	A_{1g}	1368.39 (A_g)	1368.53 (B_g)		
1391.39	E_{2g}	1393.81 (A_g)	1395.47 (A_g)	1396.01 (B_g)	1397.82 (B_g)
1399.56	B_{1u}	1401.63 (A_u)	1405.23 (B_u)		
1406.88	E_{1u}	1409.71 (B_u)	1410.20 (A_u)	1410.74 (A_u)	1411.05 (B_u)
1439.59	E_{2g}	1442.23 (A_g)	1443.14 (B_g)	1443.40 (B_g)	1443.68 (A_g)
1446.08	E_{2g}	1448.98 (B_g)	1449.47 (A_g)	1449.87 (B_g)	1449.95 (A_g)
1485.81	B_{2u}	1488.85 (A_u)	1490.07 (B_u)		
1492.28	E_{1u}	1495.52 (B_u)	1495.84 (A_u)	1496.67 (A_u)	1496.87 (B_u)
1533.93	A_{2g}	1537.57 (B_g)	1538.38 (A_g)		
1540.88	B_{1u}	1543.42 (A_u)	1543.50 (B_u)		
1591.25	A_{1g}	1593.45 (B_g)	1594.08 (A_g)		

Continued on next page

Isolated Molecule Frequency (cm^{-1})	Irrep	Equivalent frequencies (cm^{-1}) and irreps in β-coronene			
1607.70	E_{1u}	1609.87 (B_u)	1610.54 (A_u)	1610.65 (B_u)	1611.20 (A_u)
1607.72	E_{2g}	1609.61 (B_g)	1609.93 (A_g)	1610.20 (A_g)	1611.11 (B_g)
3088.11	A_{2g}	These involve out of plane motions of only the hydrogen atoms and do not match those calculated in the crystalline structure			
3088.68	E_{1u}				
3089.54	E_{2g}				
3089.91	B_{1u}				
3105.86	B_{2u}				
3106.44	E_{2g}				
3107.48	E_{1u}				
3108.39	A_{1g}				

Appendix B

Polarisation dependence of intramolecular vibrations

Figures B-1 and B-2 show polarised Raman measurements of γ- and β-coronene respectively with the output analyser in a horizontal position. Analysis of these spectra and equivalent figures with the output analyser in a vertical position are detailed in Chapter 4.

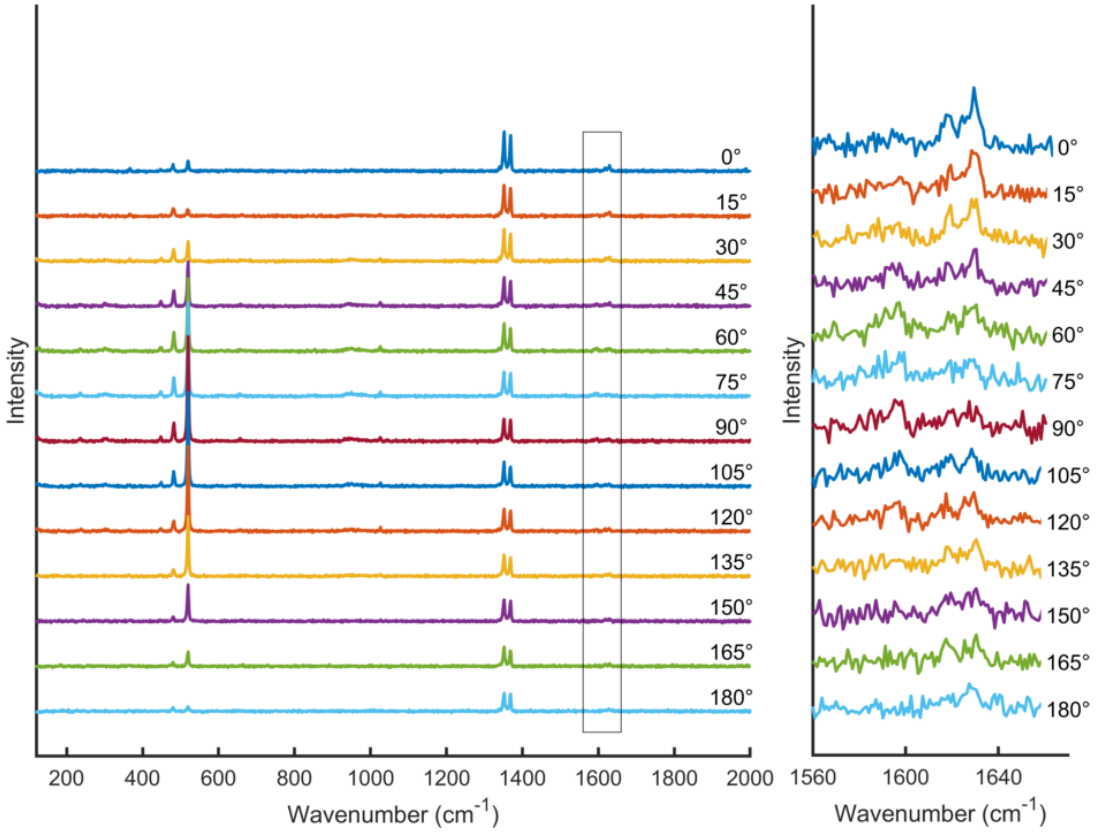

Figure B-1: Polarisation angle dependence of Raman spectra of a γ-coronene crystal at room temperature with a horizontal output analyser. Individual spectra are offset for clarity. Background envelopes have been removed. The region highlighted by the box in (a) is shown in greater detail in (b).

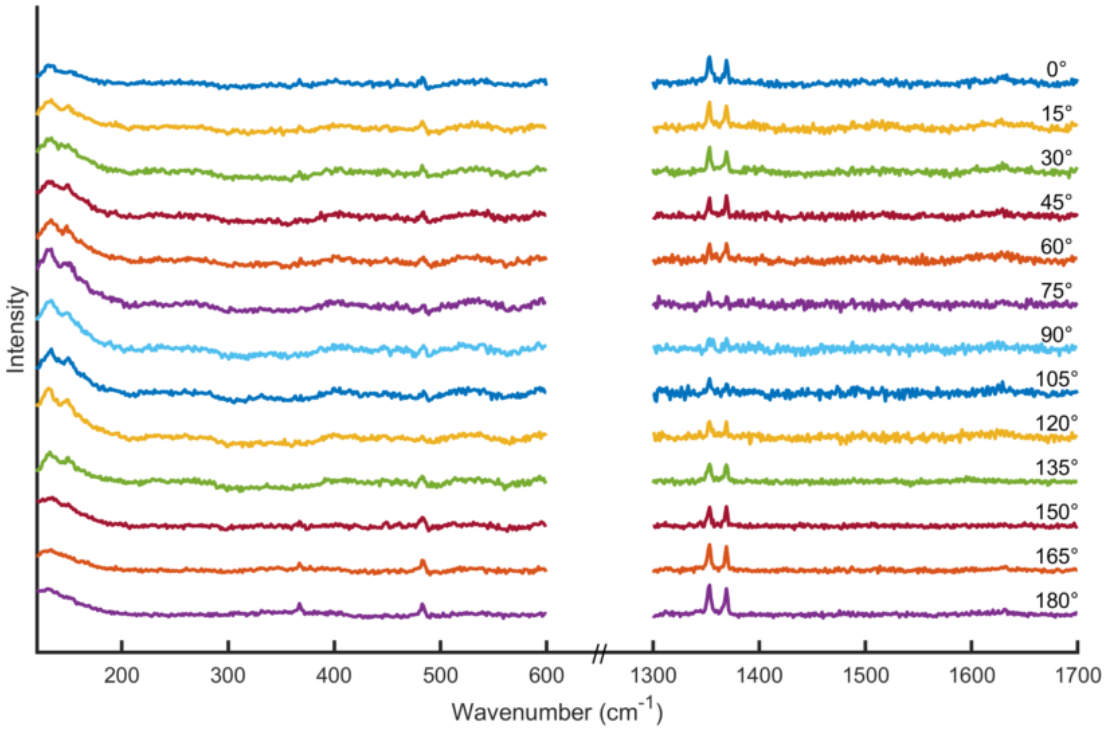

Figure B-2: Polarisation angle dependence of Raman spectra of a β-coronene crystal fragment at 110 K with a horizontal output analyser. Individual spectra are offset for clarity. Background envelopes have been removed. Due to excessive background noise the range 600 cm^{-1} to 1300 cm^{-1} is excluded.

Bibliography

[1] Xi Zhang, P Bauerle, T Aida, P Skabara, and C Kagan. Organic Electronics for a Better Tomorrow: Innovation, Accessibility, Sustainability. In *A White Pap. From Chem. Sci. Soc. Summit San Fr. California, United States*. 2012.

[2] Neena Pandey, Abhipsa Pal, et al. Impact of digital surge during Covid-19 pandemic: A viewpoint on research and practice. *International Journal of Information Management*, page 102171, 2020.

[3] Joseph S Chang, Antonio F Facchetti, and Robert Reuss. A circuits and systems perspective of organic/printed electronics: Review, challenges, and contemporary and emerging design approaches. *IEEE Journal on Emerging and Selected Topics in Circuits and Systems*, 7(1):7–26, 2017.

[4] Beatrice Fraboni, Alessandro Fraleoni-Morgera, Yves Geerts, Alberto Morpurgo, and Vitaly Podzorov. Organic single crystals: An essential step to new physics and higher performances of optoelectronic devices. *Advanced Functional Materials*, 26(14):2229–2232, 2016.

[5] Vitaly Podzorov. Organic single crystals: Addressing the fundamentals of organic electronics. *MRS Bulletin*, 38(1):15–24, 2013.

[6] Hui Jiang and Wenping Hu. The emergence of organic single-crystal electronics. *Angewandte Chemie International Edition*, 59(4):1408–1428, 2020.

[7] Aldo Brillante, Ivano Bilotti, Raffaele Guido Della Valle, Elisabetta Venuti, and Alberto Girlando. Probing polymorphs of organic semiconductors by lattice phonon Raman microscopy. *CrystEngComm*, 10(8):937–946, 2008.

[8] Jason Potticary, Lui R Terry, Christopher Bell, Alexandros N Papanikolopoulos, Peter CM Christianen, Hans Engelkamp, Andrew M Collins, Claudio Fontanesi, Gabriele Kociok-Köhn, Simon Crampin, et al. An unforeseen polymorph of

coronene by the application of magnetic fields during crystal growth. *Nature Communications*, 7, 2016.

[9] Ajit Ram Verma and Padmanabhan Krishna. *Polymorphism and Polytypism in Crystals*. John Wiley & Sons Inc, 1965.

[10] Joel Bernstein. *Polymorphism in Molecular Crystals*. Oxford University Press, New York, 2002. ISBN 0198506058.

[11] Gregory JO Beran. Modeling polymorphic molecular crystals with electronic structure theory. *Chemical Reviews*, 116(9):5567–5613, 2016.

[12] Mariana Rossi, Piero Gasparotto, and Michele Ceriotti. Anharmonic and quantum fluctuations in molecular crystals: A first-principles study of the stability of paracetamol. *Physical Review Letters*, 117(11):115702, 2016.

[13] Eun Hee Lee. A practical guide to pharmaceutical polymorph screening & selection. *Asian Journal of Pharmaceutical Sciences*, 9(4):163–175, 2014.

[14] Christoph G Salzmann, Paolo G Radaelli, Ben Slater, and John L Finney. The polymorphism of ice: Five unresolved questions. *Physical Chemistry Chemical Physics*, 13(41):18468–18480, 2011.

[15] Ryo Yamane, Kazuki Komatsu, Jun Gouchi, Yoshiya Uwatoko, Shinichi Machida, Takanori Hattori, Hayate Ito, and Hiroyuki Kagi. New diversity form of ice polymorphism: Discovery of second hydrogen ordered phase of ice VI. 2020. arXiv preprint arXiv:2006.10928 [cond-mat.mtrl-sci].

[16] Kenta Hongo, Mark A Watson, Roel S Sánchez-Carrera, Toshiaki Iitaka, and Alán Aspuru-Guzik. Failure of conventional density functionals for the prediction of molecular crystal polymorphism: A quantum Monte Carlo study. *The Journal of Physical Chemistry Letters*, 1(12):1789–1794, 2010.

[17] Jonas Nyman and Graeme M Day. Static and lattice vibrational energy differences between polymorphs. *CrystEngComm*, 17(28):5154–5165, 2015.

[18] Aurora J Cruz-Cabeza, Susan M Reutzel-Edens, and Joel Bernstein. Facts and fictions about polymorphism. *Chemical Society Reviews*, 44(23):8619–8635, 2015.

[19] John A Pople. Nobel lecture: Quantum chemical models. *Reviews of Modern Physics*, 71(5):1267, 1999.

[20] CCDC. CSP Blind Tests, 2017. URL www.ccdc.cam.ac.uk/Community/initiatives/cspblindtests.

[21] José Luis Amorós and Marisa Amorós. *Molecular Crystals; Their Transforms and Diffuse Scattering*, volume 6. Wiley, 1968.

[22] Markus Schwoerer and Hans Christoph Wolf. Molecular and lattice dynamics in organic molecular crystals. *Organic Molecular Solids*, pages 89–124, 2008.

[23] Gautam R Desiraju and A Gavezzotti. Crystal structures of polynuclear aromatic hydrocarbons. Classification, rationalization and prediction from molecular structure. *Acta Crystallographica Section B: Structural Science*, 45(5):473–482, 1989.

[24] Mark Botoshansky, Frank H Herbstein, and Moshe Kapon. Towards a complete description of a polymorphic crystal: The example of perylene. *Helvetica Chimica Acta*, 86(4):1113–1128, 2003.

[25] Yan Zhao and Donald G Truhlar. A prototype for graphene material simulation: Structures and interaction potentials of coronene dimers. *The Journal of Physical Chemistry C*, 112(11):4061–4067, 2008.

[26] Henna Ruuska and Tapani A Pakkanen. Ab initio study of interlayer interaction of graphite: Benzene- coronene and coronene dimer two-layer models. *The Journal of Physical Chemistry B*, 105(39):9541–9547, 2001.

[27] Acrísio Lins de Aguiar, Aldilene Saraiva-Souza, Zachary Bullard, Dayvison Weber Maia, Antônio Gomes Souza Filho, Eduardo Costa Girão, and Vincent Meunier. Electronic and magnetic structures of coronene-based graphitic nanoribbons. *Physical Chemistry Chemical Physics*, 16(8):3603–3609, 2014.

[28] S Blumstengel, S Sadofev, and F Henneberger. Electronic coupling of optical excitations in organic/inorganic semiconductor hybrid structures. *New Journal of Physics*, 10(6):065010, 2008.

[29] Stephen R Langhoff. Theoretical infrared spectra for polycyclic aromatic hydrocarbon neutrals, cations, and anions. *The Journal of Physical Chemistry*, 100(8): 2819–2841, 1996.

[30] Yoshihiro Kubozono, Hiroki Mitamura, Xuesong Lee, Xuexia He, Yusuke Yamanari, Yosuke Takahashi, Yuta Suzuki, Yumiko Kaji, Ritsuko Eguchi, Koki Akaike, et al. Metal-intercalated aromatic hydrocarbons: A new class of carbon-based superconductors. *Physical Chemistry Chemical Physics*, 13(37):16476–16493, 2011.

[31] iRocks.com Rob Lavinsky. MD-258272 Carpathite, Accessed 23/10/2020. URL https://www.irocks.com/minerals/specimen/14902.

[32] Koichi Ohno, Takashi Kajiwara, and Hiroo Inokuchi. Vibrational analysis of electronic transition bands of coronene. *Bulletin of the Chemical Society of Japan*, 45(4):996–1004, 1972.

[33] Takahiro Yamamoto, Shigeru Nakatani, Tadashi Nakamura, Ken-ichi Mizuno, Atsuo H Matsui, Yuichi Akahama, and Haruki Kawamura. Exciton-phonon coupling and pressure-induced structural phase changes in coronene crystals. *Chemical Physics*, 184(1-3):247–254, 1994.

[34] S Nakatani, T Nakamura, K Mizuno, and AH Matsui. Interband and intraband exciton scattering in corenene crystal. *Journal of Luminescence*, 58(1-6):343–346, 1994.

[35] Anita M Orendt, Julio C Facelli, Shi Bai, Amarjit Rai, Michele Gossett, Lawrence T Scott, Juliana Boerio-Goates, Ronald J Pugmire, and David M Grant. Carbon-13 shift tensors in polycyclic aromatic compounds. 8. 1 A low-temperature NMR study of coronene and corannulene. *The Journal of Physical Chemistry A*, 104(1):149–155, 2000.

[36] R Totoki, T Aoki-Matsumoto, and K Mizuno. Density of states of the lowest exciton band and the exciton bandwidth in coronene single crystals. *Journal of Luminescence*, 112(1):308–311, 2005.

[37] Wen-Kuei Wong and Edgar F westrum Jr. Thermodynamics of polynuclear aromatic molecules: II. Low-temperature thermal properties of perylene, coronene, and naphthacene. *Molecular Crystals and Liquid Crystals*, 61(3-4):207–228, 1980.

[38] Jason Potticary, Rebecca Boston, Liana Vella-Zarb, Alex Few, Christopher Bell, and Simon R Hall. Low temperature magneto-morphological characterisation of coronene and the resolution of previously observed unexplained phenomena. *Scientific Reports*, 6, 2016.

[39] Stephen J Blundell and Katherine M Blundell. *Concepts in Thermal Physics*. Oxford Univ. Press, 2006.

[40] George Socrates. *Thermodynamics and Statistical Mechanics*. Butterworths, 1971.

[41] Roger Bowley and Mariana Sanchez. *Introductory Statistical Mechanics*. Clarendon Press Oxford, 1996.

[42] M. Ferrabone. The thermal decomposition of magnesite, 2016. URL www.theochem.unito.it/crystal_tuto/mssc2013_cd/tutorials/index.html.

[43] Mermin Ashcroft and N. David Mermin. *Solid State Physics*. Holt, Rinehart and Winston, New York ; London, 1977. ISBN 0030839939.

[44] JO Hirschfelder and JW Linnett. The energy of interaction between two hydrogen atoms. *The Journal of Chemical Physics*, 18(1):130–142, 1950.

[45] Richard A Swalin and Allen L King. Thermodynamics of solids. *American Journal of Physics*, 30(10):778–778, 1962.

[46] Atsushi Togo, Laurent Chaput, Isao Tanaka, and Gilles Hug. First-principles phonon calculations of thermal expansion in Ti_3SiC_2, Ti_3AlC_2, and Ti_3GeC_2. *Physical Review B*, 81(17):174301, 2010.

[47] Atsushi Togo and Isao Tanaka. First principles phonon calculations in materials science. *Scripta Materialia*, 108:1–5, 2015.

[48] Jonas Nyman and Graeme M Day. Modelling temperature-dependent properties of polymorphic organic molecular crystals. *Physical Chemistry Chemical Physics*, 18(45):31132–31143, 2016.

[49] Sean P Delaney, Tiffany M Smith, Duohai Pan, Shawn X Yin, and Timothy M Korter. Low-temperature phase transition in crystalline aripiprazole leads to an eighth polymorph. *Crystal Growth & Design*, 14(10):5004–5010, 2014.

[50] National Center for Biotechnology Information. PubChem Compound Summary for CID 60795, Aripiprazole. URL https://pubchem.ncbi.nlm.nih.gov/compound/Aripiprazole.

[51] Kai-Erik Peiponen, Axel Zeitler, and Makoto Kuwata-Gonokami. *Terahertz Spectroscopy and Imaging*, volume 171. Springer, 2013.

[52] Jens Neu and Charles A Schmuttenmaer. Tutorial: An introduction to terahertz time domain spectroscopy (THz-TDS). *Journal of Applied Physics*, 124(23):231101, 2018.

[53] Harold Y Hwang, Sharly Fleischer, Nathaniel C Brandt, Bradford G Perkins Jr, Mengkun Liu, Kebin Fan, Aaron Sternbach, Xin Zhang, Richard D Averitt, and Keith A Nelson. A review of non-linear terahertz spectroscopy with ultrashort tabletop-laser pulses. *Journal of Modern Optics*, 62(18):1447–1479, 2015.

[54] Edward PJ Parrott and J Axel Zeitler. Terahertz time-domain and low-frequency Raman spectroscopy of organic materials. *Applied Spectroscopy*, 69(1):1–25, 2015.

[55] Peter J Larkin. *Infrared and Raman Spectroscopy: Principles and Spectral Interpretation*. Elsevier, Amsterdam [Netherlands] ; Boston, 2011. ISBN 1-4933-0127-6.

[56] Mark Ladd. *Symmetry and Group Theory in Chemistry*. Elsevier, 1998.

[57] Robert S Mulliken. Report on notation for the spectra of polyatomic molecules. *The Journal of Chemical Physics*, 23(11):1997–2011, 1955.

[58] Richard M Martin. *Electronic Structure: Basic Theory and Practical Methods*. Cambridge University Press, 2004.

[59] Feliciano Giustino. *Materials Modelling Using Density Functional Theory: Properties and Predictions*. Oxford University Press, 2014.

[60] Pierre Hohenberg and Walter Kohn. Inhomogeneous electron gas. *Physical Review*, 136(3B):B864, 1964.

[61] Walter Kohn and Lu Jeu Sham. Self-consistent equations including exchange and correlation effects. *Physical Review*, 140(4A):A1133, 1965.

[62] Narbe Mardirossian and Martin Head-Gordon. Thirty years of density functional theory in computational chemistry: An overview and extensive assessment of 200 density functionals. *Molecular Physics*, 115(19):2315–2372, 2017.

[63] Kieron Burke. Perspective on density functional theory. *The Journal of Chemical Physics*, 136(15):150901, 2012.

[64] John P Perdew, Kieron Burke, and Matthias Ernzerhof. Generalized gradient approximation made simple. *Physical Review Letters*, 77(18):3865, 1996.

[65] Yingkai Zhang and Weitao Yang. Comment on "Generalized gradient approximation made simple". *Physical Review Letters*, 80(4):890, 1998.

[66] Axel D Becke. Density-functional exchange-energy approximation with correct asymptotic behavior. *Physical Review A*, 38(6):3098, 1988.

[67] Chengteh Lee, Weitao Yang, and Robert G Parr. Development of the Colle-Salvetti correlation-energy formula into a functional of the electron density. *Physical Review B*, 37(2):785, 1988.

[68] Axel D Becke. Density-functional thermochemistry. III. The role of exact exchange. *The Journal of Chemical Physics*, 98(7):5648–5652, 1993.

[69] John P Perdew, Matthias Ernzerhof, and Kieron Burke. Rationale for mixing exact exchange with density functional approximations. *The Journal of Chemical Physics*, 105(22):9982–9985, 1996.

[70] John P Perdew and Yue Wang. Accurate and simple analytic representation of the electron-gas correlation energy. *Physical Review B*, 45(23):13244, 1992.

[71] Yoshitaka Umeno, Takahiro Shimada, Yusuke Kinoshita, and Takayuki Kitamura. *Methodology of Quantum Mechanics/Atomic Simulations. In: Multiphysics in Nanostructures. Nanostructure Science and Technology.* Springer, 2017.

[72] Georg Kresse and Jürgen Hafner. Ab initio molecular dynamics for liquid metals. *Physical Review B*, 47(1):558, 1993.

[73] DE Ellis. *Density Functional Theory of Molecules, Clusters, and Solids*, volume 12. Springer Science & Business Media, 1995.

[74] C Ennis, R Auchettl, DRT Appadoo, and EG Robertson. Density functional theory for prediction of far-infrared vibrational frequencies: Molecular crystals of astrophysical interest. *Monthly Notices of the Royal Astronomical Society*, 471(4): 4265–4274, 2017.

[75] Xi Wu, Feiyu Kang, Wenhui Duan, and Jia Li. Density functional theory calculations: A powerful tool to simulate and design high-performance energy storage and conversion materials. *Progress in Natural Science: Materials International*, 29(3):247–255, 2019.

[76] Francisco Colmenero, Laura J Bonales, Joaquín Cobos, and Vicente Timon. Density functional theory study of the thermodynamic and Raman vibrational properties of γ-UO_3 polymorph. *The Journal of Physical Chemistry C*, 121(27): 14507–14516, 2017.

[77] Matthew D King, William D Buchanan, and Timothy M Korter. Application of London-type dispersion corrections to the solid-state density functional theory simulation of the terahertz spectra of crystalline pharmaceuticals. *Physical Chemistry Chemical Physics*, 13(10):4250–4259, 2011.

[78] Kapil Adhikari, Kenneth M Flurchick, and Loredana Valenzano. A hybrid density functional study on the effects of pressure on paracetamol and aspirin polymorphs. *Computational and Theoretical Chemistry*, 1062:90–98, 2015.

[79] Bhupesh Goyal, Kinshuk Raj Srivastava, Anil Kumar, G Naresh Patwari, and Susheel Durani. Probing the role of electrostatics of polypeptide main-chain in protein folding by perturbing N-terminal residue stereochemistry: DFT study with oligoalanine models. *RSC Advances*, 6(114):113611–113619, 2016.

[80] Jacky Even, Laurent Pedesseau, Eric Tea, Samy Almosni, Alain Rolland, Cédric Robert, Jean-Marc Jancu, Charles Cornet, Claudine Katan, Jean-François Guillemoles, et al. Density functional theory simulations of semiconductors for photovoltaic applications: Hybrid organic-inorganic perovskites and III/V heterostructures. *International Journal of Photoenergy*, 2014, 2014.

[81] Camilla Pellegrini, Henning Glawe, and Antonio Sanna. Density functional theory of superconductivity in doped tungsten oxides. *Physical Review Materials*, 3(6): 064804, 2019.

[82] Chris J Pickard and RJ Needs. High-pressure phases of silane. *Physical Review Letters*, 97(4):045504, 2006.

[83] Olga Degtyareva, Miguel Martínez Canales, Aitor Bergara, Xiao-Jia Chen, Yang Song, Viktor V Struzhkin, Ho-kwang Mao, and Russell J Hemley. Crystal structure of SiH_4 at high pressure. *Physical Review B*, 76(6):064123, 2007.

[84] Ming Wah Wong. Vibrational frequency prediction using density functional theory. *Chemical Physics Letters*, 256(4-5):391–399, 1996.

[85] Dirk Porezag and Mark R Pederson. Infrared intensities and Raman-scattering activities within density-functional theory. *Physical Review B*, 54(11):7830, 1996.

[86] Philip J Hasnip, Keith Refson, Matt IJ Probert, Jonathan R Yates, Stewart J Clark, and Chris J Pickard. Density functional theory in the solid state. *Philosophical Transactions of the Royal Society A: Mathematical, Physical and Engineering Sciences*, 372(2011):20130270, 2014.

[87] Tomáš Bučko, Sébastien Lebègue, Jürgen Hafner, and Janos G Angyan. Tkatchenko-Scheffler van der Waals correction method with and without self-consistent screening applied to solids. *Physical Review B*, 87(6):064110, 2013.

[88] Stefan Grimme. Density functional theory with London dispersion corrections. *Wiley Interdisciplinary Reviews: Computational Molecular Science*, 1(2):211–228, 2011.

[89] Jiří Klimeš and Angelos Michaelides. Perspective: Advances and challenges in treating van der Waals dispersion forces in density functional theory. *The Journal of Chemical Physics*, 137(12):120901, 2012.

[90] Florian Brown-Altvater, Tonatiuh Rangel, and Jeffrey B Neaton. Ab initio phonon dispersion in crystalline naphthalene using van der Waals density functionals. *Physical Review B*, 93(19):195206, 2016.

[91] Kyuho Lee, Éamonn D Murray, Lingzhu Kong, Bengt I Lundqvist, and David C Langreth. Higher-accuracy van der Waals density functional. *Physical Review B*, 82(8):081101, 2010.

[92] Stefan Grimme. Semiempirical GGA-type density functional constructed with a long-range dispersion correction. *Journal of Computational Chemistry*, 27(15): 1787–1799, 2006.

[93] Stefan Grimme. Accurate description of van der Waals complexes by density functional theory including empirical corrections. *Journal of Computational Chemistry*, 25(12):1463–1473, 2004.

[94] Thomas R Juliano Jr and Timothy M Korter. London force correction disparity in the modeling of crystalline asparagine and glutamine. *The Journal of Physical Chemistry A*, 118(51):12221–12228, 2014.

[95] Matthew D King and Timothy M Korter. Modified corrections for London forces in solid-state density functional theory calculations of structure and lattice dynamics of molecular crystals. *The Journal of Physical Chemistry A*, 116(25):6927–6934, 2012.

[96] Matthew D King and Timothy M Korter. Application of London-type dispersion corrections in solid-state density functional theory for predicting the temperature-dependence of crystal structures and terahertz spectra. *Crystal Growth & Design*, 11(5):2006–2010, 2011.

[97] Matthew D King, Wayne Ouellette, and Timothy M Korter. Noncovalent interactions in paired DNA nucleobases investigated by terahertz spectroscopy and solid-state density functional theory. *The Journal of Physical Chemistry A*, 115 (34):9467–9478, 2011.

[98] Matthew D King, Thomas N Blanton, Scott T Misture, and Timothy M Korter. Prediction of the unknown crystal structure of creatine using fully quantum mechanical methods. *Crystal Growth & Design*, 11(12):5733–5740, 2011.

[99] Igor Fedorov, Yurii Zhuravlev, and Victor Berveno. Properties of crystalline coronene: Dispersion forces leading to a larger van der Waals radius for carbon. *Physica Status Solidi (B)*, 249(7):1438–1444, 2012.

[100] R Scott Rowland and Robin Taylor. Intermolecular nonbonded contact distances in organic crystal structures: Comparison with distances expected from van der Waals radii. *The Journal of Physical Chemistry*, 100(18):7384–7391, 1996.

[101] Axel D Becke and Erin R Johnson. Exchange-hole dipole moment and the dispersion interaction. *The Journal of Chemical Physics*, 122(15):154104, 2005.

[102] János G Ángyán. On the exchange-hole model of London dispersion forces. *The Journal of Chemical Physics*, 127(2):024108, 2007.

[103] Axel D Becke and Erin R Johnson. Exchange-hole dipole moment and the dispersion interaction revisited. *The Journal of Chemical Physics*, 127(15):154108, 2007.

[104] Andreas Heßelmann. Derivation of the dispersion energy as an explicit density-and exchange-hole functional. *The Journal of Chemical Physics*, 130(8):084104, 2009.

[105] Alexandre Tkatchenko and Matthias Scheffler. Accurate molecular van der Waals interactions from ground-state electron density and free-atom reference data. *Physical Review Letters*, 102(7):073005, 2009.

[106] Stefan Grimme, Jens Antony, Stephan Ehrlich, and Helge Krieg. A consistent and accurate ab initio parametrization of density functional dispersion correction (DFT-D) for the 94 elements H-Pu. *The Journal of Chemical Physics*, 132(15): 154104, 2010.

[107] Stefan Grimme, Stephan Ehrlich, and Lars Goerigk. Effect of the damping function in dispersion corrected density functional theory. *Journal of Computational Chemistry*, 32(7):1456–1465, 2011.

[108] X Chu and A Dalgarno. Linear response time-dependent density functional theory for van der Waals coefficients. *The Journal of Chemical Physics*, 121(9):4083–4088, 2004.

[109] Petr Jurečka, Jiří Šponer, Jiří Černỳ, and Pavel Hobza. Benchmark database of accurate (MP2 and CCSD (T) complete basis set limit) interaction energies of small model complexes, DNA base pairs, and amino acid pairs. *Physical Chemistry Chemical Physics*, 8(17):1985–1993, 2006.

[110] A Otero-De-La-Roza and Erin R Johnson. A benchmark for non-covalent interactions in solids. *The Journal of Chemical Physics*, 137(5):054103, 2012.

[111] Max Dion, Henrik Rydberg, Elsebeth Schröder, David C Langreth, and Bengt I Lundqvist. Van der Waals density functional for general geometries. *Physical Review Letters*, 92(24):246401, 2004.

[112] Susumu Yanagisawa, Koji Okuma, Takeshi Inaoka, and Ikutaro Hamada. Recent progress in predicting structural and electronic properties of organic solids with the van der Waals density functional. *Journal of Electron Spectroscopy and Related Phenomena*, 204:159–167, 2015.

[113] Jiří Klimeš, David R Bowler, and Angelos Michaelides. Chemical accuracy for the van der Waals density functional. *Journal of Physics: Condensed Matter*, 22 (2):022201, 2009.

[114] Alexandre Tkatchenko, Robert A DiStasio Jr, Roberto Car, and Matthias Scheffler. Accurate and efficient method for many-body van der Waals interactions. *Physical Review Letters*, 108(23):236402, 2012.

[115] Alberto Ambrosetti, Anthony M Reilly, Robert A DiStasio Jr, and Alexandre Tkatchenko. Long-range correlation energy calculated from coupled atomic response functions. *The Journal of Chemical Physics*, 140(18):18A508, 2014.

[116] Anthony M Reilly and Alexandre Tkatchenko. Understanding the role of vibrations, exact exchange, and many-body van der Waals interactions in the cohesive properties of molecular crystals. *The Journal of Chemical Physics*, 139(2):024705, 2013.

[117] Hui Zhang and Shaoqing Wang. Vibration effects on the structural stability of Al-Ti intermetallics by first-principles calculations. *Journal of Materials Science & Technology*, 26(12):1071–1077, 2010.

[118] Michael T Ruggiero and J Axel Zeitler. Resolving the origins of crystalline anharmonicity using terahertz time-domain spectroscopy and ab initio simulations. *The Journal of Physical Chemistry B*, 120(45):11733–11739, 2016.

[119] Zbigniew A Dreger, Yuchuan Tao, Boris B Averkiev, Yogendra M Gupta, and Thomas M Klapotke. High-pressure stability of energetic crystal of dihydroxylammonium 5, 5-bistetrazole-1, 1-diolate: Raman spectroscopy and DFT calculations. *The Journal of Physical Chemistry B*, 119(22):6836–6847, 2015.

[120] Natalia Bedoya-Martinez, Andrea Giunchi, Tommaso Salzillo, Elisabetta Venuti, Raffaele Guido Della Valle, and Egbert Zojer. Toward a reliable description of the lattice vibrations in organic molecular crystals: The impact of van der Waals interactions. *Journal of Chemical Theory and Computation*, 14(8):4380–4390, 2018.

[121] GJ Kearley, MR Johnson, and J Tomkinson. Intermolecular interactions in solid benzene. *The Journal of Chemical Physics*, 124(4):044514, 2006.

[122] Jongtaek Kim, O-Pil Kwon, Fabian DJ Brunner, Mojca Jazbinsek, Seung-Heon Lee, and Peter Gunter. Phonon modes of organic electro-optic molecular crystals for terahertz photonics. *The Journal of Physical Chemistry C*, 119(18):10031–10039, 2015.

[123] Jongtaek Kim, O-Pil Kwon, Mojca Jazbinsek, Young Choon Park, and Yoon Sup Lee. First-principles calculation of terahertz absorption with dispersion correction of 2, 2-Bithiophene as model compound. *The Journal of Physical Chemistry C*, 119(22):12598–12607, 2015.

[124] Sean P Delaney, Duohai Pan, Shawn X Yin, Tiffany M Smith, and Timothy M Korter. Evaluating the roles of conformational strain and cohesive binding in crystalline polymorphs of aripiprazole. *Crystal Growth & Design*, 13(7):2943–2952, 2013.

[125] IA Fedorov, F Marsusi, TP Fedorova, and YN Zhuravlev. First principles study of the electronic structure and phonon dispersion of naphthalene under pressure. *Journal of Physics and Chemistry of Solids*, 83:24–31, 2015.

[126] A Van de Walle and G Ceder. Correcting overbinding in local-density-approximation calculations. *Physical Review B*, 59(23):14992, 1999.

[127] Ctirad Červinka, Michal Fulem, Ralf Peter Stoffel, and Richard Dronskowski. Thermodynamic properties of molecular crystals calculated within the quasi-harmonic approximation. *The Journal of Physical Chemistry A*, 120(12):2022–2034, 2016.

[128] Mattias P Andersson and Per Uvdal. New scale factors for harmonic vibrational frequencies using the B3LYP density functional method with the triple-ζ basis set 6-311+ G (d, p). *The Journal of Physical Chemistry A*, 109(12):2937–2941, 2005.

[129] Jamal Lasri, Naser Eltaher Eltayeb, Matti Haukka, and Yousef Alghamdi. Crystal and molecular structure studies of (Z)-N-methyl-C-4-substituted phenyl nitrones

by XRD, DFT, FTIR and NMR methods. *Journal of Molecular Structure*, 1128: 70–78, 2017.

[130] MP Andersson, R Asmundsson, and Per Uvdal. Anharmonic resonances in the C–H stretch region of ethoxy adsorbed on W (110): Vibrational spectroscopy and calculations. *Surface Science*, 532:221–226, 2003.

[131] Alexey Bosak and Michael Krisch. Phonon density of states probed by inelastic x-ray scattering. *Physical Review B*, 72(22):224305, 2005.

[132] Liu Yi Wang, Zhong Lin and Ze Zhang, editors. *X-ray and Neutron Scattering In: Handbook of Nanophase and Nanostructured Materials*. Springer US, 2002. ISBN 978-0-387-23814-2. URL https://doi.org/10.1007/0-387-23814-X_12.

[133] I Natkaniec, EL Bokhenkov, B Dorner, J Kalus, GA Mackenzie, GS Pawley, U Schmelzer, and EF Sheka. Phonon dispersion in d8-naphthalene crystal at 6K. *Journal of Physics C: Solid State Physics*, 13(23):4265, 1980.

[134] Kristian Berland and Per Hyldgaard. Exchange functional that tests the robustness of the plasmon description of the van der Waals density functional. *Physical Review B*, 89(3):035412, 2014.

[135] Nathan S Abraham and Michael R Shirts. Thermal gradient approach for the quasi-harmonic approximation and its application to improved treatment of anisotropic expansion. *Journal of Chemical Theory and Computation*, 14(11):5904–5919, 2018.

[136] Johannes Hoja and Alexandre Tkatchenko. First-principles stability ranking of molecular crystal polymorphs with the DFT+ MBD approach. *Faraday Discussions*, 211:253–274, 2018.

[137] Alessandro Erba. On combining temperature and pressure effects on structural properties of crystals with standard ab initio techniques. *The Journal of Chemical Physics*, 141(12):124115, 2014.

[138] Alessandro Erba, M Shahrokhi, R Moradian, and Roberto Dovesi. On how differently the quasi-harmonic approximation works for two isostructural crystals: Thermal properties of periclase and lime. *The Journal of Chemical Physics*, 142 (4):044114, 2015.

[139] Johannes Hoja, Anthony M Reilly, and Alexandre Tkatchenko. First-principles modeling of molecular crystals: Structures and stabilities, temperature and

pressure. *Wiley Interdisciplinary Reviews: Computational Molecular Science*, 7 (1):e1294, 2017.

[140] Jessica L McKinley and Gregory JO Beran. Identifying pragmatic quasi-harmonic electronic structure approaches for modeling molecular crystal thermal expansion. *Faraday Discussions*, 211:181–207, 2018.

[141] Jessica L McKinley and Gregory JO Beran. Improving predicted nuclear magnetic resonance chemical shifts using the quasi-harmonic approximation. *Journal of Chemical Theory and Computation*, 15(10):5259–5274, 2019.

[142] Ctirad Červinka and Gregory JO Beran. Ab initio thermodynamic properties and their uncertainties for crystalline α-methanol. *Physical Chemistry Chemical Physics*, 19(44):29940–29953, 2017.

[143] Chihiro Hamaguchi and C Hamaguchi. *Basic Semiconductor Physics*, volume 9. Springer, 2010.

[144] Lorenzo Maschio, Bernard Kirtman, Michel Rérat, Roberto Orlando, and Roberto Dovesi. Ab initio analytical Raman intensities for periodic systems through a coupled perturbed Hartree-Fock/Kohn-Sham method in an atomic orbital basis. I. Theory. *The Journal of Chemical Physics*, 139(16):164101, 2013.

[145] AH Matsui and Ken-ichi Mizuno. Crystallization and excitonic luminescence of coronene crystals. *Journal of Physics D: Applied Physics*, 26(8B):B242, 1993.

[146] J Henderson, Matteo Masino, Lauren E Hatcher, G Kociok-Kohn, Tommaso Salzillo, Aldo Brillante, Paul R Raithby, Alberto Girlando, and Enrico Da Como. New polymorphs of perylene: Tetracyanoquinodimethane charge transfer cocrystals. *Crystal Growth & Design*, 18(4):2003–2009, 2018.

[147] Material and Chemical Characterisation Facility (MC^2). URL www.bath.ac.uk/research-facilities/material-and-chemical-characterisation-facility-mc2.

[148] J. Potticary. *Personal communication*. 17/18/2017.

[149] Richard Goddard, Matthias W Haenel, William C Herndon, Carl Krueger, and Maximilian Zander. Crystallization of Large Planar Polycyclic Aromatic Hydrocarbons: The Molecular and Crystal Structures of Hexabenzo [bc, ef, hi, kl, no, qr] coronene and Benzo [1, 2, 3-bc: 4, 5, 6-b'c'] dicoronene. *Journal of the American Chemical Society*, 117(1):30–41, 1995.

[150] Dejan-Krešimir Bučar, Robert W Lancaster, and Joel Bernstein. Disappearing polymorphs revisited. *Angewandte Chemie International Edition*, 54(24):6972–6993, 2015.

[151] T.K. Nielsen and L. Borka. The Polymorphism of Benzocaine Picrate. *Acta Pharm. Suecica*, 9:503–505, 1972.

[152] David H Case, Vijay K Srirambhatla, Rui Guo, Rona E Watson, Louise S Price, Hector Polyzois, Jeremy K Cockcroft, Alastair J Florence, Derek A Tocher, and Sarah L Price. Successful computationally directed templating of metastable pharmaceutical polymorphs. *Crystal Growth & Design*, 18(9):5322–5331, 2018.

[153] N. I. Davydova V. A. Karpova L. A. Klimova M. A. Kovner M. M. Suchinskii A. A. Terekhov L. M. Babkov, V. I. Glyadkovskii and E. V. Shpolskii. Vibration and luminescence spectra, calculation of frequencies and shapes of vibrations and interpretation of vibrational spectra and vibrational structure of coronene luminescence spectra. *Optics and Spectroscopy*, 34:38–40, 1973.

[154] Arvid Bakke, BN Cyvin, JC Whitmer, SJ Cyvin, JE Gustavsen, and P Klaeboe. Condensed Aromatics. Part II. The five-parameter approximation of the in-plane force field of molecular vibrations. *Zeitschrift für Naturforschung A*, 34(5):579–584, 1979.

[155] SJ Cyvin, BN Cyvin, J Brunvoll, JC Whitmer, and P Klaeboe. Condensed aromatics. Part XX. Coronene. *Zeitschrift für Naturforschung A*, 37(12):1359–1368, 1982.

[156] Koichi Ohno and Hideaki Shinohara. Theoretical synthesis of vibrational spectra of polycyclic aromatic hydrocarbons. Infrared spectra of coronene. *Journal of Molecular Structure*, 352:475–479, 1995.

[157] C Joblin, L d'Hendecourt, A Léger, and D Defourneau. Infrared spectroscopy of gas-phase PAH molecules. 1: Role of the physical environment. *Astronomy and Astrophysics*, 281:923–936, 1994.

[158] Ulrich Fleischer and Peter Pulay. Raman spectrum of coronene: A scaled quantum mechanical force field study. *Journal of Raman Spectroscopy*, 29(6):473–481, 1998.

[159] Petar D Todorov, Leonardus W Jenneskens, and Joop H van Lenthe. Assignment of phantom bands in the solid-state infrared and Raman spectra of coronene: The importance of a minute out-of-plane distortion. *The Journal of Chemical Physics*, 132(3):034504, 2010.

[160] George M Sheldrick. Crystal structure refinement with SHELXL. *Acta Crystallogr. C*, 71(1):3–8, 2015.

[161] Christian B Hübschle, George M Sheldrick, and Birger Dittrich. ShelXle: A Qt graphical user interface for SHELXL. *J. Appl. Crystallogr.*, 44(6):1281–1284, 2011.

[162] Nicola Bannister, Jonathan Skelton, Gabriele Kociok-Köhn, Tim Batten, Enrico Da Como, and Simon Crampin. Lattice vibrations of γ- and β-coronene from Raman microscopy and theory. *Physical Review Materials*, 3:125601, 2019.

[163] Robert J Meier. On art and science in curve-fitting vibrational spectra. *Vibrational Spectroscopy*, 39(2):266–269, 2005.

[164] RJ Wells. Rapid approximation to the Voigt/Faddeeva function and its derivatives. *Journal of Quantitative Spectroscopy and Radiative Transfer*, 62(1):29–48, 1999.

[165] Sanjar M Abrarov and Brendan M Quine. Efficient algorithmic implementation of the Voigt/complex error function based on exponential series approximation. *Applied Mathematics and Computation*, 218(5):1894–1902, 2011.

[166] Walter Gautschi. Efficient computation of the complex error function. *SIAM Journal on Numerical Analysis*, 7(1):187–198, 1970.

[167] Peter E Blöchl. Projector augmented-wave method. *Physical review B*, 50(24): 17953, 1994.

[168] Georg Kresse and D Joubert. From ultrasoft pseudopotentials to the projector augmented-wave method. *Physical Review B*, 59(3):1758, 1999.

[169] Atsushi Togo, Fumiyasu Oba, and Isao Tanaka. First-principles calculations of the ferroelastic transition between rutile-type and $CaCl_2$-type SiO_2 at high pressures. *Physical Review B*, 78(13):134106, 2008.

[170] A. Fonari and S. Stauffer. vasp_raman.py, 2013. URL github.com/raman-sc/VASP/.

[171] Jonathan M Skelton, Lee A Burton, Adam J Jackson, Fumiyasu Oba, Stephen C Parker, and Aron Walsh. Lattice dynamics of the tin sulphides SnS_2, SnS and Sn_2S_3: Vibrational spectra and thermal transport. *Physical Chemistry Chemical Physics*, 19(19):12452–12465, 2017.

[172] J. Skelton. Phonopy-Spectroscopy, 2018. URL github.com/JMSkelton/Phonopy-Spectroscopy/.

[173] Olga Kataeva, Mikhail Khrizanforov, Yulia Budnikova, Daut Islamov, Timur Burganov, Alexander Vandyukov, Konstantin Lyssenko, Benjamin Mahns, Markus Nohr, Silke Hampel, et al. Crystal growth, dynamic and charge transfer properties of new coronene charge transfer complexes. *Crystal Growth & Design*, 16(1): 331–338, 2015.

[174] Barbara Lafuente, Robert T Downs, Hexiong Yang, and Nate Stone. The power of databases: the RRUFF project. In *Highlights in Mineralogical Crystallography*, pages 1–29. Walter de Gruyter GmbH, 2016.

[175] M. A. Kovner L. M. Babkov. Out-of-plane vibrations of the coronene molecule. *Optics and Spectroscopy*, 35:214, 1973.

[176] So Hirata, Kandis Gilliard, Xiao He, Jinjin Li, and Olaseni Sode. Ab initio molecular crystal structures, spectra, and phase diagrams. *Accounts of Chemical Research*, 47(9):2721–2730, 2014.

[177] Tommaso Salzillo, Andrea Giunchi, Matteo Masino, Natalia Bedoya-Martınez, Raffaele G Della Valle, Aldo Brillante, Alberto Girlando, and Elisabetta Venuti. An alternative strategy to polymorph recognition at work: The emblematic case of coronene. *Crystal Growth & Design*, 18(9):4869–4873, 2018.

[178] Łukasz Szeleszczuk, Dariusz Maciej Pisklak, Tomasz Gubica, Klaudia Matjakowska, Sławomir Kaźmierski, and Monika Zielińska-Pisklak. Application of combined solid-state NMR and DFT calculations for the study of piracetam polymorphism. *Solid State Nuclear Magnetic Resonance*, 97:17–24, 2019.

[179] Chandler Greenwell, Jessica L McKinley, Peiyu Zhang, Qun Zeng, Guangxu Sun, Bochen Li, Shuhao Wen, and Gregory JO Beran. Overcoming the difficulties of predicting conformational polymorph energetics in molecular crystals via correlated wavefunction methods. *Chemical Science*, 2020.

[180] Jan Gerit Brandenburg, Jason Potticary, Hazel A Sparkes, Sarah L Price, and Simon R Hall. Thermal expansion of carbamazepine: Systematic crystallographic measurements challenge quantum chemical calculations. *The Journal of Physical Chemistry Letters*, 8(17):4319–4324, 2017.

[181] R Ramírez, N Neuerburg, M-V Fernández-Serra, and CP Herrero. Quasi-harmonic approximation of thermodynamic properties of ice Ih, II, and III. *The Journal of Chemical Physics*, 137(4):044502, 2012.

[182] Alessandro Erba, Jefferson Maul, and Bartolomeo Civalleri. Thermal properties of molecular crystals through dispersion-corrected quasi-harmonic ab initio calculations: The case of urea. *Chemical Communications*, 52(9):1820–1823, 2016.

[183] Michael T Ruggiero, J Axel Zeitler, and Alessandro Erba. Intermolecular anharmonicity in molecular crystals: Interplay between experimental low-frequency dynamics and quantum quasi-harmonic simulations of solid purine. *Chemical Communications*, 53(26):3781–3784, 2017.

[184] Ctirad Červinka and Gregory JO Beran. Ab initio prediction of the polymorph phase diagram for crystalline methanol. *Chemical Science*, 9(20):4622–4629, 2018.

[185] Roberto Dovesi, Alessandro Erba, Roberto Orlando, Claudio M Zicovich-Wilson, Bartolomeo Civalleri, Lorenzo Maschio, Michel Rérat, Silvia Casassa, Jacopo Baima, Simone Salustro, et al. Quantum-mechanical condensed matter simulations with CRYSTAL. *Wiley Interdisciplinary Reviews: Computational Molecular Science*, 8(4):e1360, 2018.

[186] Feng Zhang, Houng-Wei Wang, Keisuke Tominaga, and Michitoshi Hayashi. Mixing of intermolecular and intramolecular vibrations in optical phonon modes: Terahertz spectroscopy and solid-state density functional theory. *Wiley Interdisciplinary Reviews: Computational Molecular Science*, 6(4):386–409, 2016.

[187] Jun Yang, Weifeng Hu, Denis Usvyat, Devin Matthews, Martin Schütz, and Garnet Kin-Lic Chan. Ab initio determination of the crystalline benzene lattice energy to sub-kilojoule/mole accuracy. *Science*, 345(6197):640–643, 2014.

[188] Xiao-Miao Zhao, Jiang Zhang, Adam Berlie, Zhen-Xing Qin, Qiao-Wei Huang, Shan Jiang, Jian-Bo Zhang, Ling-Yun Tang, Jing Liu, Chao Zhang, et al. Phase transformations and vibrational properties of coronene under pressure. *The Journal of Chemical Physics*, 139(14):144308, 2013.